A RAMAN SCATTERING STUDY

OF LATTICE VIBRATIONS IN CRYSTALS

JOHN W. ARTHUR

Ph.D. Thesis

University of Edinburgh

JULY, 1974.

'The greatest fortune of thinking man is to have explored the explorable, and in quietude to reverence the unexplorable'

Goethe

ACKNOWLEDGEMENTS

The author wishes to express his gratitude to those who have helped in many ways, to make this work possible.

To Dr. W. Taylor and Professor W. Cochran for their supervision and encouragement.

To Drs. D.J. Lockwood, G.S. Pawley, H. Montgomery and Professor R.A. Cowley for their often sought advice.

To Dr. R.P. Rinaldi and Mr. G.A. Mackenzie for their assistance and collaboration at various stages.

To all of those whose friendship throughout this work counted no less.

For the facilities of the Department of Physics and the Regional Computing Centre at Edinburgh, and for the financial support of the Science Research Council, he is also grateful.

Thanks are due to Dr. J. Sherwood who provided the sulphur crystal, and to Dr. T. Luty who grew the decafluoro-biphenyl crystal.

ABSTRACT

The Raman scattering of lattice vibrations in molecular crystals is treated by an approximation based on the polarisability concept. Expressions relating the scattered intensity to the zone centre eigenvectors have been obtained in terms of a molecular polarisability. The application of this treatment to deriving information about eigenvectors from Raman scattering measurements is discussed, and a sum rule is given for checking intensity correlations.

Three systems have been designed and constructed for the automatic collection of data in Raman scattering experiments. Complementary to these, a program library has been developed for the handling and analysis of the collected data. These systems have been successfully applied to the gathering and analysis of data in several experiments.

The lattice vibration spectrum of the molecular crystal orthorhombic sulphur has been measured over the range 5 - 100 cm^{-1}, for all polarisations. In the analysis of the results, making use of the program library, it has been possible to clarify certain of the spectra which are subject to accidental depolarisation, and thereby to properly measure the phonon frequencies and intensities. The expressions developed for the scattering intensities are then applied to sulphur, and certain components of the zone centre eigenvectors deduced. Further, they are applied to a calculation of the Raman spectrum using eigenvectors predicted by the lattice dynamical calculation of Rinaldi. An improvement to the general calculation of the cross-section, which takes into account the local field, is proposed.

The lattice vibration spectrum of the molecular crystal decafluorobiphenyl, $C_{12}F_{10}$, has been measured for the first time. Several internal vibrations have also been measured, in the range 130 - 250 cm^{-1}, and it is deduced that these originate from vibrations internal to the individual phenyl rings, C_6F_5, while the inter-ring vibrations occur at much lower frequencies. An inter-ring vibration has been observed at 54 cm^{-1} in the melt. The problem of internal-external mode coupling, within the harmonic approximation, is discussed, and from the observed A_1 spectrum it is concluded that this effect is important. A polarisability calculation has been made, taking this into account, and this is applied to a calculation of the spectrum. The analysis leads us to conclude that the single external vibration of A_1 symmetry couples strongly to an internal torsional vibration of the molecule, quite possibly the vibration observed in the melt at 54 cm^{-1}. The eigenvectors of the coupled modes are deduced. Several 'extra' peaks which are observed in the lattice vibration region are held to originate from the other low frequency inter-ring vibrations. A way of treating decafluorobiphenyl in a lattice dynamical calculation is proposed.

The spectra of the ferroelectric crystals NH_4HSO_4 and $RbHSO_4$ have been measured over the range 7 - 3000 cm^{-1}, and at temperatures ranging both above and below their second-order phase transitions. The internal vibrations of the bisulphate ion are observed to undergo splittings and shifts in frequency with the onset of the ferroelectric phase. This may be accounted for by an LO - TO effect. Anomalous scattering at low frequency has been observed in the form of a 'Rayleigh wing' which gives way to an underdamped mode at temperatures below 190K. In

addition a peak of strongly temperature dependent intensity has been observed near 52 cm^{-1}. Although no direct connexion between these features and the phase transition has been established, the possibility of a 'soft' mode is not ruled out. The observations tend to support the accepted order-disorder model of the transition.

CONTENTS

C O N T E N T S (Contd.)

C O N T E N T S (Contd.)

CHAPTER 1

LATTICE VIBRATIONS AND LIGHT SCATTERING

In this chapter we review the basic problem of the dynamics of crystals. We establish the formalism of lattice vibrations and emphasize the role played by symmetry. This is followed by a development of the Raman scattering cross-section for crystals, with comments on its application.

1.1 Introduction

Crystals are a major class of solid of which special symmetries are the distinguishing feature. Two types of symmetry are implied - translational symmetry from cell to cell - and point symmetry - to do with the regularity of shape of the basic cell. These symmetries combine. Symmetries are classified according to the notion of a group, e.g. Tinkham[1]. There are 32 point groups consistent with the symmetries of a molecular solid, and combined with translational symmetries, belonging to cyclic groups, there are 230 distinct space groups according to which all perfect crystals may be classed. The point group plays the predominant role in the classification of physical properties, e.g. Nye[2], and throughout this work use will be made of symmetry properties. In fact it is the symmetry of crystals which allows understanding of a vast number of their physical properties on a microscopic basis. In the problem we are immediately concerned with, the dynamics of crystals, there are for all practical purposes an infinite number of degrees of freedom. As we shall see, translational

symmetry makes this many body problem tractable, and for crystals with highly symmetrical unit cells there is even greater simplification.

A crystal comprises nuclei of various types and electrons. In almost all cases it is possible to treat the dynamical problems of the electrons and nucleons according to the Born-Oppenheimer approximation[3]. The problem of lattice dynamics is concerned essentially with the motions of the heavy nuclei, which in the context of a crystalline structure can be pictured as lattice vibrations. The zeroth-order approximation for lattice vibrations is the Einstein model in which each nucleus is harmonically bound to its equilibrium position by its own "spring". There is no coupling between nuclei and there are no dispersive lattice waves. The harmonic approximation[3] allows for this coupling and dispersive lattice waves are found: this gives an adequate description of most crystals at reasonably low temperatures. From this basic approximation many refinements may be made, as required, to take into account the electronic motion and anharmonic corrections, but usually the same framework is maintained and the concept of a lattice vibration is still valid.

1.2 The Dynamics of a Crystal

In a crystal the equations of motion in the harmonic approximation have an elegant solution. The nuclear part of the Hamiltonian is of the form:

$$2H = \sum_{\ell K} \left\{ m_K \dot{u}(\ell K)^2 + \sum_{\ell' K'} V\binom{\ell \ \ell'}{K \ K'} u(\ell K) u(\ell' K') \right\}. \qquad (1.1)$$

ℓ indexes lattice cells and K combines indices for atoms within the cell and for x, y, z. The harmonic approximation is assumed to be valid for small nuclear displacements $\underline{u}$. A plane wave solution of the form:

$$u(\ell K) = \frac{A\, e_K}{\sqrt{N m_K}} \exp(i(\underline{Q}.\underline{R}(\ell) - \omega t)) \qquad (1.2)$$

is sought with:

$$\sum_K e_K^2 = 1$$

and

$$N = \sum_\ell 1 \ . \qquad (1.3)$$

A is the wave amplitude, $\underline{Q}$ wavevector, and $\{e_K\}$ the components of the polarisation vector; $\underline{R}(\ell)$ is the position of the ℓth cell, and ω is the frequency. This gives:

$$2H = \omega^2 |A|^2 + \frac{1}{N} \sum_\ell |A|^2 \sum_{KK'} e_K e_{K'} \Bigg[\sum_{\ell'} V\binom{\ell \ -\ell'}{K \ K'} \times \exp(i\, \underline{Q}.(\underline{R}(\ell) - \underline{R}(\ell'))) \Bigg] , \qquad (1.4)$$

but translational symmetry implies:

$$\sum_{\ell'} V\binom{\ell \ -\ell'}{K \ K'} \exp(i\, \underline{Q}.(\underline{R}(\ell) - \underline{R}(\ell')))$$

$$= \sum_{\ell''} V\binom{\ell'' \ \ell''}{K \ K'} \exp(i\, \underline{Q}.(\underline{R}(\ell'')) = V_{KK'}(\underline{Q}) \ . \qquad (1.5)$$

Thus, the Hamiltonian is reduced to the quadratic form:

$$2H = A^2 \left(\omega^2 + \sum_{\kappa\kappa'} e_\kappa V_{\kappa\kappa'}(\underline{Q}) e_{\kappa'}\right) . \qquad (1.6)$$

This equation has at most $3n$ degrees of freedom where n is the number of atoms in the primitive cell, and $V(\underline{Q})$ has some analogy with the fourier transform of $V(\underline{R})$, the interatomic potential. The $\{e_\kappa\}$ are not yet specified, but chosen appropriately (1.6) becomes $3n$ decoupled equations. The $\{e_\kappa\}$ are, of course, the elements of the orthogonal matrix which diagonalises $V_{\kappa\kappa'}(Q)$. We can then write

$$2H = A^2 \left(\omega^2 + \omega^2(\underline{Q}, j)\right) \qquad (1.7)$$

where we define the $3n$ choices of orthogonal $\{e_\kappa\}$ by:

$$\sum_{\kappa\kappa'} e^j_\kappa(Q) V_{\kappa\kappa'}(Q) e^{j'}_{\kappa'}(Q) = \omega^2(\underline{Q}, j)\delta_{jj'} . \qquad (1.8)$$

The dynamical problem has been simplified to $3nN$ simple harmonic oscillators defined by (1.7) and (1.8). Completeness of the solution, however, requires that

$$u(\ell, \kappa) = \sum_{Q,j} \frac{A(\underline{Q}, j)}{\sqrt{Nm_\kappa}} e^j_\kappa(Q) \exp(i\, \underline{Q}.\underline{R}(\ell)) \qquad (1.9)$$

for arbitrary $u(\ell, \kappa)$. This can be done provided that the equation can be inverted to give $A(\underline{Q}, j)$. In fact taking:

$$A(\underline{Q}, j) = \sum_{\ell'\,\kappa'} \sqrt{\frac{m_\kappa}{N}}\, u(\ell'\,\kappa') e^j_{\kappa'} \exp(-i\, \underline{Q}.\underline{R}(\ell')), \qquad (1.10)$$

gives, from (1.9),

$$u(\ell\,\kappa) = \frac{1}{N} \sum_{\ell'\kappa'} u(\ell'\kappa') \sum_{j} e^{j}_{\kappa} e^{j}_{\kappa'} \sum_{\underline{Q}} \exp(i\,\underline{Q}.(\underline{R}(\ell)-\underline{R}(\ell'))). \tag{1.11}$$

But we have

$$\sum_{j} e^{j}_{\kappa} e^{j}_{\kappa'} = \delta_{\kappa\kappa'} \tag{1.12}$$

and

$$\sum_{\underline{Q}} \exp(i\,\underline{Q}.(R(\ell) - R(\ell')) = N\delta_{\ell\ell'} \tag{1.13}$$

which gives the desired result. Relation (1.13) obtains because of the translational symmetry of the lattice, and it is conjugate to the relationship associated with Bragg scattering

$$\sum_{\ell} \exp(i\,\underline{Q}.\underline{R}(\ell)) = N\,\delta\,\underline{Q},\,\underline{G} \tag{1.14}$$

where $\underline{G}$ is any reciprocal lattice vector. It is to be emphasised that $\underline{Q}$ need only be chosen from the smallest set of vectors, those contained in the first Brillouin Zone[4]. All other values of $\underline{Q}$ are degenerate with a value inside the zone giving, in all, only $3N - 2$ inequivalent values. (The crystallographic aspects of the reciprocal lattice, Brillouin Zone and Bragg scattering are discussed at length for example by Kittel[5]).

1.3 Symmetry

The eigenvectors $\hat{e}_j = e^{j}_{\kappa}\,\hat{i}_{\kappa}$ form a basis for representing the displacements of all atoms in the unit cell. There are $3n$ possible values for j and κ, but there may be fewer values of $\omega^2(\underline{Q}, j)$ at a given $\underline{Q}$. This is not

always accidental, for the point symmetry of the crystal, loosely the symmetry of the unit cell, determines the number of independent force constants. At a given $\underline{Q}$ the largest number of nondegenerate eigenvalues may be determined by deductions from group theory. Also the patterns of displacements of the eigenvectors may be classified according to their symmetry. At $\underline{Q} = 0$, the zone centre, the eigenvectors transform as a subgroup of the point group and may be classified according to the irreducible representations of the point group. Use of this fact will be made later in discussing particular results.

We now briefly examine the consequences of translational symmetry in the solution of (1.1). At equation (1.2) we introduced plane waves to obtain a particular solution for some $\underline{Q}$. This resulted in $\underline{Q}$ being a label for a particular set of eigenvalues of the Hamiltonian, $\omega^2(\underline{Q}, j)$. Indeed, this fact is implied by translational symmetry. Let t_k denote a translation by a lattice vector $R(k)$; then since t_k leaves H unchanged, the equation:

$$\hat{e}^j \, H \hat{e}_j = \tfrac{1}{2}(\omega^2 + \omega_j{}^2)$$

which is equivalent to:

$$\hat{e}^j \, t_k{}^{-1} (t_k \, H \, t_k{}^{-1}) \, t_k \hat{e}_j = \tfrac{1}{2}(\omega^2 + \omega_j{}^2)$$

becomes:

$$(\hat{e}^j \, t_k{}^{-1}) \, H \, (t_k \, \hat{e}_j) = \tfrac{1}{2}(\omega^2 + \omega_j{}^2) \, . \qquad (1.15)$$

This means that $t_k \, \hat{e}_j$ is an eigenvector of equal energy to

$\hat{e}_j$. If the eigenvectors are nondegenerate this implies:

$$t_k \hat{e}_j = C_k \hat{e}_j \qquad \text{where} \qquad |C_k|^2 = 1$$

$$= (C_a)^{k_x} (C_b)^{k_y} (C_c)^{k_z} \hat{e}_j \text{ for } R(k) = k_x \underline{a} + k_y \underline{b} + k_z \underline{c}$$

$$= \exp(i \underline{Q} \cdot R(k)) \hat{e}_j \qquad (1.16)$$

for some $\underline{Q}$. But $t_k \hat{e}_j$ is just the set of displacements at a distance $R(k)$, so that the solutions must be of the form:

$$u(\ell, \kappa) = u(0, \kappa) \exp(i \underline{Q} \cdot R(\ell)) \qquad (1.17)$$

which is of the form of (1.2). This is equivalent to Bloch's theorem[6]. $\underline{Q}$, the wavevector, is in fact the label of a representation of the cyclic group of translations $\{ t_k \}$ in the crystal according to which all the eigenvectors may be classified.

1.4 Quantisation of the Lattice Waves

The eigenvectors form a basis for normal coordinates of the Hamiltonian which becomes, from (1.7):

$$2H = \sum_{Qj} |A(Q,j)|^2 (\omega^2 + \omega^2(\underline{Q}, j)) \quad . \qquad (1.18)$$

This represents the sum of contributions from $3Nn - 3$ uncoupled oscillators, each of which may be quantised in the standard fashion, giving:

$$H = \sum_{Q,j} \hbar\,\omega(Q,j)\left\{ n(\omega(Q,j)) + \tfrac{1}{2} \right\} \tag{1.19}$$

$$\langle |A(Q,j)|^{2} \rangle = \frac{\hbar}{\omega(Q,j)}\left\{ n(\omega(Q,j)) + \tfrac{1}{2} \right\} \tag{1.20}$$

and for a crystal in thermal equilibrium at temperature T, the population, $n(\omega)$, is given by

$$n(\omega) = \frac{1}{e^{\frac{\hbar\omega}{k_B T}} - 1} \quad . \tag{1.21}$$

The quantised lattice vibrations are called phonons. The eigenvectors and eigenfrequencies of the phonons are determined in the same way as they are classically by the transformation to normal coordinates. In a real crystal with anharmonic forces the solutions are no longer exact phonons, but in a perturbation treatment the concept of phonons remains. The phonons now have finite lifetimes and are altered in frequency[7]. The magnitude of these effects is temperature dependent, generally becoming greater at higher temperatures.

1.5 Raman Scattering in Crystals

The Raman effect is the inelastic scattering of light by molecular vibrations. That is, if light of a single frequency is incident on a molecular system (crystal, gas, or liquid), a fraction of it is scattered into sidebands. The energy difference in the scattering process is given out, or taken up, by a molecular, or lattice, vibration, Fig. 1.1.

FIGURE 1.1

The three first order scattering processes and the spectrum of the scattered light.

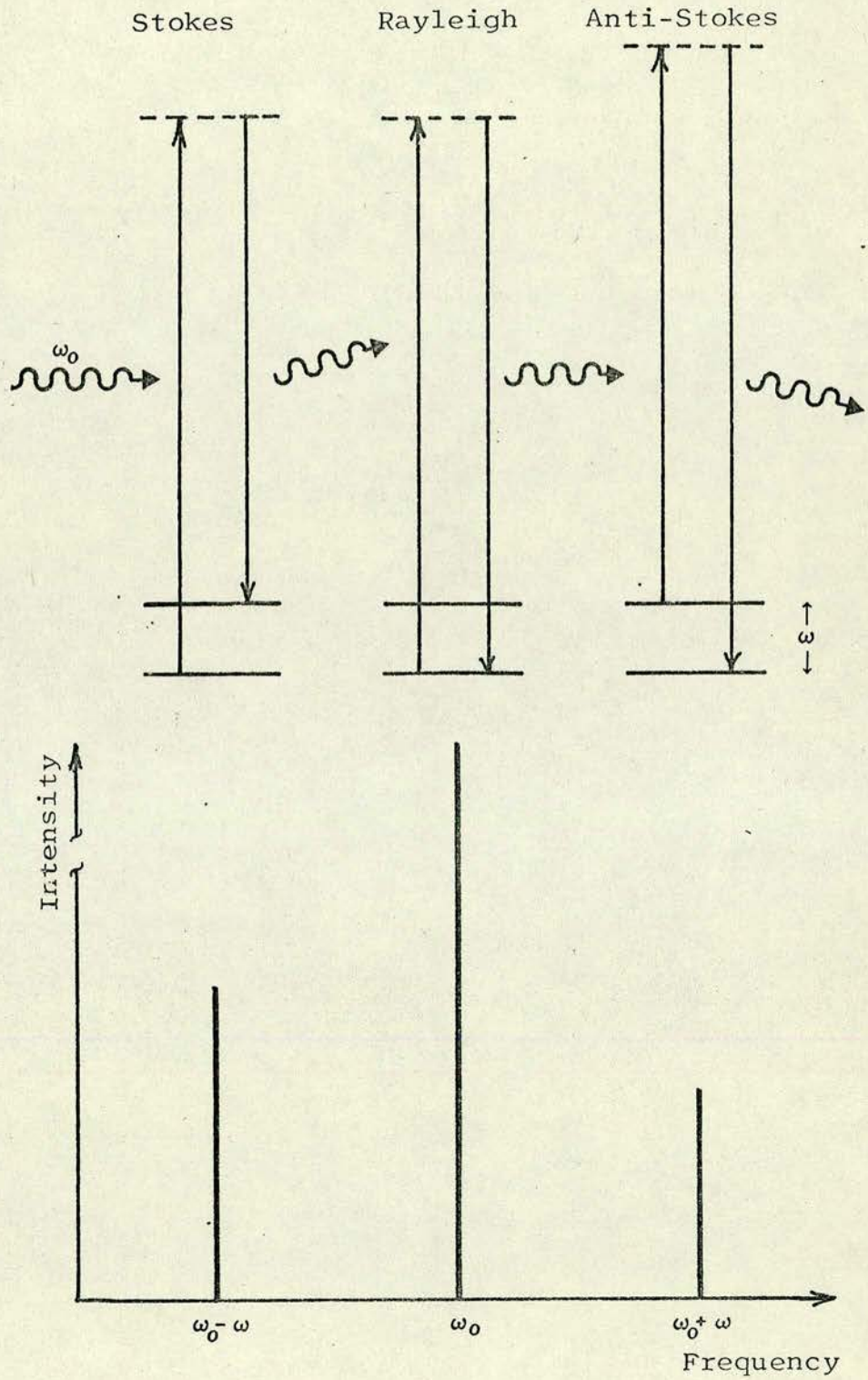
Stokes
Rayleigh
Anti-Stokes
ω_o
ω
Intensity
$\omega_o - \omega$
ω_o
$\omega_o + \omega$
Frequency

It was discovered in 1928 by Raman in studies on liquids[8], and almost simultaneously by Landsberg and Mandelstam[9] in solids. The term Raman scattering is now also applied to scattering from general types of excitations, for example plasmons, excitons and magnons, as well as phonons. In solids, Raman scattering is an important method of measuring phonon frequencies. Raman scattering of acoustic phonons is called Brillouin scattering, the term Raman scattering being reserved for scattering at higher frequency from optic phonons. The frequency range covered by Raman scattering is typically 10 to 3,000 cm^{-1}.

Raman scattering occurs in a crystal if there are phonons present which can modulate the electronic polarisability. It follows from the Born-Oppenheimer approximation that the polarisability is of the form:

$$\alpha_e = \alpha_e(\{u(\ell\kappa, t)\}) = \alpha_e(\{A(Q, j), \omega(Q_j)t\}) \quad . \tag{1.22}$$

In the presence of an exciting electric field, $\underline{E}(t)$, this gives rise to a polarisation field

$$\underline{P}(t) = \alpha_e \underline{E} = (\alpha_o + \alpha'(t))\underline{E} \quad . \tag{1.23}$$

The part $\alpha'(t)\underline{E}$ is the time dependent part which is in addition to the contribution of the static lattice. The polarisability approach was formalised quantum mechanically by Placzeck[10]. We now give a derivation which incorporates the quantisation of the light field.

1.6 The Interaction of Light with a Crystal: Polarisability

The coupling of radiation fields with electrons and atoms in transparent crystals at optical frequencies is very weak. The Hamiltonian of the total system of light and crystal may be written as the sum of the crystal term H_ℓ, the radiation term H_R and the dipole interaction term $-\underline{M}.\underline{E}$:

$$H = H_\ell + H_R - \underline{M}.\underline{E} \tag{1.24}$$

where $\underline{M}$ is the dipole moment operator of the whole crystal, and $\underline{E}$ is the electric field operator. In the weak coupling approximation the eigenstates of the uncoupled system $\langle \ell |$ of the lattice, and $\langle r|$, of the radiation, form basis states $\langle \ell | \langle r|$ for the coupled system. The electric field operator $\underline{E}$ is given in terms of the photon creation and destruction operators thus:

$$\underline{E}(k) = -i \left(\frac{h\,\omega_k}{\varepsilon_o V}\right)^{\frac{1}{2}} \underline{\varepsilon}(k)(b_k^{+} - b_{-k}) \quad . \tag{1.25}$$

We adopt a plane wave representation in a box volume V so that $\underline{k}$ is the wavevector and $\underline{\varepsilon}(k)$ the polarisation vector normal to $\underline{k}$ [11]. (1.24) then yields for $\langle H \rangle$

$$\begin{aligned}
\langle H \rangle &\doteq \langle \ell r \,|\, H \,|\, \ell r \rangle \\
&= \langle \ell \,|\, H_\ell \,|\, \ell \rangle + \langle r \,|\, H_r \,|\, r \rangle + \\
&\sum_\alpha \langle \ell \,|\, M_\alpha \,|\, \ell \rangle \langle r \,|\, E_\alpha \,|\, r \rangle + \\
&\frac{1}{\hbar} \sum_{\alpha\beta} \sum_{ms} \frac{\langle \ell | M_\alpha | m \rangle \langle m | M_\beta | \ell \rangle \langle r | E_\alpha | s \rangle \langle s | E_\beta | r \rangle}{(\omega_{\ell m} + \omega_{rs})}
\end{aligned} \tag{1.26}$$

to second order terms.

Using the properties of the photon operators the matrix elements become, for particular waves belonging to $\underline{k}$ and $\underline{k}'$:

$$\langle r \,|\, E_\alpha \,|\, s \rangle \langle s \,|\, E_\beta \,|\, r \rangle \;\propto$$

$$\langle r \,|\, b_k^{+} - b_{-k} \,|\, s \rangle \langle s \,|\, b_{k'}^{+} - b_{-k'} \,|\, r \rangle \, \varepsilon_\alpha(k) \, \varepsilon_\beta(k') \,. \quad (1.27)$$

Introducing the number representation for the states of the radiation field the only nonvanishing terms are with $k' = -k$:

$$\langle n(k) \,|\, b^{+}_k \,|\, n(k) - 1 \rangle \langle n(k) - 1 \,|\, b_k \,|\, n(k) \rangle$$

$$+ \langle n(k) \,|\, b_k \,|\, n(k) + 1 \rangle \langle n(k) + 1 \,|\, b^{+}_k \,|\, n(k) \rangle$$

$$= \left[n(k) \right] + \left[n(k) + 1 \right] \,. \quad (1.28)$$

Therefore the interaction energy, $-\underline{M}.\underline{E}$, may be evaluated as:

$$\langle \ell r \,|\, - \underline{M}.\underline{E} \,|\, \ell r \rangle$$

$$= \sum_{\alpha\beta} \Bigg[\left\{ \sum_m{}' \frac{\langle \ell | M_\alpha | m \rangle \langle m | M_\beta | \ell \rangle}{\hbar(\omega_{\ell m} - \omega_k)} \right\} n(k) \, \varepsilon_\alpha(k) \, \varepsilon_\beta(k)$$

$$+ \left\{ \sum_m{}' \frac{\langle \ell | M_\alpha | m \rangle \langle m | M_\beta | \ell \rangle}{\hbar(\omega_{\ell m} + \omega_k)} \right\} (n(k) + 1) \varepsilon_\alpha(k) \, \varepsilon_\beta(k) \Bigg] \,. \quad (1.29)$$

In the limit of $n(k)$ becoming large this is of the form

$$\sum_{\alpha\beta} \left[P^{\ell\ell}_{\alpha\beta}(\omega_k) + P^{\ell\ell}_{\alpha\beta}(-\omega_k) \right] E_\alpha E_\beta \sim \underline{P}.\underline{E} \qquad (1.30)$$

which shows that the matrix element terms can be identified as the matrix elements of the polarisability operator.

1.7 The Scattering

According to Fermi's "Golden Rule", applied in second order, the transition rate from initial state $|\ell\ r\rangle$ to final state $|n\ t\rangle$ is given by

$$w(\ell r \rightarrow nt) = \frac{2\pi}{\hbar^3} \left| \sum'_{\substack{\alpha\beta \\ m\ s}} \frac{\langle n|M_\alpha|m\rangle\langle m|M_\beta|\ell\rangle\langle t|E_\alpha|s\rangle\langle s|E_\beta|r\rangle}{(\omega_{\ell m} + \omega_{rs})} \right|^2 \times \delta(\omega_{n\ell} + \omega_{rt}) \qquad (1.31)$$

Writing E_α and E_β in terms of photon operators for the states k and k', represented by $|n(k), n(k')\rangle$, the contribution which couples k and k' - giving rise to scattering - is of the form:

$$\langle n(k)-1,\ n(k')+1 |\ b^+_{k'}\ |\ n(k)-1,\ n(k')\rangle \quad \times$$

$$\langle n(k)-1,\ n(k')\ |\ b_k\ |n(k),\ n(k')\rangle \ \exp i(\underline{k}-\underline{k}').\underline{r}$$

$$= \sqrt{n(k)}\ \sqrt{n(k')+1}\ \exp i(\underline{k}-\underline{k}').\underline{r}\ . \qquad (1.32)$$

For this contribution $\omega_{rs} = \omega_k$ and $\omega_{rt} = \omega_k - \omega_{k'}$.

There are also seven other terms corresponding to the equivalent process, scattering from k' to k, to elastic

or Rayleigh scattering from k to k , and to two photon emission and absorption. The latter processes do not couple different photon states and do not apply to Raman scattering. Substituting (1.32) into the transition probability then gives:

$$w(\ell,r,k \longrightarrow n,t,k') = \frac{2\pi\hbar}{\varepsilon_o^2 V^2}\,\omega_k\omega_{k'} \sum_{\substack{\alpha\beta\\ \gamma\delta}} P^{n\ell}_{\alpha\beta}(k,k')\; P^{n\ell}_{\gamma\delta}(k,k') \times$$

$$n(k)(n(k')+1)\;\varepsilon_\alpha(k')\;\varepsilon_\beta(k)\varepsilon_\gamma(k')\varepsilon_\delta(k) \times$$

$$\delta(\omega_{n\ell} + \omega_{kk'}) \qquad (1.33)$$

where $$P^{n\ell}_{\alpha\beta}(k,k') = \sum_{m'} \frac{\langle n \mid M_\alpha \mid m\rangle\langle m \mid M_\beta \mid \ell\rangle}{(\omega_{\ell m} + \omega_k)} \exp(i\,\underline{\Delta k}.\underline{r}) \qquad (1.34)$$

Now since $n(k)$ is always large, we can replace it by the expression $\frac{1}{2}\varepsilon_o V\ E^2/\hbar\omega_k$ so that we then have:

$$w = \frac{\pi\omega_{k'}}{\varepsilon_o V} \sum_{\substack{\alpha\beta\\ \gamma\delta}} P^{n\ell}_{\alpha\beta}(\omega_k)\; P^{n\ell}_{\gamma\delta}(\omega_k)\; E_\beta(k)E_\delta(k)\varepsilon_\alpha(k')\varepsilon_\gamma(k') \times$$

$$\times\ (n(k')+1)\ \delta(\omega_{n\ell} + \omega_{kk'}) \quad . \qquad (1.35)$$

Finally, to get the total cross-section, we must sum over all energetically accessible states. We retain the individual crystal states $|n\rangle$ and $|\ell\rangle$ so that the sum is over all the final photon states of energy $\omega_{k'} = \omega_k - \omega_{n\ell}$, within the box volume V. The scattering rate is then:

$$w d\Omega = \frac{\omega_{k'}^{3}}{2\pi^{2}\varepsilon_{o}c^{3}} \sum_{\substack{\alpha\beta \\ \gamma\delta}} P_{\alpha\beta}^{n\ell} P_{\gamma\delta}^{n\ell} E_{\beta}E_{\delta}\varepsilon_{\alpha}\varepsilon_{\gamma} (n(k')+1). \quad (1.36)$$

This represents the number of photons per unit time scattered into the element of solid angle $d\Omega$ along the wavevector $\underline{k}'$ corresponding to a transition $|\ell\rangle \rightarrow |n\rangle$ in the crystal, with a change in wavevector $\underline{\Delta k}$ and frequency $\omega_{kk'}$. This formula is valid for all types of weak excitation, the usual case being where $n(k')$ is initially zero. When $n(k')$ is initially $\gtrsim 1$ the process becomes the stimulated Raman effect[12], having an enhanced cross-section.

1.8 Scattering from Phonons

At optical frequencies, far beyond the crystal's vibrational spectrum, the major contribution to the polarisability is from the electrons (even in polar crystals). Since in the adiabatic approximation the electrons configure themselves to the nuclear coordinates, there is however a modulation of the electronic polarisability by phonons, as outlined in Section 1.5. This may be expressed as follows. We define $P_{\alpha\beta}(k,k')$ by:

$$P_{\alpha\beta}^{n\ell}(k,k') = \langle e, v \mid P_{\alpha\beta}(k,k') \mid e', v' \rangle \quad (1.37)$$

where e labels electronic states dependent on the nuclear coordinates $\underline{R}$, and v labels the phonon states. In insulating crystals we may take the electrons to be always in the ground state at normal temperatures for the purposes of evaluating (1.37). Therefore we have:

$$P^{n\ell}_{\alpha\beta}(k,k') = \langle 0, v | P_{\alpha\beta}(k,k') | v', 0 \rangle$$

$$= \langle v | \langle 0 | P_{\alpha\beta}(k,k') | 0 \rangle | v' \rangle$$

$$= \langle v | P_{\alpha\beta}(k,k',\underline{R}) | v' \rangle \quad . \qquad (1.38)$$

The $\underline{R}$ dependence of $|0\rangle$ becomes incorporated in $P_{\alpha\beta}(\omega)$ when the matrix element is formed, and so we then write this as $P_{\alpha\beta}(\omega,\underline{R})$. A detailed account of the theory behind the elimination of the electronic coordinates is given by Born and Huang[3]. Loudon[13] uses a different approach, however, where the electronic process is considered in more detail. Since in the present work we shall never consider the electronic processes in detail, the polarisability method is more appropriate. The Raman scattering of phonons comes about because of this dependence of the electronic polarisability on the nuclear coordinates $\underline{R}$, and for small nuclear displacements we may express this dependence as

$$P_{\alpha\beta}(k\,k',R) = P^{o}_{\alpha\beta}(k\,k') +$$

$$+ \sum_{\substack{\ell \\ k}} P^{1}_{\alpha\beta}\binom{\ell\ k}{\kappa, k'} u(\ell\kappa) + \sum_{\substack{\ell\ell' \\ \kappa\kappa'}} P^{2}_{\alpha\beta}\binom{\ell\ \ell'\ k}{\kappa\ \kappa'\ k'} u(\ell\kappa)u(\ell'\kappa') + \ldots . \qquad (1.39)$$

Transforming to normal coordinates, (1.2), and retaining only terms up to first order in the expansion we then have:

FIGURE 1.2

Showing the allowed wavevectors of photons, $\underline{k}$, and phonons, $\underline{Q}$, for 90° scattering geometry. The difference between k_s^+ and k_s^- has been exaggerated to show how the relative areas of the shaded regions account for the factor $\frac{\omega_{k'}^2}{c^2}$ in going from (1.35) to (1.36).

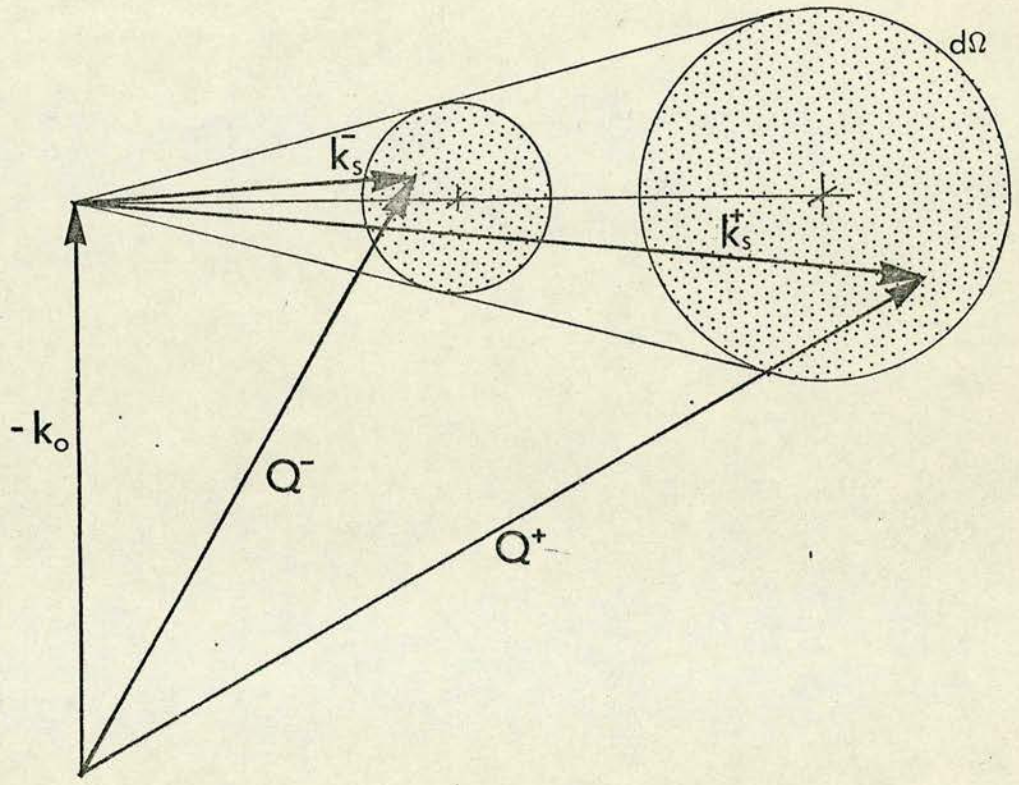
dΩ
k_s^-
k_s^+
$-k_o$
Q^-
Q^+

$$\underline{\underline{P}}(k\,k',R) = \underline{\underline{P}}^{o}(k,k') +$$

$$+ \sum_{\substack{\ell\kappa \\ Qj}} \frac{A(Q,j}{\sqrt{Nm_\kappa}}\, e^{j}_{\kappa}(Q)\, \exp(iQ.R(\ell))\, \underline{\underline{P}}^{1}\begin{pmatrix}\ell & k\\ \kappa & k'\end{pmatrix} \quad (1.40)$$

$$= \underline{\underline{P}}^{o}\begin{pmatrix}k\\ k'\end{pmatrix} + \sum_{Qj} A(Q,j) \sum_{\ell\kappa} \frac{e^{j}_{\kappa}(Q)}{\sqrt{Nm_\kappa}}\, \underline{\underline{P}}^{1}\begin{pmatrix}\ell & k\\ \kappa & k'\end{pmatrix} \exp(iQ.R(\ell)) \quad (1.41)$$

We can perform the sum over ℓ, but making reference to the definition of $P_{\alpha\beta}(k,k')$ in (1.34) we must include the $\exp(i\,\Delta k.r)$ dependence. This accounts for the varying phases of the incident and scattered light waves as they progress through the crystal. We therefore write

$$\underline{\underline{P}}^{1}\begin{pmatrix}\ell & k\\ \kappa & k'\end{pmatrix} = \underline{\underline{P}}^{1}\begin{pmatrix}0\\ \kappa\end{pmatrix} k)\exp(i\,\Delta k.R(\ell)) \quad (1.42)$$

and obtain, using (1.14):

$$\underline{\underline{P}}(kk',R) = \underline{\underline{P}}^{o}(kk') + \sum_{j} A(Q,j)\, \underline{\underline{P}}^{1}(j,k) \quad (1.43)$$

where $$\underline{G} + \underline{Q} + \Delta k = 0 \quad (1.44)$$

and $$\underline{\underline{P}}^{1}(j,k) = \sum_{\kappa} \frac{e^{j}_{\kappa}(Q)}{\sqrt{M_\kappa}}\, \underline{\underline{P}}^{1}\begin{pmatrix}0\\ \kappa\end{pmatrix}, k) \quad . \quad (1.45)$$

Equation (1.44) is often called the conservation of crystal momentum. In practice $|\Delta k| \ll |G|$, so that effectively $\underline{Q} = 0$ in first order scattering. The interpretation of (1.45) is that $\underline{\underline{P}}^{1}(j,k)$ is the change of electronic polarisibility induced by the presence of a mode $A(Q,j)$ in the crystal.

In Chapter Three we discuss a model for evaluating this term in molecular crystals, but for the present we treat it as some unknown parameter depending only on the electronic properties of the crystal at frequency ω_k. We can now evaluate the $P^{n\ell}_{\alpha\beta}$ factors occurring in (1.36) simply by taking the matrix elements of (1.43) between phonon states, as indicated in (1.38). We then obtain the first order Raman scattering for phonons as:

$$wd\Omega = \frac{\omega_{k'}^3}{2\pi^2\varepsilon_o c^3} \sum_j \frac{\hbar}{\omega_j}\Big[(n(\omega_j)+1)\delta(\omega_k-\omega_{k'}-\omega_j) + n(\omega_j)\delta(\omega_k - \omega_{k'} + \omega_j)\Big] \times (n(k') + 1)$$

$$\times \sum_{\alpha\beta} P^1_{\alpha\beta}(j, k)\; P^{*1}_{\gamma\delta}(j,k) E_\beta\, E_\delta\, \varepsilon_\alpha\, \varepsilon_\gamma \; . \qquad (1.46)$$

The first term in the square brackets represents scattering with loss of photon energy, $\omega_{k'} = \omega_k - \omega_j$ and this is called Stokes scattering. The second term is scattering with energy gain called anti-Stokes scattering. The difference in the cross-section for these two types of scattering can not be explained by a classical theory.

1.9 Application.

We now briefly discuss various points about the application of (1.46) to experimental situations. Firstly, the last factor in the cross-section simplifies when the incident and scattered light is polarised along crystal axes. In this case, this term becomes:

$$\sum_{\substack{\alpha\beta \\ \gamma\delta}} P^1_{\alpha\beta} P^{*1}_{\gamma\delta} E_\beta E_\delta \varepsilon_\alpha \varepsilon_\gamma \rightarrow \sum_{\alpha\beta} \left| \varepsilon_\alpha P^1_{\alpha\beta} E_\beta \right|^2 . \quad (1.47)$$

Most experimental geometries are chosen in this fashion, and indeed in crystals which are birefringent this form should be adhered to, since otherwise the general complexities of light propagation in an anisotropic medium must be considered. Further, we have dropped the wave vector dependence in the cross-section, assuming $\underline{Q}$ to be effectively zero. This is not valid in piezoelectric materials[46],[14], where phonons having a dipole moment are highly dispersive near $\underline{Q} = 0$ because of direct interaction with the photon field. Another point of importance is that in real crystals the finite lifetime of the phonons gives rise to linewidth in the scattering. When the inverse lifetime is much smaller than the phonon frequency, this may be treated by replacing the delta functions by expressions of the form

$$\delta(\omega - \omega_j) \rightarrow \frac{\Gamma_j/2\pi}{(\omega - \omega_j)^2 + \frac{\Gamma_j^2}{4}} \qquad \Gamma_j \ll \omega_j , \quad (1.48)$$

where Γ_j is the inverse lifetime of the phonon.

Useful information about the symmetry of the phonons observed in a particular spectrum can be gained from the reduction of the scattering tensor, $P^1_{\alpha\beta}$, according to the irreducible representations of the point group of the crystal. $P_{\alpha\beta}$ transforms as a symmetric second rank tensor (i.e. like x^2, y^2, z^2, xy, xz and yz) . The rule is that a phonon can give rise to first order scattering only through a component of $P_{\alpha\beta}$ that transforms under the same irreducible representation.

FIGURE 1.3

Projection of the phonon dispersion curves at $Q = 0$ onto the Raman spectrum.

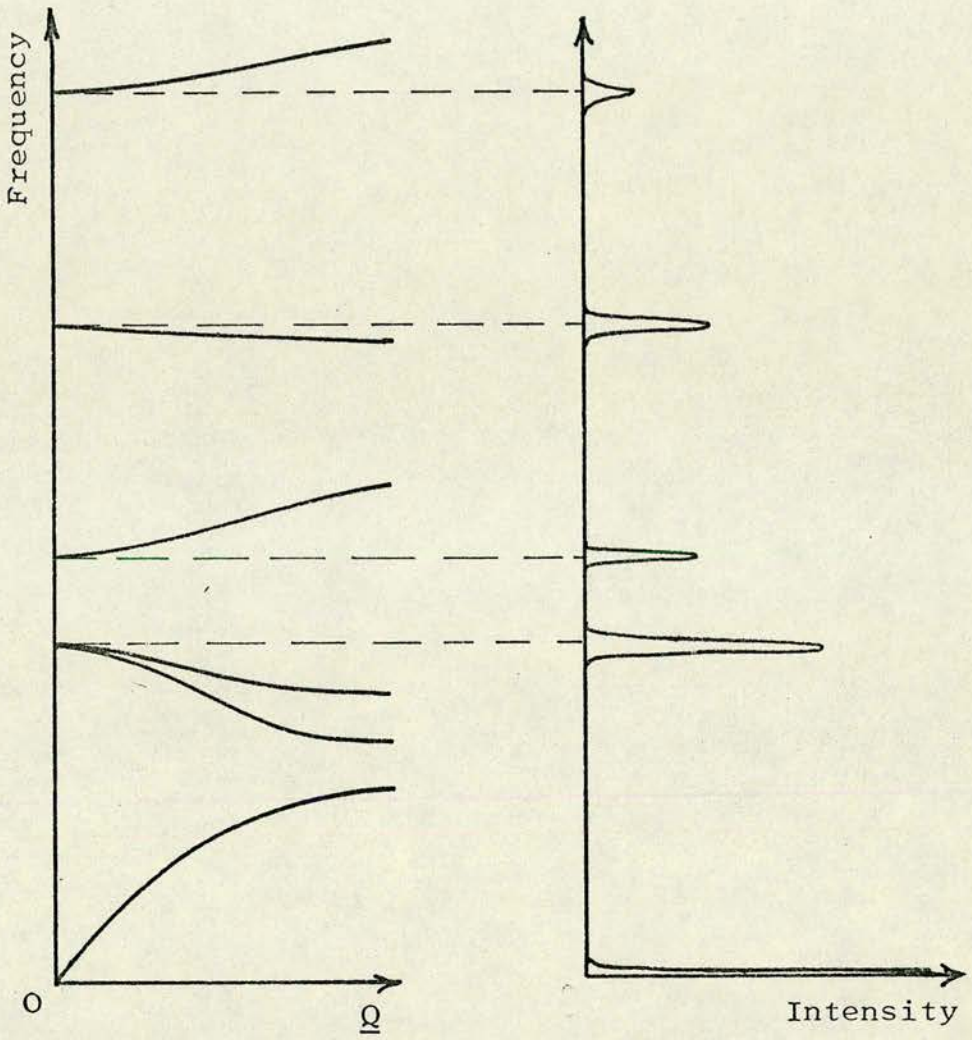
Frequency
O
Ω
Intensity

Figure 1.3 depicts the projection of the phonon dispersion curves of some crystal onto the Raman spectrum. In the majority of cases, however, little can be said about the scattered intensities and on this point the diagram is only illustrative.

CHAPTER 2

EXPERIMENTAL TECHNIQUE

Here we review the basics of the Raman scattering experiment and discuss the desirability of introducing automated data collection and control. Three systems which were developed to meet this need are described. The potential of the last of these systems is evaluated with a view to its future development.

2.1 Background

In common with other scattering experiments Raman scattering requires a source of probe particles and an analyser of scattered particles. The purpose of the experiment is to measure the response of the scattering material to a stimulus at a single frequency, wavevector and polarisation. The ideal probe is a powerful source of well collimated monochromatic radiation at a suitable frequency and polarisation. The ideal source is unquestionably the laser. The analyser should be able to measure the response at a given frequency over the required range near to the probe frequency. Additionally, the analyser should be able to discriminate well against the probe frequency when measurements are being made at a nearby frequency. The instrument used for this purpose in Raman spectroscopy is a grating monochromator. Often two or three monochromator stages are required to reach a sufficiently high discrimination against the probe frequency

FIGURE 2.1

Configuration of a typical Raman spectrometer showing sample illumination, collection optics and signal detection.

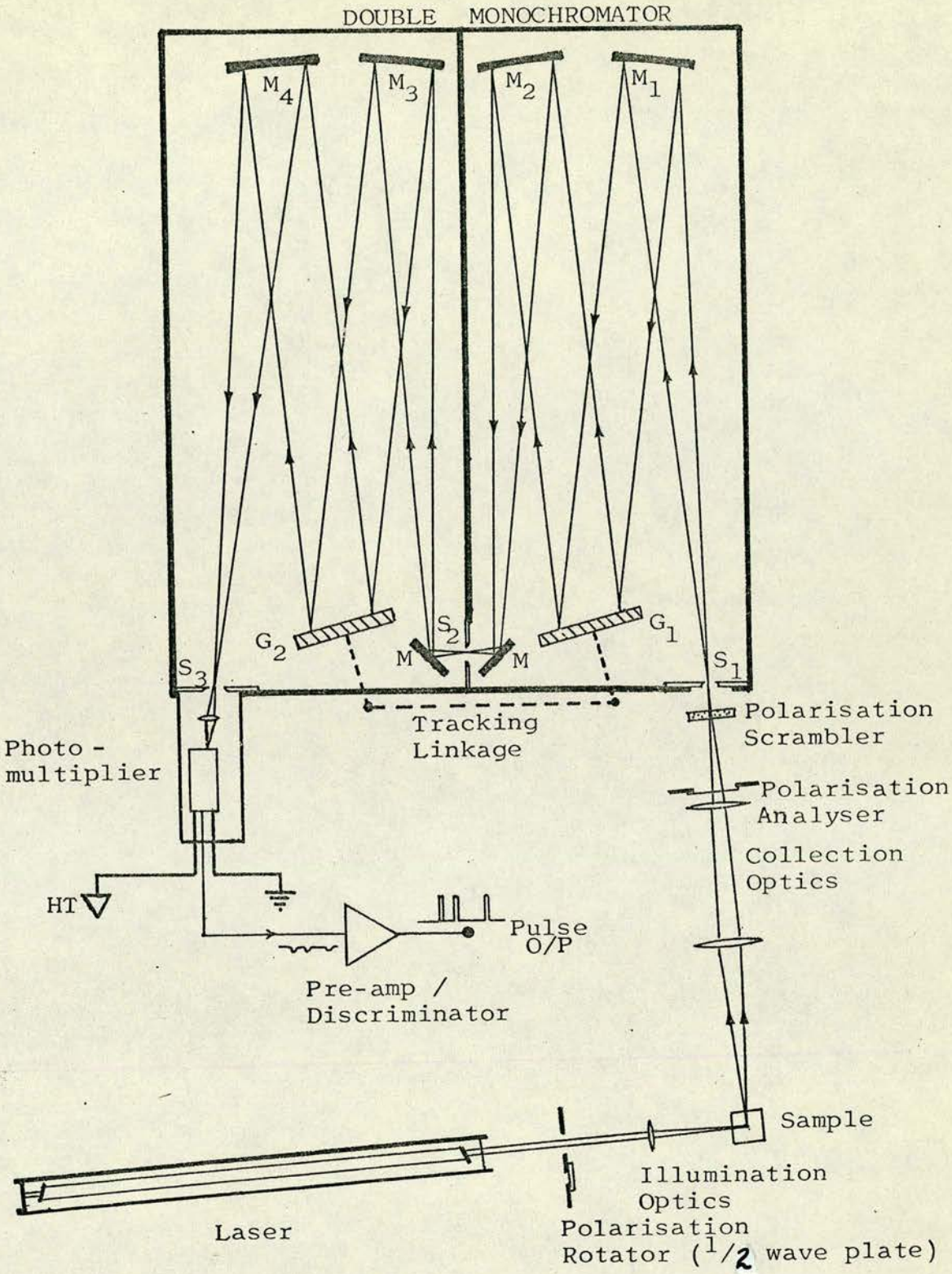

G - Grating

S - Slit

M - Mirror

at near frequencies. The analyser requires a detector and this is most commonly a good photomultiplier capable of detecting the weakest signals. Figure 2.1 gives the layout of a typical experiment. The monochromator shown is one of several types commercially available. In a typical experiment the result is obtained by integrating the pulse output from the photomultiplier preamplifier and displaying this (the photo-current) on a chart recorder as the gratings are scanned.

The greater part of this chapter is concerned with various developments of the basic experimental system. These developments are aimed at automation of the experiment. The reasons for this are many, but the two main ones deal with the problems of experimental control and data acquisition. In the spectroscopy of phase transitions many spectra must be collected at different temperatures (or pressures or applied fields) ideally under completely reproducible conditions. This introduces the problems of collecting and analysing vast amounts of data and of experimental control. We show how these problems may be solved using digital control and data acquisition systems, already discussed in part by Arthur and Lockwood[15]. The use of computers figures largely in these systems, albeit at different levels. The Systems,1, 2 and 3, will be described in the order in which they were built. Full details of the electronics involved are supplied in appendices I to III: only simplified diagrams to aid discussion are presented here. All the experimental results presented in later chapters, excepting the earliest on AHS, ammonium bisulphate, were obtained using these systems, as they progressed.

2.2 System 1

System 1 was conceived for the purpose of automatically programming on manually set switches (see Figure 2.2) the information necessary to scan the spectrometer a selected number of times over a chosen frequency range. Furthermore a multichannel scaler, MCS, was to be used as a storage medium for the spectrum so that the data of subsequent runs could be added together to do signal averaging. This last proposition requires a high degree of reproducibility in the scanning of the spectrometer. Figure 2.3 shows how System 1 acts as a control unit linking with the functions of spectrometer and MCS.

2.2.1 Wavenumber drive

The spectrometer is scanned in wavenumber by a stepper motor which drives the gratings through a special mechanical linkage. In the Spex Ramalab instrument used here, the linkage ratio is such that one motor step changes the wavenumber setting by 1/120 cm^{-1} (on average), according to the direction of scanning. An electronic switch steps the motor. In conventional operation the stepping pulses are supplied by 50 Hz mains cycles, and the speed of scanning is varied by a gear box. Here this method of operation is completely abandoned and the motor stepping pulses are supplied by the control system. The motor steps may then be programmed in any desired fashion and counted up to give a representation of the frequency shift from some datum position. Hence:

$$\nu\ (cm^{-1}) = \frac{\Sigma\ steps}{120} \qquad (2.1)$$

FIGURE 2.2

Front panel of the control unit of System 1 showing the programming switches and information displays.

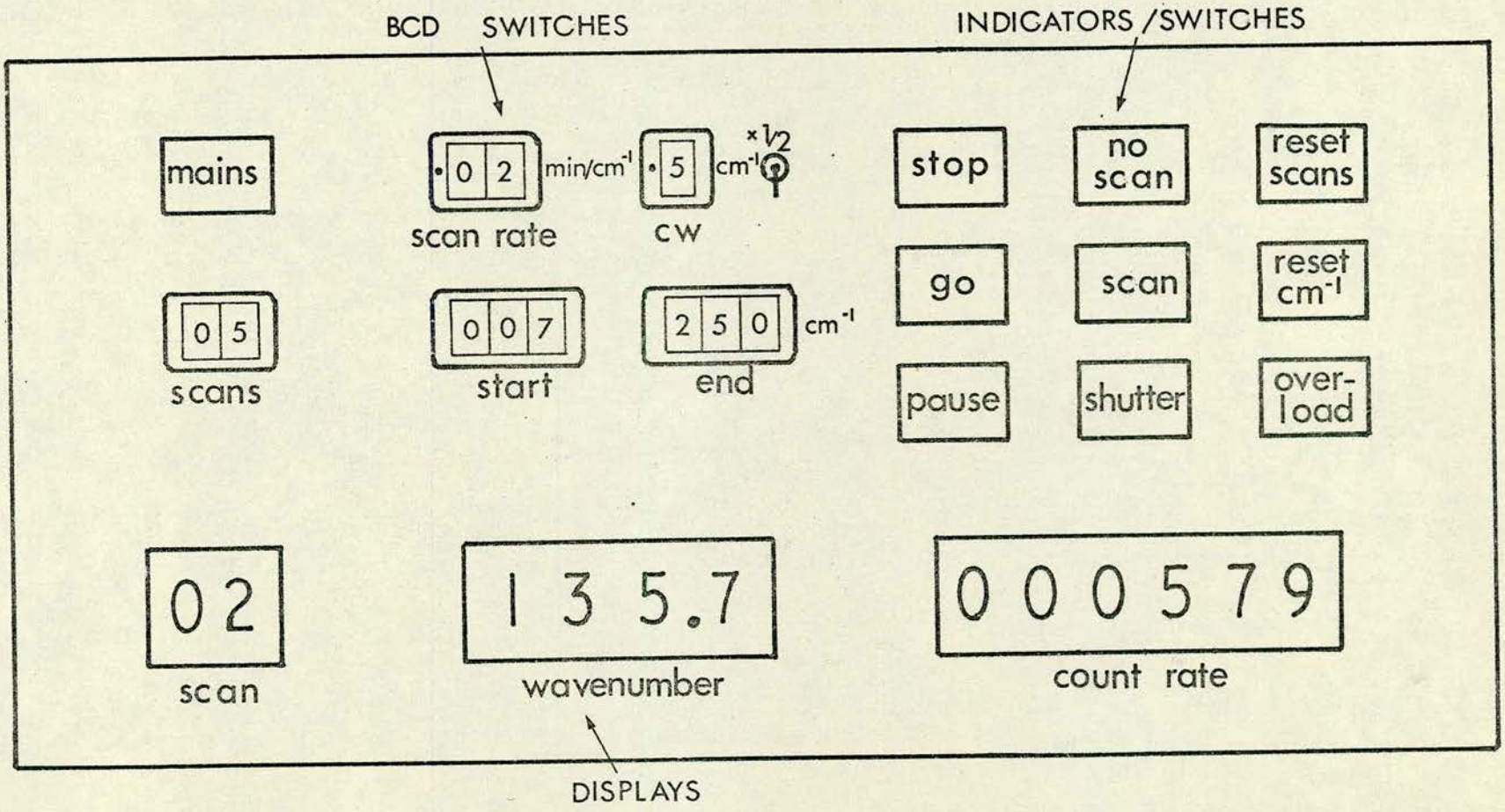
BCD SWITCHES
INDICATORS /SWITCHES
mains
0 2
min/cm⁻¹
scan rate
5
cm⁻¹
×½
cw
stop
no scan
reset scans
go
scan
reset cm⁻¹
pause
shutter
over-load
0 5
scans
0 0 7
start
2 5 0
cm⁻¹
end
0 2
scan
1 3 5.7
wavenumber
0 0 0 5 7 9
count rate
DISPLAYS

FIGURE 2.3

Linkage of the control unit of System 1 to the MCS and spectrometer.

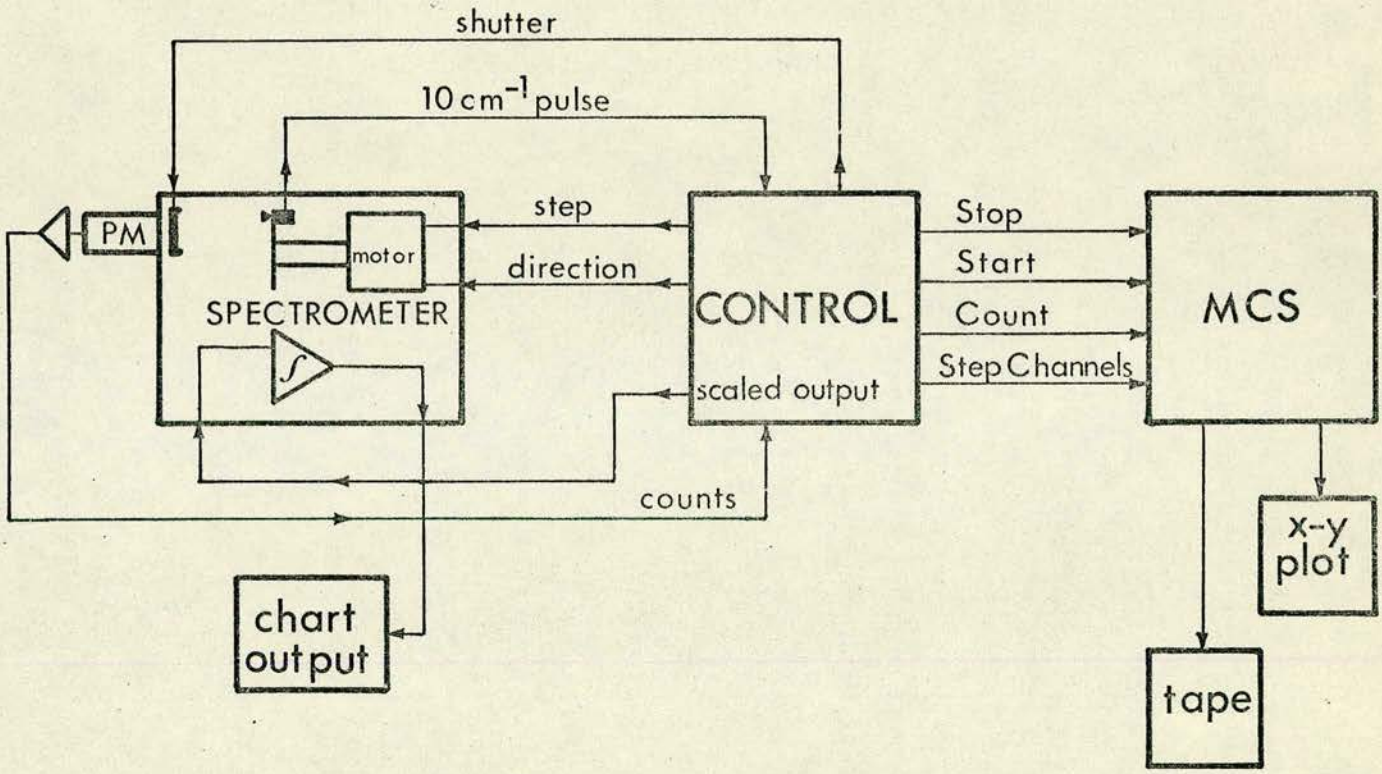
shutter
10 cm^{-1} pulse
PM
motor
SPECTROMETER
step
direction
CONTROL
scaled output
Stop
Start
Count
Step Channels
MCS
counts
chart output
x-y plot
tape

2.2.2 Data acquisition

The signal intensity is measured as a particle cross-section (photon counts/unit time/unit frequency interval). All that is required is a scaler to total the photon counts from the P.M. detector in a set time interval. The use of a multichannel scaler allows an entire spectrum to be recorded and stored. The count-time and unit frequency range are determined by the frequency of motor stepping pulses and by the number of pulses per channel in the MCS. These parameters may be conveniently obtained from programmable digital divider circuits. We have now specified the essential requirements of the system for setting the parameter ν and measuring $I(\nu)$ by digital means. The purpose of the rest of the circuitry is to provide automatic control and data recording for this operation.

2.2.3 Scanning

It is normally required that the spectrometer be started at a particular point and scanned at a steady rate over the spectrum to some end point where scanning is stopped. Since the wavenumber position is logged on the motor step counter, equation (2.1), it is quite easy to compare its value with the settings on two sets of switches giving the start and end points of the scan, respectively. If the spectrometer is not at the start position this must be found before scanning takes place. Unfortunately a complication arises at this point, for the linkage mechanism which scans the gratings is subject to a substantial amount of backlash ($\sim$ 20 - 40 cm^{-1}). One must therefore ensure

that the spectrometer is scanned up to the starting point, in the proper direction, for at least this amount. To do this the spectrometer is always scanned to 100 cm^{-1} below the starting point and thereafter back to the starting point. Circuitry within the control subtracts the 100 cm^{-1} from the setting on the 'start' switch.

In operation there are four possible states of the system: scanning, reversing to 100 cm^{-1} below the start, slewing up to the start, and stop. These states are given the abbreviated names: SCAN, REV, FF, STOP. To save time REV and FF states drive the motor at full slew rate. Other functions such as starting up the MCS, displaying results in the MCS, and setting the photomultiplier protective shutter are initiated by changing from one of these states to another. Table 2(I) and Figure 2.4 show the basic operation of the control according to the various states. These should be read with reference to the previous Figures, 2.2 and 2.3 . Figure 2.4 also shows additional features such as the ratemeter which continuously monitors the signal, the scan counter which allows scans to be repeated and accumulated, and an overload protection device which trips the P.M. shutter on an excessive signal.

2.2.4 Operating the control

Figure 2.2 explains much of the detail of operating the control. Thumbwheel switches simplify the problem of selecting the scan parameters. Indicators and digital displays are provided to show the progress of the scan.

FIGURE 2.4

Schematic of the operation of the control unit of System 1.

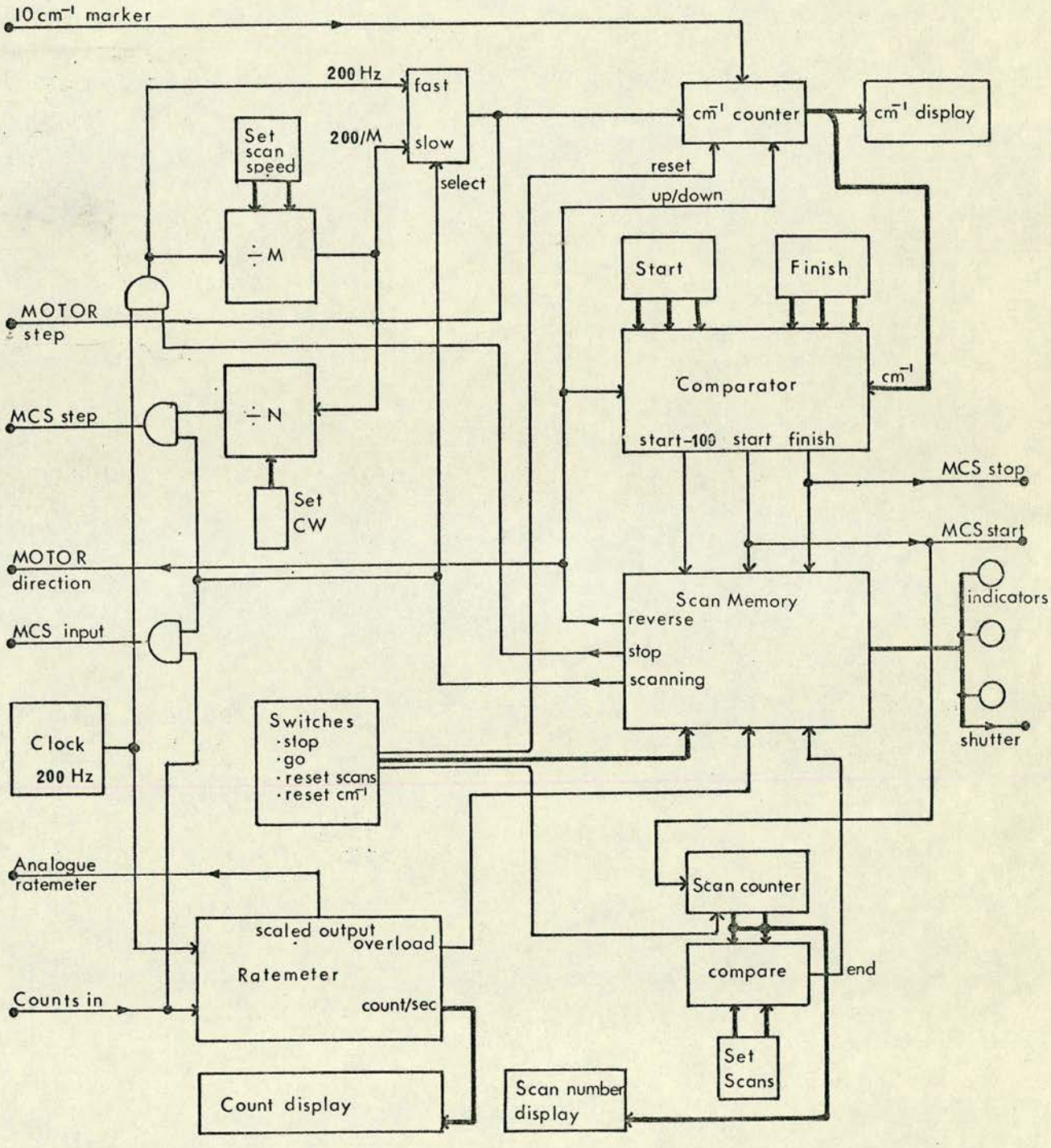
10 cm⁻¹ marker
200 Hz
fast
slow
200/M
select
Set scan speed
÷M
cm⁻¹ counter
cm⁻¹ display
reset
up/down
Start
Finish
Comparator
start-100
start
finish
cm⁻¹
MOTOR step
MCS step
÷N
Set CW
MCS stop
MCS start
MOTOR direction
MCS input
Scan Memory
reverse
stop
scanning
indicators
shutter
Clock 200 Hz
Switches
·stop
·go
·reset scans
·reset cm⁻¹
Analogue ratemeter
Scan counter
scaled output
overload
Ratemeter
count/sec
compare
end
Counts in
Set Scans
Count display
Scan number display

TABLE 2(I)

Signals and Transitions during the Various Phases of Operation

Signal	Stop	Reverse	Fast Forward	Scan
Motor step	0	Full speed	Full speed	Scan speed
MCS step	0	0	0	After N steps
Motor direction	X	0	1	1
MCS input	0	0	0	Count in
Shutter	1	1	1	0
Start-100		●——→		
Start (MCS start)			●——→	
Finish (MCS stop)		←——	———	——●
End	←——●	(at Start-100 after last scan)		
Increment Scan Counter			●——→	

0 = Off; 1 = On; X = Irrelevant; ●——→ = at this transition.

FIGURE 2.5

Multiscanning data for two consecutive scans taken under identical conditions.

———— Run 1

--------- Run 2

xxxxxxxxx difference

The profile of the peak is the resolution function of the spectrometer. The manufacturers of the spectrometer claim reproducibility of 0.3 cm^{-1} in conventional operation. The result shown here is within 0.1 cm^{-1}, the channel width.

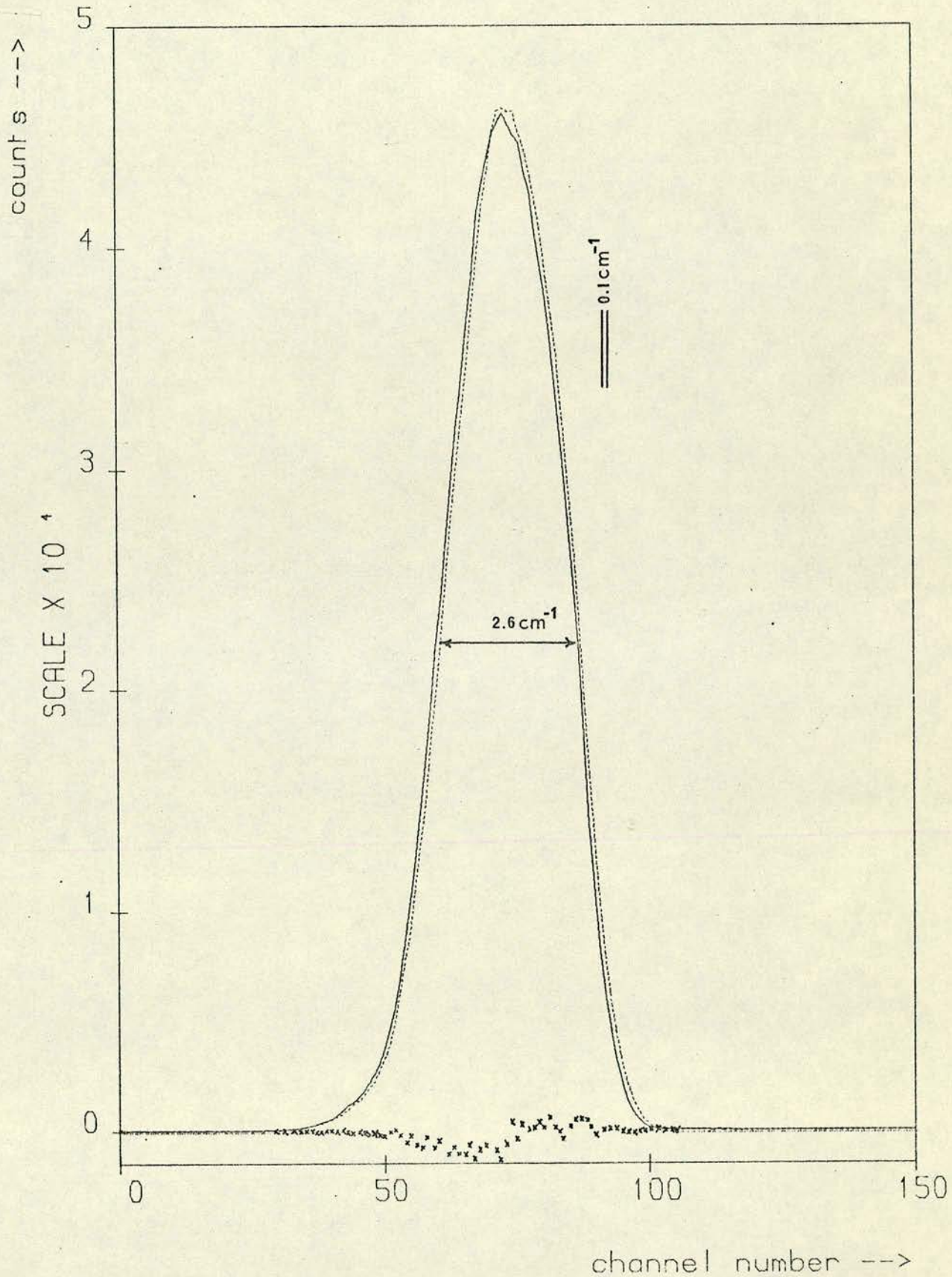
counts -->
SCALE X 10 ⁴
5
4
3
2
1
0
0.1cm⁻¹
2.6cm⁻¹
0
50
100
150
channel number -->

To operate the spectrometer the scan counter and wavenumber counter must initially be reset to zero. To ensure failsafe operation of the wavenumber counter, it is 'locked-on' to a marker pulse given out by the spectrometer at 10 cm^{-1} intervals. This is done by resetting the lower order digits of the counter to zero on the occurrence of this pulse. If the marker position is set to coincide with the position of the exciting frequency, this also gives a proper datum point. The spectrometer is first of all hand scanned to just above the datum position, at which point the wavenumber counter is reset to zero. Thereafter the counter picks up its proper calibration from the marker pulse. Before scanning, the appropriate parameters are set on the programming switches; scan start, scan end. The GO switch is depressed and scanning takes place automatically, with the data being collected in the MCS.

2.2.5 Multiscanning

Under automatic control maximum reproducibility in wavenumber calibration is obtained and two spectra taken consecutively under the same control settings have virtually identical calibration (i.e. within 1 channel of minimum width 0.1 cm^{-1}). This is shown in the data of Figure 2.5 where the channel width is 0.1 cm^{-1} and the peak shape is the resolution function of the spectrometer convoluted with a box function 0.1 cm^{-1} wide. With such reproducibility the spectra may be added together without any noticeable "smearing out", i.e. loss of resolution, and with a gain in the signal to noise ratio, S/N. The scan counter allows

this to be done by accumulating the preselected number of identical scans in the memory of the MCS. This technique, multiscanning, improves the signal to noise, firstly by obtaining a larger sample and, secondly, by averaging out fluctuations in experimental conditions from one scan to another. Because the data is displayed by the MCS after each scan, the total number of scans required to obtain an acceptable S/N ratio can be evaluated as the experiment takes place.

As well as adding successive spectra it is possible instead to subtract every other spectrum by using the add/subtract facility on the MCS. The result is a difference spectrum. If all the spectra are run under the same conditions, this will just be noise. If, however, some experimental parameter is altered from run to run, say a change in pressure or applied electric field, the result is then the difference spectrum for that parameter. Because in this type of experiment only small differences may be involved, the accumulation of several repeated scans is important in order to show the difference above the level of noise. For two signals which have average values y and $y+\delta y$ (number of photon counts) the noise level is approximately $\sqrt{y}$ [16]. In the difference signal, δy, the noise level is approximately $\sqrt{2y}$. We then have for 2n scans, alternate ones subtracted, a resulting difference signal $n\,\delta y$ with a noise level of $\sqrt{2n\,y}$. For this to be observable we require

$$n \gtrsim \frac{2}{y} \Big/ \left(\frac{\delta y}{y}\right)^2 . \qquad (2.2)$$

For example, a 1°/o change in a signal level of about 1,000 counts would begin to be discernible after about 20 scans.

2.2.6 Evaluation

Compared with conventional methods this system has major advantages: the operation is automatic and programmable; the results are accumulated in a MCS; safety features are incorporated; data is finally obtained both graphically and on paper tape; a high degree of reproducibility is obtained; and finally, multiscanning and difference techniques can be used. It has disadvantages in the respect that once the system has been built, it is inflexible and unadaptable. Any change in the operation would require a major redesign and reconstruction. As a working system, however, it has proved very useful in obtaining the results of Chapter Six, RHS and AHS, and it has also been used by D.J. Lockwood and B.H. Torrie[17-19] in obtaining recent results on $K Mn F_3$. W. Taylor has planned to make use of the difference spectrum facility in an attempt to observe electric field induced first order scattering in the alkali halides[20]. Only the spectrometer and MCS have actually given trouble during long hours of operation.

FIGURE 2.6

Schematic diagram of the basic 'stop and count' control.

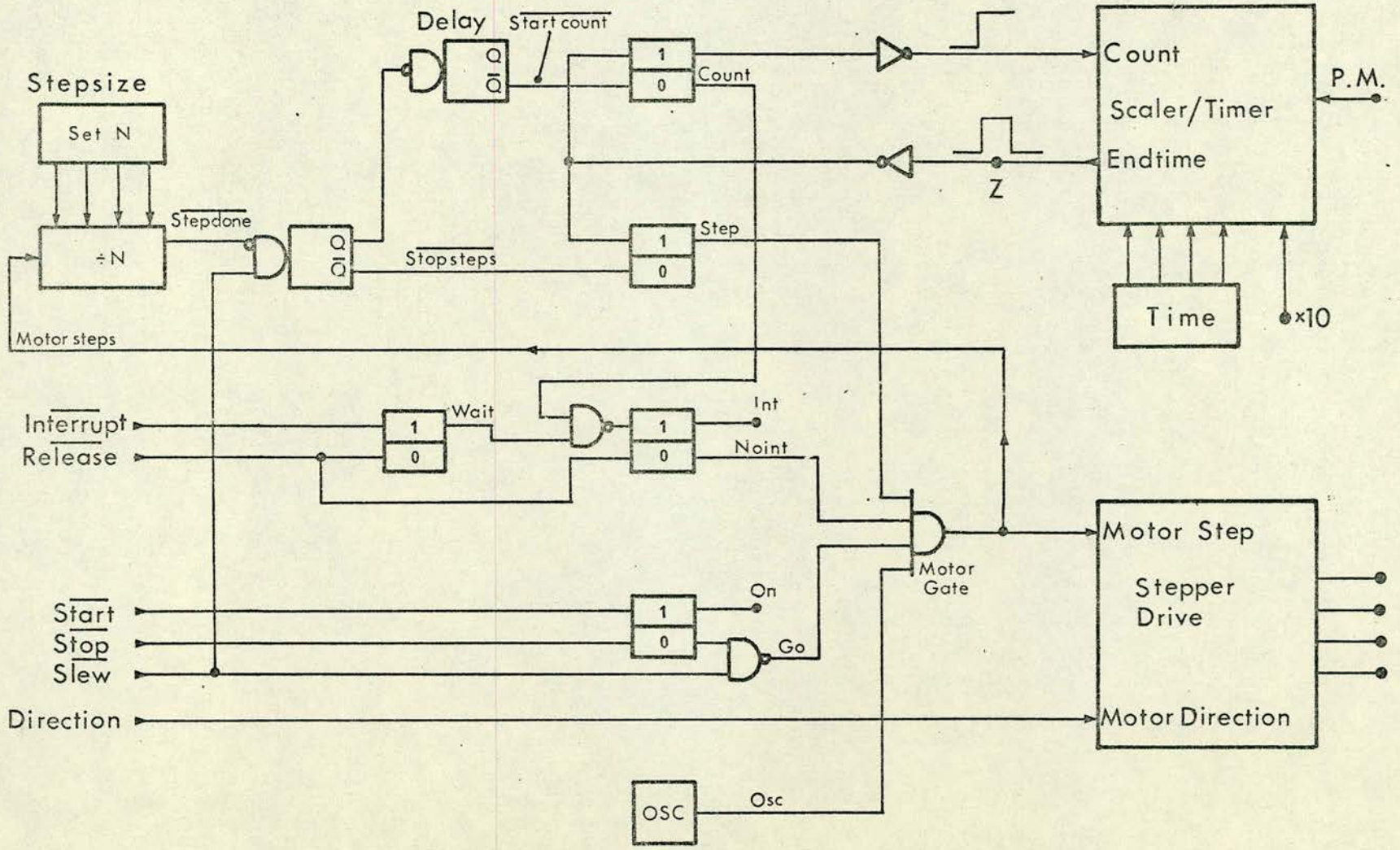
Delay
Start count
Stepsize
Set N
÷N
Stepdone
Stopsteps
Motor steps
Count
Step
Count
Scaler/Timer
Endtime
P.M.
Z
Time
×10
Interrupt
Release
Wait
Int
Noint
Start
Stop
Slew
On
Go
Direction
Motor Gate
Motor Step
Stepper
Drive
Motor Direction
OSC
Osc

2.3 System 2

The second system was conceived out of the necessity to simplify and reduce to the barest essentials the method of controlling the spectrometer. The spectrometer was, in this case, a SPEX-1400 wavelength scanned instrument with a d.c. motor scanning drive. At the outset the d.c. motor was replaced by a stepper motor, and no other interfacing to the spectrometer was carried out. Another initial consideration was the method of data acquisition. A scaler/timer with storage buffer for display and digital output was already available. Since this device stores only one channel of information, no multi-scanning is possible and therefore a control unit such as System 1 would have been largely redundant. The remaining question to be settled was how the control should operate, and it was decided that a 'step, stop-and-count' method would have many advantages. Firstly, the motor stepping speed is irrelevant and, secondly, the scan may be interrupted at any point without spoiling data or calibration. Furthermore the operation of the control has a cyclic nature, one cycle being 'step, stop-and-count', and this greatly simplifies the design of the control circuit. In Section 4 we discuss this feature again, with reference to computerisation of the spectrometer.

2.3.1 Function of the control

Figure 2.6 shows the basic control circuit with the scaler/timer and stepper motor drive. Detailed drawings showing the full facilities are in Appendix II. In the

circuit there are five flip-flops which control the status of the system. These are called COUNT, STEP, INT, WAIT, and ON, with the signals stored in these flip-flops labelled in the same way. The state of the flip-flops determines whether the motor steps, or the scaler counts, or whether neither happens. The motor is controlled through a four-way gate 'MOTOR GATE'. One of the inputs to this gate is a permanently running clock from which the motor steps are derived. The conditions necessary for the motor to step during normal operation are as follows:

STEP	-	on
INT	-	off
ON	-	on

That is, the three other gate inputs must be simultaneously at a logical '1', Assuming that the control is indeed in stepping state, stepping pulses pass to the motor and simultaneously to the STEPSIZE counter. The step-size is programmed into this counter from a digital thumbwheel switch having selectable b c d outputs from 0 through 9. After stepsize motor steps a pulse (level = 0) $\overline{\text{STEPDONE}}$ is generated. This signals that a step of the desired size has been completed. The action of this signal is immediately to cancel the STEP condition (STEP = 0) and after a delay to set the COUNT condition (COUNT = 1). The delay allows time for the motor to complete its step and become stationary. The appearance of the COUNT flag initiates counting in the scaler and starts the count-period timer. During the counting period the control circuit merely waits, and the steady current supplied to the motor windings holds its

position fixed. Concurrently, photomultiplier pulses are accumulated in the scaler until eventually the preset count time expires, thereby generating a pulse 'ENDTIME' (level = 1). This is a crucial point because it signifies the end of a cycle of operation. The STEP and COUNT flip-flops are restored to their former statuses (STEP = 1, COUNT = 0) and the process repeats itself: STEP... COUNT... STEP...COUNT... . During each cycle the scaler can transfer the previous count to a printer, paper tape punch or other device.

Some means of arresting the repetition of these cycles is required, other than switching off the power supply. The 'INT' and 'ON' flip-flops fulfil this function. If 'ON' is set to an 'off' condition, motor steps are inhibited. This means the cycles are stopped at the next occurrence of the STEP condition: any count in progress is taken to completion. The other possibility is that INT is set to 'on' (this is equivalent to NOINT being set to 'off'). Another flip-flop, WAIT, is used in this situation. A command from the front panel switch $\overline{\text{INTERRUPT}}$ sets WAIT to a logical '1'. At the next occurrence of a COUNT condition this causes (by means of a gate) the COUNT signal to set INT to 'on'. This implies that an existing step condition and the following count are taken to completion. Using this method a step cannot be broken in the middle, and on resumption of normal operation, caused by the signal $\overline{\text{RELEASE}}$, a new step is started without losing uniformity of step size. This facility is tremendously useful, but it is not possible to incorporate it in a conventional system relying on a uniform scan speed. The ON flip-flop, on the other hand, is used as a master stop-go control. When it is set to

'stop' (ON = '0'), it is possible to slew the motor in either direction by means of the $\overline{\text{SLEW}}$ signal. This is a means of returning the spectrometer to the starting position: this has to be done manually, unlike System 1.

The version of this control circuit actually in use contains additional circuitry. There is a programmable counter to halt the scan automatically after a given number of steps. Also the scaler count time is programmed from a built-in clock (operated from the mains frequency). The T × 10 function allows the count time to be expanded by a factor of ten when it becomes necessary to use long count times.

2.3.2 Operation and Evaluation

In operation the control is easy to use. The spectrometer is slewed to the starting point of the scan, the required parameters stepsize, count time, number of steps, are entered on the switches and then the 'GO' button is pushed. The scaler outputs the photon-counts onto a paper tape on which various other information recording the parameters of the scan have previously been punched. A Teletype is used for this purpose. The scan may be left unattended until it stops by itself. As examples of the use of the interrupt facility, one might pause to insert neutral density filters into the optics for recording of, say, the exciting line, or to change the gain setting on the graph plotter output.

Although multiscanning is not possible, this has proved most useful as a second system. The essential point is that data can be recorded in computer compatible form. Another

point is that the simple circuit of the control makes it potentially useful as the basis of a more complex system of modular construction. In fact, System 1 would have been much improved if it had been built in this manner.

The present system was used in the collection of the data for sulphur and decafluorobiphenyl (Reference (21), and in Chapters Four and Five).

2.4 Computerisation

The motivation behind the systems described above was to produce data in a form directly assimilable by a computer (e.g. paper tape). The natural culmination of this project is to effect a direct link between the computer and the spectrometer. This has many obvious advantages: the problem of data collection is simplified because the data passes directly to the computer; data reduction can run concurrently with the experiment; the computer can directly control the experiment in an interactive manner. This last advantage is the major one, and the one which should have most bearing on changing and improving experimental technique.

The system described in this section is the starting point of an envisaged system giving nearly complete experimental control via a computer. The computer in this instance is a DEC PDP11/45, a medium scale system operating in a time-shared mode between several independent users. The problem of interfacing the computer to the spectrometer was approached with the attitude that the computer should be treated simply as a 'black box' with a specified function. The details of

the operation of the computer have little relevance to our purpose. The specification of the interface is such that the spectrometer appears to the computer as some kind of peripheral device with which it can exchange data. It does not matter to the computer whether it is exchanging data with a spectrometer or, say, a paper tape reader/punch. Data is transferred to or from the computer by any program using read or write instructions. These instructions depend on the programming language used and somewhere within them they must make a reference to the particular input and output channels allocated to the interface. In a time-shared computer system this kind of detail is taken care of by the supervisor program and not by the user. This is to our advantage, and all we require to know is the following:

OUTPUT: The routine PUT(X) transfers the 16 bit word 'X' to the spectrometer interface.

INPUT: The routine GET(X) transfers the 16 bit word 'X' from the spectrometer interface to the location X within the program.

With this type of operation there is no reference made to time. The operation is not then essentially real time. This fact greatly simplifies both the programming and the operation of the interface.

2.4.1 Introducing the computer

In Section 2.3 we described the simple control unit designed to programme the stepper motor and scaler count time. The description of its operation in terms of a cycle

FIGURE 2.7

Flow of data and operational cycle for computerisation of the 'step and count' control unit.

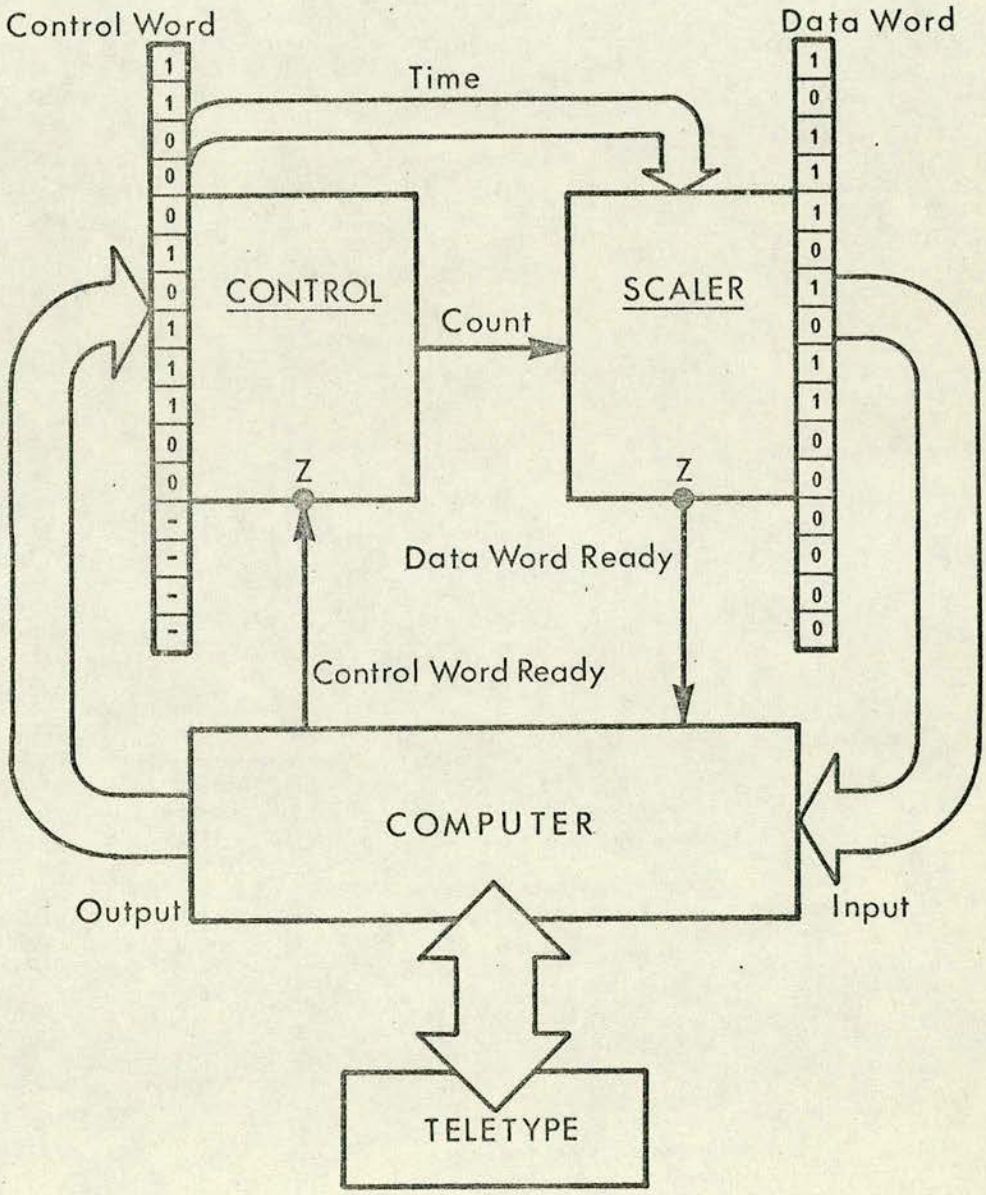
Control Word
Data Word
Time
CONTROL
SCALER
Count
Z
Z
Data Word Ready
Control Word Ready
COMPUTER
Output
Input
TELETYPE

of events was emphasised, largely because of the advantages gained by being able to interrupt between cycles without disturbing the experiment. Referring again to Figure 2.6 we see that the completion of an operational cycle is signalled by a pulse ENDTIME (point Z on the diagram). If we were to break the wire at Z no new cycle could proceed. Apart from signalling the end of a cycle, ENDTIME also indicates that new data is available from the scaler. At this point we might pause to:

(a) transfer data from the scaler

(b) set a new course of action for the next cycle by changing the programming switches.

This is the point then at which we must introduce the computer into the cycle of operations. Instead of paper tape readout, function (a) is carried out by transferring data directly to the computer, and instead of using manually programmed switches or special logic circuits, function (b) is programmed from data, a 'command word', sent from the computer. Figure 2.7 shows this method of operation schematically. The experimenter communicates with the control via a teletype which sends data to the control program running in the computer. This program sends, through the output channel of the computer, a "control word" which replicates the function of the control's programming switches. The presence of this control word is signalled by a flag 'Control Word Ready' which, in effect, generates an ENDTIME pulse at Z. This initiates a step-count cycle as determined by the 'control

FIGURE 2.8

The control word sent from the computer can be made to emulate the function of the programming switches. A switch 'select' controls a set of two-way selector gates, thereby providing a choice of manual or computer control.

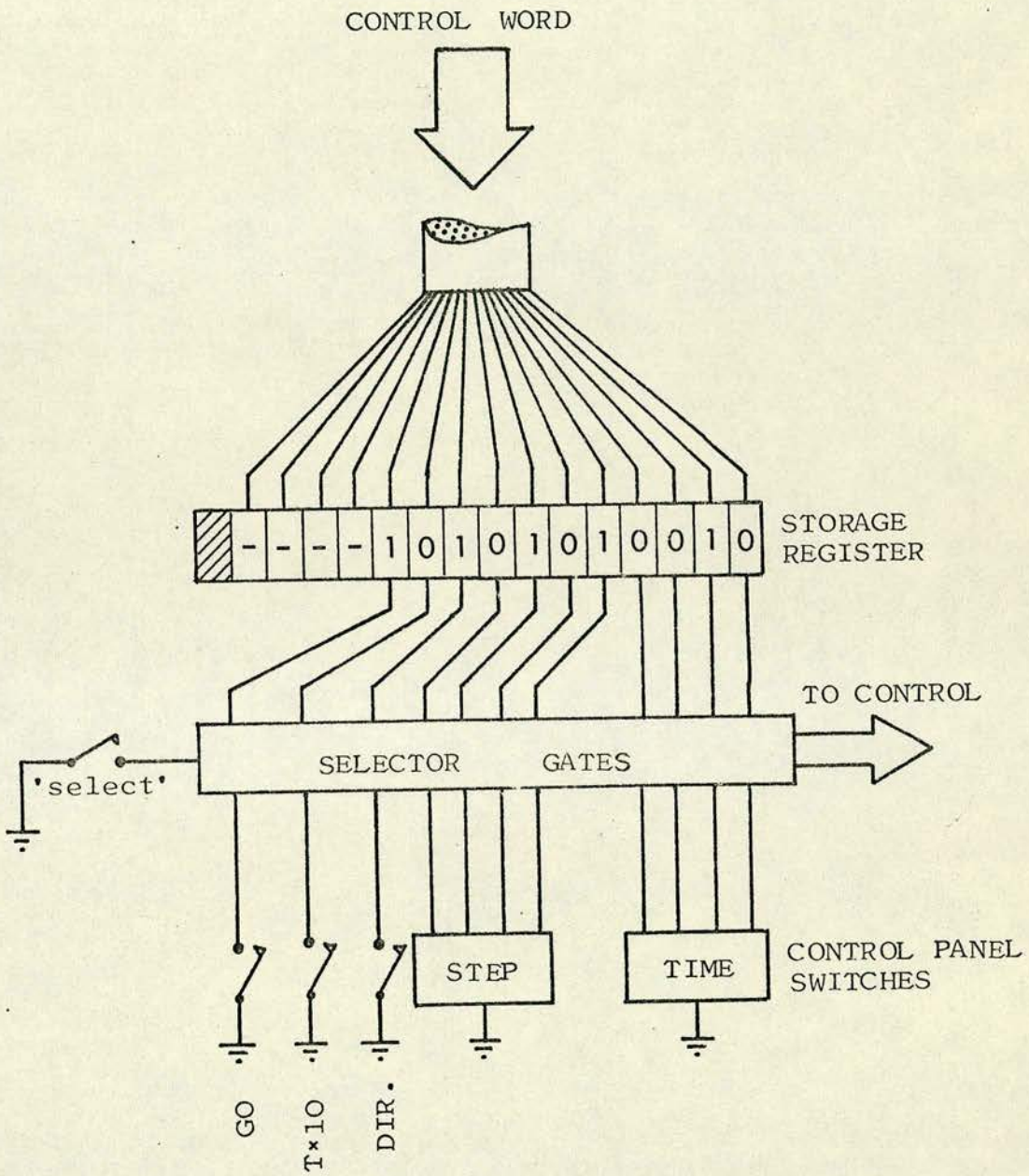
CONTROL WORD
- - - - 1 0 1 0 1 0 1 0 0 1 0
STORAGE REGISTER
TO CONTROL
SELECTOR GATES
'select'
STEP
TIME
CONTROL PANEL SWITCHES
GO
T×10
DIR.

word'. The cycle proceeds to the count phase and, when complete, the ENDTIME pulse goes back to the computer as a flag "Data Word Ready". The data word is just the binary coded number representing the photon count recorded by the scaler. The following short program serves to illustrate what goes on in the computer for a very simple experiment to collect counts at 100 data points and then return to the starting point.

```
      I = 1
      DIR = 1              (direction is forward)
      STEP = 5             (5 motor steps per increment)
      TIME = 2             (2 seconds counting time
5     PUT (DIR*128 + STEP*16 + TIME)
      GET (COUNT (I))
      I = I + 1
      IF (I.LE.100) GO TO 5
      DIR = 0              (direction is reverse)
      TIME = 0             (count time of zero)
6     PUT (DIR*128 + STEP*16 + TIME)
      I = I-1
      IF (I.GT.1) GO TO 6
      STOP
```

The control word is seen to be derived from manipulation of the control variables DIR (direction), STEP (stepsize) and TIME (count time). Figure 2.8 shows the format of the control word and how it relates to the normal function of the manual programming switches. In the diagram a set of selector gates allows either the computer programmed control

word or the programming switches to be used to operate the control. In this manner, operation without the computer is possible, provided that the connection at Z is made when manual operation is selected. From the data acquisition aspect, the data word is read after each step by the routine GET and stored in an array, COUNT. This might have been used later in a data analysis program.

This system is therefore very simple. It makes minimal demands on the computer in terms of the interfacing and special programming required, and control for the spectrometer is based on a simple modification of the central module of system 2. There are also no real-time demands on the computer (calling for 'instantaneous' response). The timing is arranged by the cycle of operations shown in Fig. 2.7. Each event in the cycle - program calculations, sending the control word, the control stepping the spectrometer, the scaler counting, the scaler sending a data word - proceeds in its own time. Because of the fast response of the computer only minimal 'dead time' or 'latency' is introduced, and during that part of the cycle where the program is idle and waiting for a response from the interface (signalling ENDTIME), the supervisor program intervenes to give this 'idle time' to another user. This latter process is quite transparent to the experiment; it is part of the normal function of the computer. That the computer can make efficient use of this 'idle' time is one of the strongest reasons for recommending sharing a computer over having a computer dedicated to one experiment.

FIGURE 2.9

Demultiplexing and multiplexing techniques for driving 8 separate input and output channels from an individual computer input/output channel.

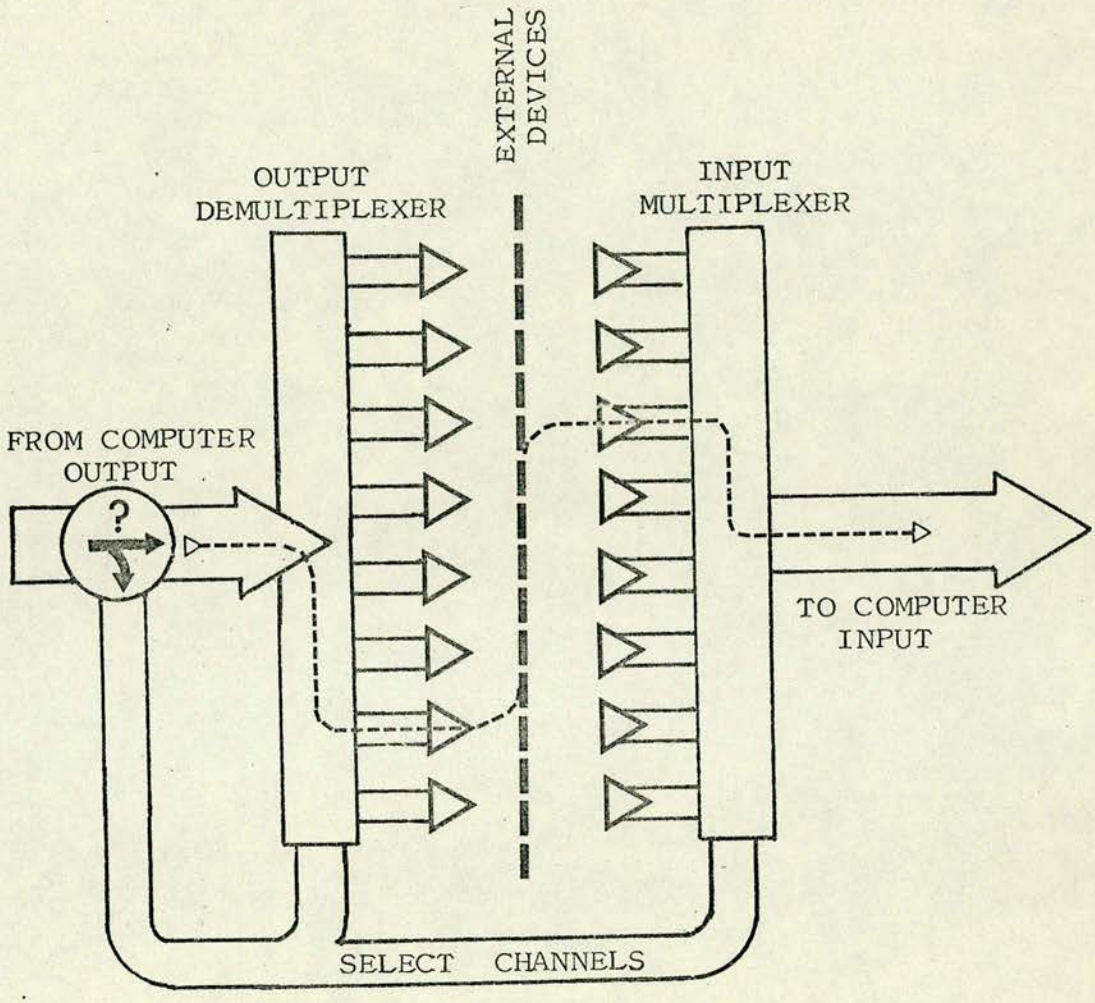

------ DATA PATHS

? { bit 15 = 0 ..select channels
  { bit 15 = 1 ..transfer data to selected channel

2.4.2 Fanning out

In the construction of the interface required to do the task described above, it was decided that provision should be made to interface any other experimental equipment that might be required. The motivation for this was that, firstly, it would be quite simple to do this and, secondly, for phase transition spectroscopy some sort of programmable temperature control is desirable. Further, graphical output was considered to be important as a means of observing the experiment as it progressed, and a digital voltmeter for accurate sample temperature monitoring also seemed a worthwhile addition. Before long one realises that there is essentially no limitation to the number of experimental parameters which may be controlled or recorded by the computer. While expansion of the experimental control to such a stage of advancement would be a long term project, it was nevertheless decided that the foundations of such a system should be laid, starting with the basic element, the spectrometer.

Rather than build several interfaces for different devices, one can be made to do the job of many. Figure 2.9 shows how this may be done using the techniques of multiplexing (switching one of many lines into one line) and demultiplexing (switching one line back into one of many). The single computer input/output channels may each be switched into one of eight subchannels, for input, and output. The switching is performed by a special form of command word. Bit 15 of every command word (16 bits long

FIGURE 2.10

The allocation of subchannels to various experimental tasks.

$$[\alpha'_m] = [\alpha_m] + \delta\theta\,[\,\Omega\alpha_m - \alpha_m\Omega\,]. \qquad (3.5)$$

The second term in (3.5) is the polarisability differential needed to calculate the spectrum. Since small rotations commute we can write this as:

$$[\delta\alpha_m] = \begin{bmatrix} 0 & & \\ & 0 & b-c \\ & b-c & 0 \end{bmatrix}\delta\theta_x + \begin{bmatrix} 0 & & c-a \\ & 0 & \\ c-a & & 0 \end{bmatrix}\delta\theta_y + \begin{bmatrix} 0 & a-b & \\ a-b & 0 & \\ & & 0 \end{bmatrix}\delta\theta_z \qquad (3.6)$$

$$a = \alpha_{xx} \qquad b = \alpha_{yy} \qquad c = \alpha_{zz} .$$

Transforming to crystal coordinates and using a tensor notation, this then gives:

$$[\delta\alpha_c]_{\alpha\beta} = \sum_{k\ell m} (R_{k\alpha}\, R_{\ell\beta}\, \varepsilon_{k\ell m}(\alpha_{kk} - \alpha_{\ell\ell}))\delta\theta_m$$

$$= \sum_m P^m_{\alpha\beta}\,\delta\theta_m \qquad (3.7)$$

where ε_{ijk} is the Levi-Cevitta tensor. It remains to express the $\delta\theta_m$ in terms of the normal modes, remembering that only modes at the zone centre contribute to the scattering. Using (1.45) and (1.46) we have finally for the scattering intensities:

$$\mathcal{J}_{\alpha\beta}(\omega_j)_{\text{Stokes}} \propto \sum_{jj'} \frac{h}{\omega_j}(n(\omega_j)+1)e^j_m\, e^{j'}_{m'}\, \frac{P^m_{\alpha\beta}\, P^{m'}_{\alpha\beta}}{\sqrt{I_{mm} I_{m'm'}}} \qquad (3.8)$$

$$= \eta\,\frac{h}{\omega_j}\,(n(\omega_j)+1)\,(P_{j\alpha\beta})^2 \qquad (3.9)$$

structure, including the shape of the molecules. The spectrum is then calculated as if the crystal were a gas of oriented molecules - giving rise to the name "oriented-gas" approximation. This approximation will be valid only for weak inter-atomic forces which are insufficient to perturb the electronic configuration of the molecules, and hence it is appropriate only to molecular crystals.

At first we assume a crystal with only one molecule in the primitive cell and then extend this to more complex cases. We denote by α_m the molecular polarisability and express this in the diagonal form. Here the molecular symmetry can be helpful in determining the principal axes. These are related to the crystallographic axes by an orthogonal transformation, and therefore the crystalline polarisability, α_c, is given by

$$[\alpha_c] = [R^+ \alpha_m R] \tag{3.2}$$

where R is written down from the crystal structure. Now if the molecule oscillates with amplitude $\delta\theta$ about a given axis $[x, y, z]$, expressed in the molecular system, then we have a change in polarisability:

$$[\alpha'_m] = [1 + \delta\theta\Omega][\alpha_m][1 - \delta\theta\Omega] + [0(\delta\theta^2)] \tag{3.3}$$

where

$$[\Omega] = \begin{bmatrix} 0 & -z & y \\ z & 0 & -x \\ -y & x & 0 \end{bmatrix} \quad \text{with } x^2 + y^2 + z^2 = 1. \tag{3.4}$$

Taking this to first order in $\delta\theta$, this becomes

centre and symmetry assignments. It is not possible to use intensity measurements to derive information about the eigenvectors without a knowledge of the mode polarisabilities. The intensities of peaks in the Raman spectra of many molecular crystals have been interpreted in terms of a simple model expounded by Ito et al.[28]. The particular approach taken by Ito et al., however, involves the assumption that the normal modes of the crystal correspond to rotations of the molecules about their principal inertia axes. This assumption has been justly criticized by Pawley[24]. Here we develop this model, without assumptions about the normal modes, to calculate the mode polarisabilities in terms of the zone centre eigenvectors: this will be applied in later chapters to sulphur and decafluorobiphenyl. We now outline the model, derive expressions for the polarisabilities and consider their application.

3.2 The Cross-section

The approximation used in calculating the Raman spectrum is the assumption that the rigid molecules alone contribute to the polarisability and that rotational oscillations modulate the polarisability. Translatory oscillations have no effect in this lowest order approximation: their inclusion would require a model of the electronic properties. An example of such a model is the anharmonic 'shell-model' used by Cowley and Bruce[29, 30] to calculate two-phonon spectra in alkali halides. This model is appropriate where it is also used for the calculation of the lattice dynamics of the crystal, but that that is not the case here. The only essential *a priori* information for our model is a knowledge of the crystal

however, we shall not be concerned with the spectra of the internal molecular vibrations and we direct our attention to the external vibrations.

The study of the external vibrations gives information about the inter-molecular potential. For simple enough molecular crystals with high symmetry, the external vibrations may be understood in terms of a small number of parameters, elements of the $V(Q)$ matrix. An example of such a calculation is for hexamethylenetetramine, which is cubic with only one molecule in the primitive cell. This was done by Pawley[22], and Cochran and Pawley[23], but no information about the intermolecular potential itself is gained from this type of approach. From a postulated atom-atom potential, however, the $V(Q)$ matrices may in principle be evaluated directly and (3.1) solved for the normal modes. The first work of this kind was carried out by Pawley[24] on napthalene and anthracene. Since then other crystals have been studied in similar calculations, for example paradichlorobenzene[25] and carbon dioxide[26]. Recently Dolling, Pawley and Powell[27] have recalculated hexamethylene tetramine, using this approach. Even for simple crystals and elementary potential functions this is a problem requiring very lengthy calculation, the end product being the eigenvectors and eigenfrequencies at various points in the Brillouin zone.

To date comparison with experiment has been made using Raman scattering and neutron scattering measurements. Both techniques have their limitations. Raman scattering information has previously been limited to frequencies at the zone

$$2H = \sum_{\ell} \Big\{ m_{\kappa} \dot{u}(\ell, \kappa)^2 + I_{\kappa\kappa} \dot{\theta}(\ell \kappa)^2 + \sum_{\ell'\kappa'} V_{tt}\begin{pmatrix} \ell & \ell' \\ \kappa & \kappa' \end{pmatrix} u(\ell\kappa)u(\ell'\kappa') + V_{tr}\begin{pmatrix} \ell & \ell' \\ \kappa & \kappa' \end{pmatrix} u(\ell\,\kappa)\theta(\ell'\,\kappa') + V_{rr}\begin{pmatrix} \ell & \ell' \\ \kappa & \kappa' \end{pmatrix} \theta(\ell\kappa)\theta(\ell'\,\kappa') \Big\} \quad , \tag{3.1}$$

where $\{I_{\kappa\kappa}\}$ are the principal moments of inertia, $\theta(\ell\kappa)$ is the component of a small rigid rotation about the κ-th principal axis. V_{tt}, V_{tr}, V_{rr} are the potential energy matrices coupling translations, translations with rotations, and rotations.

Since this can be cast in the form of (1.1) with an extension of the κ notation to cover θ_x, θ_y, θ_z (with $m_\kappa = m$ for $\kappa = 1,2,3$ and I_{xx}, I_{yy} and I_{zz} for $\kappa = 4,5,6$) the theory is largely unchanged, but now there are $6n - 3$ external optic modes at the zone centre where n is the number of molecular units in the primitive cell.

Generally speaking the internal vibration spectrum is similar to that of the free molecule. Shifts in frequency and lifting of degeneracies are observed, however, but these effects may be considered as a static perturbation due to the inter-molecular forces. The largest shifts and splittings observed are typically of the same order as the lattice frequencies. Experimentally, the spectra of molecules in solids do appear different from those in liquids and gases. In the latter the spectra are averaged over molecules in all orientations, whereas in a crystal the spectra show interference effects from specifically oriented molecules. For the present,

CHAPTER 3

MOLECULAR CRYSTALS

In this chapter we review the application of Raman spectroscopy to obtaining information about the lattice vibrations of molecular crystals. The possibility of deriving information about eigenvectors is stressed. Expressions for the polarisabilities of the modes are developed in terms of the eigenvectors and the molecular polarisability. A simple rule is given for treating more than one molecule in the primitive cell, and a sum rule is worked out for the intensities of the spectra.

3.1 Introduction

The importance of Raman scattering in the study of molecular crystals is that information about lattice vibration frequencies and eigenvectors may be gained quite readily. This is possible because a first order approximation to the polarisability is obtainable. In a molecular crystal there are only weak interactions of Van der Waals type between groups of atoms which retain a molecular character. On this assumption the vibration spectrum is divided into two regions, one of low frequency inter-molecular vibrations, and one of high frequency intra-molecular vibrations. These regions are called, respectively, the external and internal vibration spectra. In the adiabatic approximation for the external vibrations the molecules are treated as rigid, thus each molecule contributes 6 external degrees of freedom to a Hamiltonian:

design problems. System 3 shows how this module may be used in a complex computer oriented system. This kind of system, at any level of sophistication, has the advantage over all others of complete flexibility. The extent of the flexibility depends only on the operating program and the limitations of the computer. Another advantage comes of the sharing of the resources of a reasonably large computer; this brings facilities within the experimenters' reach which would otherwise be out of the question. The choice of which type of system to adopt depends on the amount of flexibility required and on what kind of computer is available.

subchannels requested. Appendix III also gives details on the operation of input/output routines at machine instruction level.

As proposed, this system may be constructed in steps as each new subchannel is required. At the present time the graph plotter, the spectrometer control and the photon-count scaler have been installed, giving a basic configuration of a system for the operation of a CODERG T800 triple monochromator. It is hoped that, as part of a future programme, the system will be brought into full activity, with the concurrent development of control programs to service all of the subchannels. In Chapter Six we discuss the need for this kind of experimental system for the spectroscopic study of phase transitions.

2.5 Summary

We have described three separate systems of widely differing levels of sophistication. System 1 is intended to allow programmable data collection with a fixed number of options - such as the region to be scanned and the number of times. Nothing fruitful could be gained from an attempt to expand this type of system to accomplish more functions, for it is already overcomplicated. System 2, on the other hand, is only a rudimentary system, but the central part of it, the control, is designed so that it could flexibly fit in as a component of a larger system constructed on a 'module' concept. Not only is this a convenient method of construction, it simplifies many

(4) Two stepper motors are controlled. Each carries a turret mounted with optical devices such as a neutral density filter, a blocking filter, $\frac{1}{2}$ wave plate, and polarisation analysers. This allows polarised spectra to be run, and the filters are safety measures to prevent photomultiplier over-exposure in certain high signal intensity conditions.

(5) - (7) These are unused and are available to other experiments.

Input Subchannels

(0) The photon-count scaler.

(1) Control signals; status signals and warning signals, as might be derived from limit switches or other warning signals. The intention is that the system should be self checking against unexpected situations.

(2) Not yet allocated.

(3) Digital voltmeter used to sample the thermocouple voltages and laser power as selected by the reed relays.

(4) - (7) These are unused and are available to other experiments.

As far as programming is concerned, there is very little change introduced except for the need to specify subchannels. The input/output routines are now

```
PUT  (X, OUTCH)
```

and

```
GET  (X, INCH)
```

where OUTCH and INCH are the numbers of the input and output

with bits designated 15, most significant, through 0, least significant) is used as a flag as follows:

bit 15 = 0 - use word to select the new subchannels for input and output.

bit 15 = 1 - ordinary data word to be passed to the selected subchannel.

Full circuit information is given in Appendix III.

2.4.3 Allocation of Subchannels

Figure 2.10 shows the allocation of the subchannels to particular functions, some of which are interrelated. These we now describe with the intention of giving a broad outline of the possibilities.

Output Subchannels

(0) An X - Y plotter driven by two digital to analogue converters (DAC's). This provides graphic output of experimental results.

(1) The spectrometer control module, also providing count time information for the photon count scaler.

(2) The cryostat temperature controller with its control point reference voltage supplied by a DAC. This allows programmed temperature control.

(3) A set of reed relays which select one of many voltages to be read by a digital voltmeter (DVM). In this way various thermocouples measuring sample temperature and the laser power meter may be monitored in turn.

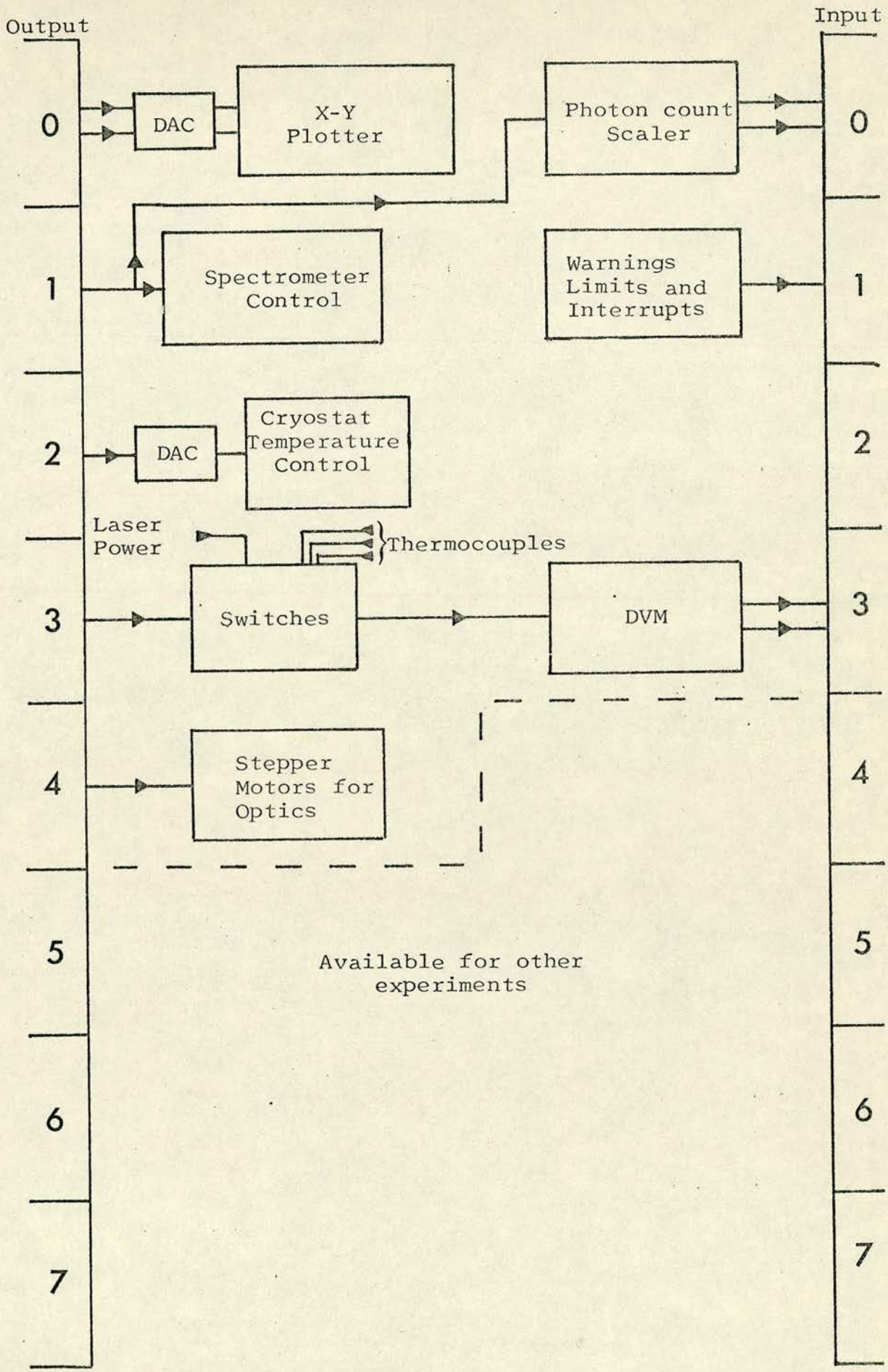
Output
Input
0
DAC
X-Y Plotter
Photon count Scaler
0
1
Spectrometer Control
Warnings Limits and Interrupts
1
2
DAC
Cryostat Temperature Control
2
Laser Power
Thermocouples
3
Switches
DVM
3
4
Stepper Motors for Optics
4
5
Available for other experiments
5
6
6
7
7

where $P_{j\alpha\beta} = \sum_m \frac{P^m_{\alpha\beta}}{\sqrt{I_{mm}}} e^j_m$ (3.10)

and η represents the scattering efficiency. We call $P_{j\alpha\beta}$ the scattering tensor.

3.3 The Interpretation of the Spectra

The application of the equations relating the scattered intensities to the eigenvectors depends on a knowledge of the molecular polarisability. This information, however, we do not generally have at hand.

Fortunately there are many cases which can be treated in spite of this difficulty. There are three cases to consider: molecules which are optically isotropic, uniaxial, or biaxial. In the first case there is no spectrum, for all the $(a_{kk} - a_{\ell\ell})$ vanish. In the second, there is a spectrum and there is only one nonzero value of $(a_{kk} - a_{\ell\ell})$, which implies there are no adjustable polarisability parameters as far as relative intensities are concerned.

In the last case, however, there are still two adjustable parameters. In theory it is possible to fix these parameters from the components of the spectrum, $\mathcal{J}_{\beta\gamma}(\omega_j)$, by measuring total integrated intensities. Using (2.9) and the orthonormality relations for the $\{ e^j_m \}$ we have:

$$\Sigma(\beta\gamma) = \sum_j \frac{\omega_j}{n(\omega_j)+1} \mathcal{J}_{\beta\gamma}(\omega_j) = \sum_m \eta \frac{(P^m_{\beta\gamma})^2}{I_{mm}} \quad (3.1)$$

$$= \sum_{\substack{k\ell m \\ \text{cyclic}}} \eta \frac{R^2_{k\beta} R^2_{\ell\gamma}}{I_{mm}} (a_{kk} - a_{\ell\ell})^2 \quad (3.12)$$

$\Sigma(\beta\gamma)$ is defined by (3.11) as a weighted sum of intensities in the lattice spectrum of polarisation $\beta\gamma$. Putting β and γ = x, y, and z in turn gives six equations in the three unknowns $(a_{kk} - a_{\ell\ell})^2$. Since the intensities are measured on some arbitrary scale the η term may be dropped. This over-determined set of equations provides the required parameters and serves as a consistency check of the correlation between intensity scales of the six different spectra. The problem of measuring the six components of the spectra under identical gain conditions is notoriously difficult because the sample must be reoriented at least three times during the experiment. If, however, for each orientation the diagonal and three off-diagonal components of the spectra are measured - giving a total of twelve spectra- we can use the following correlation scheme to determine the relative gain conditions:

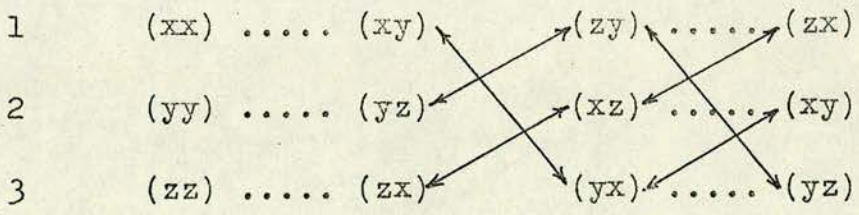

(3.13)

The components linked by ..... can be measured under the same gain conditions, because it merely requires that the polarisation analyser be turned through 90° between otherwise identical runs. The components linked ⟷ are the same so that the ratio of the observed intensities gives the ratio of the scattering efficiencies between runs. The stability of the experimental gain conditions is a major obstacle to the successful application of this technique. Other difficulties arise out of polarisation "leak-through" and inaccurate orientation of the

crystal. At best there may still be several percent discrepancy in the correlation of the intensities.

Assuming that we can find suitable relative values for the $(\alpha_{kk} - \alpha_{\ell\ell})$ the next step is to write down, from a group theoretical analysis, the symmetry coordinates for rotational oscillations. These are written down in terms of a set of local molecular coordinates to conform with equation (3.7). The symmetry coordinates dictate the most general form that eigenvectors transforming according to a particular representation may take. Their use allows us therefore to calculate that part of the scattering tensor which transforms under a particular irreducible representation. The general statement of the rule is that an eigenvector which transforms according to the irreducible representation Γ gives contributions to those components of the scattering tensor which combine to transform under Γ. Loudon[14] has tabulated "Raman tensors" which show how the scattering tensor breaks down according to irreducible representation for all the crystal point groups.

For crystals of orthorhombic symmetry, or lower, there are many simplifications; these we will investigate because they apply to the crystals treated herein. For these crystals the representations of the point groups are all one-dimensional. Furthermore each component of the scattering tensor corresponds to scattering from eigenvectors of only one particular symmetry. In working out the scattering for cases where there is more than one molecule in the primitive cell, but where they are all related by symmetry, we can still arrive at a simple result. Firstly we choose just one molecule,

say 1, from which all the other molecules may be generated by operations of the space group. The local molecular coordinate systems of these molecules are generated from those of type 1 by a specified set of operations of the point group. The contribution to the scattering amplitude is then written down for molecule type 1; this we call S_1 and it is of the form:

$$S_1 = \sum_m P_{1m} \, \delta\theta_{1m} \quad . \tag{3.14}$$

For displacements of the molecules according to an eigenvector transforming as Γ^j, the contributions of the other molecules are:

$$S_K^j = \sum_m (A_K \, P_{1m} \, A_K^{-1}) \, \chi_K^j \, \delta\theta_{1m}^j \quad , \tag{3.15}$$

where χ_K^j is a phase factor identical with the character of the operation A_K under the representation Γ^j: A_K is the operation of the point group which generates the K-th molecule from type 1. Thus the total scattering summed over all the molecules is

$$S^j = \sum_K S_K^j = \sum_m \left\{ \sum_K (A_K \, P_{1m} \, A_K^{-1}) \, \chi_K^j \right\} \delta\theta_{1m}^j$$

$$= \sum_m P_{1m}^j \, \delta\theta_{1m}^j \quad , \tag{3.16}$$

where P_{1m}^j is simply the projection out of P_{1m} of that part which transforms irreducibly under Γ^j. This result can be formulated as a simple rule: write down P_1 and decompose it according to the irreducible representations of the point group, as shown by looking up character tables, or

by Loudon[14]; the scattering tensor may then be readily evaluated for each mode in terms of the components of the eigenvector for just one molecule. This is a result which will be applied in the following chapters, but it is stressed that it is not generally valid for crystals with symmetry higher than orthorhombic.

CHAPTER 4

ORTHORHOMBIC SULPHUR

The theory of the previous chapter is applied to an analysis of the Raman spectrum of orthorhombic sulphur. Useful information is obtained about the eigenvectors of the lattice modes at the zone centre, in addition to accurate frequencies. The results are discussed in the light of the model calculations of Pawley and Rinaldi[31-35].

4.1 Background

Orthorhombic sulphur, hereafter referred to simply as sulphur, is a molecular crystal with one type of molecule, a ring of S_8. Since it is a monatomic crystal, it would appear to be a suitable choice for a dynamical calculation based on a single atom-atom pair potential. Pawley and Rinaldi[31, 33] and Rinaldi[34,35] have carried out structural and dynamical calculations for sulphur based on an atom-atom potential of the form:

$$V(r) = \frac{-A}{r^6} + B \exp(-\alpha r) \quad . \qquad (4.1)$$

The molecules are treated as rigid, and only non-bonded atom pairs interact through this potential. The crystal potential $\sum_{i<j} V(r_i - r_j)$ is expanded in the harmonic approximation to give:

$$\Phi = -\Phi_o + \sum_j F_j u_j + \sum_{ij} V_{ij} u_i u_j + O(u^3). \qquad (4.2)$$

FIGURE 4.1

Configuration of the S_8 molecules within the primitive cell of orthorhombic sulphur.

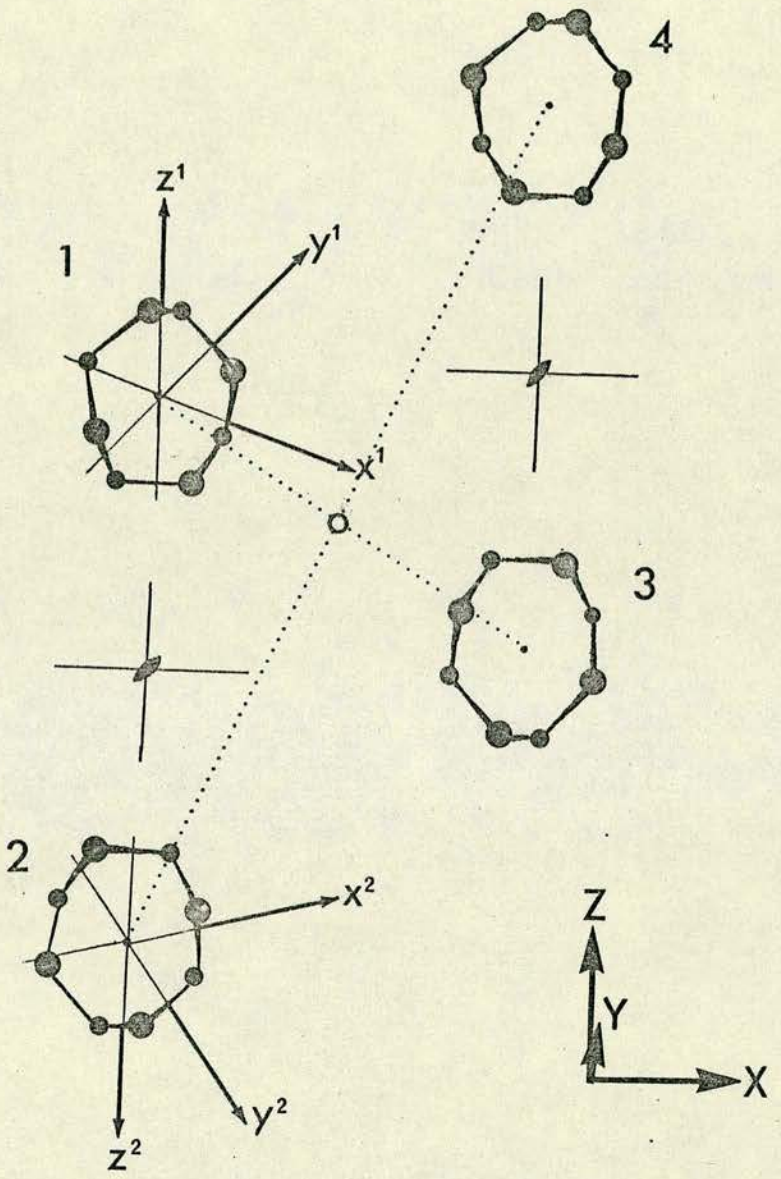

● sulphur

The first term is a measure of the heat of sublimation, and the second must vanish for small displacements, $\underline{u}$, about equilibrium. These conditions allow A and B to be expressed in terms of α, which is then taken as the variable parameter. From this Rinaldi[35] has calculated model eigenvectors and eigenfrequencies for α in the range 2.5 to 4.

The test of this model is a comparison of calculation with neutron and Raman scattering data. Rinaldi[34] has done this for the frequency calculations. We now show, with the results of Chapter Three, that in sulphur, information about one component of each zone centre eigenvector may be derived from the Raman spectrum. The observed spectrum was reported in a recent paper by Arthur and Mackenzie[21], and an analysis was given therein for the A_g and B_{1g} spectra. This work is extended here to cover the other spectra, of symmetry B_{2g} and B_{3g}, and a comparison is made with Rinaldi's calculations. An improvement to the oriented gas model is proposed in order to account for some observed short-comings.

4.2 Group Theory

The space group of orthorhombic sulphur is D_{2h}^{24} and there are four molecules in the primitive cell, Figure 4.1. The S_8 molecule has point group D_{4d}, with the $\underline{x}$ axis taken to be the unique fourfold axis. In the crystal each molecule occupies a site of symmetry C_2 with a C_2' twofold axis, which we call the $\underline{z}$ axis, aligned with the crystal $\underline{Z}$ axis, also a twofold axis. From Reference (31) we find that a molecule, labelled 1 say, has its $\underline{x}$ axis oriented at $\phi = 141^\circ\ 18'$ to the crystal $\underline{X}$ axis. Thus the transformation

between molecular and crystal coordinate systems is represented by the matrix:

$$R = \begin{bmatrix} \cos\phi & \sin\phi & 0 \\ \sin\phi & \cos\phi & 0 \\ 0 & 0 & 1 \end{bmatrix} \doteq \begin{bmatrix} -.780 & .625 & \\ -.625 & -.780 & \\ & & 1 \end{bmatrix} \qquad (4.3)$$

With the other molecules labelled 2, 3 and 4, 2 is related to 1 by $C_2(x)$, and 3 and 4 are related to 1 and 2 by inversion. The character table given in Table 4(I) below shows the elements of symmetry of the point group and the representations. It is apparent that, as far as Raman scattering is concerned, only the top left part of the table is really necessary. The decomposition of the various spaces is shown in an abbreviated fashion. S_E represents (x, y, z), Euclidean space, S_E^* represents the space of rotations (R_x, R_y, and R_z), S_{cell} is the space of permutations of the molecular labels, or sites, and S_{vibr} is the space of lattice vibrations. The method of product spaces is used, following Montgomery[36]. It is seen that there are 21 lattice vibrations at the zone centre, 13 of which are even and Raman active, and 9 of which are odd (but still not expected to be infrared active since the molecules have no net charge). The three acoustic vibrations, transforming as S_E, have been discarded. Table 4(II) shows symmetry coordinates for these modes expressed in the local molecular coordinate systems defined therein.

TABLE 4(I)

Character Table and Group Theory for the Lattice Vibrations of Orthorhombic Sulphur

D_{2h}	E	C_{2x}	C_{2y}	C_{2z}	i	σ_{yz}	σ_{xz}	σ_{xy}	Occurrence in spectrum
A_g	1	1	1	1	1	1	1	1	xx, yy, zz
B_{1g}	1	-1	-1	1	1	-1	-1	1	xy
B_{2g}	1	-1	1	-1	1	-1	1	-1	xz
B_{3g}	1	1	-1	-1	1	1	-1	-1	yz
A_u	1	1	1	1	-1	-1	-1	-1	
B_{1u}	1	-1	-1	1	-1	1	1	-1	
B_{2u}	1	-1	1	-1	-1	1	-1	1	
B_{3u}	1	1	-1	-1	-1	-1	1	1	
$\chi(S_E)$	3	-1	-1	-1	-3	1	1	1	~ $B_{1u} + B_{2u} + B_{3u}$
$\chi(S_E^*)$	3	-1	-1	-1	3	-1	-1	-1	~ $B_{1g} + B_{2g} + B_{3g}$
$\chi(S_{cell})$	4	0	0	4	0	0	0	0	~ $A_g + B_{1g} + A_u + B_{1u}$

TABLE 4(I) (Contd.)

$$S_{Vibr} = S_{cell} \times (S_E + S_E^*) - S_E$$

$$(A_g + B_{1g} + A_u + B_{1u}) \times (B_{1g} + B_{1u} + B_{2g} + B_{2u} + B_{3g} + B_{3u}) - B_{1u} - B_{2u} - B_{3u}$$

$$= \{2A_g + 2B_{1g} + 4B_{2g} + 4B_{3g}\} + \{2A_u + B_{1u} + 3B_{2u} + 3B_{3u}\}$$

xx yy zz — xy — xz — yz — inactive

The Raman tensors are of the form:

$$\begin{bmatrix} a & & \\ & b & \\ & & c \end{bmatrix} \quad \begin{bmatrix} & d & \\ d & & \\ & & \end{bmatrix} \quad \begin{bmatrix} & & e \\ & & \\ e & & \end{bmatrix} \quad \begin{bmatrix} & & \\ & & f \\ & f & \end{bmatrix}$$

A_g B_{1g} B_{2g} B_{3g}

TABLE 4(II)

Symmetry Coordinates for the Normal Modes of Orthorhombic Sulphur

e_m^j	x^1	y^1	z^1	R_x^1	R_y^1	R_z^1	x^2	y^2	z^2	R_x^2	R_y^2	R_z^2
A_g	0	0	c	0	0	γ	0	0	c	0	0	γ
B_{1g}	0	0	c	0	0	γ	0	0	-c	0	0	$-\gamma$
B_{2g}	a	b	0	α	β	0	-a	-b	0	$-\alpha$	$-\beta$	0
B_{3g}	a	b	0	α	β	0	a	b	0	α	β	0

The local coordinates are defined in the following way. Molecule (1) is related to the crystal axes system by

$$\begin{bmatrix} c & s & \\ -s & c & \\ & & 1 \end{bmatrix} \qquad \begin{aligned} c &= \cos \phi \\ s &= \sin \phi \end{aligned}$$

whereas molecule (2) is related by

$$\begin{bmatrix} c & -s & \\ -s & -c & \\ & & -1 \end{bmatrix}$$

The symmetry coordinates given in Reference (21) are expressed in the crystal system, and are not the same as those given here. Molecules 3 and 4 are not represented because they are simply related by inversion to 1 and 2.

4.3 The Raman Cross-section

To find the polarisabilities of these modes we note that for the free sulphur molecule $I_{xx} \neq I_{yy} = I_{zz}$ and $\alpha_{xx} \neq \alpha_{yy} = \alpha_{zz}$, we write:

$$(\alpha_{xx} - \alpha_{yy}) \frac{1}{\sqrt{I_{zz}}} = (\alpha_{xx} - \alpha_{zz}) \frac{1}{\sqrt{I_{yy}}} = \beta \, . \quad (4.4)$$

The R_{ij} are given by (4.3), so that from (3.7) and (3.10) we have, for each mode of the appropriate symmetry:

$$\begin{aligned} P_j xx &= -P_j yy = \beta \sin 2\phi \; e^j_{\theta z}(1), \quad P_j zz = 0 \\ P_j xy &= \beta \cos 2\phi \; e^j_{\theta z}(1) \\ P_j xz &= \beta \cos \phi \; e^j_{\theta y}(1) \\ P_j yz &= -\beta \sin \phi \; e^j_{\theta y}(1) \end{aligned} \quad (4.5)$$

The result (4.5) can be arrived at either by summing the symmetry related contributions of all the molecules directly, or by applying the rule discussed in Chapter 3, which we now do as an example. The scattering for molecule type 1 is found to be of the form:

$$(\alpha_{xx}-\alpha_{yy}) \begin{bmatrix} \sin 2\phi & \cos 2\phi & \\ \cos 2\phi & -\sin 2\phi & \\ & & 0 \end{bmatrix} \delta\theta^1_z + (\alpha_{xx}-\alpha_{zz}) \begin{bmatrix} & & \cos\phi \\ & & -\sin\phi \\ \cos\phi & -\sin\phi & 0 \end{bmatrix} \delta\theta^1_y \quad (4.6)$$

These are decomposed, as shown by Table 4(I), according to the irreducible representations of D_{2h} to give:

$$
\begin{aligned}
(\alpha_{xx} - \alpha_{yy}) &\begin{bmatrix} \sin 2\phi & & \\ & -\sin 2\phi & \\ & & 0 \end{bmatrix} \delta\theta_z^1 && - A_g \\
(\alpha_{xx} - \alpha_{yy}) &\begin{bmatrix} 0 & \cos 2\phi & \\ \cos 2\phi & 0 & \\ & & 0 \end{bmatrix} \delta\theta_z^1 && - B_{1g} \\
(\alpha_{xx} - \alpha_{zz}) &\begin{bmatrix} & & \cos\phi \\ & & 0 \\ \cos\phi & 0 & 0 \end{bmatrix} \delta\theta_y^1 && - B_{2g} \\
(\alpha_{xx} - \alpha_{zz}) &\begin{bmatrix} & & 0 \\ & & -\sin\phi \\ 0 & -\sin\phi & 0 \end{bmatrix} \delta\theta_y^1 && - B_{3g}
\end{aligned}
\qquad (4.7)
$$

Substitution of the eigenvector components shows that this is the same result as (4.5). As well as being simple this method is also graphic, and it gives results which are efficient for computation.

It has turned out then that the mode polarisabilities of equation (4.5) are expressed quite simply in terms of one component of an eigenvector. The reasons for this are that α_{yy} is equal to α_{zz}, so that rotations about the molecular x axis produce no change in the polarisability, and that $\delta\theta_y$ and $\delta\theta_z$ never occur together in the same representation (see Table 4(II)). It should then be possible to associate the intensity of each peak in the Raman spectrum with the mean-square amplitude of a particular component of an eigenvector. This situation is fortunate, for we can use the measured spectra together with (4.5) and (3.9) to estimate the components with no adjustable parameters.

TABLE 4(III)

Measured frequencies, in cm^{-1}, and assignments with normalised intensities:

	A_g			B_{1g}	B_{2g}	B_{3g}
	xx	yy	zz	xy	xz	yz
Frequency	51.1	51.1	-	40.0	29.0	26.5
Intensity	912[1]	483[2]	0	71.8	89	239
	51.1	51.1	-	54	49.0	42.3
	987[1]	524[2]	0	8.0	225	418
					60.8	53.3
					159	221
					73.8	64.5
					198	10.6

The normalised intensity is defined as

$$I = \int \frac{\mathcal{I}(\omega)}{\omega(n(\omega)+1)} \, d\omega$$

on an arbitrary scale.

Notes 1, 2) The single observed intensity has been divided between the modes for the purposes of comparing with Rinaldi's calculation. See discussion in Section 4.5.

4.4 Experimental

The Raman spectrum of sulphur was first observed by Krishnamurti[37], and the first measurements giving polarisation data on the external modes were by Ozin[38].

The measurements for the present work were reported initially in Reference (21). They were made on a 6 × 4 × 3 mm sample with faces cut and polished perpendicular to the crystal axes. The sample was cut from a crystal, grown from CS_2 solution, provided by Dr. J. Sherwood of Strathclyde University. System 2 was used to gather the data with a helium-neon laser providing the source at 6328Å and 80mW power. The spectrometer resolution was about 1.1 cm^{-1} (f.w.h.m.). Calibration checks were made against the exciting line, the plasma line at 6383Å, and the rotational spectrum of air. Analysis by the peak finding routine, Appendix IV, showed the reproducibility and accuracy of calibration to be better than $\pm$ .3 cm^{-1} over the entire range of measurement, 0 - 100 cm^{-1}. All data were taken at room temperature for three orientations of the crystal, covering all polarisations. Intensity correlations were made during the analysis, and a maximum discrepancy of 10% between the worked out intensity scales was estimated.

The positions of the peaks in the spectrum were found by the peak finding routine, and the intensity under each peak was estimated by fitting damped harmonic oscillator functions to the spectra; this procedure is described in detail in the following chapter. It is simpler to work with 'normalised' intensities defined by:

$$I = \int \frac{J(\omega)}{\omega(n(\omega)+1)} \, d\omega \qquad (4.8)$$

FIGURE 4.2

The A_g (yy) spectrum.

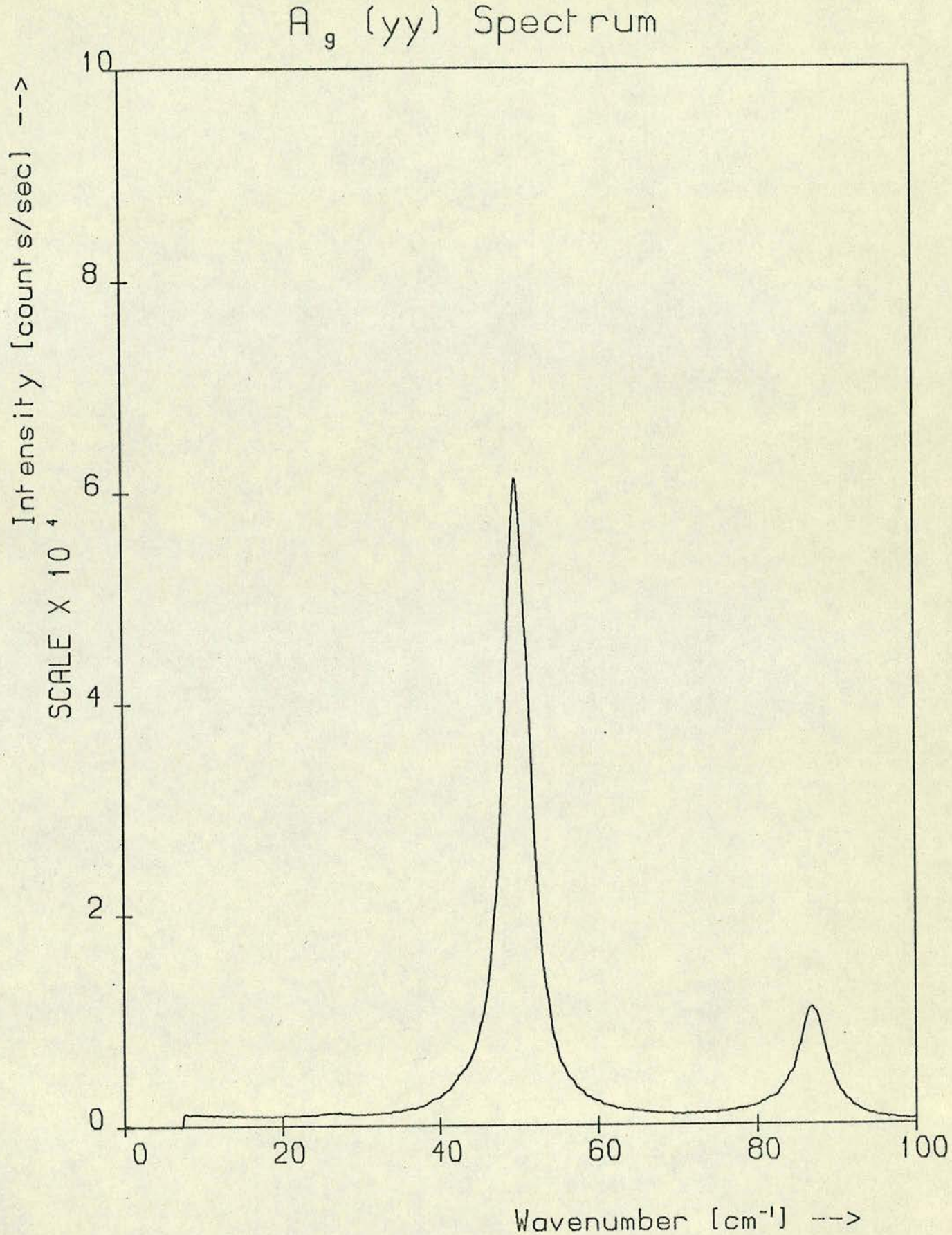
A g (yy) Spectrum
Intensity [counts/sec] -->
SCALE X 10 4
10
8
6
4
2
0
0
20
40
60
80
100
Wavenumber [cm-1] -->

FIGURE 4.3

The A_g (zz) spectrum showing a large number of accidental peaks below 87 cm^{-1}. These can be accounted for by a linear combination of xz and yz spectra, shown in dashed lines. The corrected spectrum, shown as a dotted line, is absent of significant peaks, other than that belonging to the internal mode.

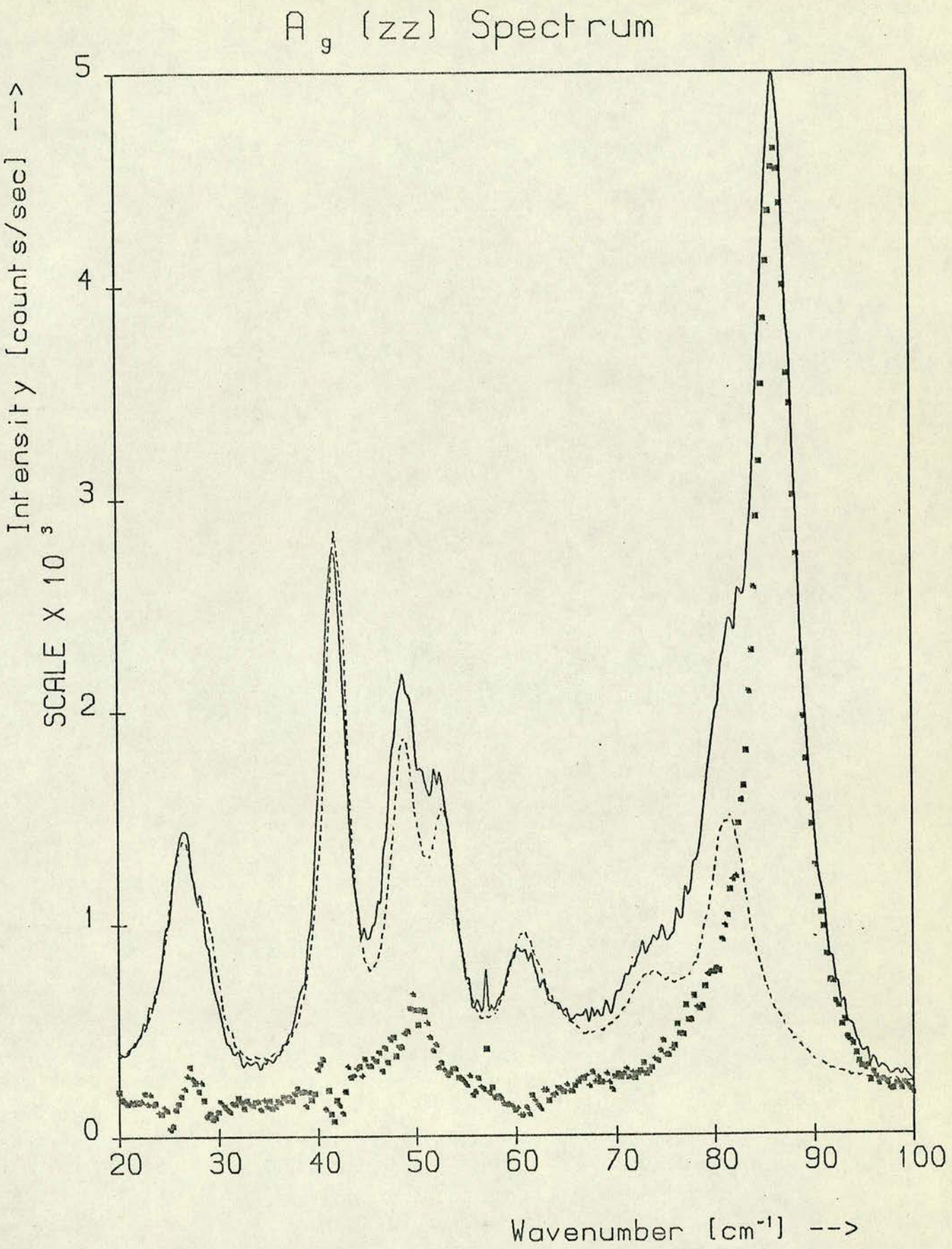
A g (zz) Spectrum
Intensity [counts/sec] -->
SCALE X 10 3
0
1
2
3
4
5
20
30
40
50
60
70
80
90
100
Wavenumber [cm-1] -->

FIGURE 4.4

The B_{1g} (xy) spectrum which has been similarly corrected to show only two significant peaks. The extraneous peak at 50 cm^{-1} comes from the yy and zx spectra.

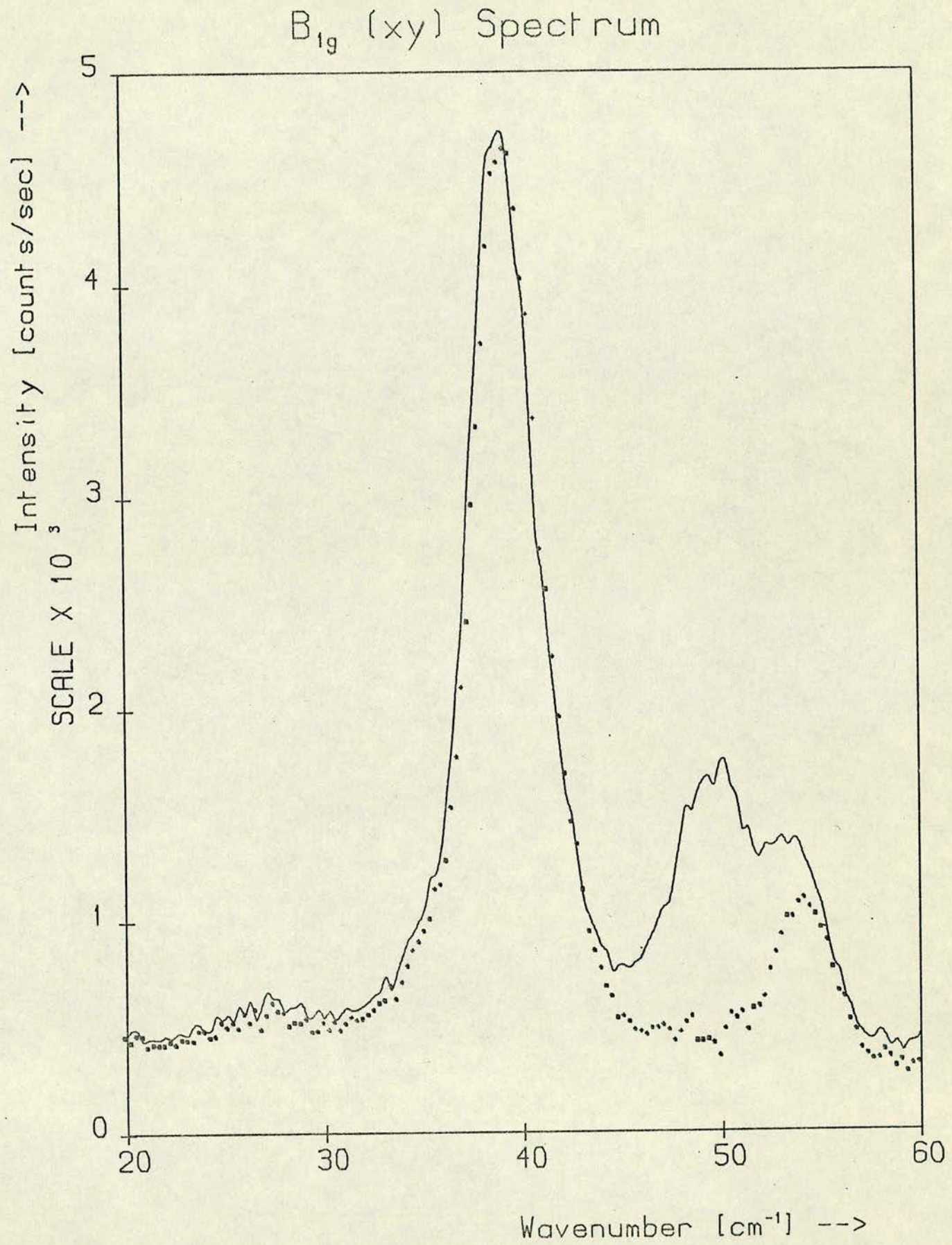
B_{1g} (xy) Spectrum
Intensity [counts/sec] -->
SCALE X 10^3
0
1
2
3
4
5
20
30
40
50
60
Wavenumber [cm^{-1}] -->

FIGURE 4.5

The B_{2g} (zx) spectrum. The mode at 74 cm^{-1} might well be of mixed internal-external character.

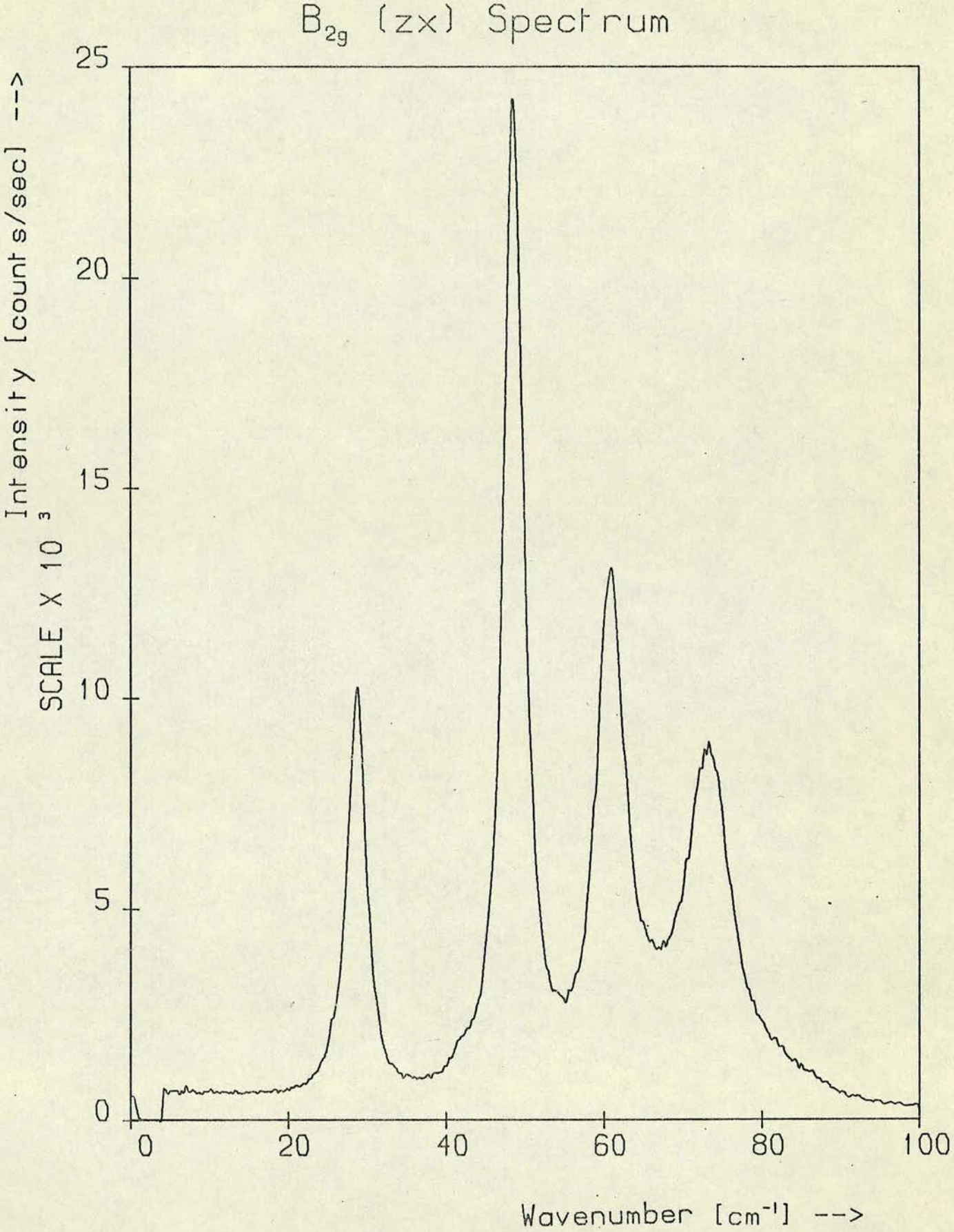
B_{2g} (zx) Spectrum
Intensity [counts/sec] -->
SCALE X 10^3
25
20
15
10
5
0
0
20
40
60
80
100
Wavenumber [cm^{-1}] -->

FIGURE 4.6

The B_{3g} (yz) spectrum showing the expected four peaks and the internal mode at 81 cm^{-1}.

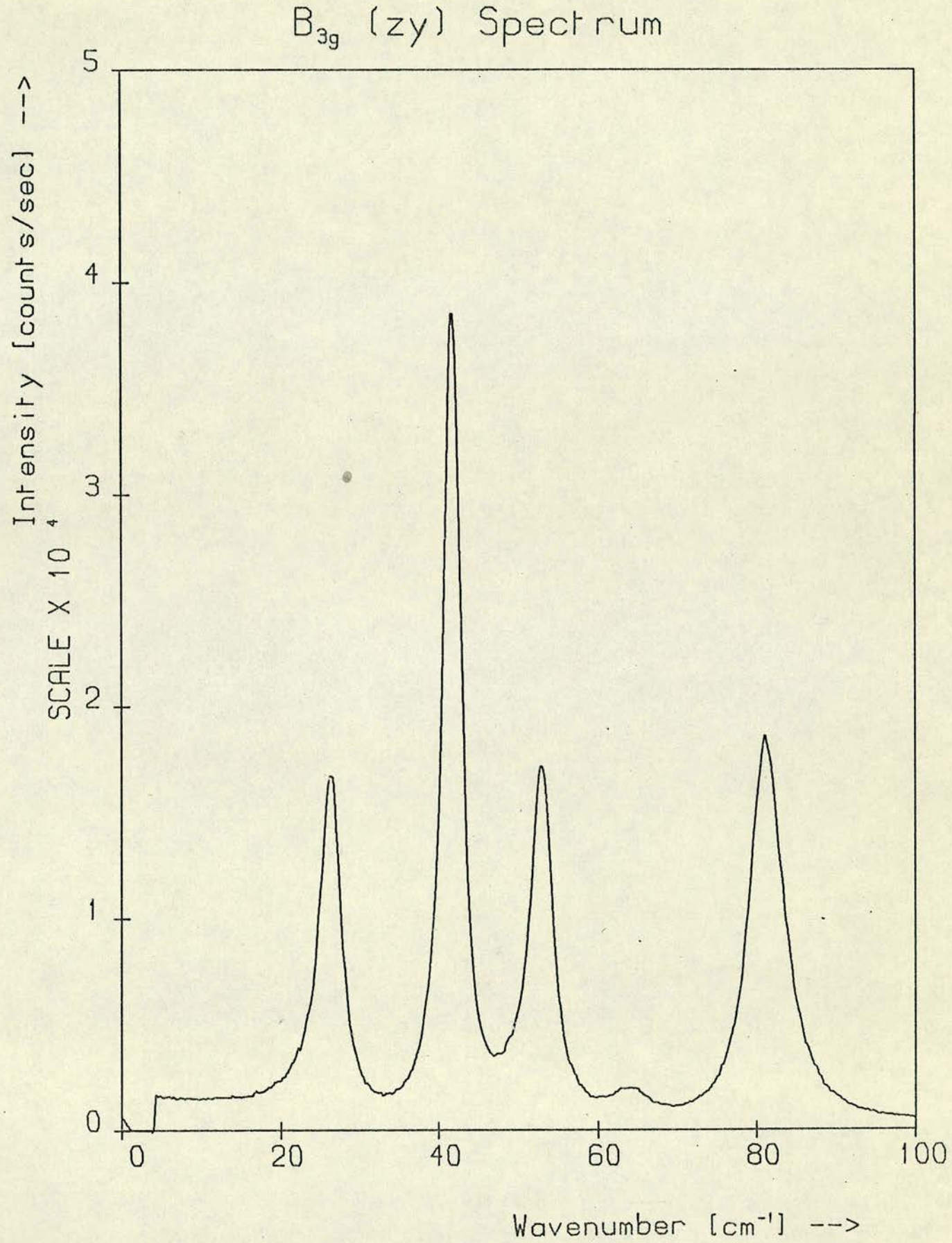
B_{3g} (zy) Spectrum
Intensity [counts/sec] -->
SCALE X 10^4
0
1
2
3
4
5
0
20
40
60
80
100
Wavenumber [cm^{-1}] -->

where $\mathcal{J}(\omega)$ is the fitted spectral function. I, so defined, has the temperature dependent population factor removed. The result of the above analysis is summarised in Table 4(III).

There is a practical difficulty, however, in identifying the proper peaks in each spectrum. This arises for the following reasons: two phonons, close in frequency, may be unresolvable because of their finite linewidth and instrumental resolution effects, birefringence and internal 'scattering' in the crystal make a complete polarisation analysis impossible, and finally in sulphur there is a low frequency internal mode at 86 cm^{-1} (39) which overlaps with the high frequency end of the external mode spectrum. This last difficulty also presents a serious theoretical problem, both to the model calculation and to the Raman scattering intensities.

The solution of the first problem is to decrease the temperature and thus decrease the phonon linewidths. Unfortunately sulphur is quite brittle and shatters easily under thermal strain. Powder samples have been used at low temperatures (40) but then a polarisation analysis is impossible. This problem was not considered to be serious enough to merit special attention and the spectra were recorded at room temperature.

The second problem was more serious, and the expectedly absent zz spectrum actually shows many peaks below 86 cm^{-1}, all of which were eventually discounted as originating from spectra of other polarisations. Here good use was made of the computer processing routines, Appendix (IV), and it was found possible to reproduce this spectrum with a linear combination of the xz and yz spectra. The fit, Figure 4.3, is good:

the difference spectrum, shown in dots, is the proper zz spectrum and there are indeed no significant peaks in the lattice region. A similar technique was applied to the xy spectrum, Figure 4.4, and it was found that just two peaks remain, as expected. This difference technique should also prove useful in crystals of symmetry higher than orthorhombic where it is not a general rule that only one irreducible representation occurs in a given polarised spectrum.

The last problem concerns the validity of the adiabatic approximation that the internal and external modes do not couple. Any external mode close in frequency to the internal mode at 86 cm^{-1} may couple with it to produce a mode of mixed internal-external character. This mode at 86 cm^{-1} is of symmetry E_2 in the free molecule and gives rise to 8 internal modes in the crystal as follows:

$$S_{int} \sim \{A_g + B_{1g} + B_{2g} + B_{3g} + A_u + B_{1u} + B_{2u} + B_{3u}\} .$$

Therefore in the crystal there is a possibility of coupling in all the spectra since the rule is that modes of the same symmetry may couple, and all the irreducible representations of D_{2h} occur in S_{int}. In all the spectra, other than the one of B_{2g} symmetry, the experimental results suggest that this coupling is perhaps only weak, for in each case there is a peak in the spectrum, at around 80 cm^{-1}, well separated and easily distinguished from the other peaks at lower frequencies. In the B_{2g} spectrum, Figure 4.5, the situation is not so clear. This is a problem, however, which can not be evaluated properly just by looking at the spectrum and a non-rigid molecule calculation to estimate the effect of coupling

would be required. The mixing of the eigenvectors not only changes the components but introduces into the Raman scattering polarisability contributions from both internal and external vibrations. This can quite drastically change the observed intensities and we might well expect disagreement between the rigid molecule calculation and experiment on this account.

4.5 The Eigenvectors

The equations (4.5) show how we expect the mode polarisabilities to relate to the eigenvectors. We can invert these equations, making use of (3.10), to give certain components of the eigenvectors in the form:

$$\left(e^{j}_{\theta z}(1)\right)^2 = \frac{\omega_j^2}{\beta^2 \sin^2 2\phi} I^j_{xx} = \frac{\omega_j^2}{\beta^2 \sin^2 2\phi} I^j_{yy} \qquad j = 1,2$$

$$\left(e^{j}_{\theta z}(1)\right)^2 = \frac{\omega_j^2}{\beta^2 \cos^2 2\phi} I^j_{xy} \qquad j = 3,4$$

$$\left(e^{j}_{\theta y}(1)\right)^2 = \frac{\omega_j^2}{\beta^2 \cos^2 \phi} I^j_{xz} \qquad j = 5,6,7,8$$

$$\left(e^{j}_{\theta y}(1)\right)^2 = \frac{\omega_j^2}{\beta^2 \sin^2 \phi} I^j_{yz} \qquad j = 9,10,11,12 \quad , \tag{4.9}$$

using the normalised intensities defined above. We also have the normalisation condition:

$$\sum_m e_m^{j\,2} = \sum_j e_m^{j\,2} = 1 \qquad (4.10)$$

which allows us to fix β^2 simply as a scale factor.

To apply these equations we must first of all associate each component with a peak in the spectrum of the appropriate symmetry. This is straightforward for the B_{1g} and B_{3g} spectra, but for the A_g and B_{2g} we must first of all make certain clarifications.

In the A_g spectrum we can identify only one peak in the lattice vibration region, Figure 4.2. There is no indication of a second peak corresponding to the prediction of two A_g external modes. Two situations may then obtain: (a) one of the modes is purely rotational, with a non-zero polarisability, and the other is purely translatory, with no polarisability; (b) the modes are accidentally degenerate. A careful examination of the secular equation for two modes shows that although (b) implies (a) when the modes are exactly degenerate, the modes may still be nearly degenerate with no restriction on the eigenvectors. Although we cannot distinguish these situations in our experiment, and we therefore cannot uniquely determine the eigenvectors of the A_g modes, we can check whether this situation is borne out by Rinaldi's calculation.

In the B_{2g} spectrum we must decide what to do about the mode, at 74 cm^{-1}, of dubious internal-external character. For the purpose of checking Rinaldi's calculation we simply assume that this mode is a pure external vibration. Bearing these points in mind, we may now apply (4.9) and (4.10) to the

FIGURE 4.7

Calculated spectra of orthorhombic sulphur for

$\alpha_{yy} = \alpha_{zz} \neq \alpha_{xx}$

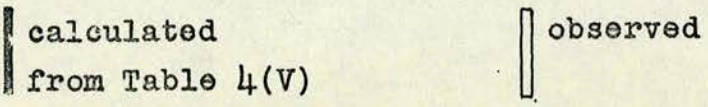

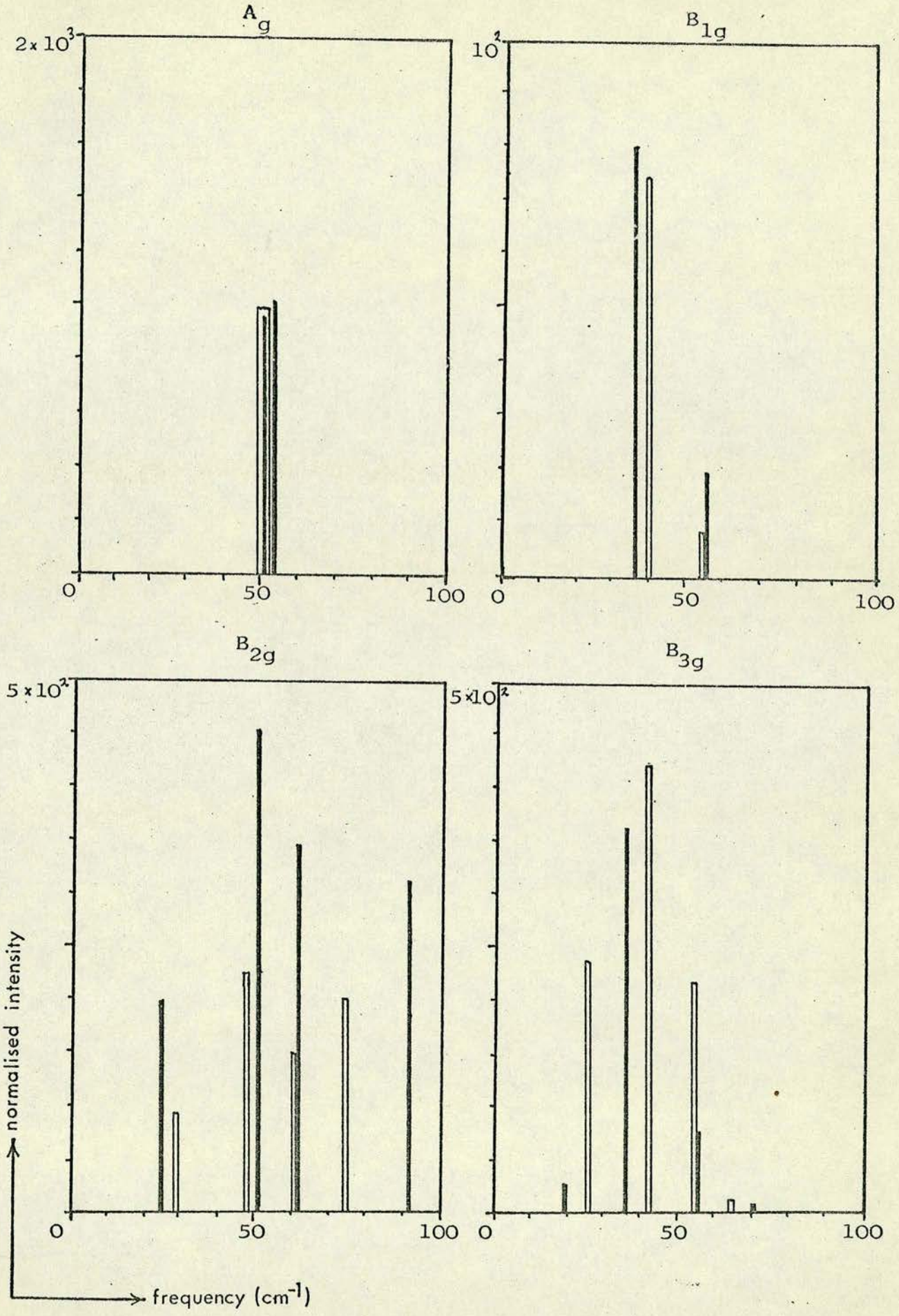
A g
2 x 10^3
0
50
100
B 1g
10^2
0
50
100
B 2g
5 x 10^2
0
50
100
B 3g
5 x 10^2
0
50
100
normalised intensity
frequency (cm^-1)

results of Table 4(III) to obtain the squares of the components of the eigenvectors. These are tabulated in Table 4(IV), together with the values taken from Rinaldi's best model, the results of which we reproduce in Table 4(V). The values of β^2, which we have adopted as a scale factor expected to be identical for all spectra, are also tabulated. They lie in the range 1.08×10^7 to 2.03×10^7. That the values of β^2 are different, notably so in the xx and yy components of the A_g spectrum, reflects a shortcoming in the model which we discuss at length in the final section of this chapter. However, at this stage, we can only say that such disperse values of β^2 make our intensity correlations meaningless. We can, nevertheless, still obtain useful information from the individual spectra.

To further facilitate comparison with Rinaldi's model we can use equations (4.5) to calculate the spectra from the eigenvectors. To resolve the problem of how to treat the A_g modes, we note that Rinaldi's calculation puts the frequencies of the two modes at 51 and 53 cm^{-1} - quite close indeed. If we accept that $2cm^{-1}$ is probably within the accuracy of the calculation, then Rinaldi's model is consistent with situation (b) described above - that the A_g modes are nearly degenerate. In contrast, we suggested in Reference (21) that situation (a) might obtain - that the modes are pure translatory and pure rotatory respectively - but in the light of Rinaldi's results this would not seem to be the case.

Figure 4.7 shows simplified diagrams of the experimental spectra and the spectra calculated in this manner. The normalised intensities are simply represented by a bar: the expected near degeneracy of the A_g modes is represented

TABLE 4(IV)

Calculated values of the $(e_m^j)^2$

	Mode	Frequency	e_m^j	$(e_m^j)^2$ calc.	$(e_m^j)^2$ Rinaldi	$\beta^2 \times 10^{-7}$
A_g	1	51.1	$e^1_{\theta z}(1)$	-	.120	2.03 in xx
	2	51.1	$e^2_{\theta z}(1)$	-	.130	1.08 in yy
B_{1g}	3	40.0	$e^3_{\theta z}(1)$	.208	.203	1.16
	4	54	$e^4_{\theta z}(1)$	.042	.047	
B_{2g}	5	29.0	$e^5_{\theta y}(1)$	.008	.032	1.50
	6	49.0	$e^6_{\theta y}(1)$	.059	.082	
	7	60.8	$e^7_{\theta y}(1)$	.064	.068	
	8	73.8	$e^8_{\theta y}(1)$	.118	.062	
B_{3g}	9	26.5	$e^9_{\theta y}(1)$	.026	.006	1.62
	10	42.3	$e^{10}_{\theta y}(1)$	.118	.220	
	11	53.3	$e^{11}_{\theta y}(1)$	.099	.021	
	12	64.5	$e^{12}_{\theta y}(1)$	.007	.003	
		cm^{-1}				

TABLE 4(V)

Calculated zone centre eigenvectors of orthorhombic sulphur, (Rinaldi 1974)

	Branch	ν	x^1	y^1	z^1	α^1	β^1	γ^1
1	A_g	51	0	0	.360	0	0	.346
2		53	0	0	-.346	0	0	.360
3	B_{1g}	38	0	0	-.219	0	0	.449
4		55	0	0	-.449	0	0	-.219
5	B_{2g}	26	.006	.084	0	.45	-.179	0
6		52	.103	-.390	0	-.043	-.291	0
7		63	.274	.285	0	-.158	-.261	0
8		92	.405	-.094	0	.111	.253	0
9	B_{3g}	19	.043	-.334	0	.360	-.079	0
10		37	.047	-.063	0	.156	.468	0
11		54	-.068	.358	0	.309	-.144	0
12		71	.491	.073	0	-.003	-.058	0
		cm^{-1}						

$I_{xx} = 4.369 \qquad I_{yy} = I_{zz} = 2.378.$

$V(r) = -\frac{A}{r^6} + B \exp(-\alpha r).$

$A = 1167$ kcal/mole $Å^6$

$B = 13957$ kcal/mole

$\alpha = 2.9\ Å^{-1}$

FIGURE 4.8

The calculated spectra of orthorhombic sulphur for the following best fitting parameters:

	$\alpha_{xx} - \alpha_{yy}$	$\alpha_{yy} - \alpha_{zz}$
A_g	.689	0
B_{1g}	.657	0
B_{2g}	.503	.009
B_{3g}	1.014	-.370

▌Calculated ▯Observed

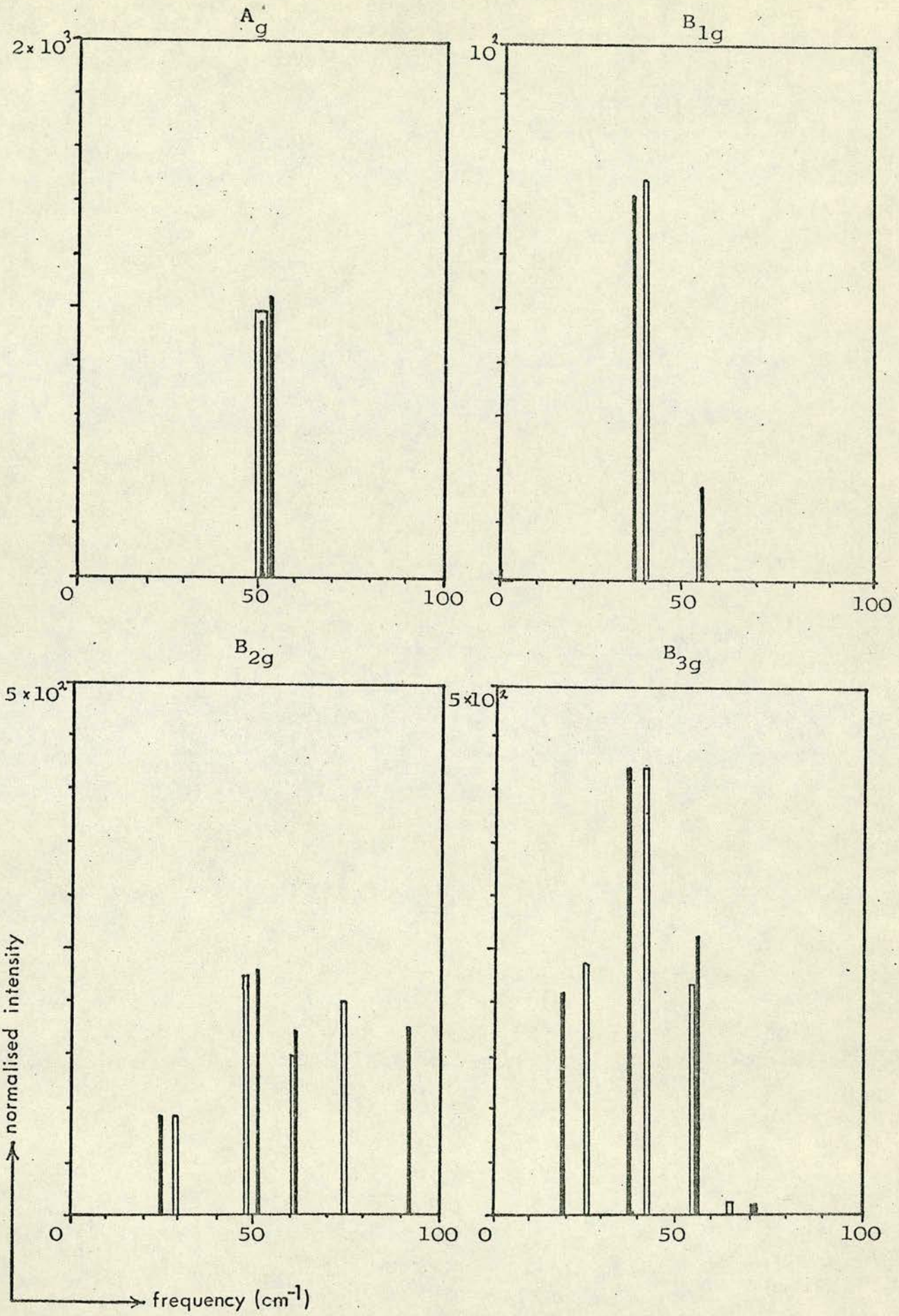
A g
2 x 10^3
0
50
100
B 1g
10^2
0
50
100
B 2g
5 x 10^2
0
50
100
B 3g
5 x 10^2
0
50
100
normalised intensity
frequency (cm^-1)

FIGURE 4.9

The calculated spectra of orthorhombic sulphur for the single set of parameters:

$\alpha_{xx} - \alpha_{yy} = .7079$ $\alpha_{yy} - \alpha_{zz} = -.173$

▌ calculated ▯ observed

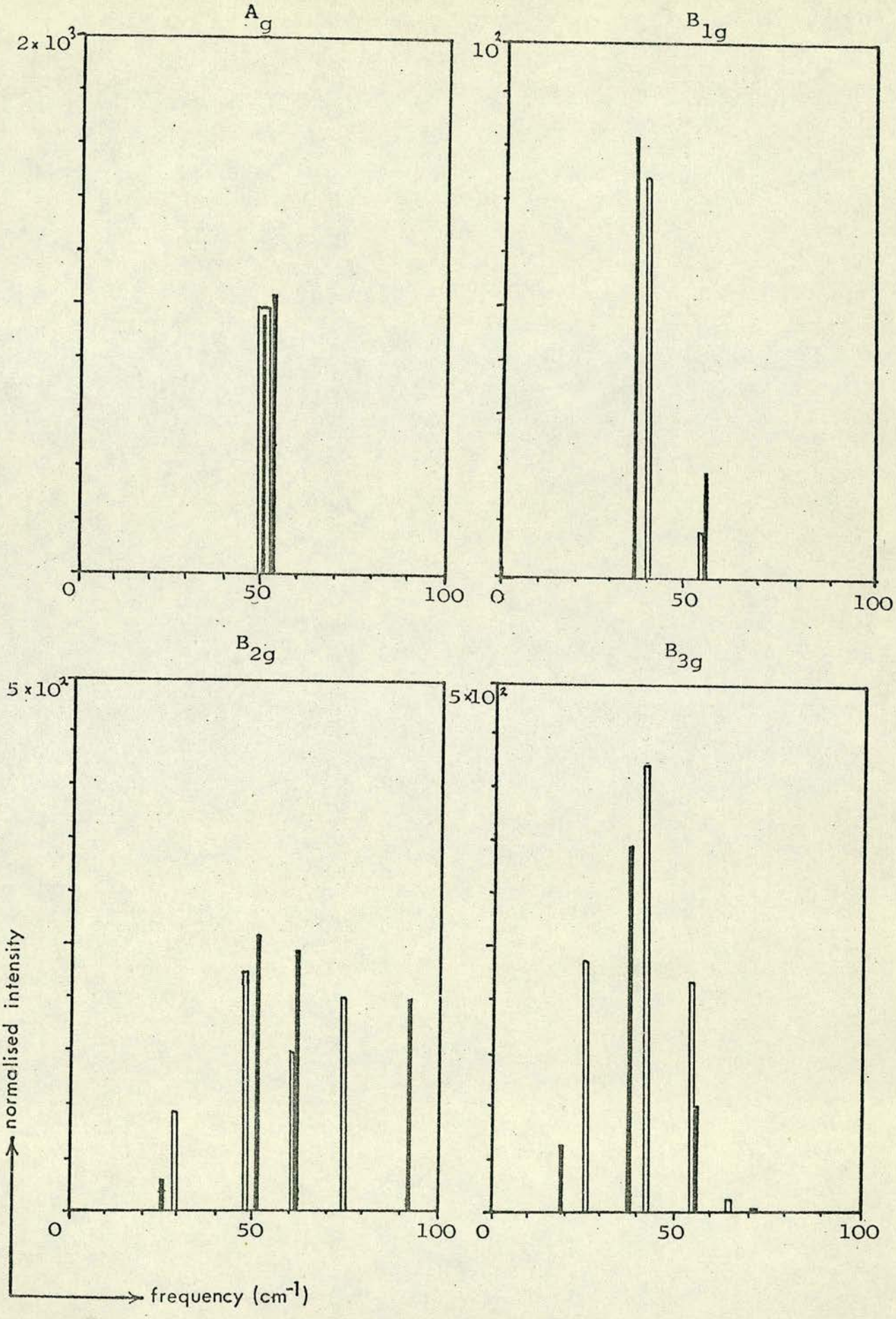
A_g
2 x 10^3
0
50
100
B_1g
10^2
0
50
100
B_2g
5 x 10^2
0
50
100
B_3g
5 x 10^2
0
50
100
normalised intensity
frequency (cm^-1)

using a bar of double width to depict the observed intensity.

The simpler A_g and B_{1g} spectra show remarkably good agreement, whereas the more complex B_{2g} and B_{3g} do not. If we accept the validity of the intensity calculation we should conclude that the 6-exp rigid molecule model is inadequate to describe the B_{2g} and B_{3g} spectra. On the other hand, the assumption that in the crystal $\alpha_{yy} = \alpha_{zz}$ still holds, may be at fault. If this were the case the A_g and B_{1g} spectra would remain unchanged, but in the B_{2g} and B_{3g} spectra there would now be contributions from rotational oscillations about the molecular x axis. The polarisabilities of (4.5) would now have the more complicated form:

$$\begin{aligned} P_j\,xx &= -P_j\,yy = \beta \sin 2\phi\, e^j_{\theta z}\,, \quad P_j\,zz = 0 \\ P_j\,xy &= \beta \cos 2\phi\, e^j_{\theta z} \\ P_j\,xz &= \gamma \cos\phi\, e^j_{\theta y} + \varepsilon \sin\phi\, e^j_{\theta x} \\ P_j\,yz &= -\gamma \sin\phi\, e^j_{\theta y} + \varepsilon \cos\phi\, e^j_{\theta x} \end{aligned} \qquad (4.11)$$

where $\beta = \dfrac{(\alpha_{xx}-\alpha_{yy})}{\sqrt{I_{zz}}}$, $\gamma = \dfrac{(\alpha_{xx}-\alpha_{zz})}{\sqrt{I_{yy}}}$, $\varepsilon = \dfrac{(\alpha_{zz}-\alpha_{yy})}{\sqrt{I_{xx}}}$.

There are now three adjustable parameters, and with these each of the spectra may now be fitted quite well (Figure 4.8) provided that they are chosen slightly differently for each spectrum. An attempt to find one set of $\{\alpha_{ii}\}$ which fit all the spectra and conform with the intensity sum rules (3.12) gives a less encouraging result (Figure 4.9). The correlation of measured intensities between spectra of different polarisations

is not good enough however (with about 10°/o variability) to make this a strict test.

4.6 Evaluation of the Model Calculation

It is, first of all, notable that as far as the A_g and B_{1g} spectra are concerned both frequency and intensity measurements are in good accord with the calculations using Rinaldi's calculated eigenvectors and eigenfrequencies. With the B_{2g} and B_{3g} modes, however, there is doubt because there are discrepancies in both frequencies and intensities. We would wish to believe, on the strength of the satisfactory agreement as far as the A_g and B_{1g} modes go, that the 'oriented-gas' approximation gives a satisfactory derivation of the cross-section which should also apply to the B_{2g} and B_{3g} modes. If this were indeed the case then we should conclude that the calculated B_{2g} and B_{3g} eigenvectors are wrong, and that there is indeed a short-coming in the model of Pawley and Rinaldi. There are, however, serious theoretical objections to the 'oriented-gas' approximation as it stands. These are particularly important in sulphur, which has a large polarisability (refractive index ~ 2). They are brought to light by a detailed calculation of the polarisability, allowing for the induced depolarisation field. This requires a calculation of the local field, $\underline{E}^{loc}(\mathcal{K})$ at a molecular site $\mathcal{K}$ in terms of the applied field $\underline{E}^{o}$, for which we have:

$$\underline{E}^{loc}(K) = \underline{E}^{o} + \sum_{\ell,\mu}\left(\frac{\underline{p}(\ell,\mu)}{r^3(\ell,K\mu)} - 3\frac{\left(\underline{p}(\ell,\mu)\cdot\underline{r}(\ell,K\mu)\right)\ \underline{r}(\ell,K\mu)}{r^5(\ell,K\mu)}\right) \tag{4.12}$$

where $\underline{p}(\ell,\mu)$ is the induced dipole at the lattice site (ℓ,μ) and $\underline{r}(\ell,K\mu) = \underline{r}(0,K) - \underline{r}(\ell,\mu)$. We can write this as:

$$\underline{E}^{loc}(K) = \underline{E}^{o} + \sum_{\mu} C^{K\mu}\,\underline{p}(0,\mu) \tag{4.13}$$

where $\underline{p}(\ell,\mu) = \underline{p}(0,\mu)$ for all ℓ (at $\underline{Q} = 0$) and the $\left\{C^{K\mu}_{\alpha\beta}\right\}$ are the Coulomb coefficients for the sulphur lattice at $\underline{Q} = 0$, neglecting the electrostatic contribution. A general definition of these coefficients is given in Born and Huang[3]. They are difficult to evaluate for general crystal structures[41]. In (4.13) we can substitute:

$$\underline{p}(0,K), = \alpha^{K}\,\underline{E}^{loc}\ (K) \tag{4.14}$$

to find, in matrix notation:

$$(1 - C\alpha)\underline{E}^{loc} = \underline{E}^{o}$$

or

$$\underline{E}^{loc} = (1 - C\alpha)^{-1}\,\underline{E}^{o} \tag{4.15}$$

To establish this matrix notation we once more make use of the combination of lattice site indices with x, y and z indices. The crystal polarisability is then found to be, summing the induced dipoles in the volume of one cell:

$$P_{\alpha} = \frac{1}{V}\sum_{K} p_{\alpha}(0,K) = \frac{1}{V}\sum_{K\lambda}\left[\alpha(1 - C\alpha)^{-1}\right]^{\alpha\beta}_{K\lambda}\ E^{o}_{\beta}\ . \tag{4.16}$$

Only when $\|C\alpha\| \ll 1$ does this reduce to the simple form

$$P_\alpha = \frac{1}{V} \sum_\kappa \alpha_\kappa^{\alpha\beta} E_\beta^\circ \qquad (4.17)$$

assumed in the oriented gas approximation.

We may now proceed, as in original approximation, to expand α in terms of a static part α°, and a fluctuating part α' which may be expanded as a function of the eigenvectors of the molecular motion. For $\alpha' \ll \alpha^\circ$ (4.16) becomes, in matrix form:

$$\underline{P} = \alpha^\circ(1 - C\alpha^\circ)^{-1} \underline{E}^\circ + \left[1 + \alpha^\circ(1-C\alpha^\circ)^{-1} C\right] \alpha' \left[(1-C\alpha^\circ)^{-1}\right] \underline{E}^\circ . \qquad (4.18)$$

The matrices C, α° and α' are all symmetric, and using this property it is easy to show that

$$\left[1 + \alpha^\circ(1-C\alpha^\circ)^{-1}C\right] = \left[(1-C\alpha^\circ)^{-1}\right]^{tr} \qquad (4.19)$$

and that the polarisability is symmetric, as usual. Using (4.19) we can express the differential polarisability through:

$$\delta\underline{P} = \left[(1 - C\alpha^\circ)^{-1}\right]^{tr} \alpha' \left[(1 - C\alpha^\circ)^{-1}\right] \underline{E}^\circ . \qquad (4.20)$$

The interaction energy $\underline{E}^\circ . \delta\underline{P}$ may then be written as $(\underline{E}^{loc})^* \alpha' \underline{E}^{loc}$, which is what we would expect. The local field, however, is different at each molecular site, and even making use of the symmetry properties of C, α and α', the calculation of the scattering using (4.20) is a non-trivial computational problem. In spite of such difficulty it is felt that for many molecular crystals, including sulphur, this approach would result in a useful improvement to the oriented-gas model. This would give a more accurate and sensitive test of eigenvector calculations.

CHAPTER 5

DECAFLUOROBIPHENYL

The lattice vibration spectrum of this molecular crystal is reported for the first time. A peak has been observed in the Raman spectrum of the melt at 54 cm^{-1}, showing the presence of at least one very low frequency internal vibration of the molecule. It has been discovered that in the A_1 symmetry lattice spectrum there is considerable coupling between this mode and a lattice vibration. The extent of this coupling is estimated using the theory of Chapter Three.

5.1 The Crystal Structure

For brevity we refer to decafluorobiphenyl by its formula $C_{12}F_{10}$: whether we refer to the crystal or molecule should be clear from the context. Little experimental work exists on this substance, but its structure has been reported by Neronova[42]. Other work on $C_{12}F_{10}$ relates to the properties of the molecule, the structure of which is shown in Figure 5.1. It can be seen that the molecule has a twisted shape, rather like a two-bladed propeller. The angle ϕ is 62° in the crystal. For molecules of such a configuration having only a single C-C bond joining two large planar rings, very low frequency internal vibrations might be expected. The molecule has point group 222 (D_2) and we adopt the axis system shown in the figure to unambiguously define the representations of the point group.

The space group of the crystal is Fdd2 (C_{2v}^{19}) and there

FIGURE 5.1

The conformation of the $C_{12}F_{10}$ molecule.

FIGURE 5.2

The crystal structure of decafluorobiphenyl.

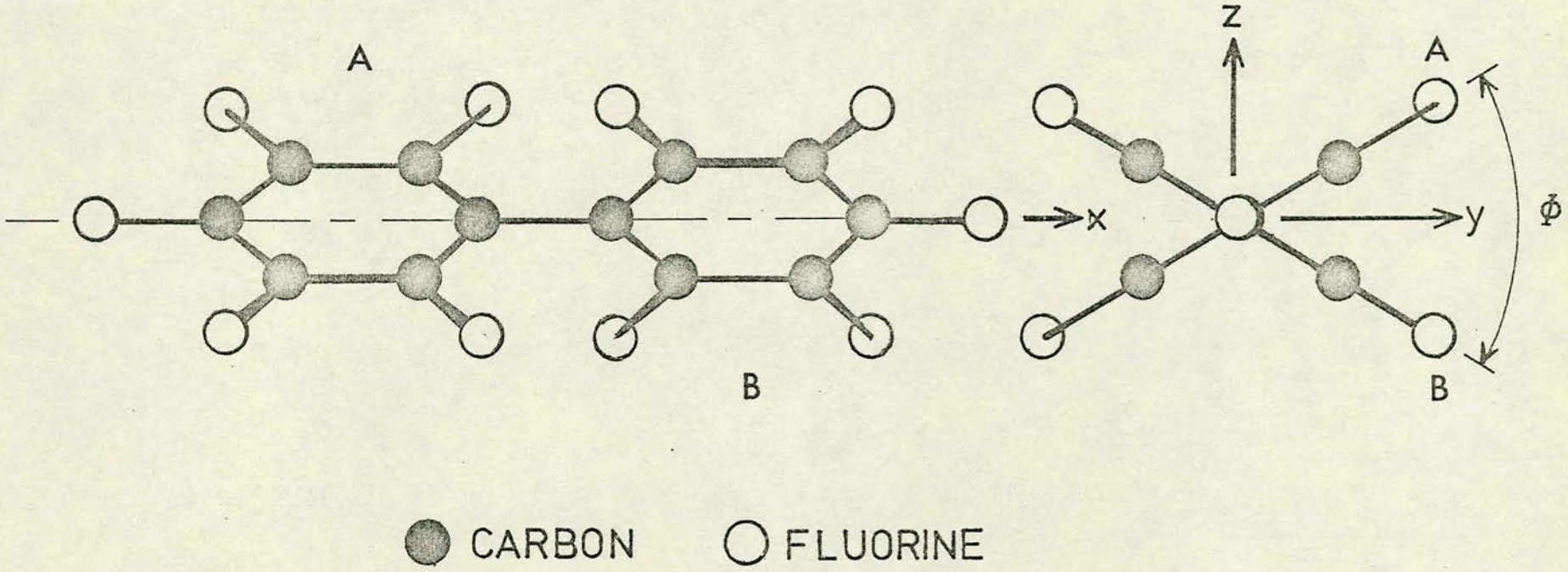
A
B
Z
A
B
x
y
Φ
CARBON
FLUORINE

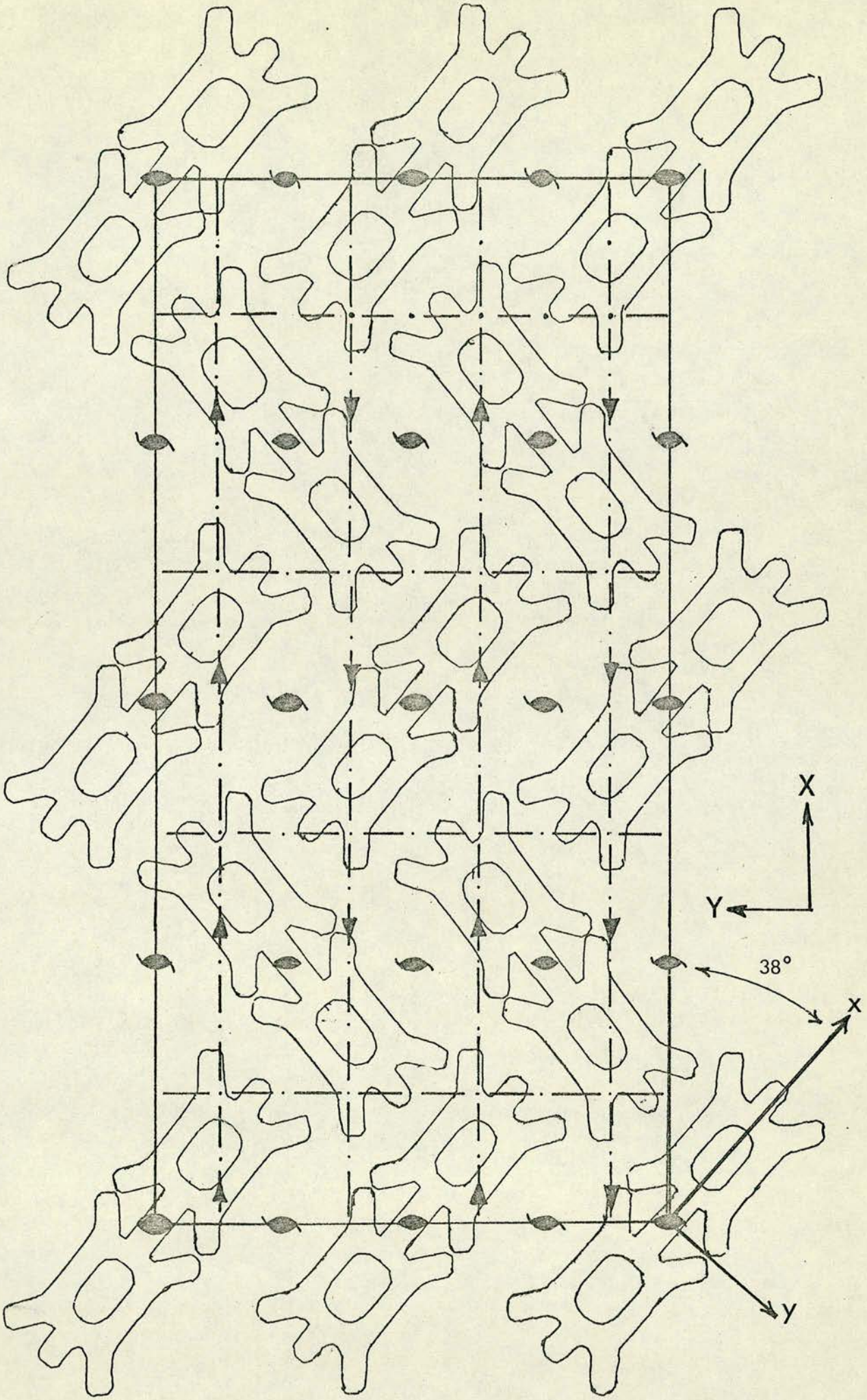
X
Y
38°
x
y

are two molecules in the primitive cell. The c axis projection of the unit cell is shown in Figure 5.2. In contrast, biphenyl, $C_{12}H_{10}$, has the space group $P2_1/c$ (C_{2h}^5). The important difference is that in biphenyl the $C_{12}H_{10}$ molecules become planar in the crystalline phase.

5.2 Experimental

The sample used in the experiments was grown from the melt using a rather crude zone refiner. A small section of single crystal was produced and this was cleaved from the boule, oriented under a polarising microscope, and finally polished, yielding a small parallelepiped of about 1 × 3 × 4 mm reasonably suitable for optical work. The crystallographic axes were identified by X-ray diffraction oscillation photographs. The sample contained many small cracks, and the sublimation of the material (m.p. 68°C) led to rapid deterioration of the surfaces. The condition of the surfaces could be improved by light polishing on soft tissue paper. Although the sample was quite colourless and transparent it was found that local surface heating could cause further deterioration by pitting. A solution to these problems was found by mounting the sample on a glass slide, in optical contact with it, using a thin film of some inert oil (silicone oil or refractive index liquid). This greatly enhanced the transmission of the incident laser beam into the sample. The experiments were initially performed on System 2, using the 6328Å line of the helium-neon laser to excite the spectra:

the laser was operated at about 80 mW output. The spectra were obtained for three orientations of the crystal, giving a complete set of data over the range 0 - 100 cm^{-1}. Subsequent runs to measure the internal mode frequencies were abandoned because of poor signal and unwanted peaks from plasma lines at 179 and 182 cm^{-1}. The plasma lines in these results were, however, useful as a calibration check. System 1 was used to complete this part of the work, using 80 mW of the 5145 $\mathring{A}$ line of the argon-ion laser. The larger light throughput and blue sensitivity of this system gave nearly an order of magnitude of increase in signal, enabling the weak internal modes to be clearly observed. The measurements were made over a range 0 - 250 cm^{-1} and the results were compatible with those obtained in the first set of experiments. The spectra are shown in Figures 5.3 to 5.14, after intensity correlation. The peak finding routine was applied to the data and the results of this are given in Table 5(I).

5.3 The Internal Modes of Vibration

It has already been mentioned that we expect very low frequency internal vibrations. If this is indeed the case then our immediate interest is to observe what effect this has on the lattice vibrations. The possibility of low frequency internal modes in $C_{12}F_{10}$ has been treated by Almenningen *et al.*[43] and Steele[44]. Steele's calculation (based on a molecule of D_{2h} symmetry) shows that perhaps four low frequency modes exist below 130 cm^{-1}. Most of the other internal mode frequencies have been reported by Steele, and

FIGURE 5.3

The xx spectrum of A_1 symmetry over the range 10 - 100 cm^{-1}.

———— experiment

- - - - - - - - - fit

Figure 5.4

The xx spectrum over the range 100 - 250 cm^{-1} showing the much weaker internal modes.

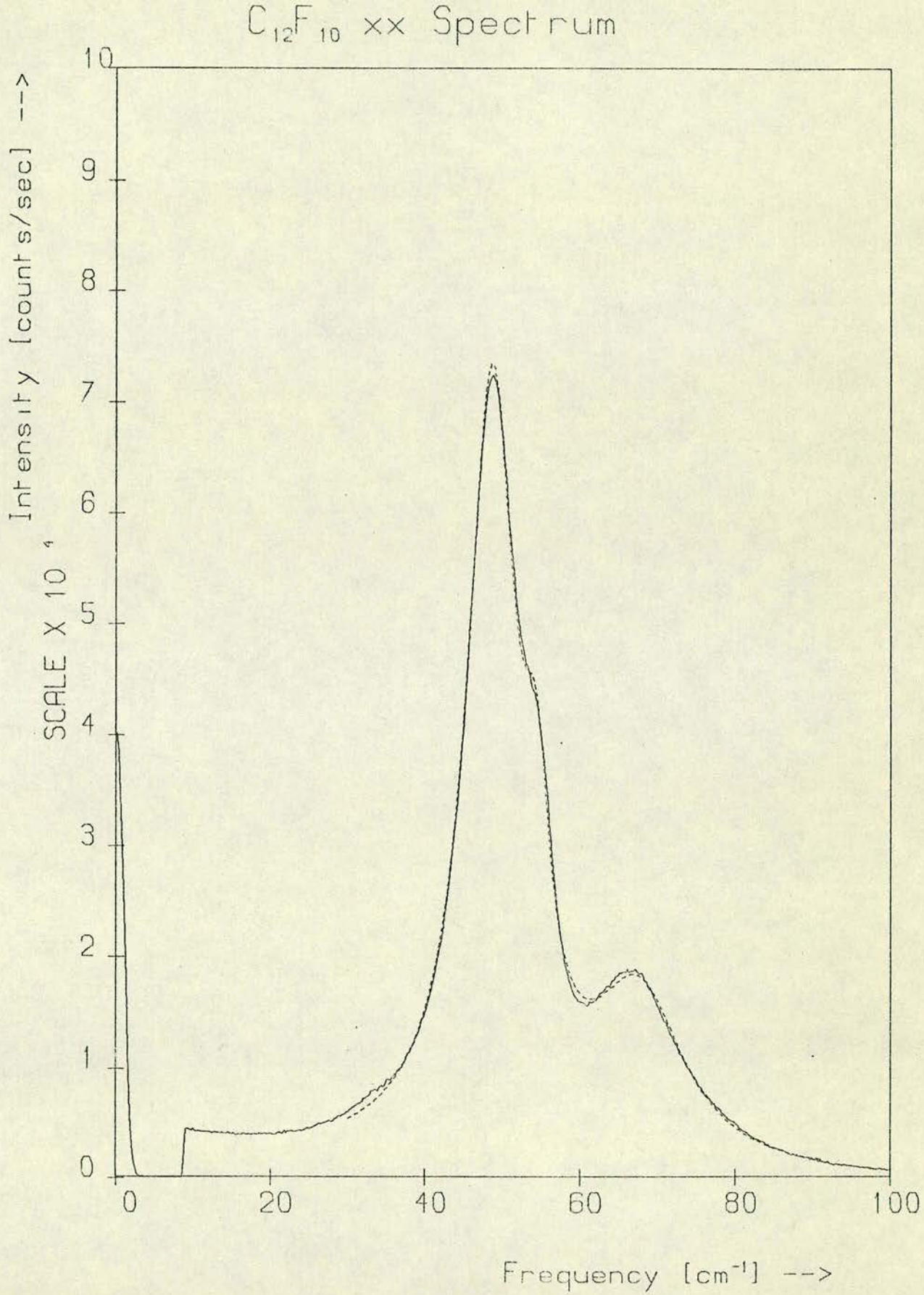
$C_{12}F_{10}$ xx Spectrum
Intensity [counts/sec] -->
SCALE X 10^4
10
9
8
7
6
5
4
3
2
1
0
0
20
40
60
80
100
Frequency [cm^{-1}] -->

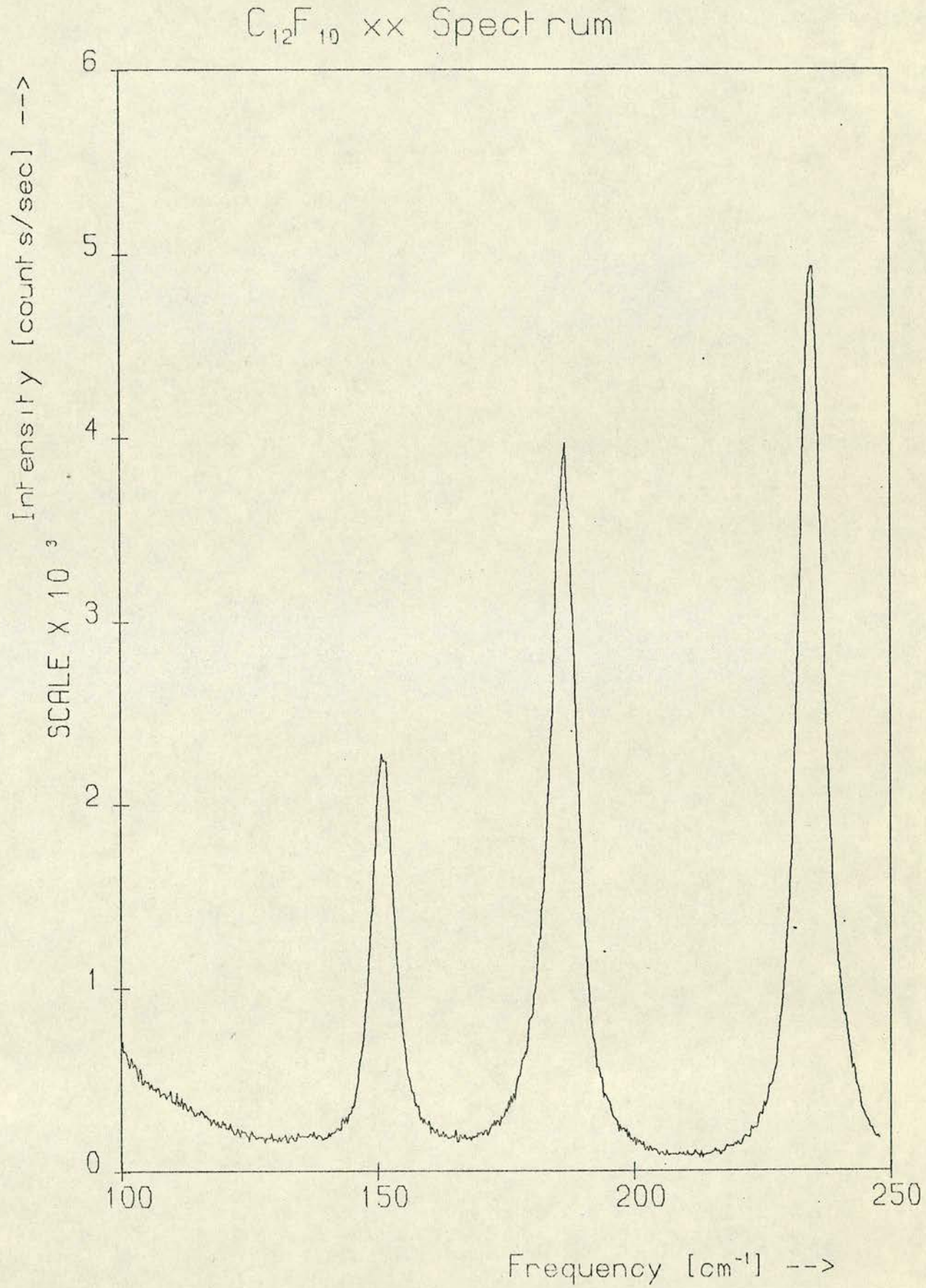
$C_{12}F_{10}$ xx Spectrum
Intensity [counts/sec] -->
SCALE X 10^3
0
1
2
3
4
5
6
100
150
200
250
Frequency [cm^{-1}] -->

FIGURE 5.5

The yy spectrum of A_1 symmetry over the range 10 - 100 cm^{-1}.

———— experiment

--------- fit

FIGURE 5.6

The yy spectrum over the range 100 - 250 cm^{-1} showing the internal modes.

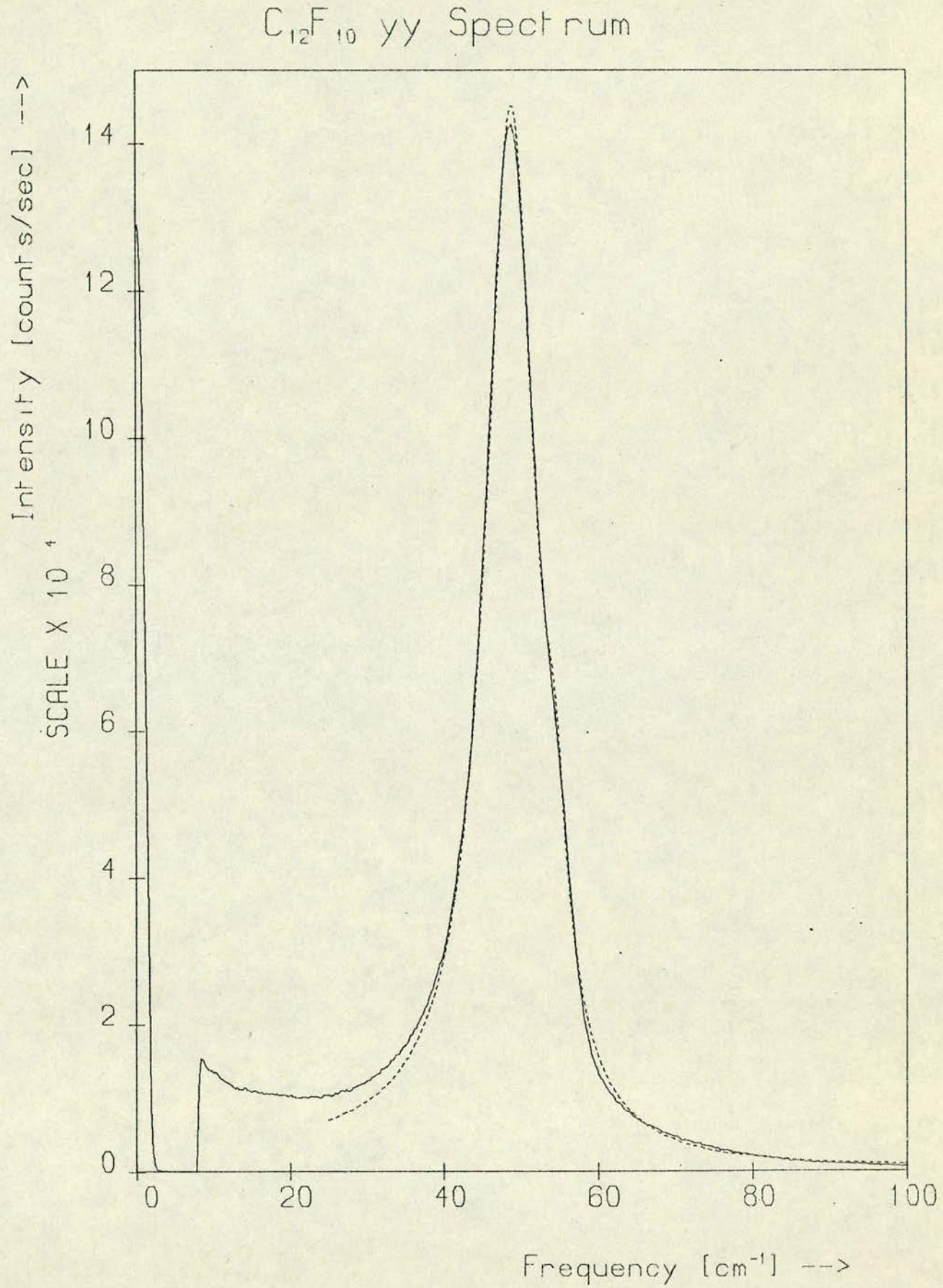
$C_{12}F_{10}$ yy Spectrum
Intensity [counts/sec] -->
SCALE X 10^{4}
14
12
10
8
6
4
2
0
0
20
40
60
80
100
Frequency [cm^{-1}] -->

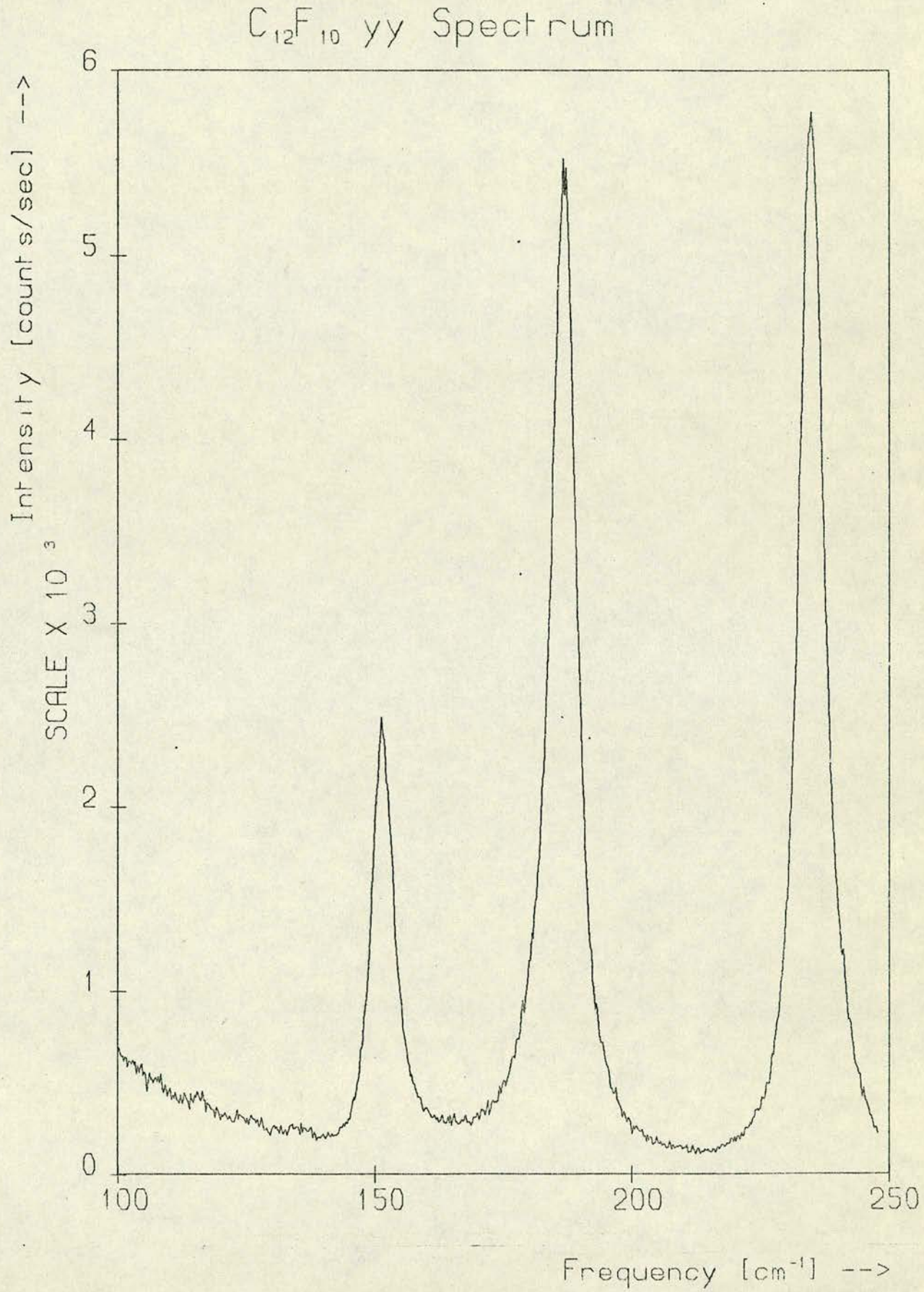
$C_{12}F_{10}$ yy Spectrum
Intensity [counts/sec] -->
SCALE X 10^3
0
1
2
3
4
5
6
100
150
200
250
Frequency [cm^{-1}] -->

FIGURE 5.7

The zz spectrum of A_1 symmetry over the range 10 - 100 cm^{-1}.

———— experiment

-------- fit

FIGURE 5.8

The zz spectrum over the range 100 - 250 cm^{-1} showing extremely weak internal modes.

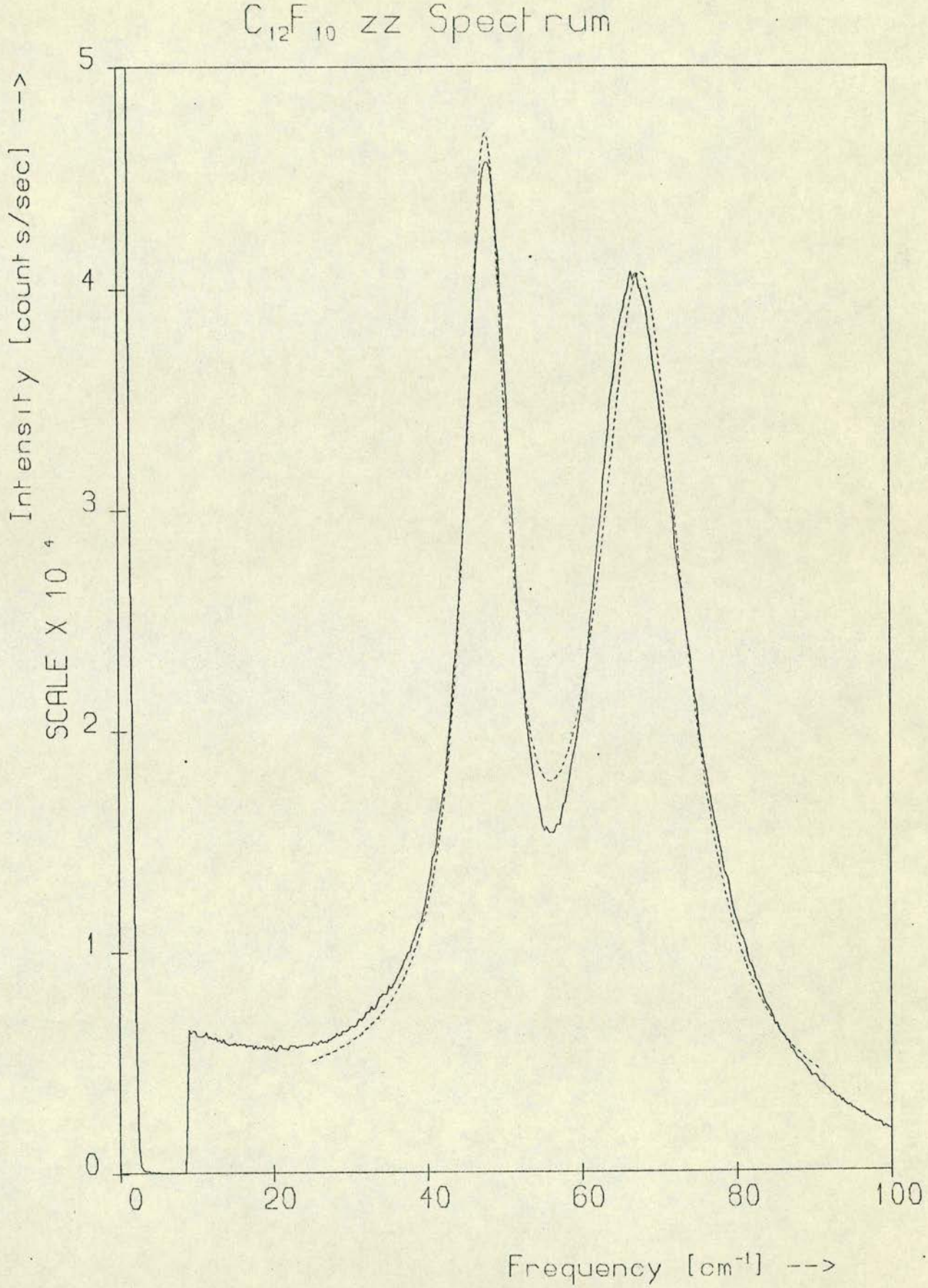
$C_{12}F_{10}$ zz Spectrum
Intensity [counts/sec] -->
SCALE X 10^4
5
4
3
2
1
0
0
20
40
60
80
100
Frequency [cm^{-1}] -->

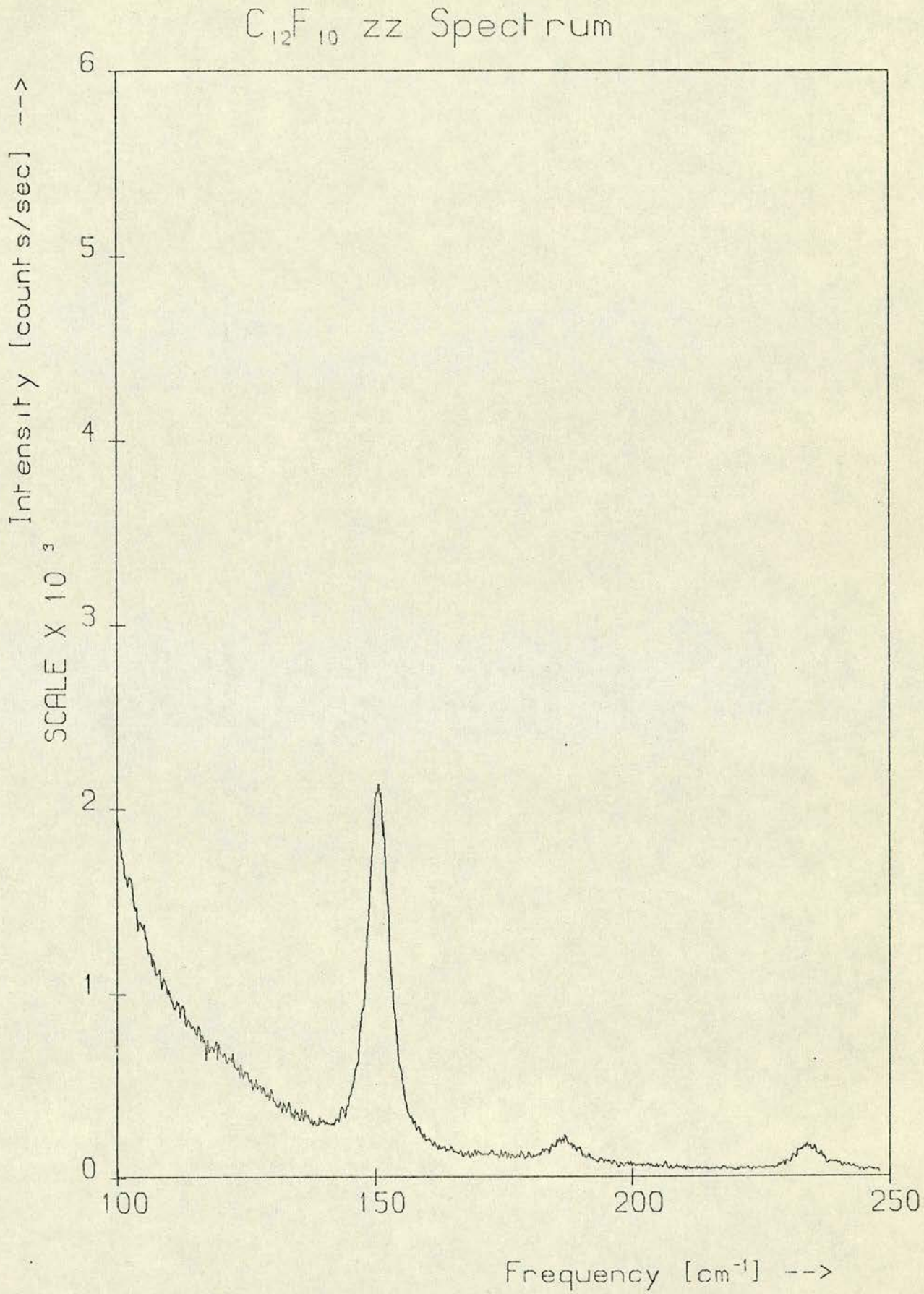
$C_{12}F_{10}$ zz Spectrum
Intensity [counts/sec] -->
SCALE X 10^3
0
1
2
3
4
5
6
100
150
200
250
Frequency [cm^{-1}] -->

FIGURES 5.9 AND 5.10

The A_2 (xy) spectrum.

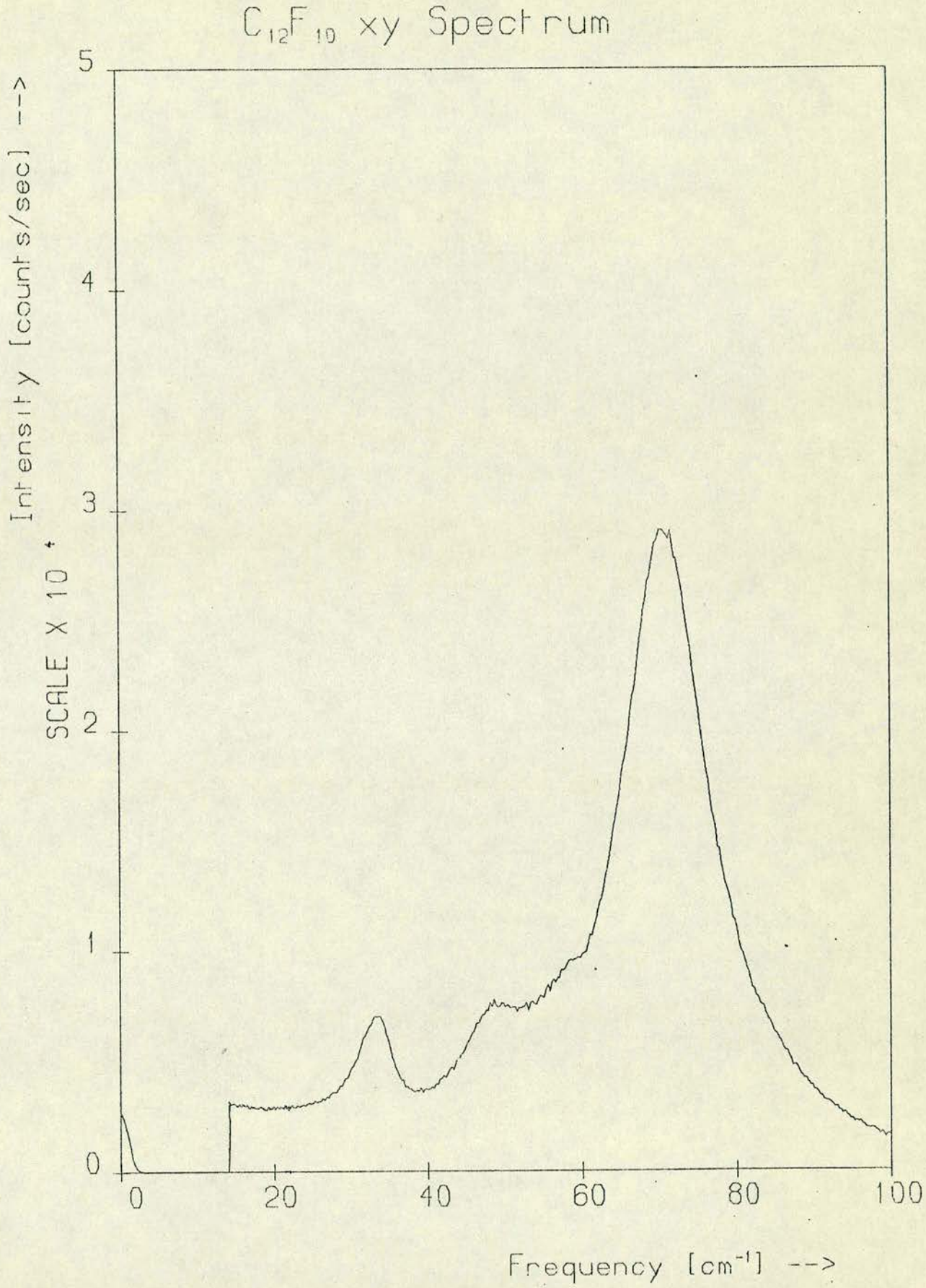
$C_{12}F_{10}$ xy Spectrum
Intensity [counts/sec] -->
SCALE X 10 ⁴
5
4
3
2
1
0
0
20
40
60
80
100
Frequency [cm⁻¹] -->

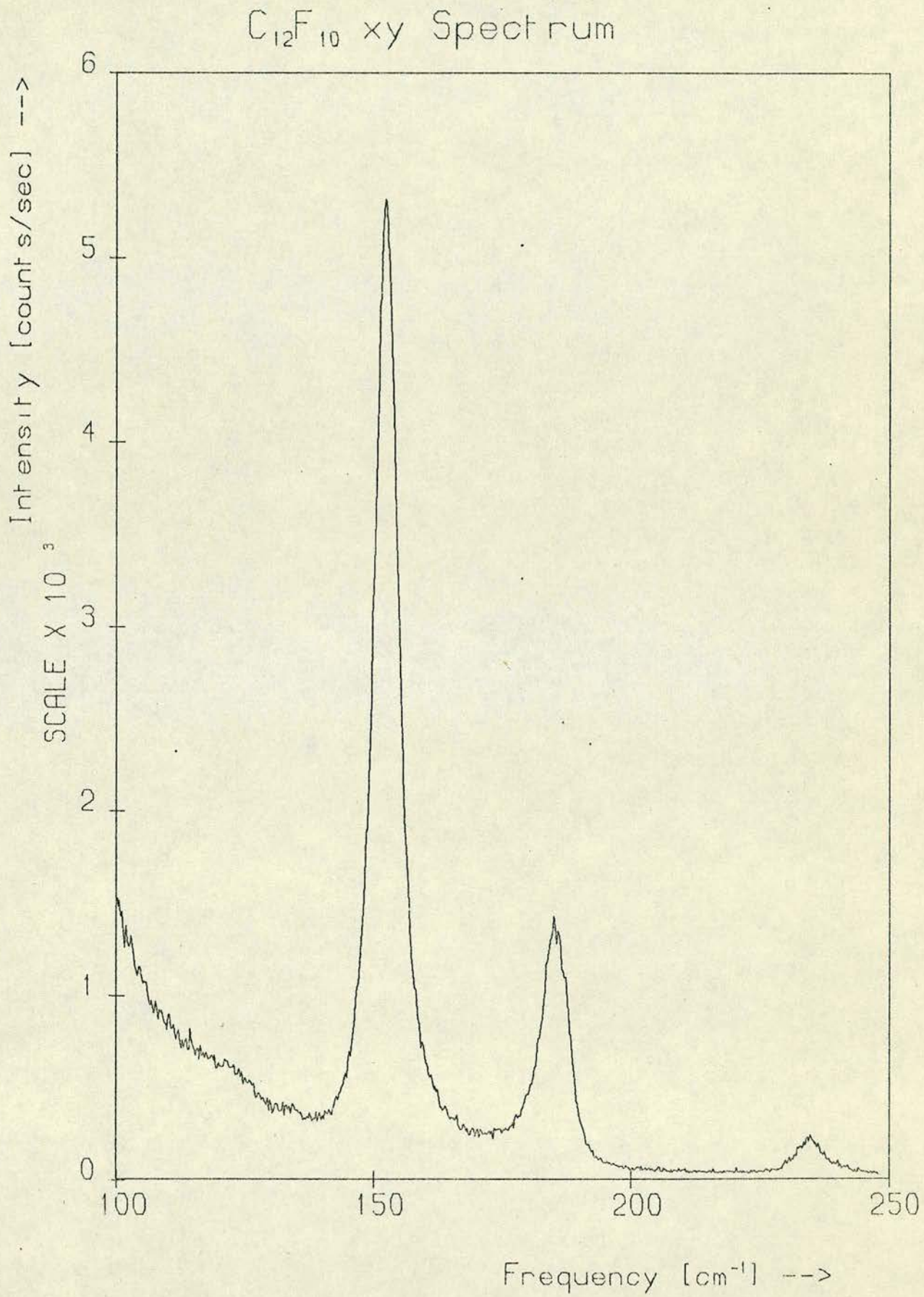
$C_{12}F_{10}$ xy Spectrum
Intensity [counts/sec] -->
SCALE X 10^3
0
1
2
3
4
5
6
100
150
200
250
Frequency [cm^{-1}] -->

FIGURES 5.10 AND 5.11

The B_1 (xz) spectrum

x = extraneous.

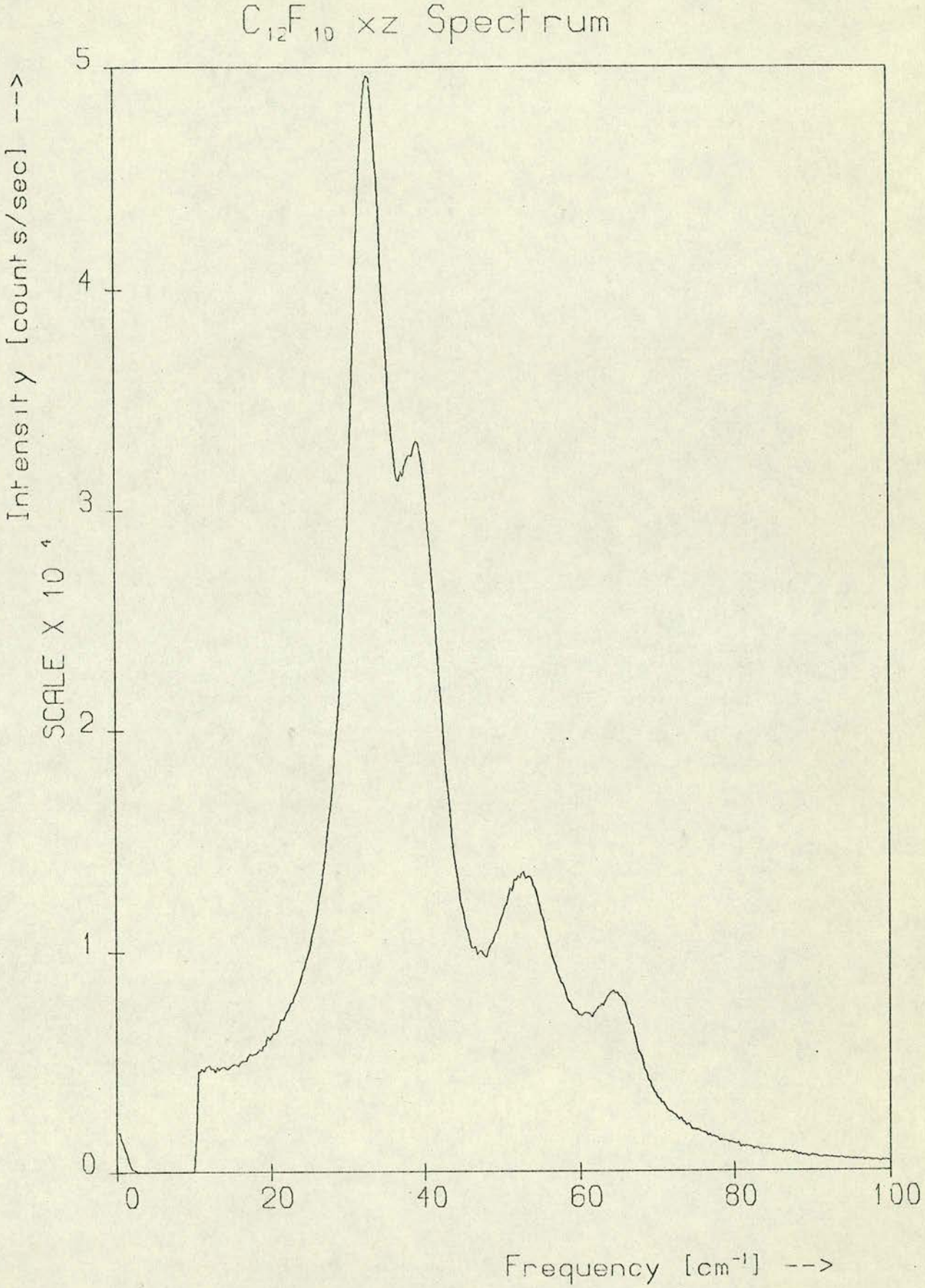
C12F10 xz Spectrum
Intensity [counts/sec] -->
SCALE X 10 4
5
4
3
2
1
0
0
20
40
60
80
100
Frequency [cm-1] -->

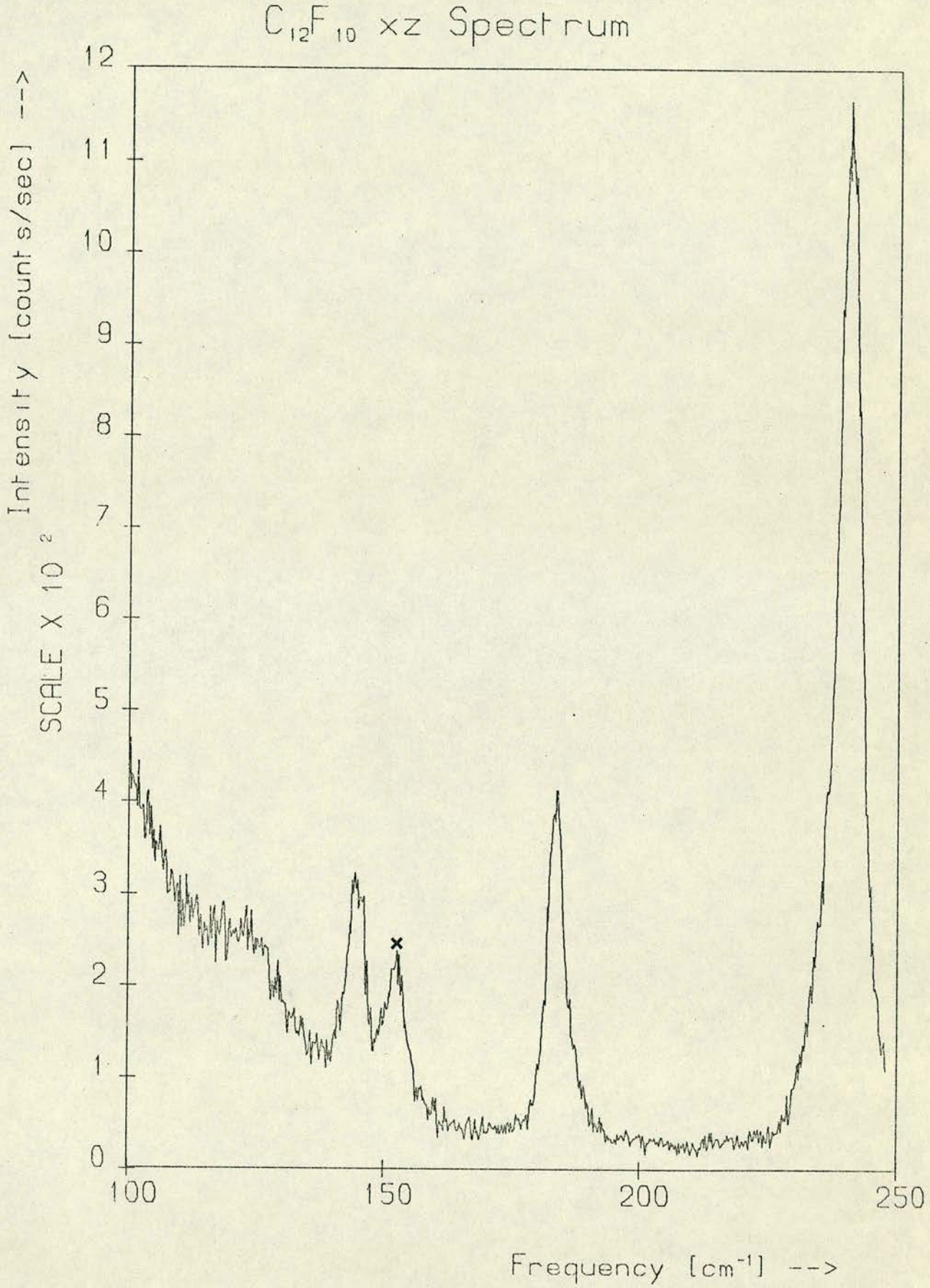
$C_{12}F_{10}$ xz Spectrum
Intensity [counts/sec] -->
SCALE X 10^2
0
1
2
3
4
5
6
7
8
9
10
11
12
100
150
200
250
Frequency [cm^{-1}] -->

FIGURES 5.13 AND 5.14

The B_2 (yz) spectrum.

x = extraneous.

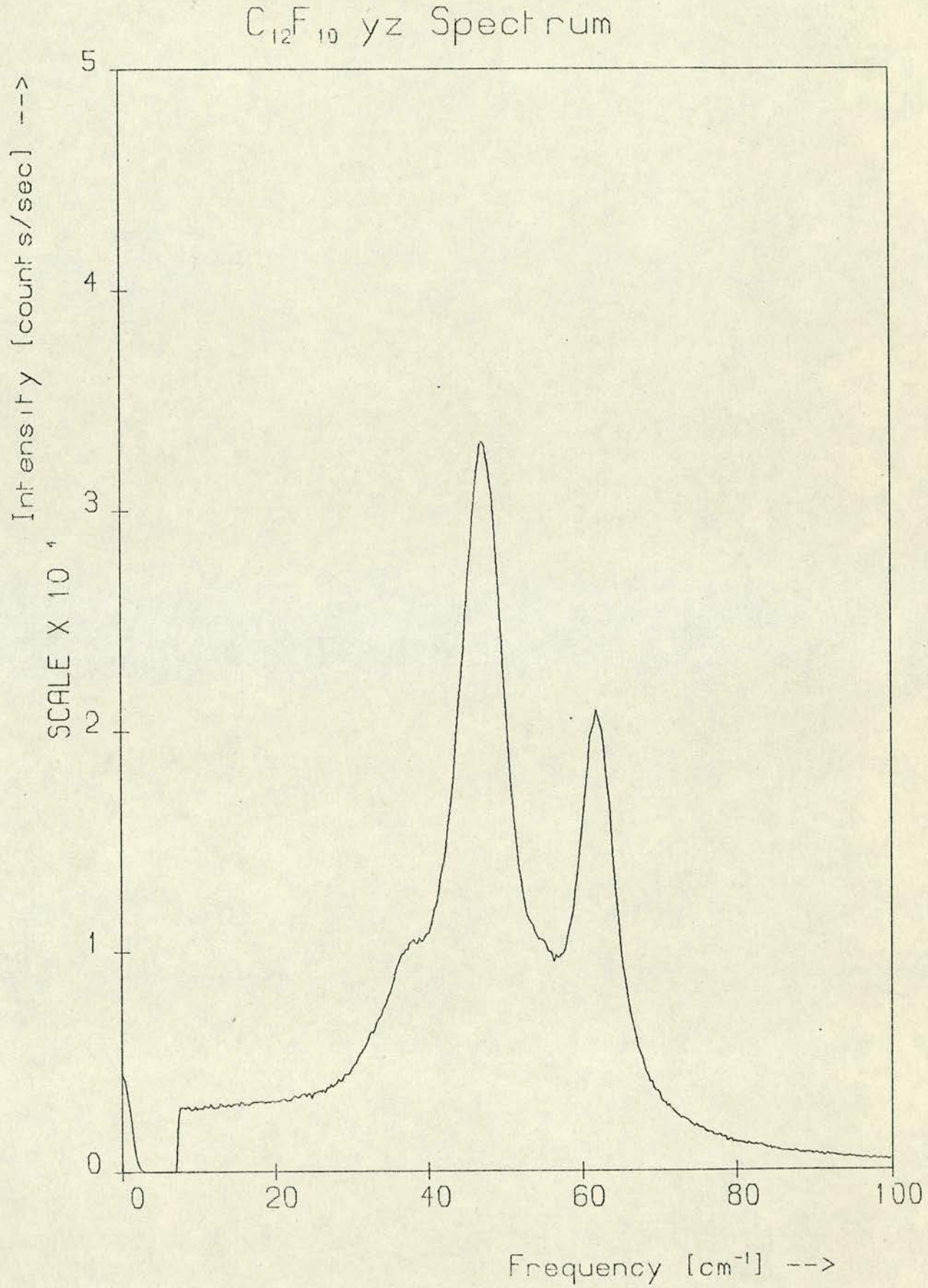
$C_{12}F_{10}$ yz Spectrum
Intensity [counts/sec] -->
SCALE X 10^4
5
4
3
2
1
0
0
20
40
60
80
100
Frequency [cm^{-1}] -->

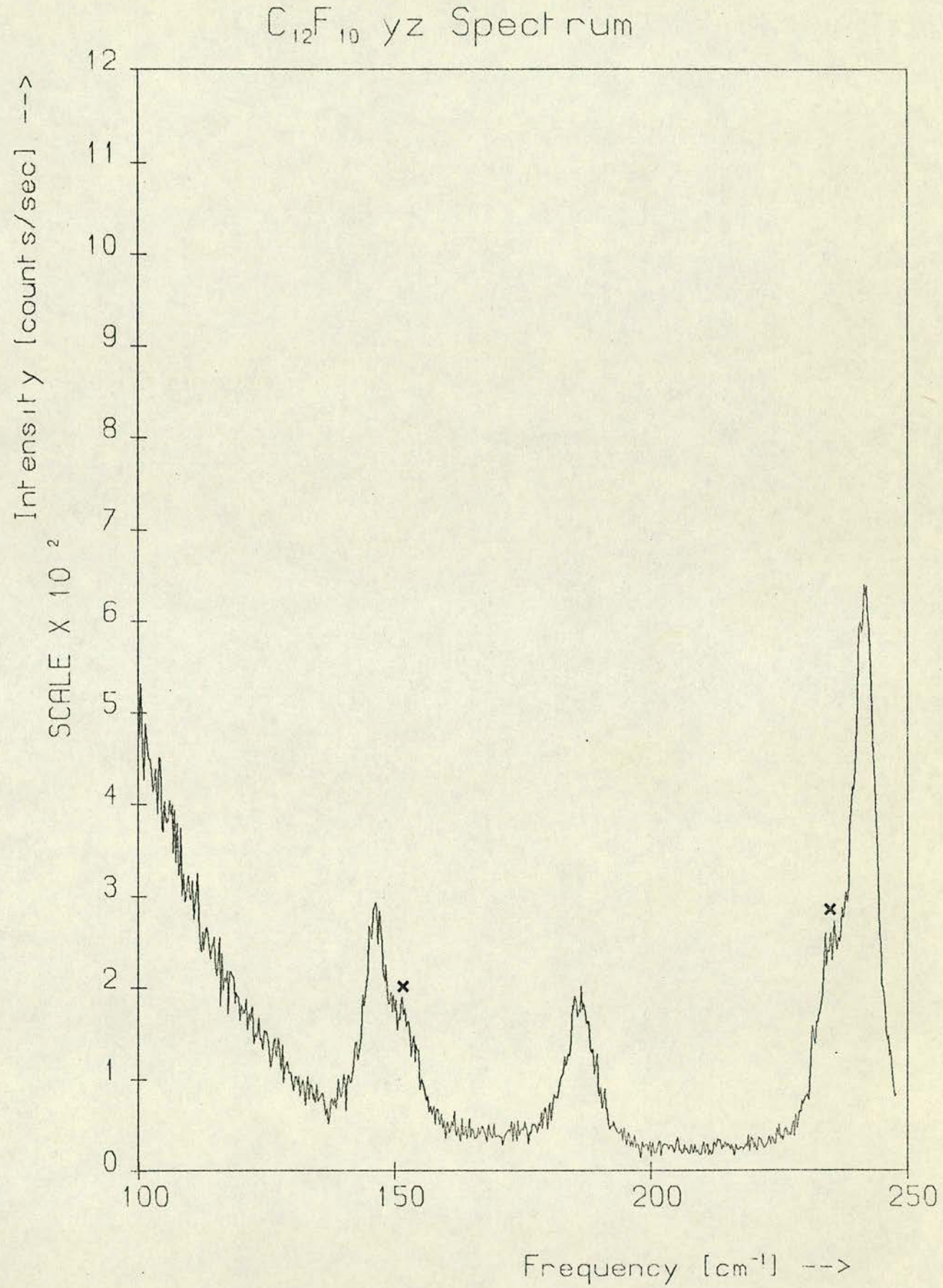
$C_{12}F_{10}$ yz Spectrum
Intensity [counts/sec] -->
SCALE X 10^2
12
11
10
9
8
7
6
5
4
3
2
1
0
100
150
200
250
Frequency [cm^{-1}] -->

TABLE 5(I)

Measured frequencies, assignments and peak heights
(not corrected for different scattering efficiencies)

Frequency at peak	Representation	Actual Peak Height					
		xx	yy	zz	xy	xz	yz
32.9	B_1^c					50080	
33.4	A_2^c				7018		
38.0	B_2^c						sh
38.8	B_1^c					32990	
47.1	B_2^c						33090
48.1^1,48.7^2	A_1^c	72380^2	121300^2	48870^1			
49.3	A_2^c				7427		
52.8	B_1^c					13660	
54.4	B_1^m, A_1^c	sh	w.sh	-			
58.9	A_2^c				sh		
61.9	B_2^c						20760
64.3	B_1^c					8193	
66.4^2,67.1^1	A_1^c	18600^2	-	43280^1			
70.8	A_2^c				29010		
126	?				w.sh	w.sh	

TABLE 5(I) (Contd.)

Frequency at peak	Representation	Actual Peak Height					
		xx	yy	zz	xy	xz	yz
144.8	B_3^m, B_1^c					310	
146.3	B_3^m, B_2^c						292
151.1	A^m, A_1^c	2236	2082	2255			
152.5	A^m, A_2^c				5296	X	X
183.5	B_3^m, B_1^c					397	
185.4	A^m, A_2				1400		
186.1	B_3^m, B_2^c						175
186.6	A^m, A_1^c	3883	4619	1214			
234.1^1, 234.8^2	B_1^m, A_1^c	4916^2	4854^2	182^1			X
234.8	B_1^m, A_2^c				223		
240.6	B_2^m, B_1^c					1135	
241.6	B_2^m, B_2^c						634

X - accidental. 1,2 - slightly differing frequencies for xx, yy and zz.

w - weak sh - shoulder

also Steele et al.[45], but nothing was observed in the region below 130 cm^{-1}.

A picture of the internal vibrations may be built up in the following way, starting from the spectrum of the C_6F_5 rings. These rings have C_{2v} symmetry, and their modes of vibration can be classified as:

$$(10\ A_1^r + 3A_2^r + 9B_1^r + 5B_2^r)$$

$$+ 3 \text{ pure translations} + 3 \text{ rigid rotations.}$$

The superscripts r, m, and c will be used to distinguish representations of the point groups of the rings, molecules and the crystal, which might otherwise be confused. The pair of C_6F_5 rings in the molecule interact in such a way that similar vibrations of each ring mix to produce pairs of modes, transforming under D_2, as follows:

C_{2v} (ring)		D_2(molecule)
$2A_1^r$	$\longrightarrow$	$A^m + B_3^m$
$2A_2^r$	$\longrightarrow$	$A^m + B_3^m$
$2B_1^r$	$\longrightarrow$	$B_1^m + B_2^m$
$2B_2^r$	$\longrightarrow$	$B_1^m + B_2^m$

If the rings interact only weakly one expects to see in the molecular spectrum pairs of similar frequencies occurring, corresponding to each particular type of intra-ring vibration. From the data on C_6F_6, C_6F_5Cl and C_6F_5Br tabulated in Reference (45), most of these frequencies would be expected to occur above, say, 100 cm^{-1}. The rigid rotations and translations of the rings, however, combine to produce additional modes which

FIGURE 5.15

The expected behaviour of the in-ring vibrations in the molecule and in the crystal.

RING	MOLECULE	CRYSTAL
C_{2v}	D_2	C_{2v}

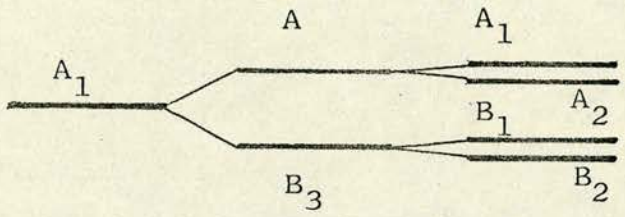

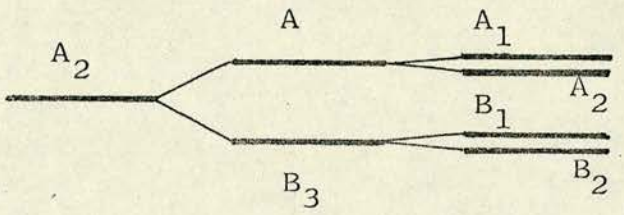

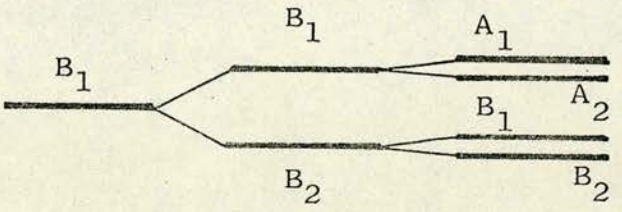

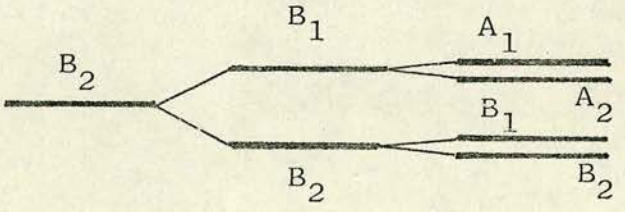

stretch, twist and bend the bridging C - C bond. There are six such modes transforming as

$$2A^m + 2B_1^m + 2B_2^m .$$

The A^m modes twist and stretch the molecule, whereas the B_1^m and B_2^m modes bend it about the z and y axes respectively. Apart from the stretching mode, these modes are presumably all of very low frequency and are the modes which have yet to be seen in the spectrum.

In the crystal the internal modes of vibration are linear combinations of the modes of each of the molecules in the primitive cell. If the molecules interact weakly as expected, we will see frequencies in the crystal only slightly different from those of the free molecule. Rather than work the group theory out directly, we show in Table 5(II) how the scattering tensors of the molecule are transformed in the crystal and then separate these out according to the representations of the point group C_{2v}. This is helpful in deducing the polarisation dependence of the internal mode spectrum. The rule for symmetry related molecules is implicit in the working out of this table, and we can also see from it how the modes themselves transform. Figure 5.15 illustrates and summarises the relationships between vibrations of the rings, molecules and crystals, and using this, together with the table, it is possible to deduce the assignments of the observed internal modes. All of the modes between 145 and 240 cm^{-1} occur in pairs with nearby frequencies. This is the expected behaviour of modes arising out of intra-ring vibrations. The A_1^c modes, appearing in xx, yy and zz at

TABLE 5(II)

Transformation of the molecular scattering tensors into crystal tensors.

Molecule D_2		Crystal C_{2v}
$R\begin{bmatrix} a & & \\ & b & \\ & & g \end{bmatrix}R^+$	$\longrightarrow$	$\begin{bmatrix} c^2a+s^2b & & \\ & s^2a+c^2b & \\ & & g \end{bmatrix} + \begin{bmatrix} 0 & sc(a-b) & \\ sc(a-b) & 0 & \\ & & 0 \end{bmatrix}$
$2 \times A^m$	$\longrightarrow$	$A_1^c + A_2^c$
$R\begin{bmatrix} & d & \\ d & & \\ & & \end{bmatrix}R^+$	$\longrightarrow$	$\begin{bmatrix} (2sc)d & & \\ & (-2sc)d & \\ & & 0 \end{bmatrix} + \begin{bmatrix} 0 & (c^2-s^2)d & \\ (c^2-s^2)d & 0 & \\ & & 0 \end{bmatrix}$
$2 \times B_1^m$	$\longrightarrow$	$A_1^c + A_2^c$
$R\begin{bmatrix} & & e \\ & & \\ e & & \end{bmatrix}R^+$	$\longrightarrow$	$\begin{bmatrix} 0 & & ce \\ & 0 & \\ ce & & 0 \end{bmatrix} + \begin{bmatrix} 0 & & \\ & 0 & -se \\ & -se & 0 \end{bmatrix}$
$2 \times B_2^m$	$\longrightarrow$	$B_1^c + B_2^c$
$R\begin{bmatrix} & & f \\ & & \\ f & & \end{bmatrix}R^+$	$\longrightarrow$	$\begin{bmatrix} 0 & & sf \\ & 0 & \\ sf & & 0 \end{bmatrix} + \begin{bmatrix} 0 & & \\ & 0 & cf \\ & cf & 0 \end{bmatrix}$
$2 \times B_3^m$	$\longrightarrow$	$B_1^c + B_2^c$

$$R = \begin{bmatrix} c & s & \\ -s & c & \\ & & 1 \end{bmatrix} \qquad \begin{aligned} c &= \cos 38^\circ \\ s &= \sin 38^\circ \end{aligned}$$

150 cm^{-1}, and the A_2^c mode in xy at 152.5 cm^{-1}, all have similarly strong intensities. From the table we see that such modes would arise out of an A^m symmetry vibration of the molecule. We see from Figure 5.15 that such a vibration of the molecule would occur together with a B_3^m symmetry vibration at a nearby frequency. On this basis the B_1^c mode at 145 cm^{-1} and the B_2^c mode at 146 cm^{-1} are expected to arise from a B_3^m mode of the molecule. Making similar use of the table and figure the A_1^c modes at 235 cm^{-1} in the xx and yy spectra are assigned to B_1^m vibrations of the molecule because of the lack of intensity in the zz and xy spectra. The nearby peaks at 240 and 242 cm^{-1} in xz and yz should then arise out of B_2 vibrations of the molecule. This scheme has been carried out also for the peaks in the 183-187 cm^{-1} region, and the final results are given in the latter part of Table 5(I). We draw the conclusion that all of these modes are intra-ring vibrations and, furthermore, that the inter-ring vibrations lie below these and overlap with the lattice vibrations.

5.4 The External Modes

In the crystal the six external degrees of freedom of each of the two molecules in the primitive cell give rise to 9 optical lattice vibrations at the zone centre, assuming rigid molecules. The group theory for classifying these modes is worked out in Table 5(III). The result is:

$$S_{\text{ext vibr}} \sim (A_1^c + 2A_2^c + 3B_1^c + 3B_2^c) .$$

An important result is that there is but one totally symmetric mode. Table 5(IV) shows the symmetry coordinates for all the modes, and it is seen that the totally symmetric mode involves only rotations of the molecules about the z axis. Similarly to sulphur, molecular rotations about the z axis, which is an axis of C_2 symmetry, should produce equal intensities in the xx and yy spectra but no intensity in the zz spectrum: this may be inferred from equation (3.7). We now go on to examine the observed spectra bearing this, and the results of the previous section, in mind. Discrepancy with such a straightforward theory is found.

5.5 The Interpretation of the Spectra of A_1 Symmetry

To recapitulate the discussion of Sections 5.3 and 5.4, we expect first of all that there will be only one A_1^c mode, which is inactive in the zz spectrum. In addition there is also the possibility of seeing a low frequency internal mode: should this be the case it would appear singled out in the zz spectrum. Figure 5.8 shows that, on the contrary, two modes are to be seen in this spectrum, one at 48 cm^{-1} and one at 67 cm^{-1}. Figure 5.5 on the other hand, shows that in the yy spectrum there is only one peak, at 48.5 cm^{-1}. It almost appears consistent with having the axes wrongly labelled. The xx spectrum, Figure 5.3, is similar to the zz, but with differing intensities for the two modes. From these considerations it was decided that the conflict with expectation might be due to mixing between internal and external modes, and that an attempt should be made to

TABLE 5(III)

The Group Theory for the Lattice Vibrations

C_{2v}	E	$C_2(z)$	$\sigma(xz)$	$\sigma(yz)$	S_E	S_E^*	S_E^{2s}
A_1^c	1	1	1	1	z		x^2, y^2, z^2
A_2^c	1	1	-1	-1		R_z	xy
B_1^c	1	-1	1	-1	x	R_y	xz
B_2^c	1	-1	-1	-1	y	R_x	yz
Γ_p	2	2	0	0	$\sim (A_1^c + A_2^c)$		

$$S_E \sim (A_1^c + B_1^c + B_2^c)$$

$$S_E^* \sim (A_2^c + B_1^c + B_2^c)$$

$$S_p \sim (A_1^c + A_2^c)$$

$$S_{cell} = S_p \times (S_E + S_E^*)$$

$$\sim (2A_1^c + 2A_2^c + 4B_1^c + 4B_2^c)$$

$$S_{ext\ vibr} = S_{cell} - S_E \sim (A_1^c + 2A_2^c + 3B_1^c + 3B_2^c)$$

Scattering tensors:

$$\begin{bmatrix} a & & \\ & b & \\ & & c \end{bmatrix} \quad \begin{bmatrix} & d & \\ d & & \\ & & \end{bmatrix} \quad \begin{bmatrix} & & e \\ & & \\ e & & \end{bmatrix} \quad \begin{bmatrix} & & \\ & & f \\ & f & \end{bmatrix}$$

A_1^c A_2^c B_1^c B_2^c

S_p is the space of permutations of the molecules.

S_{cell} is the entire motional space of the primitive cell, including acoustic vibrations.

$S_{ext\ vibr}$ is the space of external vibrations.

TABLE 5(IV)

Symmetry Coordinates Referred to Molecular Coordinate System

	x^1	y^1	z^1	θ_x^1	θ_y^1	θ_z^1	ϕ	x^2	y^2	z^2	θ_x^2	θ_y^2	θ_z^2	ϕ
A_1^c						γ	δ						γ	δ
A_2^c			c			γ	δ			-c			$-\gamma$	$-\delta$
B_1^c		b		α	β				-b		α	$-\beta$		
B_2^c	a			α	β			-a			$-\alpha$	β		

We relate the coordinate system of molecule 2 to that of molecule 1 by the $\sigma(xz)$ glide plane. Acoustic modes have been discarded. The coordinates 'δ' refer to the internal mode involving the interplanar angle ϕ .

observe low frequency modes in the free molecule spectrum, even though other attempts[44] had failed. The best way to do this is to use the melt rather than solution, for the spectrum of the solvent itself can produce swamping intensity at low frequencies. The spectrum was readily obtained and is shown in Figure 5.16. Superposed on an intense, rising wing feature there lies a weak but significant band at about 54 cm^{-1}. Steele[44] reports seeing no absorption band in the infrared spectrum below 100 cm^{-1}, but indicates that in 2H-perfluorobiphenyl, $C_{12}F_8H_2$ a band has been observed at 60 cm^{-1} by Massey and Steele[44]. This would indicate, from the fact that A^m modes are Raman active and infrared inactive, that the observed mode is of A^m symmetry. Since this mode has such a low frequency it would have to be principally torsional in nature, for we expect stretching to occur only at a much higher frequency. Any other low frequency modes were presumably of too low intensity to be seen against the very strong background.

With the presence of this very low frequency internal mode we expect the rigid molecule approximation to break down. In what follows we assume that this low frequency mode is indeed the A^m symmetry torsional mode of the $C_{12}F_{10}$ molecule, and that it couples in the crystal to the A_1^c external mode. According to Table 5(II) the modes of the molecule transform in the crystal as follows:

$$2A^m \longrightarrow A_1^c + A_2^c$$

$$2B_1^m \longrightarrow A_1^c + A_2^c$$

$$2B_2^m \longrightarrow B_1^c + B_2^c$$

$$2B_3^m \longrightarrow B_1^c + B_2^c$$

FIGURE 5.16

The unpolarised Raman spectrum of liquid $C_{12}F_{10}$ (m.p. 68°C) showing a definite feature at about 50 cm^{-1}. The fitted spectrum shown as a dashed line has the following parameters:

$$\omega_o = 54.1\ cm^{-1} \qquad \Gamma = 21.2\ cm^{-1}.$$

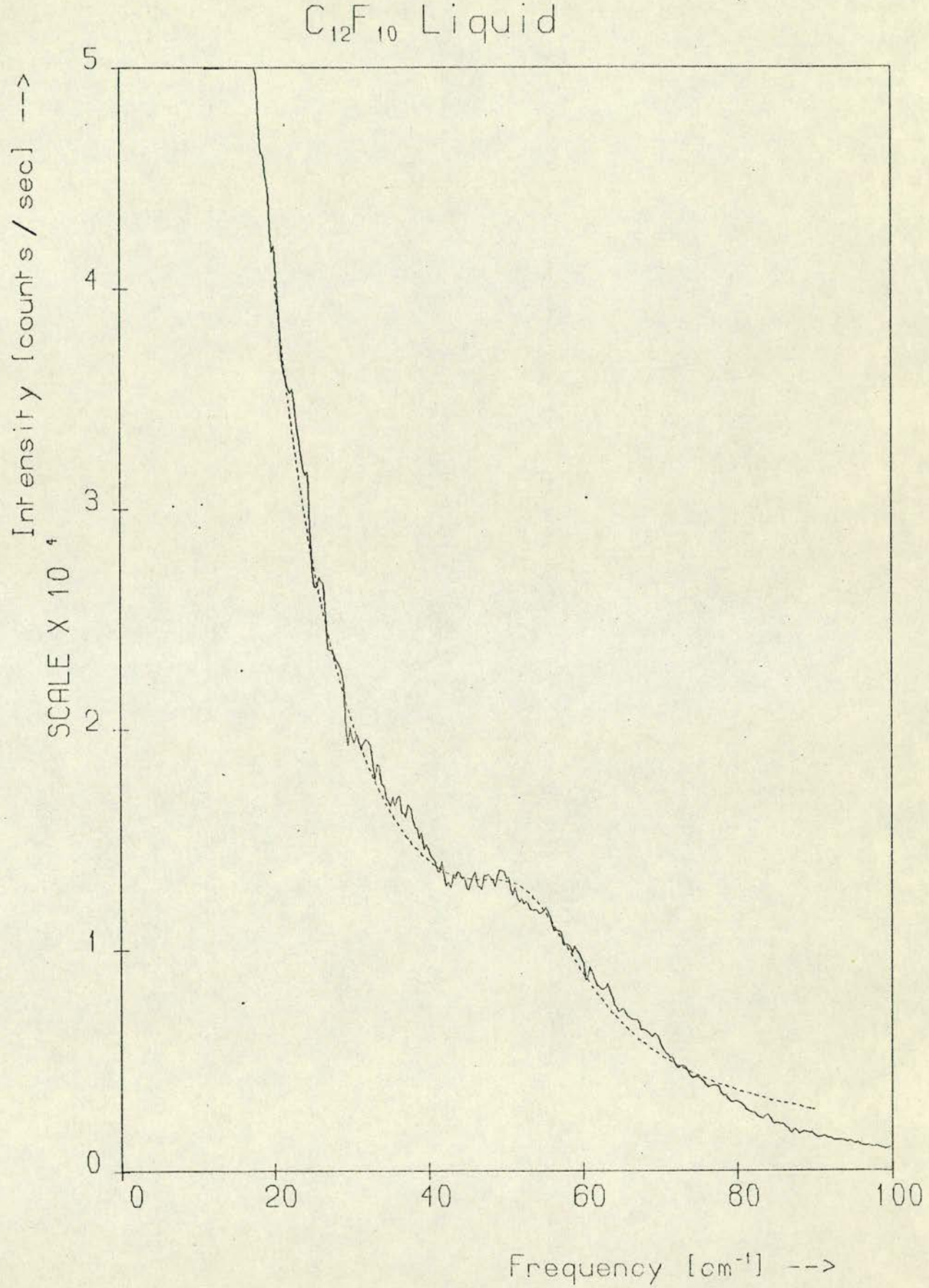
$C_{12}F_{10}$ Liquid
Intensity [counts / sec] -->
SCALE X 10^4
5
4
3
2
1
0
0
20
40
60
80
100
Frequency [cm^{-1}] -->

It is therefore conceivable that a B_1^m mode of the molecules, transforming as A_1^c in the crystal, could also couple to the external mode. For simplicity, however, we treat only coupling between the external mode and the one A^m mode. It will be shown later, however, that coupling with an A^m mode is the only possibility which could give rise to the observed intensities.

We first of all make use of our independent phenyl ring model to calculate an approximate expression for the ϕ dependence of the molecular polarisability. The two halves of the molecule are assumed to make separate and identical contributions to the polarisability of the form

$$\left[\alpha'\right] = \begin{bmatrix} \alpha'_{xx} & & \\ & \alpha'_{yy} & \\ & & \alpha'_{zz} \end{bmatrix} \qquad (5.1)$$

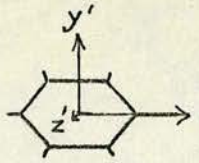

referred to the principal axes as shown. The two halves of the molecule are rotated respectively by $\pm \frac{\phi}{2}$ about the x axis, giving individual contributions to the molecular polarisability:

$$\left[\alpha(\pm\phi)\right] = \begin{bmatrix} \alpha_1 & & \\ & \alpha_2+\cos\phi\alpha_3 & \pm \sin\phi\alpha_3 \\ & \pm \sin\phi\alpha_3 & \alpha_2-\cos\phi\alpha_3 \end{bmatrix} \qquad (5.2)$$

where $\alpha_1 = \alpha'_{xx}$, $\alpha_2 = \frac{1}{2}(\alpha'_{yy} + \alpha'_{xx})$, $\alpha_3 = \frac{1}{2}(\alpha'_{yy} - \alpha'_{zz})$.

The total contribution to α is obtained by summing for the two halves and the result is:

$$\left[\alpha_m\right] = \begin{bmatrix} \alpha_1 & & \\ & \alpha_2+\cos\phi\alpha_3 & \\ & & \alpha_2-\cos\phi\alpha_3 \end{bmatrix} \qquad (5.3)$$

This model may be crude, but it does give an estimate of the parametric dependence of α_m on ϕ. It is now possible to write down the differential polarisability, analogously to eqn. 3.6 but including the ϕ dependence. We then have:

$$\left.\begin{aligned} \delta\alpha_1 = &\begin{bmatrix} \sin2\theta\alpha_\theta & & \\ & -\sin2\theta\alpha_\theta & \\ & & 0 \end{bmatrix} \delta\theta_1 \\ &+ \begin{bmatrix} \alpha_\phi(1-\cos2\theta) & & \\ & \alpha_\phi(1+\cos2\theta) & \\ & & -2\alpha\phi \end{bmatrix} \frac{\delta\phi_1}{2} \end{aligned}\right\} A_1$$

$$\left.\begin{aligned} &+ \begin{bmatrix} 0 & \cos2\theta\alpha_\theta & \\ \cos2\theta\alpha_\theta & 0 & \\ & & 0 \end{bmatrix} \delta\theta_1 \\ &+ \begin{bmatrix} 0 & \alpha_\phi\sin2\theta & \\ \alpha_\phi\sin2\theta & 0 & \\ & & 0 \end{bmatrix} \frac{\delta\phi_1}{2} \end{aligned}\right\} A_2$$

(5.4)

The parameters α_θ and α_ϕ are given by

$$\alpha_\theta = (\alpha_2 + \cos\phi\,\alpha_3 - \alpha_1) \qquad (5.5)$$

$$\alpha_\phi = \sin\phi\,\alpha_3$$

and from the crystal structure data of Reference (42), 2θ is equal to 76°.

Now, it is possible to define eigenvectors for the coupled internal-external modes (referring to Table 5(V)) as follows:

$$\hat{e}_1 = \frac{e^1_\theta}{\sqrt{I_{zz}}}\,\delta\theta + \frac{e^1_\phi}{\sqrt{I_{xx}}}\,(\frac{\delta\phi}{2})$$
$$\hat{e}_2 = \frac{e^2_\theta}{\sqrt{I_{zz}}}\,\delta\theta + \frac{e^2_\phi}{\sqrt{I_{xx}}}\,(\frac{\delta\phi}{2}) \qquad (5.6)$$

The eigenvectors are orthonormal by virtue of (1.8), so that

$$e^1_\theta = e^2_\phi = c$$
$$e^2_\theta = -e^1_\phi = -s \qquad (5.7)$$
$$c^2 + s^2 = 1$$

That is, for this simple two dimensional model the components of the eigenvectors may be represented by s and c, the sine and cosine of some angle. Considering each component of the differential polarisability in (5.4) separately, in a general form

$$\delta a = \delta a_\phi\,(\frac{\delta\phi}{2}) + \delta a_\theta\,\delta\theta\ , \qquad (5.8)$$

and using (6.5) to bring in the expressions for the eigenvectors, we have from (3.10) the following expressions for the scattered intensities

$$\mathcal{I}_{(\omega_1)\text{Stokes}} = \eta\frac{\hbar}{\omega_1}\,(n(\omega_1)+1)\,(\frac{c\delta a_\theta}{\sqrt{I_{zz}}} - \frac{s\delta a_\phi}{\sqrt{I_{xx}}})^2\,\delta(\omega-\omega_1)$$
$$\mathcal{I}_{(\omega_2)\text{Stokes}} = \eta\frac{\hbar}{\omega_2}\,(n(\omega_2)+1)\,(\frac{s\delta a_\theta}{\sqrt{I_{zz}}} + \frac{c\delta a_\phi}{\sqrt{I_{xx}}})^2\,\delta(\omega-\omega_2)\ . \qquad (5.9)$$

To compare this with experiment, the intensities of the peaks in each of the A_1 spectra, at 48 and 67 cm^{-1}, were calculated by fitting to simple harmonic oscillator response functions of the form

$$\mathcal{J}(\omega) = \frac{(H\,\omega_o^2\,\Gamma^2)\hbar\omega(n(\omega)+1)}{(\omega^2-\omega_o^2)^2 + \Gamma^2\omega^2} \quad . \tag{5.10}$$

This allows the considerable damping effect to be taken into account. We are mainly interested, however, in the total integrated intensity which is given by:

$$\int \mathcal{J}(\omega_j)\,d\omega_j \approx \pi\, H_j\, \Gamma_j\, \hbar\omega_j(n(\omega_j)+1)$$

$$= S_j\, h\omega_j(n(\omega_j)+1) \quad . \tag{5.11}$$

Using S defined in this way as $H\Gamma$ (which in the classical regime $h\omega_j \ll k_BT$ reduces simply to peak height $\times$ halfwidth/k_BT) the temperature dependent factors cancel out in what follows. The fitted values of S_j, ω_j and Γ_j were found and are shown in Table 5(V); the corresponding fitted curves are shown in Figures 5.3, 5.5 and 5.7 with dashed lines.

From (5.11) and (5.9) we see that in each of the spectra the ratio of the S factors for the peaks at 67 and 48 cm^{-1} is:

$$\frac{S_2}{S_1} = \frac{\omega_1^2}{\omega_2^2} \frac{\left(\frac{s\delta\alpha_\theta}{\sqrt{I_{zz}}} + \frac{c\delta\alpha_\phi}{\sqrt{I_{xx}}}\right)^2}{\left(\frac{c\delta\alpha_\theta}{\sqrt{I_{zz}}} - \frac{s\delta\alpha_\phi}{\sqrt{I_{xx}}}\right)^2} \quad . \tag{5.12}$$

TABLE 5(V)

Experiment on System 1, ν_o = 19436 cm^{-1}

	ω_1	Γ_1	S_1	ω_2	Γ_2	S_2	S_2/S_1	$\Sigma \times 10^{-6}$
xx	48.8	7.6	2212	68.2	15.0	952	.430	9.70
yy	49.0	8.0	4870	-	-	0	.0	11.693
zz	48.0	6.7	1142	68.5	13.8	2083	1.82	12.405

Experiment on System 2, ν_o = 15802 cm^{-1}

	ω_1	Γ_1	S_1	ω_2	Γ_2	S_2	S_2/S_1	$\Sigma \times 10^{-5}$
xx	49.1	6.6	164	68.3	14.4	80.2	.489	7.695
yy	48.1	7.4	356	-	-	0	.0	8.2365
zz	48.8	6.5	103	69.4	14.2	204	1.98	12.278
	cm^{-1}	cm^{-1}		cm^{-1}	cm^{-1}			

Note:

corrected for different scattering efficiencies.

Using the specific elements of (5.4) we can apply this equation to the observed values of S_2/S_1 for the zz, yy, and xx spectra in turn. Making use of the facts that $a_\theta^{zz} = 0$ and $S_2(yy)$ is observed to be zero, we arrive at the following results.

$$\left|\frac{c}{s}\right| = \frac{\omega_2}{\omega_1}\sqrt{\frac{S_2(zz)}{S_1(zz)}} = 1.925/2.001$$

$$\frac{a_\theta}{a_\phi} = \sqrt{\frac{I_{zz}}{I_{xx}}}\left|\frac{c}{s}\right|\left(\frac{1+\cos 2\theta}{\sin 2\theta}\right) = 4.50/4.68$$

$$\frac{S_2(xx)}{S_1(xx)} = \frac{\omega_1^2}{\omega_2^2}\left(\frac{2\left|\frac{c}{s}\right|}{\left(\left|\frac{c}{s}\right|^2 - 1\right) + \cos 2\theta\left(1 + \left|\frac{c}{s}\right|^2\right)}\right)^2 = .514/.471 \qquad (5.13)$$

The two sets of numerical values refer to the results obtained on System 1 and System 2, respectively. From the structural data of Reference (42) $\frac{I_{zz}}{I_{xx}}$ was calculated to be $(2.607 + \cos^2\frac{\phi}{2})$, giving the value 3.342 for $\phi = 62^\circ$. The results (5.13) can be checked by comparing the calculated values of $S_2(xx)/S_1(xx)$ with the observed values of 0.430 and 0.489. They agree with experiment to within 19°/o and 4°/o respectively, which is reasonably encouraging for such a simplistic model. Secondly, it is possible to check the observed intensities with the sum rule (3.11), which for this purpose is expressed as:

$$\omega_1^2 S_1 + \omega_2^2 S_2 = \eta\left(\frac{(\delta a_\theta)^2}{I_{zz}} + \frac{(\delta a_\phi)^2}{I_{xx}}\right) \qquad (5.14)$$

where η is some scale factor which is the same for all of the spectra. Applying this to (5.4), with a convenient choice of η, we have:

$$\Sigma(xx) = \omega_1^2 S_1(xx) + \omega_2^2 S_2(xx) = \sin^2 2\theta \left(\frac{a_\theta}{a_\phi}\right)^2 \frac{I_{xx}}{I_{zz}} + (1-\cos 2\theta)^2$$

$$= 6.29/6.74$$

$$\Sigma(yy) = \omega_1^2 S_1(yy) + \omega_2^2 S_2(yy) = \sin^2 2\theta \left(\frac{a_\theta}{a_\phi}\right)^2 \frac{I_{xx}}{I_{zz}} + (1+\cos 2\theta)^2$$

$$= 7.25/7.71$$

$$\Sigma(zz) = \omega_1^2 S_1(zz) + \omega_2^2 S_2(zz) = 4 = 4/4 \ .$$

(5.15)

The results of (5.13) were used to calculate the numerical estimates above for both sets of data. Comparison with the observed sums given in Table 5(V) shows that $\Sigma(xx)$ and $\Sigma(yy)$ are in the correct ratio, (about 1 : 1.15 compared with 1 : 1.19). $\Sigma(zz)$, on the other hand, is far too low; a value of about 7.8 would have been consistent with the observed spectra. It has been stressed before, however, that it is very difficult to achieve consistent intensity scales between experiments involving different crystal orientations. And, even with careful intensity correlation, our model falls short by not including the macroscopic optical properties of the crystal. Both of these problems make it difficult to assess the effectiveness of the sum rule as a test of the model.

Summing up, it has been found that the unexpected features of the A_1 spectra can be explained by the coupling of the symmetric lattice mode to a torsional vibration of the molecules. The numbers c^2 and s^2 indicate the division of energy

between the internal and external components of the actual eigenmodes. We can state our result in the following way, that 79 - 80°/o of the energy of the mode at 48 cm^{-1} is contributed by the external vibration and 21 - 20°/o is contributed by the internal vibration. For the mode at 68 cm^{-1} the situation is reversed. The higher frequency mode is then primarily of internal vibration character, a result which seems reasonable.

The external component of vibration has a larger differential polarisability than the internal component, the ratio $\alpha_\theta/\alpha_\phi$ = 4.5 - 4.7 being representative of this amount. Finally, there is evidence in the spectrum of an additional weak mode near 54 cm^{-1}. This is seen only in the xx and yy spectra. This extra mode is most probably of internal mode character. Referring to Table 5(II) we see that a B_1 internal vibration of the molecule would appear in the A_1 spectrum of the crystal in xx and yy, but not in zz. We conclude therefore that this mode arises out of the low frequency B_1 bending mode of the molecule. The question arose earlier as to whether this mode could also couple to the lattice vibration spectrum. Indeed it can, but since it has zero polarisability in zz, it would not account for the observed transfer of intensities in the zz spectrum. It can be concluded that the important effect is the one which was discussed, the coupling of the A_1 lattice vibration to a torsional motion of the molecule.

5.6 The Modes of A_2, B_1 and B_2 Symmetry

In these modes there are too many degrees of freedom to make an analysis as for the A_1 modes. In the A_2 modes we expect there to be a similar coupling between the torsional internal vibration and the lattice modes. In addition, if we count up the number of peaks in the B_1 spectrum we get four and not the expected three. The explanation which suggests itself is that the other low frequency internal modes of vibration are mixed in with the lattice spectrum. Such an additional feature, although weak, also exists in the A_1 xx and yy spectra - a narrow shoulder at 54 cm^{-1}. (This had to be included in the fitting procedure used to obtain the results of the previous section.) Another dubious feature is evident in the A_2 spectrum at 58 cm^{-1}. The whole picture of these modes is therefore quite complicated, and the only reasonable information we can derive is the set of frequencies, included in Table 5(I).

5.7 Conclusions

The Raman spectrum of decafluorobiphenyl has been of great use in illustrating many points of interest to the study of molecular crystals. It gives evidence of a situation on which the rigid molecule approximation breaks down. The major forces interacting between the fluorinated rings of the molecule are no doubt of the same weak Van der Waals type that exist between different molecules. The rings behave in the crystal rather more like individual molecules than as rigidly bound components within a complete molecule.

Any lattice dynamical calculation on $C_{12}F_{10}$ would have to take this into account: a possible way of doing this would be to treat the primitive cell as if it contained four phenyl rings rather than two molecules. The usual Van der Waals forces, between all of the rings, would be considered and the bonded rings would be taken into account by having an additional force to represent the C-C interaction.

We may now look in retrospect at the question which arose with orthorhombic sulphur, and we would be inclined to think more seriously about the mixing of internal and external modes in that crystal.

CHAPTER 6

THE FERROELECTRICS AMMONIUM AND RUBIDIUM BISULPHATE

Measurements have been made of many temperature dependent features in the spectra of ammonium and rubidium bisulphate in an effort to establish whether any of them are associated with the ferroelectric phase transition. The initial reports by Arthur et al.[47] and Arthur and Taylor[48] are augmented with additional measurements and an examination of the internal modes of the bisulphate ion in RHS. The parallels between the different materials are brought out.

6.1 Introduction

Ammonium bisulphate, NH_4HSO_4, and rubidium bisulphate, $RbHSO_4$, which we here call AHS and RHS, are isomorphous crystals exhibiting similar ferroelectric properties. The ferroelectric property of AHS was discovered by Pepinsky et al.[49], who showed that at 270K there is an anomaly in the low frequency dielectric constant ε_c, which reaches a peak value of about 1400. Above this temperature AHS exists in a centrosymmetric structure and is paraelectric; below, the crystal is polar and ferroelectric along the crystallographic c axis. When the temperature is further decreased to 154K the ferroelectric properties suddenly disappear following a transition to a phase of still lower symmetry. The transition at 270K is of second order, whereas at 154K it is of first order. This is evident from observations on the spontaneous

FIGURE 6.1

The crystal structure of AHS and RHS projected down the short b axis. The axes of the monoclinic and pseudo-orthorhombic cells are distinguished by the symbols m and o respectively.

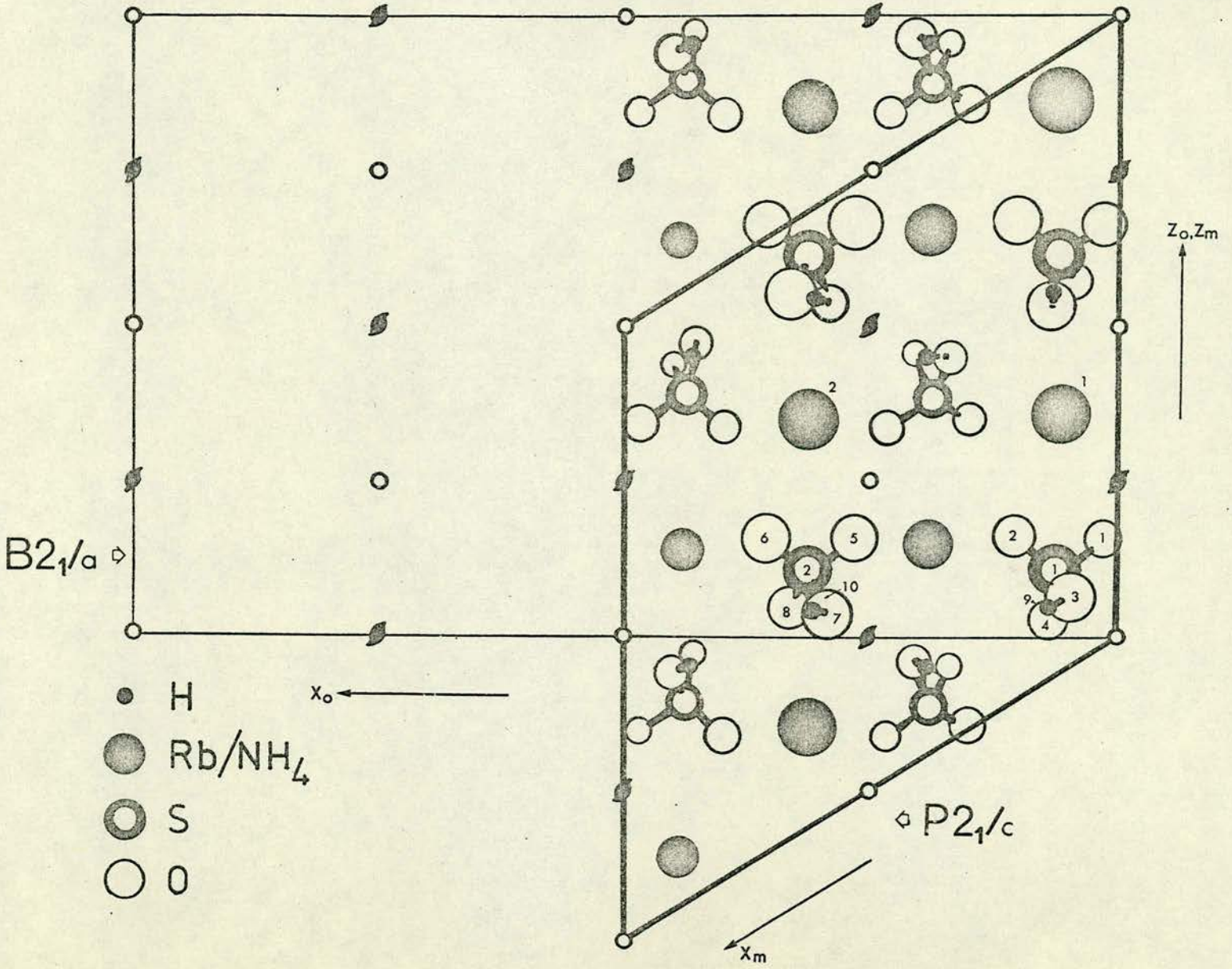
$B2_1/a$
$P2_1/c$
Z_o, Z_m
x_o
x_m
H
Rb/NH_4
S
O
1
2
3
4
5
6
7
8
9
10

polarisation, which starts off linearly at the upper transition and saturates at a value of about 0.8 $\mu C\ cm^{-2}$ some 50K below this, but eventually falls discontinuously to zero at the 154K transition point.

RHS is remarkably similar to AHS both in dielectric properties and structure. It has a second order dielectric anomaly at 258K, only 12 degrees below that in AHS[50]. In the crystal structure, shown in Figure 6.1, the Rb atom substitutes for an NH_4 group. The similarity between AHS and RHS does not extend however to the lower phase transition, which does not appear in RHS[50]. From this interesting fact it may be presumed that the lower phase transition in AHS is brought about by the NH_4 groups. This was confirmed by Miller *et al.*[51] in an NMR experiment to determine spin relaxation times. On the other hand, it is reasonable to expect that the mechanism for the upper phase transition is common to both materials. It is with this transition that our interest lies.

6.2 Other Ferroelectrics and Scattering Experiments

In ferroelectric materials of the well-known KDP class (KH_2PO_4 and its isomorphs) the protons, which are hydrogen-bonded to the PO_4 groups, play the major role in the dynamics of the phase transition. It may be valuable to compare these materials with AHS and RHS because they too are hydrogen-bonded ferroelectrics, in this case with the protons bonded to the SO_4 groups. In the paraelectric phase of the KDP type materials the protons are disordered between two equivalent sites along each of the four H-bonds in the primitive cell[52]. The earliest

model of the transition in KDP was given by Slater[52] who considered the thermodynamics of the most likely proton configurations. In the deuterated material, DKDP, there is however a large difference in transition temperature, 213K as opposed to 122K, which cannot be explained by a Slater model. This led to the proposal of the tunnelling model by Blinc[54], where the dynamical behaviour of the protons is taken into account by considering tunnelling from one H-bond site to another. The kinetic energy term introduces the particle mass into the Hamiltonian, and it is found thereby that the isotope effect may be explained.

Two other important illustrations may be gathered from KDP. The first of these is that all proton configurations[55,56] must be considered in order to correctly describe the phase transition, which is wrongly predicted as being of first order by the Slater model. Secondly, to properly give the direction of the ferroelectric axis, the motions of the other ions must be considered[57]. A theory, due to Kobayashi[58], in which the tunnelling proton motion couples with a phonon carrying a dielectric moment along the c axis, can account for this. Therefore, although the characteristic mechanism of the phase transition in KDP type materials is proton tunnelling, the real picture is very much more complicated.

Of the perovskite materials which undergo ferroelectric phase transitions barium titanate, $BaTiO_3$, is a well known example. This material has more than one phase transition, but the ferroelectric transition at 135°C [59] is illustrative of the displacive type which can be accounted for by an anharmonic lattice dynamical theory. The theory of Cochran[60],[57] shows

that a transverse optical mode possessing a dipole moment can become unstable because of competing short-range and long-range forces. Far above the transition temperature, the short-range interatomic forces dominate the long-range Coulomb forces and the crystal is stable. As the crystal is cooled, the decreasing volume of the unit cell increases the polarisability of the transverse mode, thereby increasing the magnitude of the coulomb forces. A phase transition occurs when the forces eventually cancel. The lattice dynamical picture of this process gives $\omega_o^2 \propto T - T_c$ for this unstable mode, the so-called ferroelectric soft mode. As T approaches T_c and ω_o^2 tends to zero, the atomic displacements become larger and slower, and at the point of instability they 'freeze' into a new equilibrium configuration with an attendant change of phase.

The final example we wish to give is that of sodium nitrite, $NaNO_2$. The phase transition in this material was discovered by Sawada et al.[61]. Below about 436K $NaNO_2$ is ferroelectric and the NO_2 ions lie in the b-c crystallographic plane with all the nitrogens pointing either up or down the b axis. At higher temperatures the nitrogens point either up or down the b axis in a random fashion. This at first seems to be similar to the situation of the protons in KDP, but it is different in that the motion of the nitrogens is probably very slow, much slower than any of the lattice vibrations[62]. A simple Ising model, neglecting tunnelling, gives a satisfactory description of the dielectric properties[63]. In contrast with displacive ferroelectrics, there is no phonon directly associated with the phase transition.

Because the ferroelectric properties of a material are related to the dynamics of the system - through soft modes,

tunnelling or the like - the investigation of the spectrum of the lattice vibrations and of all the excitations associated with the order-disorder mechanism is an important means of gaining information about the ferroelectric phase transition. For materials such as those we have just discussed, light scattering experiments have often done much to contribute to an understanding of the dynamics of their phase transitions. In KDP and its isomorphs, experiments by Kaminow and Damen[64] have given evidence of an overdamped soft mode associated with proton tunnelling, and more recently Katiyar et al.[65] have shown, from Raman measurements, the need to consider anharmonic coupling between this soft mode and another optic phonon. In $BaTiO_3$ [66] an overdamped soft mode of E_1 symmetry has been observed, whereas the associated ferroelectric soft mode, of A_1 symmetry, has not. Lastly, in $NaNO_2$ [67] Raman scattering has not proven so successful, principally because the ferroelectric mode is in an inaccessible frequency regime.

In the experiments described herein, the lattice vibration spectrum of AHS and RHS were measured for the first time, and existing results[68] for some of the internal vibrations have been extended. The measurements were made on single crystals of each of the materials over a wide temperature range in both the paraelectric and ferroelectric phases, in an attempt to observe features showing a definite bearing on the phase transition. Whereas in the previous chapters on sulphur and decafluorobiphenyl our interest was purely in lattice dynamics in the harmonic approximation, we now shift emphasis to temperature dependent, and therefore anharmonic, phenomena.

6.3 The Phase Transition in AHS and RHS

The structures of AHS and RHS have been worked out in both phases by Nelmes[69],[70] and Ashmore[71]. The space group is $P2_1/c$ above the transition (the upper one in AHS) and $P2_1$ below, with 8 formula units in the primitive cell, Figure 6.1. There are two independent sets of molecular units in the cell and, after Nelmes[70], we distinguish them with labels (1) and (2). In each of these sets there are four symmetry related formula units. Analysis of the X-ray diffraction thermal parameters of AHS by Nelmes[72] has shown that the transition at 270K is most likely of order-disorder type, with the set of SO_4 (1) ions being disordered in the room temperature phase. The average structure of this phase is still centrosymmetric, but when the SO_4 (1) ions order in the low temperature phase the centre of symmetry is destroyed. In distinction, the SO_4 (2) ions are ordered in both phases. A very similar picture of RHS has been established by Ashmore[71].

The motion of the SO_4 (1) ions between its two sites, $SO_4(1+)$ and $SO_4(1-)$, is best described by a small rotation about an axis lying in the a - c plane and close to the c axis. The angle of rotation is about 20°. A straightforward attempt to explain the ferroelectric moment in these crystals by associating a dipole moment with each of the SO_4 (1) ions falls short of explaining the fact that the ferroelectric axis is the c axis, for the rotatory motion is about the same axis. The role played by the protons bonded to SO_4 groups has not been established beyond doubt from the structural work, but it does appear that they are ordered in the sense that they have a fixed position relative to each ion. Bearing in mind also the

large isotope effect in KDP, the result of Kasahara and Tatsuzaki[73] is consistent with this in that they find that the transition temperature of AHS is reduced by about only 8K on deuteration (c.f. an increase of 91K in KDP). We should then be inclined to rule out proton tunnelling as the phase transition mechanism in AHS and RHS. From the picture of the phase transition given by Nelmes, we might expect similarities with $NaNO_2$. A soft lattice vibration is not ruled out, however, and as far as we know, no one has yet attempted to apply any kind of microscopic model for the ferroelectric properties of these materials.

6.4 Experimental

Some of our initial findings on AHS and RHS have already been reported[47],[48]. The work began with experiments on AHS involving measurements of the spectra in the range 10-3000 cm^{-1} for all polarisations and several representative temperatures, both above and below the upper phase transition. Conventional (i.e. not digital) experimental techniques were used in these early experiments. The sample was about 4 x 5 x 6 mm in size with faces cut perpendicular to the a, b and c crystallographic axes of the pseudo-orthorhombic unit cell[69]. These axes, being also the optic axes of the crystal, allow proper polarisation measurements to be made.

AHS is highly hygroscopic, and the crystal surfaces very rapidly deteriorate on exposure to the air. The crystal was therefore polished and mounted in the cryostat under a dry nitrogen atmosphere. When not in use the crystal was kept in silicone oil. The cryostat was an Oxford Instruments CF-100 continuous flow cryostat; the sample is mounted on a

FIGURE 6.2

The lattice vibration spectra of AHS at several temperatures.

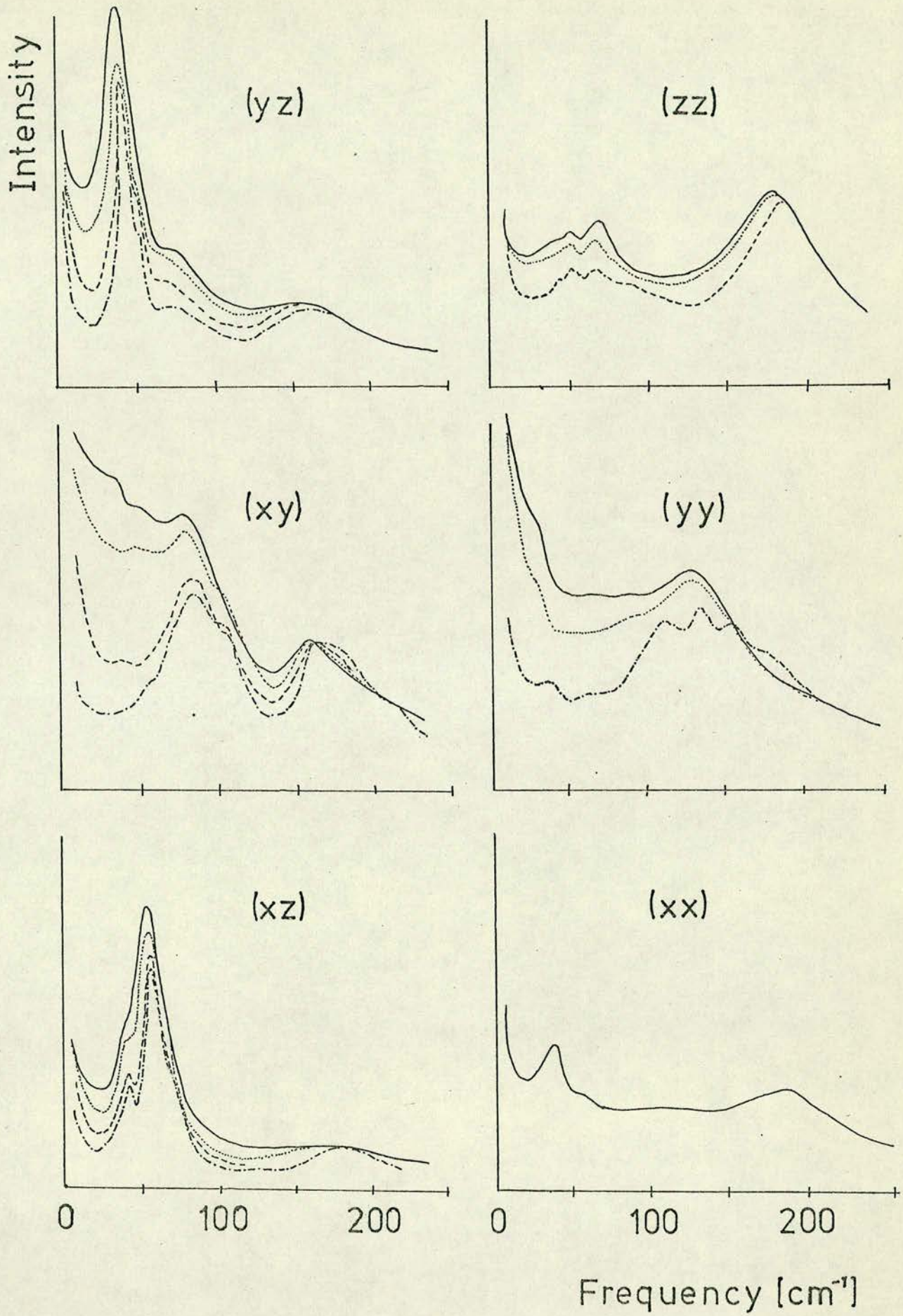
Intensity
(yz)
(zz)
(xy)
(yy)
(xz)
(xx)
0
100
200
0
100
200
Frequency [cm⁻¹]

cold finger under vacuum. The temperature was measured using the cryostat's built in linear temperature sensor - a thin film resistor - used in conjunction with a special digital voltmeter and Harwell temperature controller. The overall temperature stability was ± .5K. After the initial runs, reported in[47], it was realised that because of the complexity of the low frequency spectra, Figure 6.2, there would be little hope of distinguishing individual features. Also there was doubt as to the possible contribution that the NH_4 groups could give to the low frequency scattering. Rayleigh wing features had been observed in some of the spectra, notably the yy. It was decided therefore that experiments on the simpler isomorph RHS should be done for comparison and, if feasible, for more detailed study. One practical advantage of RHS is that there is no lower transition and much lower temperatures may be reached.

The prospect of collecting vast amounts of data - six possible polarisations, over a range of 0-3000 cm^{-1}, at several temperatures - posed a real problem, as did the prospect of attempting thereafter to investigate in any detail features of such complex spectra. It was appropriate then, to embark on the design and construction of an automated scanning and data collection system. This marked the inception of System 1, and its initial task was to collect the data on RHS. 65 separate runs were recorded, many of them with multiple scanning. As a means of analysing the data the library of on-line computer routines, described in Appendix IV, was started. This was a new venture in Raman spectroscopy, and it has since proved highly productive. The rest of the experimental equipment was the same as for AHS, and the same technique was used in the preparation of the sample.

We now present our observations on both materials, to compare them where appropriate, and to bring out any possible evidence about the nature of their ferroelectric phase transition. Several representative spectra of AHS and RHS, at one temperature well above and one temperature well below the phase transition, are displayed in Figures 6.4 - 6.25.

FIGURE 6.3

Comparison of the internal mode spectrum of the free sulphate ion, SO_4, the free bisulphate ion, HSO_4, and the bisulphate ion in RHS.

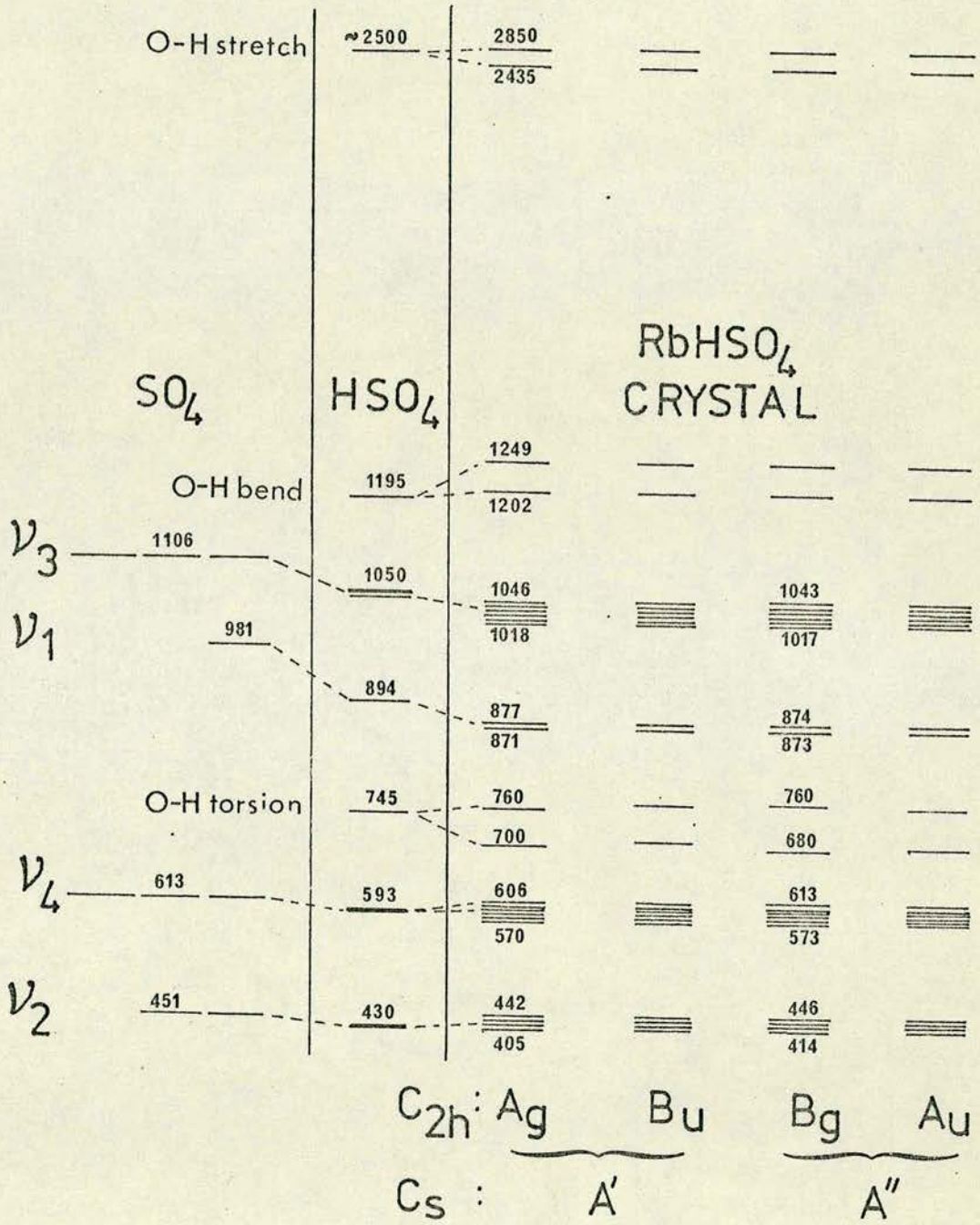
O-H stretch
≈2500
2850
2435
RbHSO4
CRYSTAL
SO4
HSO4
1249
O-H bend
1195
1202
ν3
1106
1050
1046
1043
ν1
981
1018
1017
894
877
874
871
873
O-H torsion
745
760
760
700
680
ν4
613
593
606
613
570
573
ν2
451
430
442
446
405
414
C2h: Ag Bu Bg Au
Cs : A' A''

FIGURES 6.4 AND 6.5

The Raman spectra of AHS over the range 7 - 3200 cm^{-1} at room temperature.

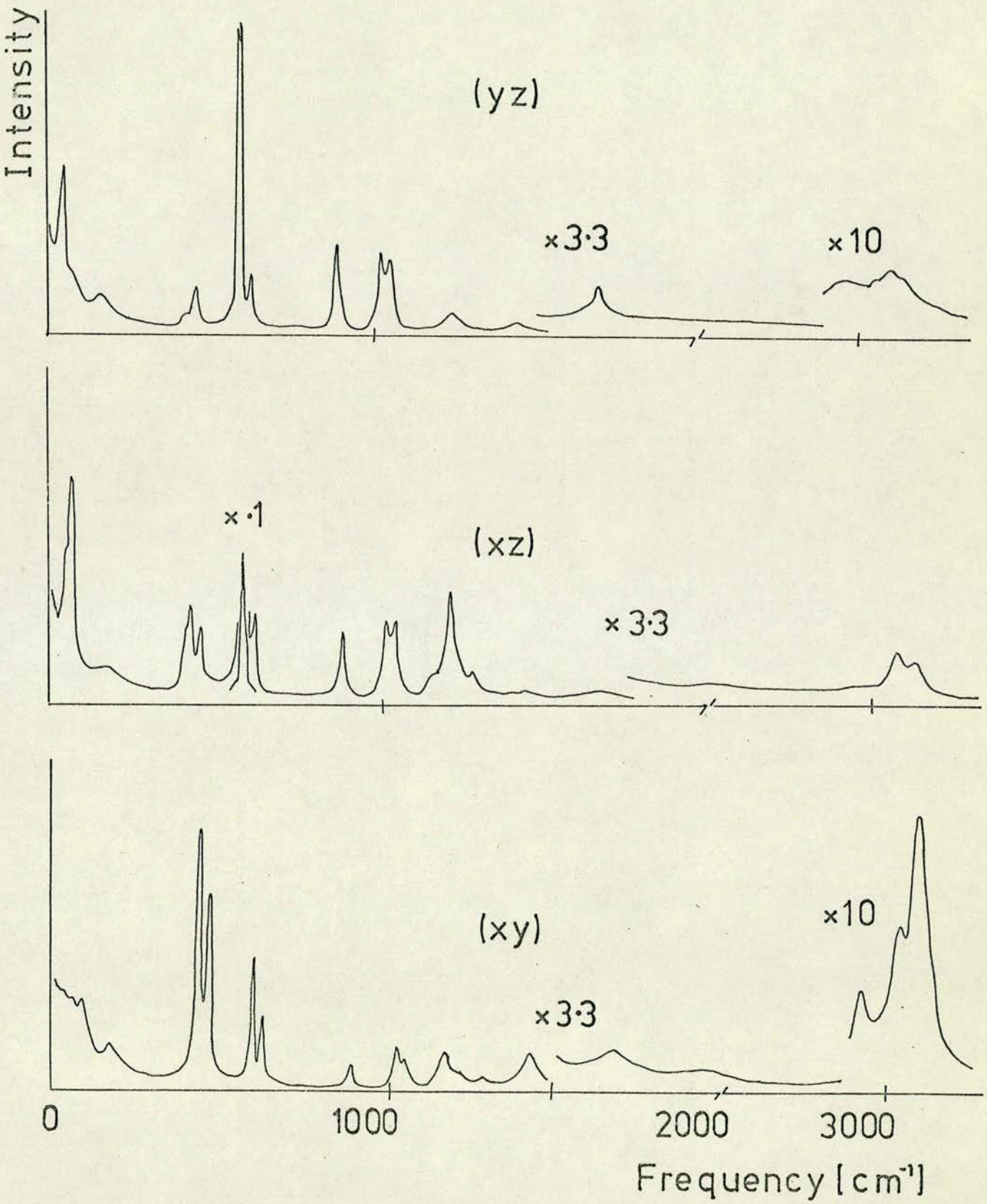
Intensity
(yz)
×3·3
×10
×·1
(xz)
×3·3
(xy)
×10
×3·3
0
1000
2000
3000
Frequency [cm⁻¹]

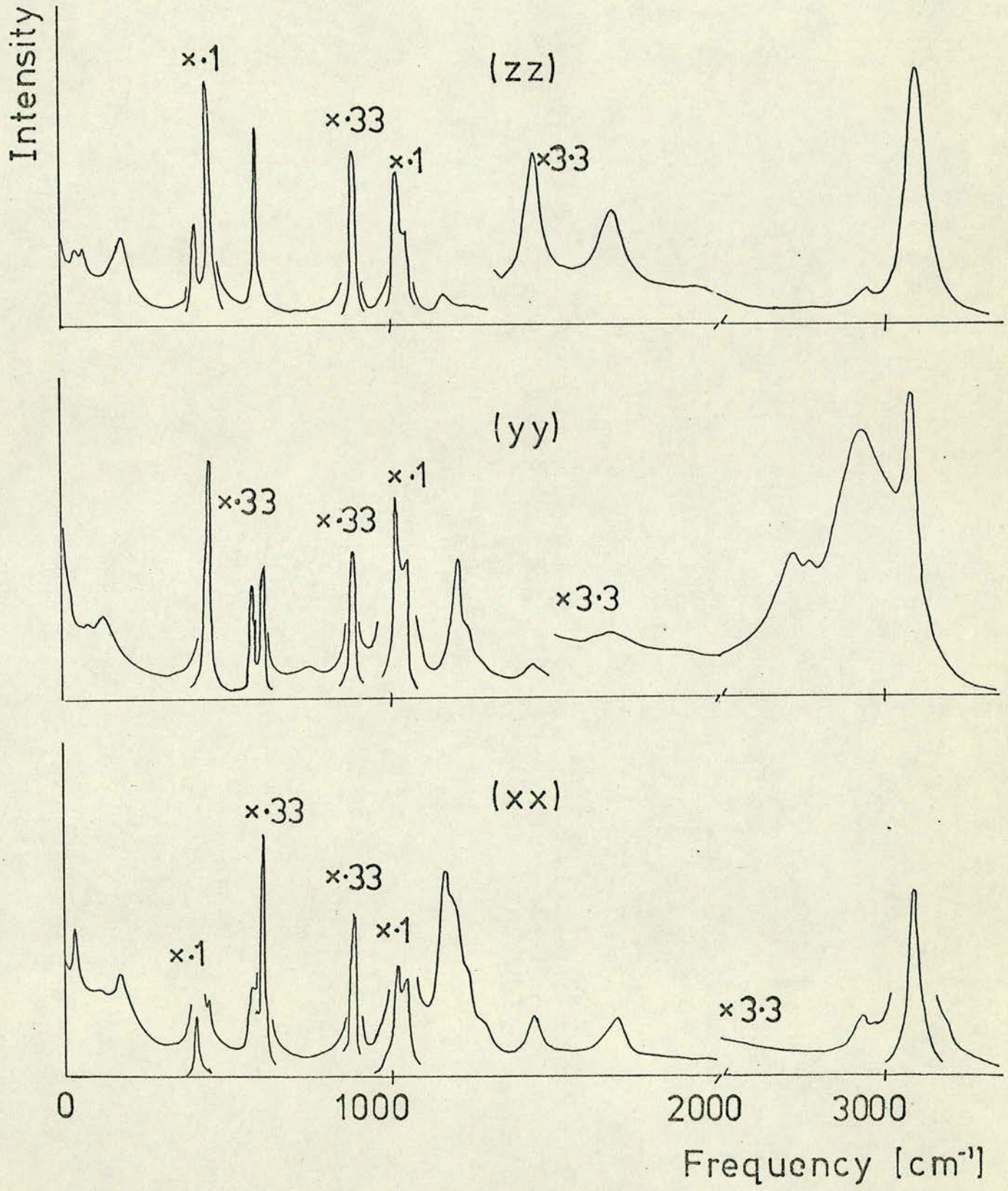
Intensity
×·1
(zz)
×·33
×·1
×3·3
(yy)
×·33
×·33
×·1
×3·3
(xx)
×·33
×·33
×·1
×·1
×3·3
0
1000
2000
3000
Frequency [cm⁻¹]

FIGURE 6.6

The yy Raman spectrum of AHS over the range 7 - 500 cm^{-1} at room temperature. Note the prominent wing below 40 cm^{-1}.

FIGURE 6.7

The yy Raman spectrum of AHS over the range 7 - 500 cm^{-1} at 156K. Note in comparison with Figure 6.6 the loss of the wing feature, and the presence of a small peak at 35 cm^{-1}

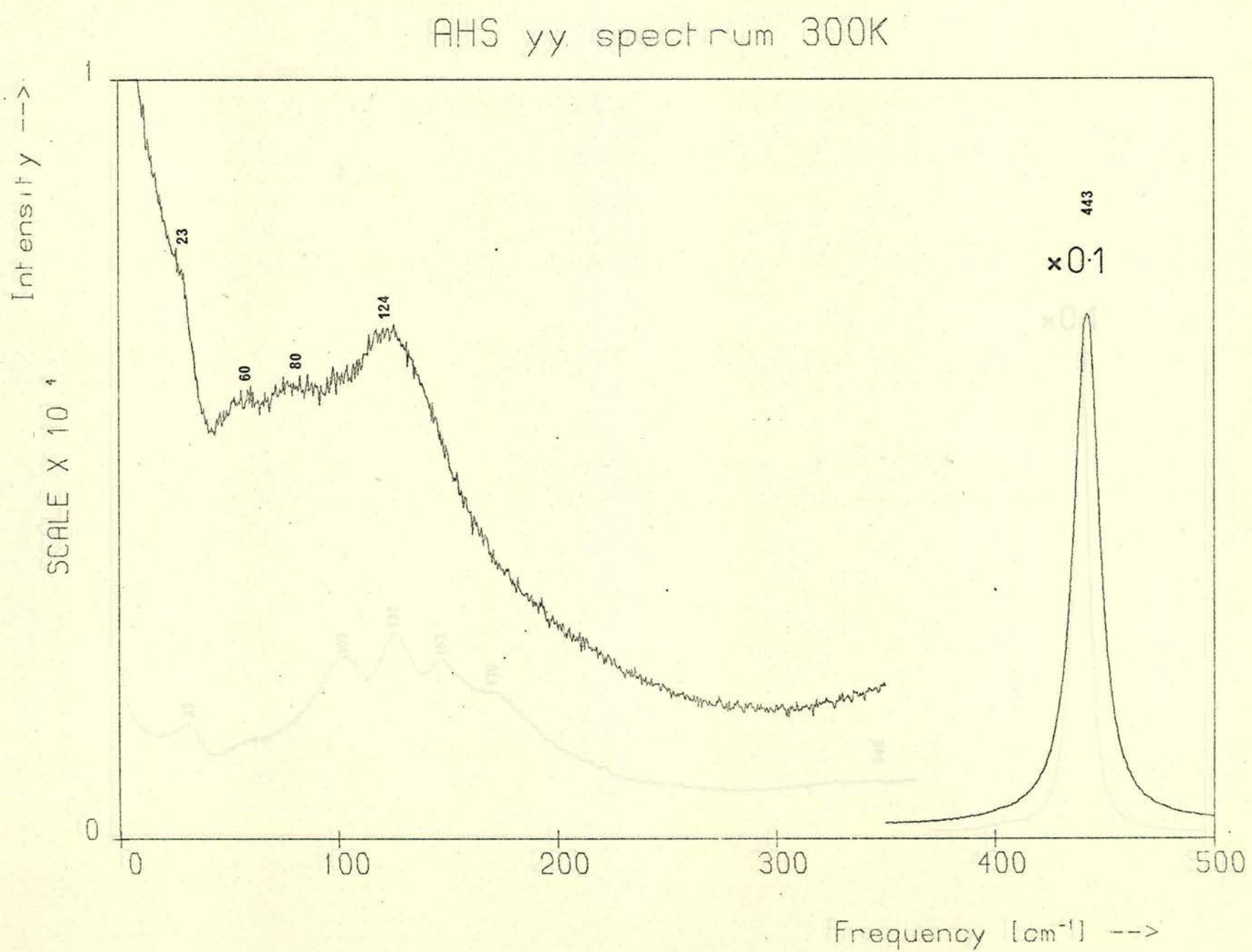
AHS yy spectrum 300K
Intensity -->
SCALE X 10 ⁴
1
0
23
60
80
124
443
×0·1
0
100
200
300
400
500
Frequency [cm⁻¹] -->

FIGURES 6.8 TO 6.13

The yy spectrum of RHS

6.8	7 - 1100 cm^{-1} at 303K
6.9	7 - 1100 cm^{-1} at 82K
6.10	7 - 200 cm^{-1} at 303K
6.11	7 - 200 cm^{-1} at 82K
6.12	1165 - 1265 cm^{-1} at 82K and 303K
6.13	2250 - 3250 cm^{-1} at 104K and 303K

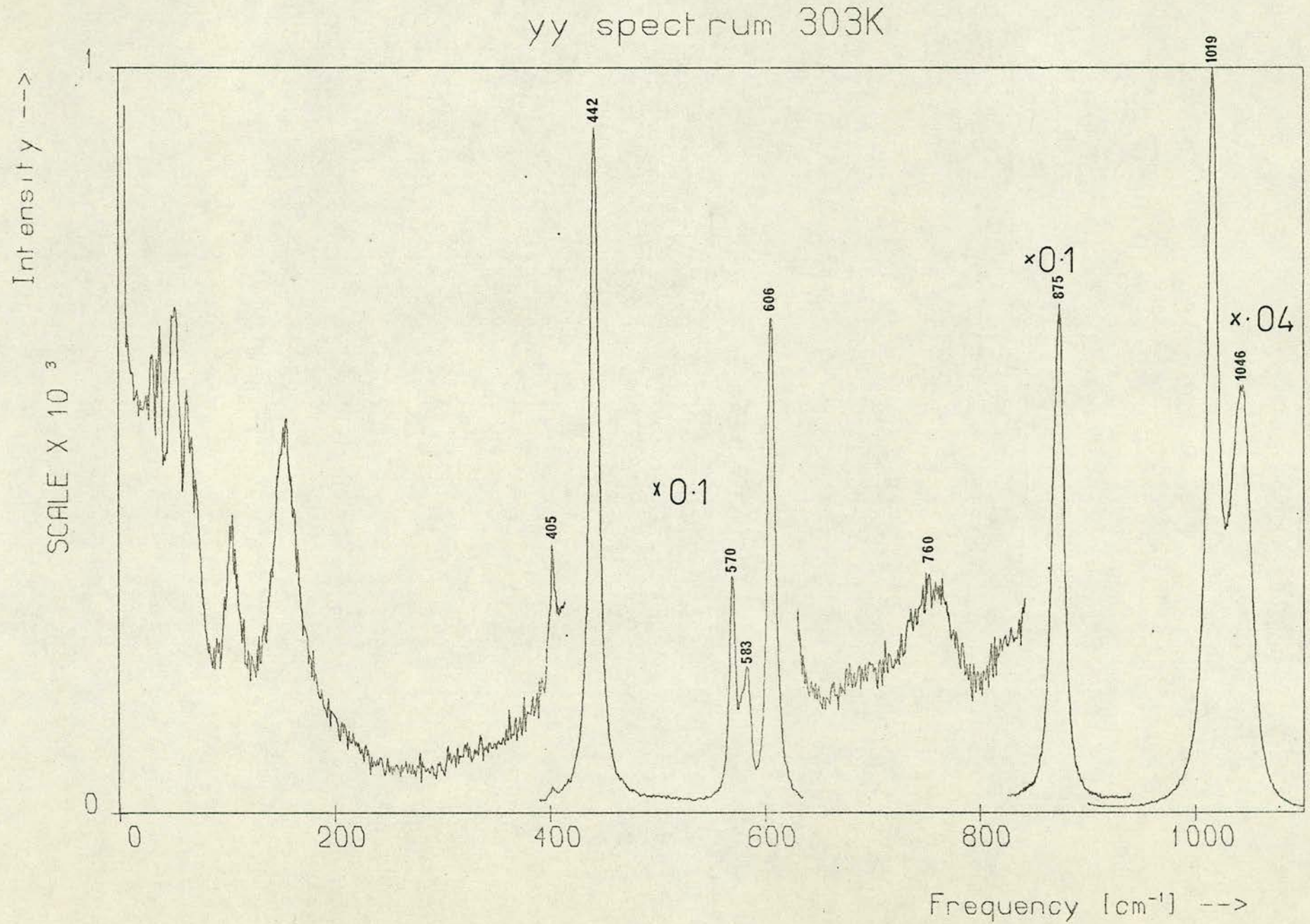
yy spectrum 303K
Intensity -->
SCALE X 10 3
1
0
0
200
400
600
800
1000
Frequency [cm-1] -->
405
442
570
583
606
760
875
1019
1046
x0·1
x0·1
x·04

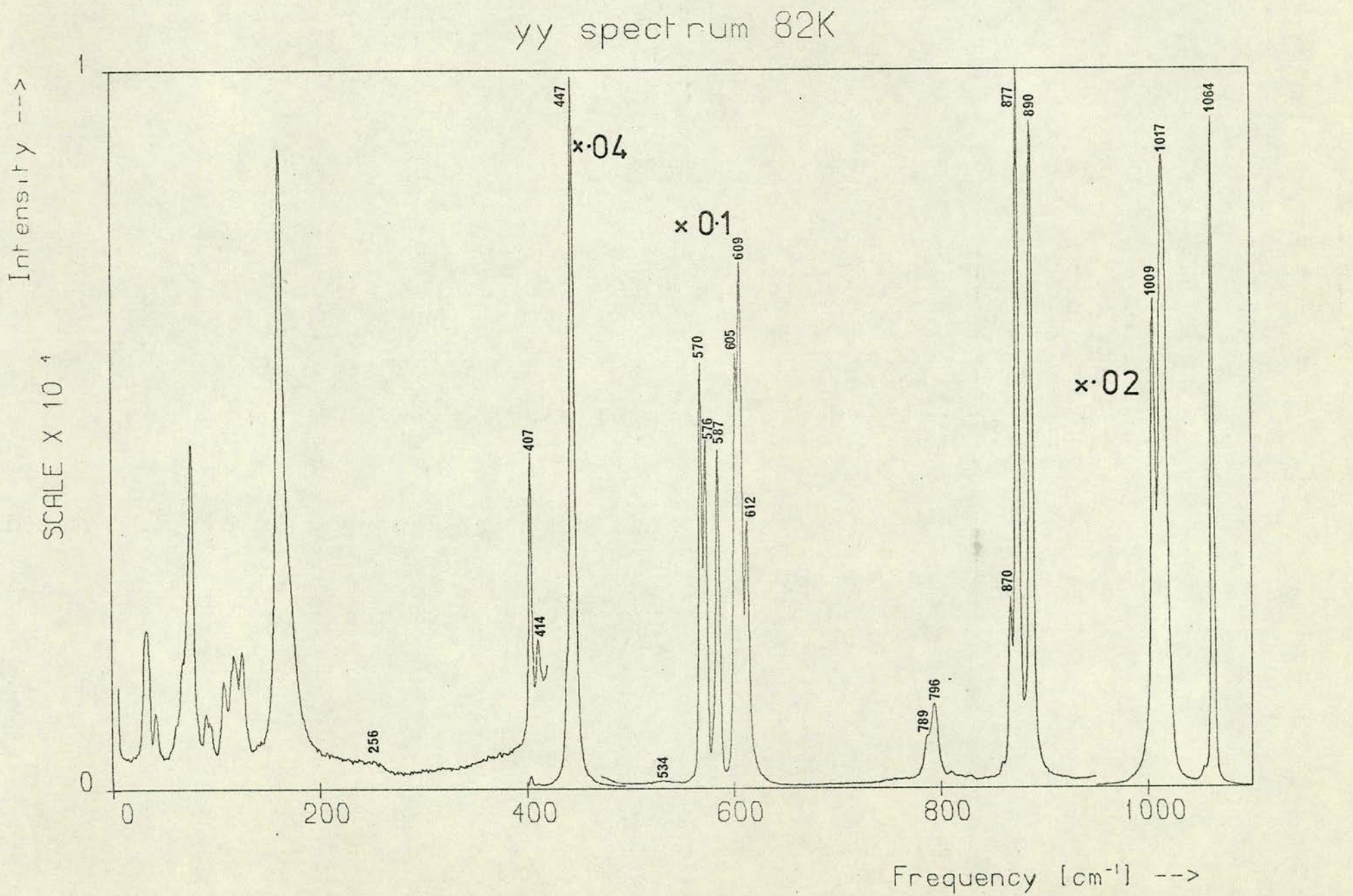
yy spectrum 82K
Intensity -->
SCALE X 10 ⁴
1
0
0
200
400
600
800
1000
Frequency [cm⁻¹] -->
×·04
× 0·1
×·02
256
407
414
447
534
570
576
587
605
609
612
789
796
870
877
890
1009
1017
1064

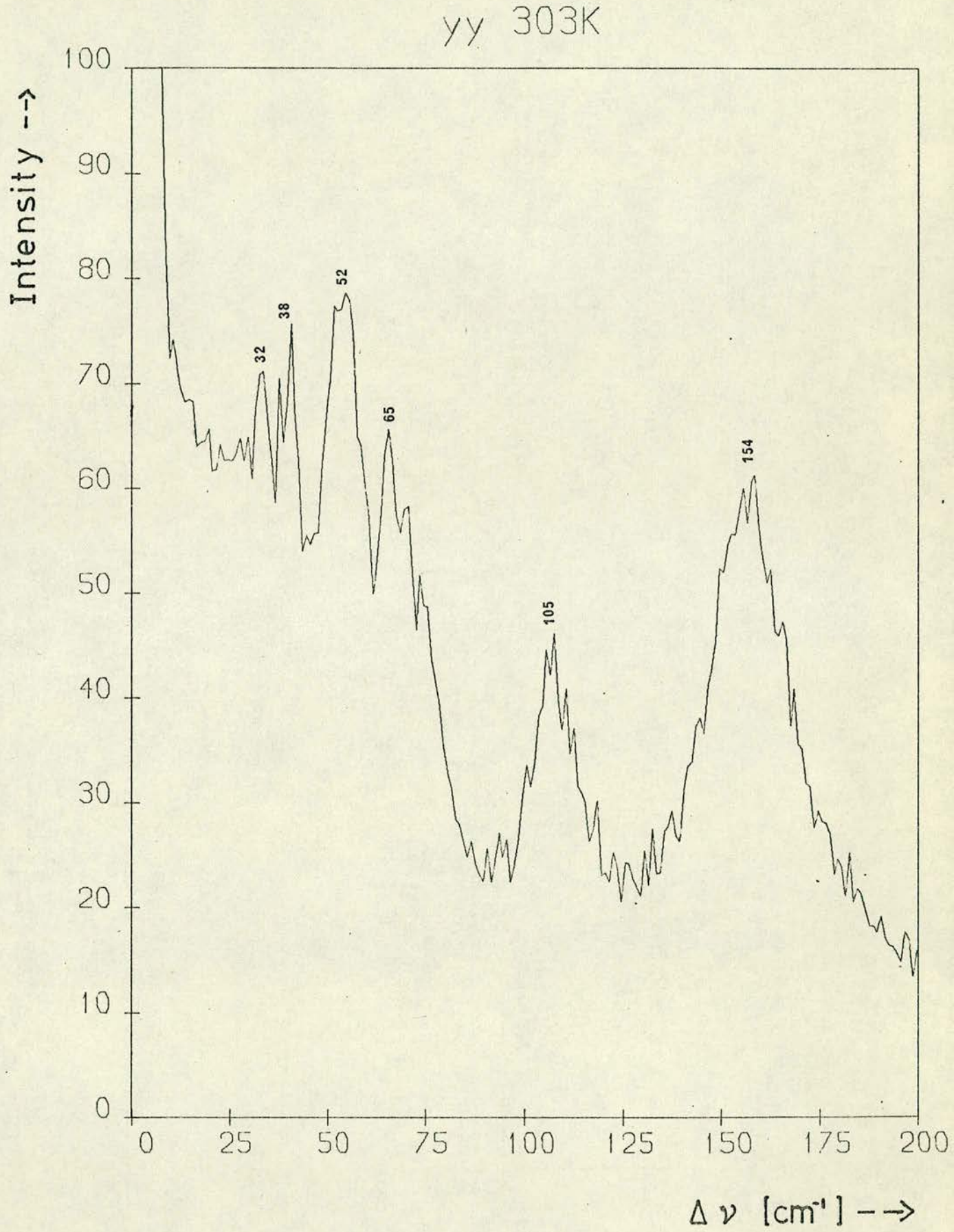
yy 303K
Intensity -->
100
90
80
70
60
50
40
30
20
10
0
32
38
52
65
105
154
0
25
50
75
100
125
150
175
200
Δ ν [cm⁻¹] -->

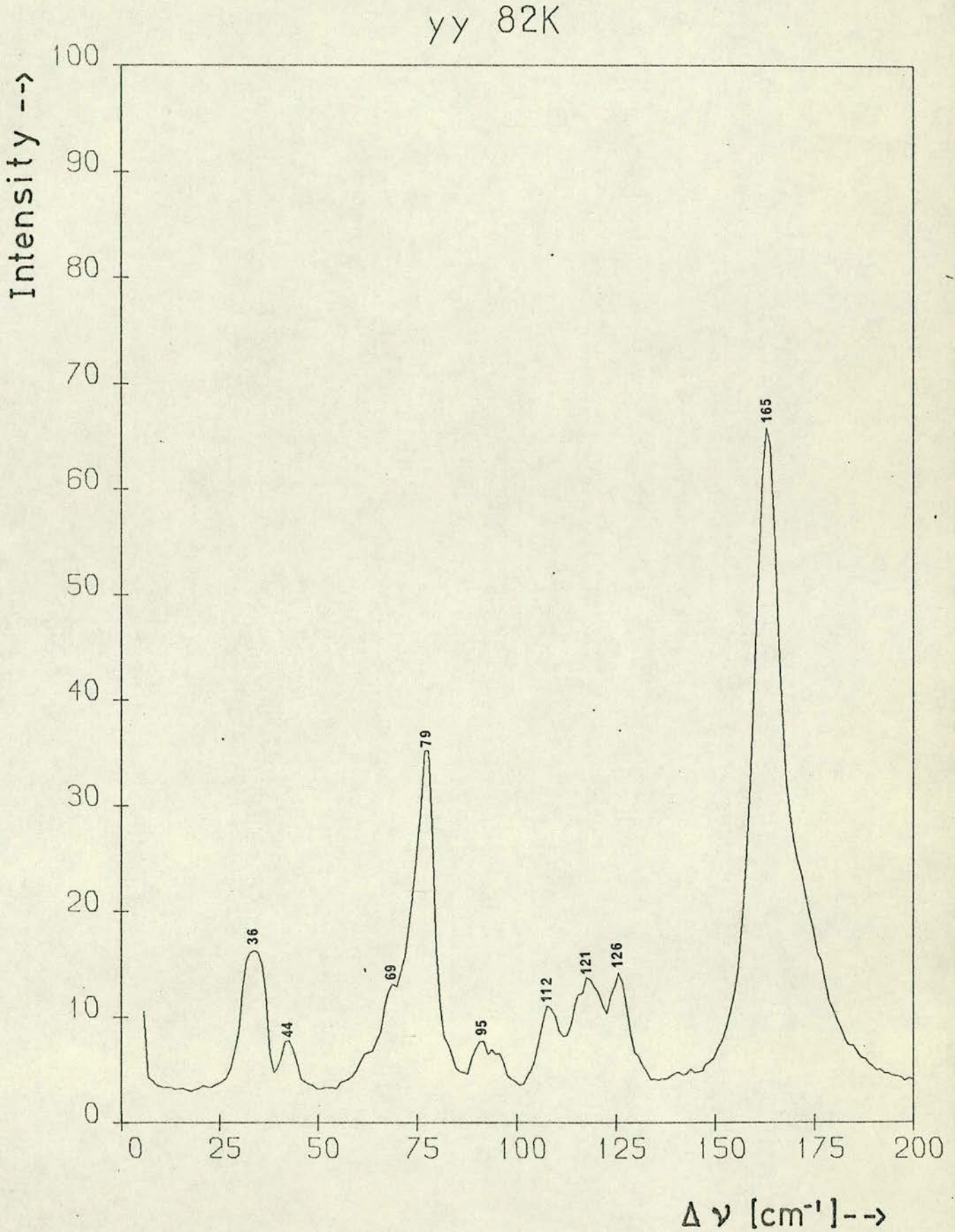
yy 82K
Intensity -->
100
90
80
70
60
50
40
30
20
10
0
0
25
50
75
100
125
150
175
200
Δ ν [cm⁻¹]-->
36
44
69
79
95
112
121
126
165

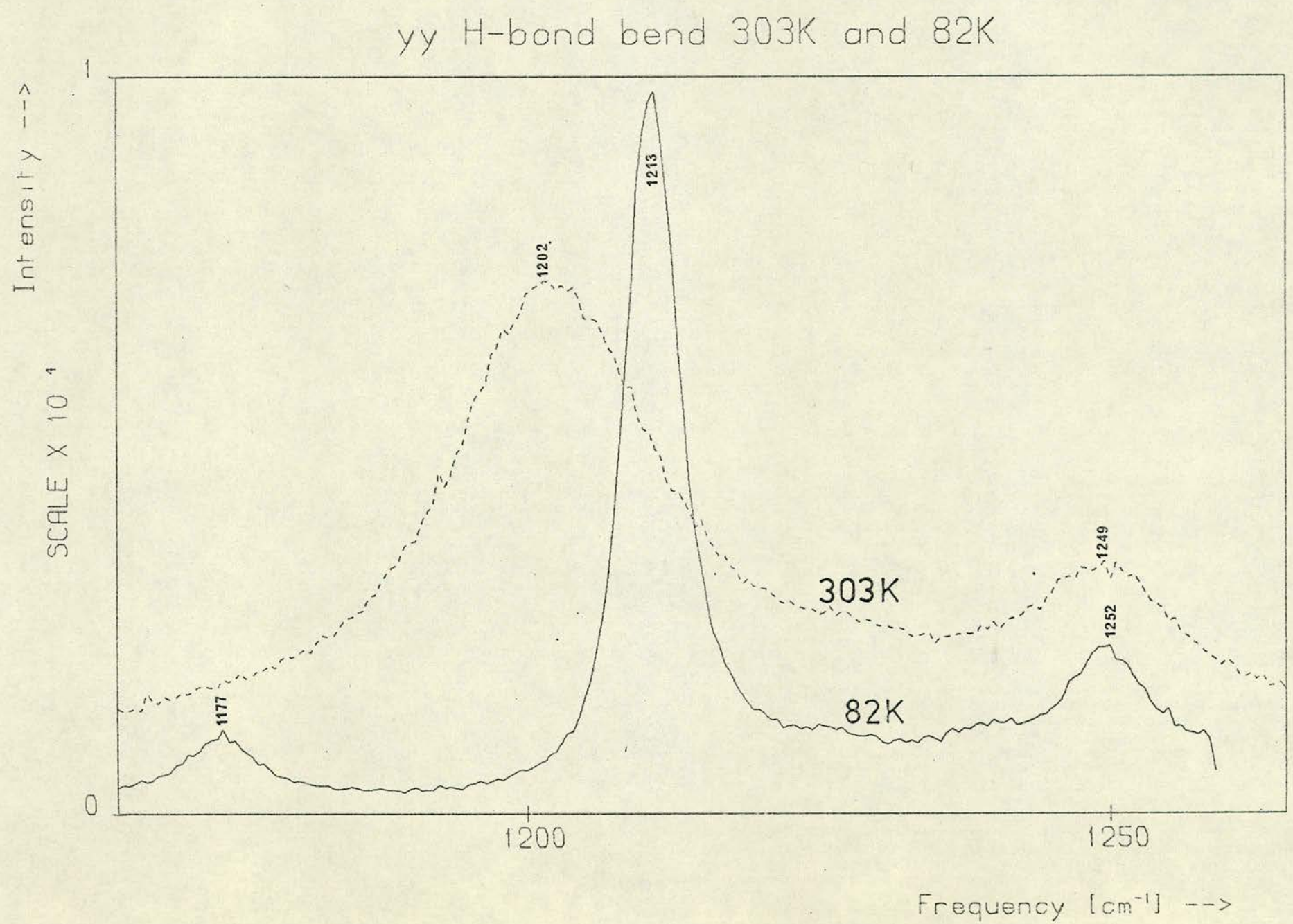
yy H-bond bend 303K and 82K
Intensity -->
SCALE X 10 ⁴
1
0
1213
1202
1177
1249
1252
303K
82K
1200
1250
Frequency [cm⁻¹] -->

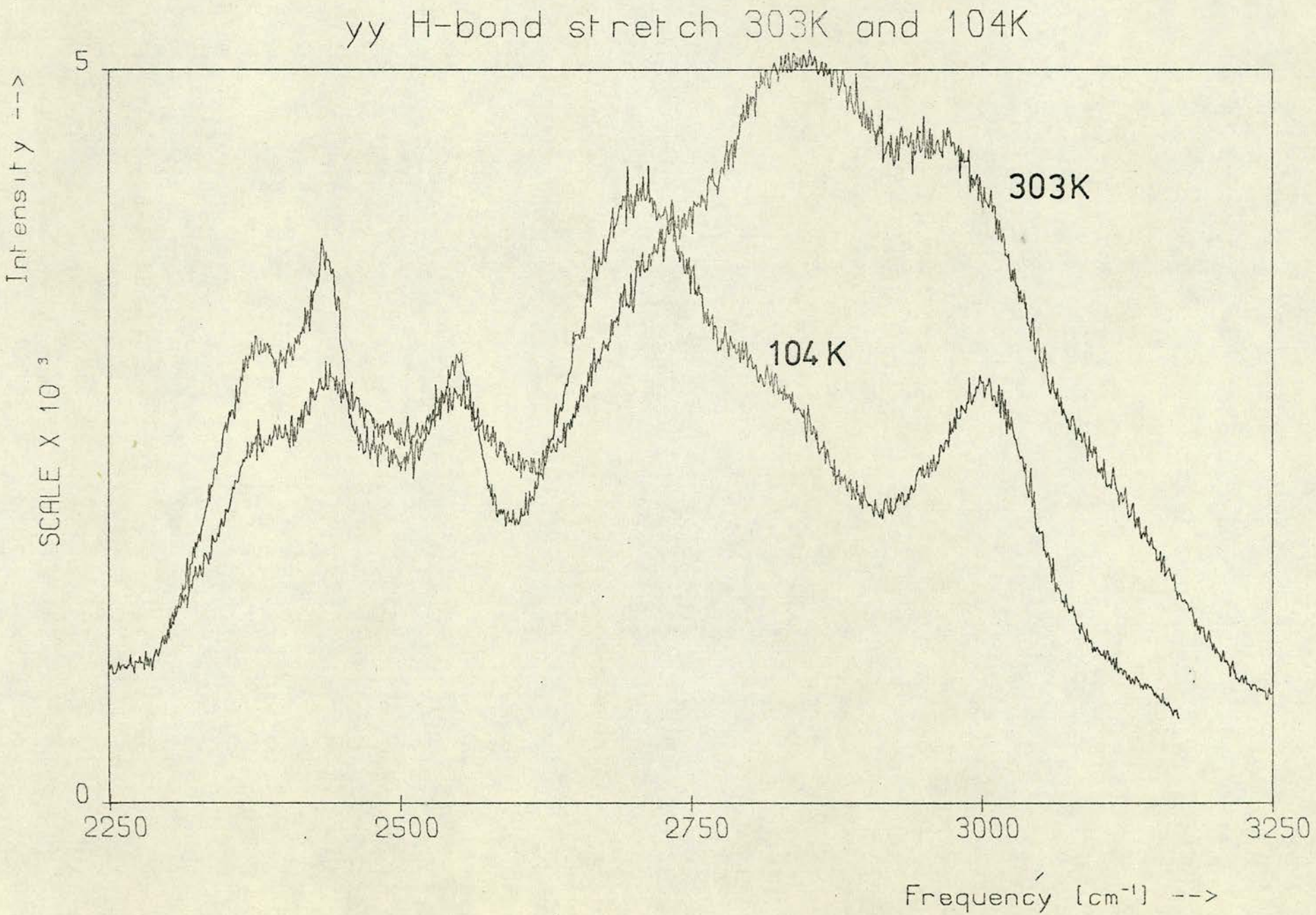
yy H-bond stretch 303K and 104K
Intensity -->
SCALE X 10 ³
5
0
303K
104 K
2250
2500
2750
3000
3250
Frequency [cm⁻¹] -->

FIGURES 6.14 TO 6.17

The xy spectrum of RHS

6.14	7 - 1100	cm^{-1}	at 303K
6.15	7 - 1100	cm^{-1}	at 104K
6.16	7 - 200	cm^{-1}	at 303K
6.17	7 - 200	cm^{-1}	at 104K

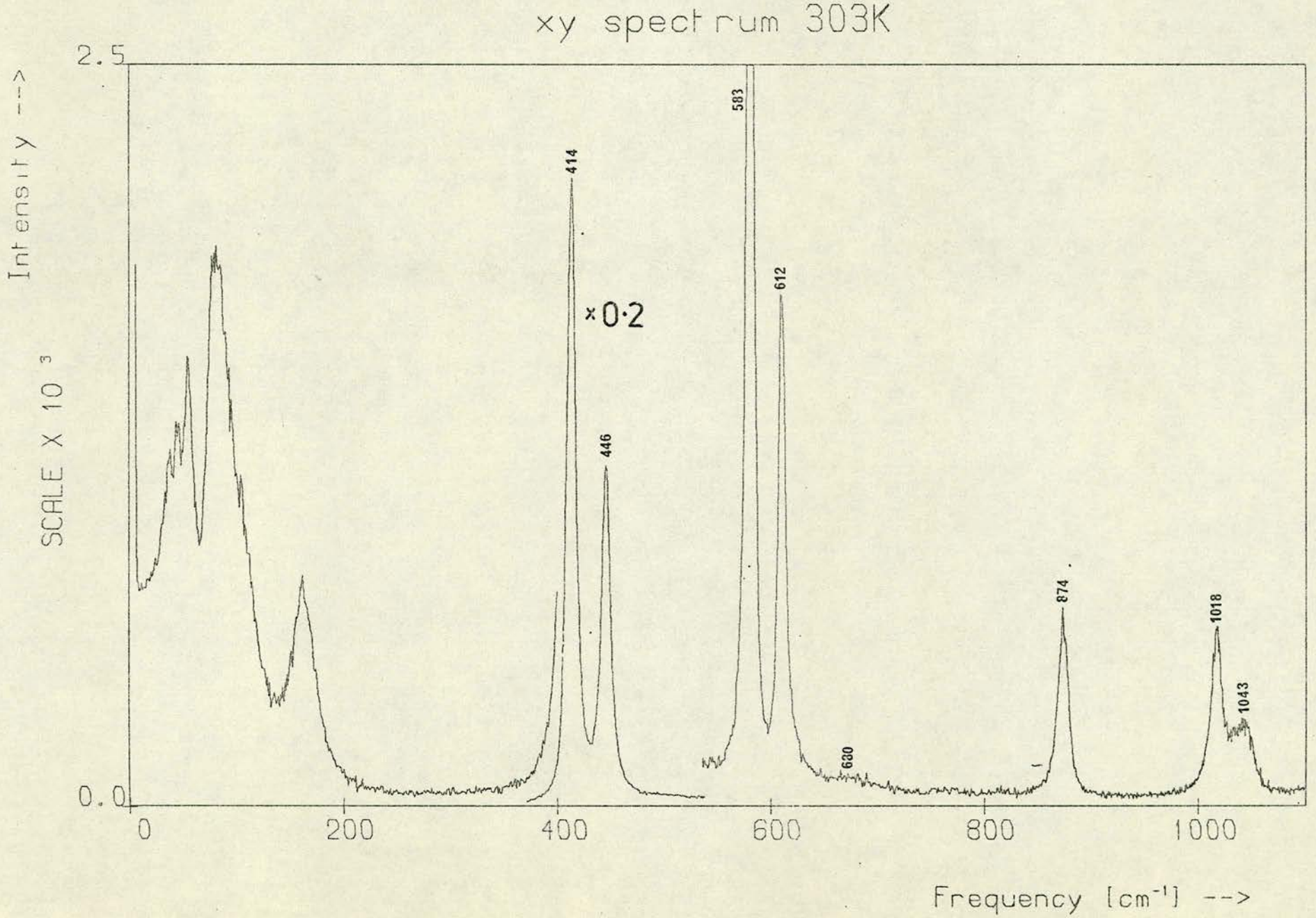
xy spectrum 303K
Intensity -->
SCALE X 10 ³
2.5
0.0
0
200
400
600
800
1000
Frequency [cm⁻¹] -->
414
446
583
612
680
874
1018
1043
×0·2

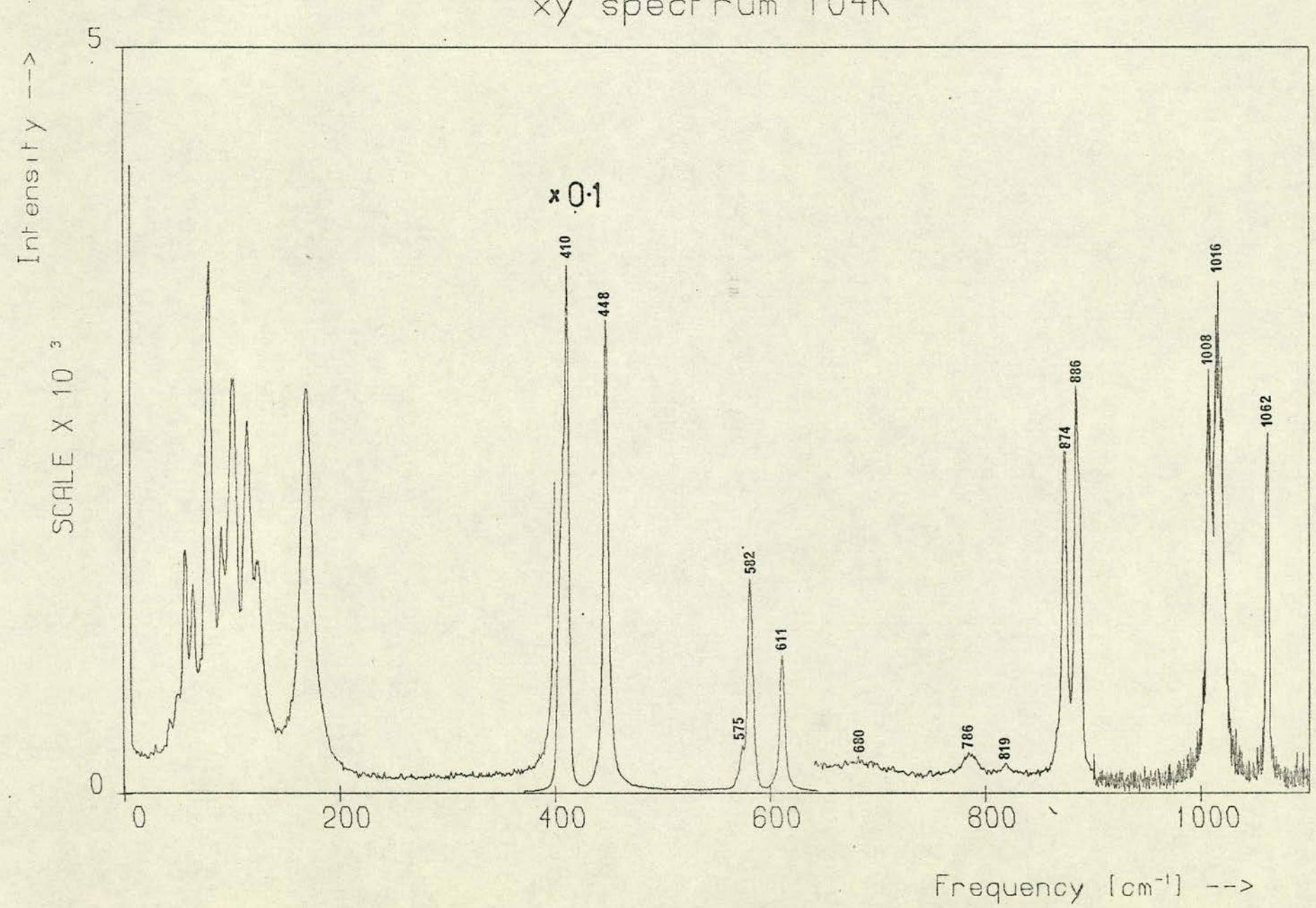
xy spectrum 104K
Intensity -->
SCALE X 10 ³
5
0
×0·1
410
448
575
582
611
680
786
819
874
886
1008
1016
1062
0
200
400
600
800
1000
Frequency [cm⁻¹] -->

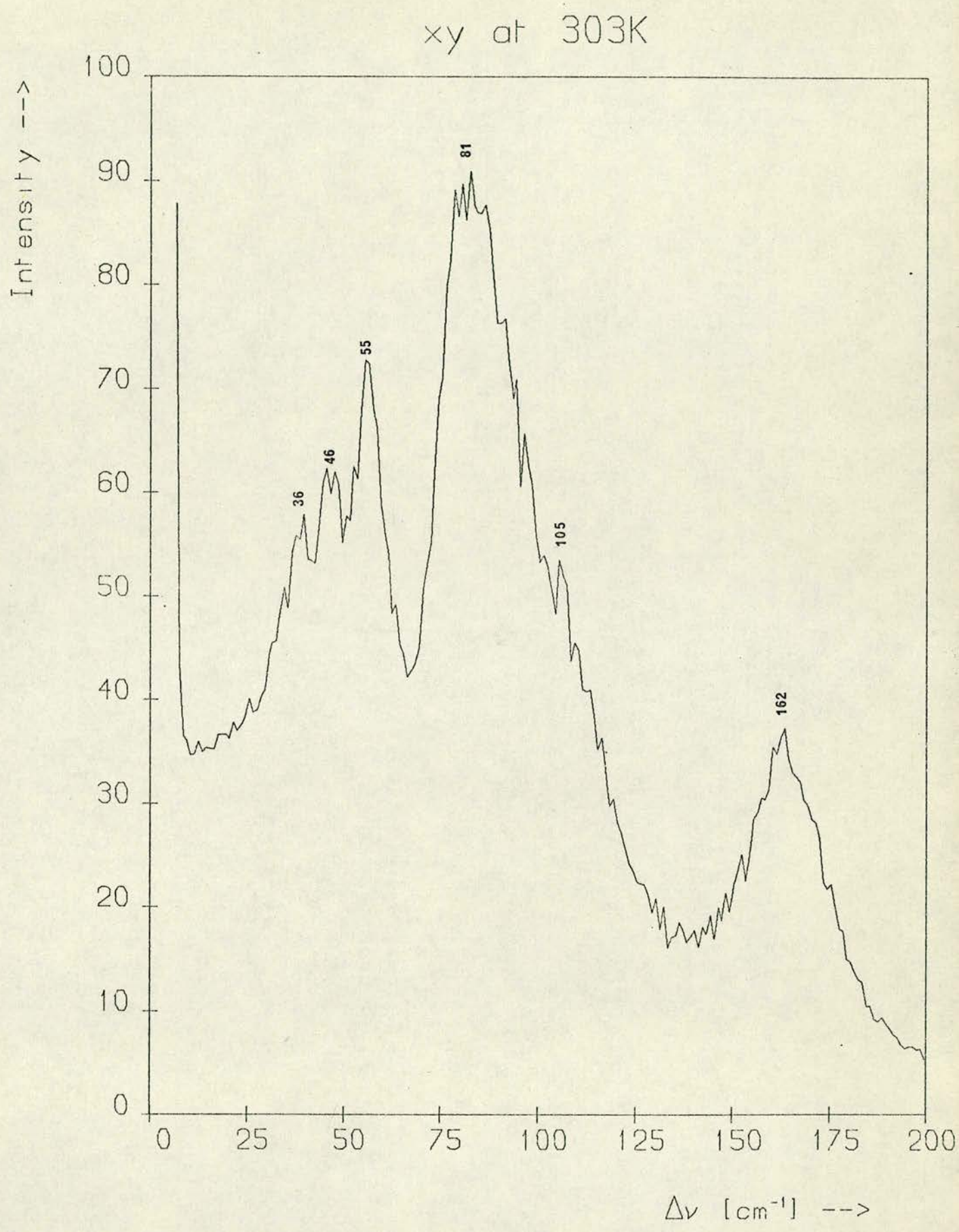
xy at 303K
Intensity -->
100
90
80
70
60
50
40
30
20
10
0
0
25
50
75
100
125
150
175
200
36
46
55
81
105
162
Δν [cm⁻¹] -->

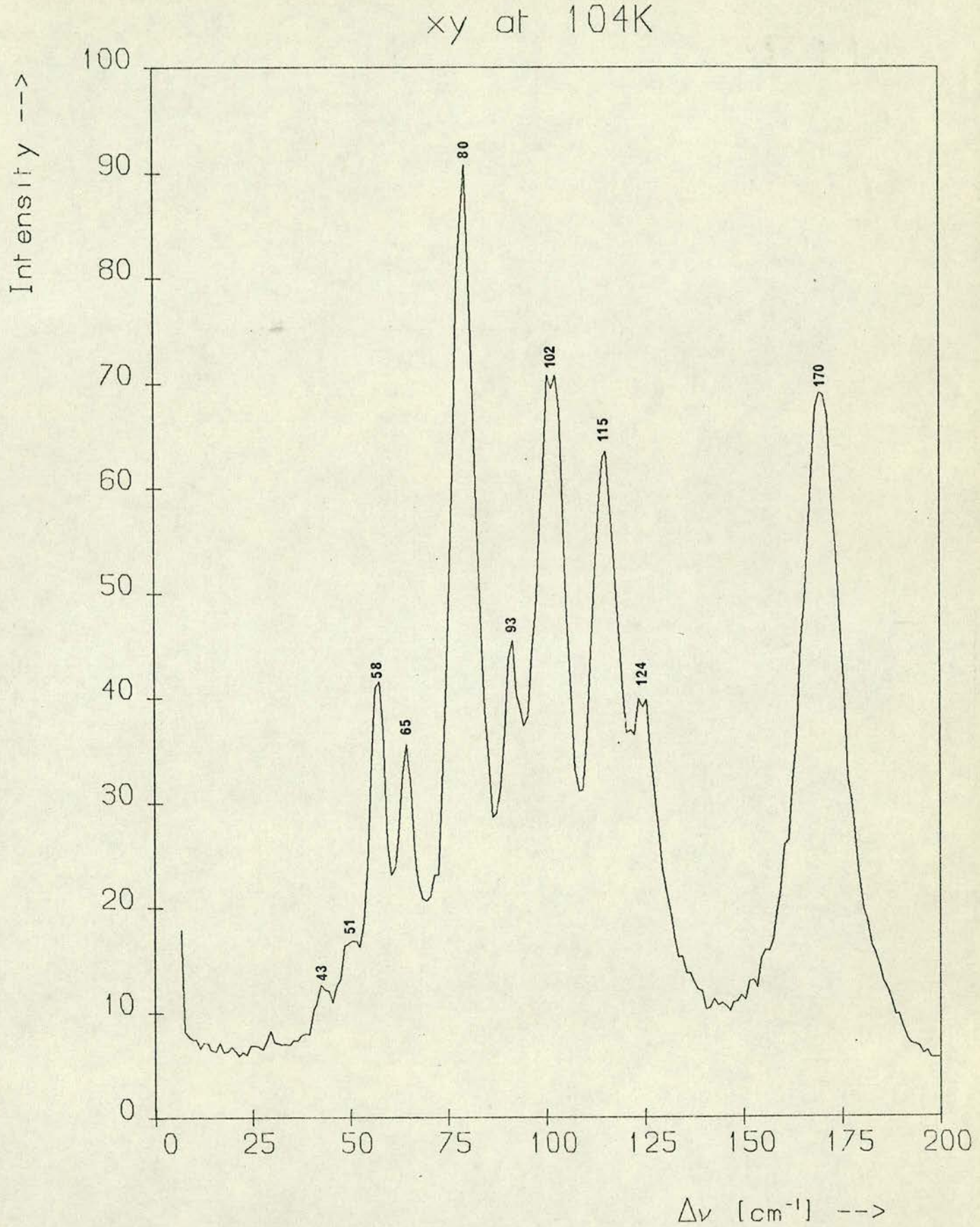
xy at 104K
Intensity -->
100
90
80
70
60
50
40
30
20
10
0
0
25
50
75
100
125
150
175
200
Δν [cm⁻¹] -->
43
51
58
65
80
93
102
115
124
170

FIGURES 6.18 TO 6.21

The xz spectrum of RHS

6.18	7 - 1025 cm^{-1} at 303K
6.19	7 - 1100 cm^{-1} at 104K
6.20	7 - 200 cm^{-1} at 303K
6.21	7 - 200 cm^{-1} at 104K

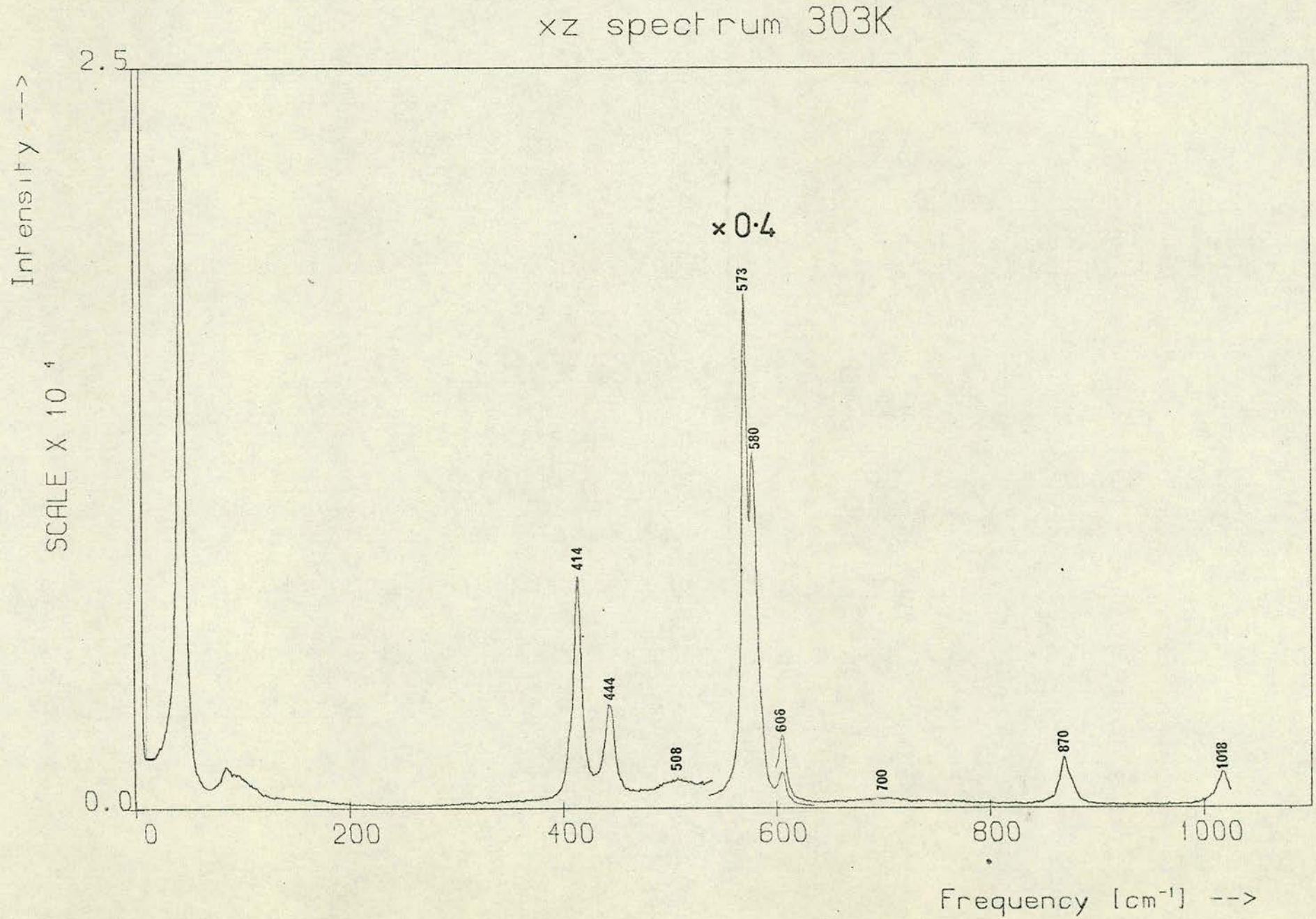
xz spectrum 303K
2.5
0.0
Intensity -->
SCALE X 10 ⁴
×0·4
573
580
414
444
508
606
700
870
1018
0
200
400
600
800
1000
Frequency [cm⁻¹] -->

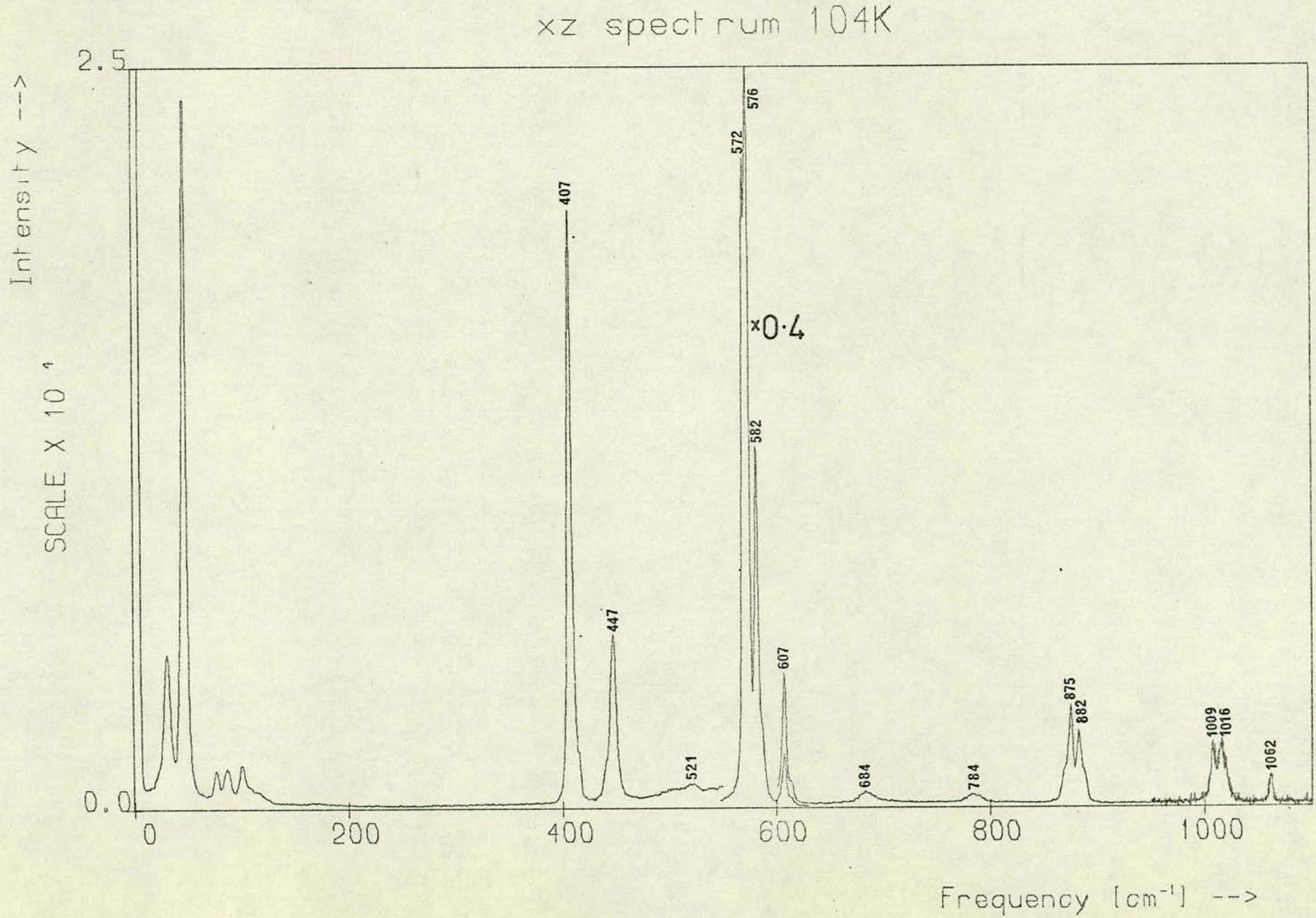
xz spectrum 104K
2.5
0.0
Intensity -->
SCALE X 10 ¹
×0·4
407
572
576
582
447
521
607
684
784
875
882
1009
1016
1062
0
200
400
600
800
1000
Frequency [cm⁻¹] -->

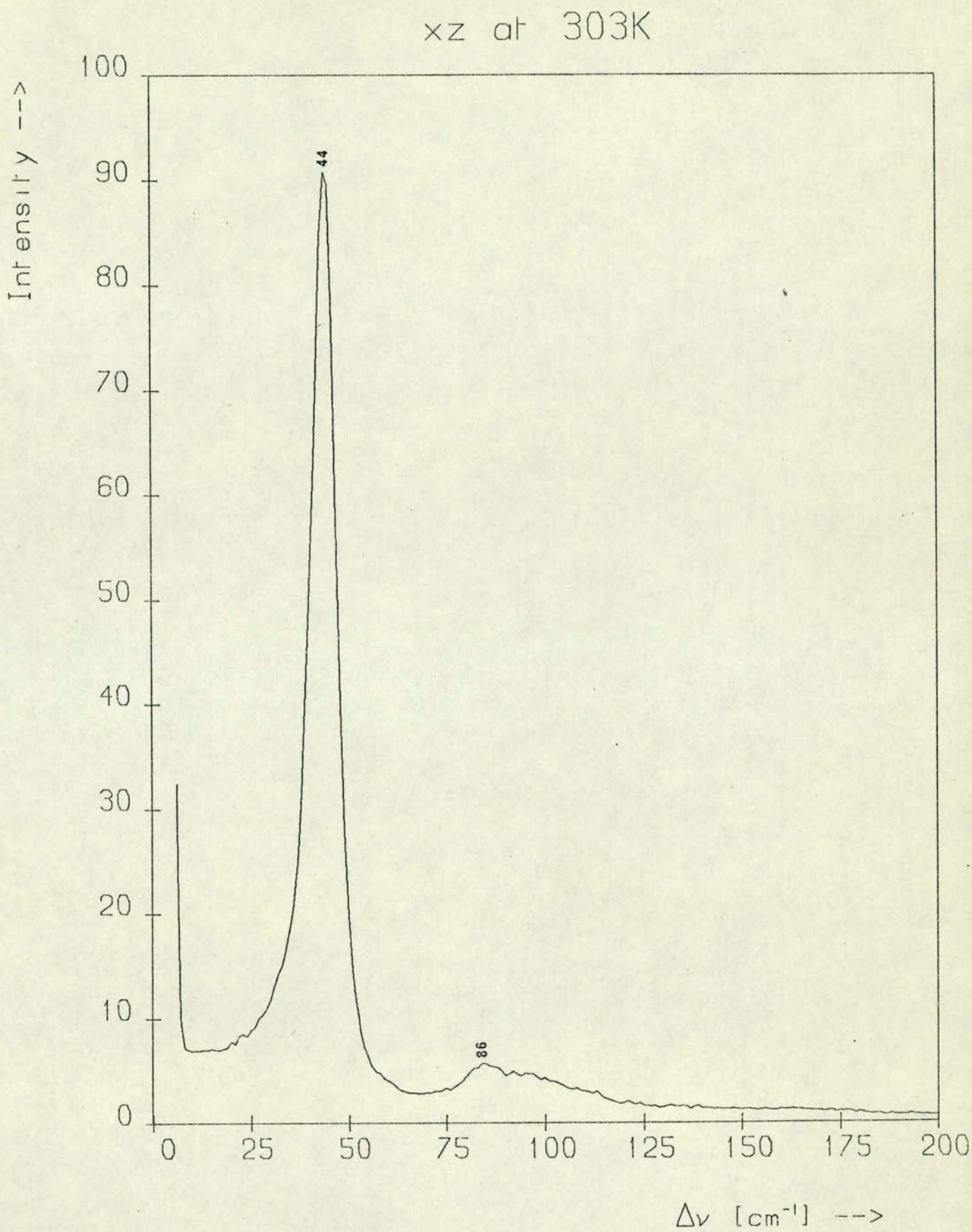
xz at 303K
Intensity -->
100
90
80
70
60
50
40
30
20
10
0
44
86
0
25
50
75
100
125
150
175
200
Δν [cm⁻¹] -->

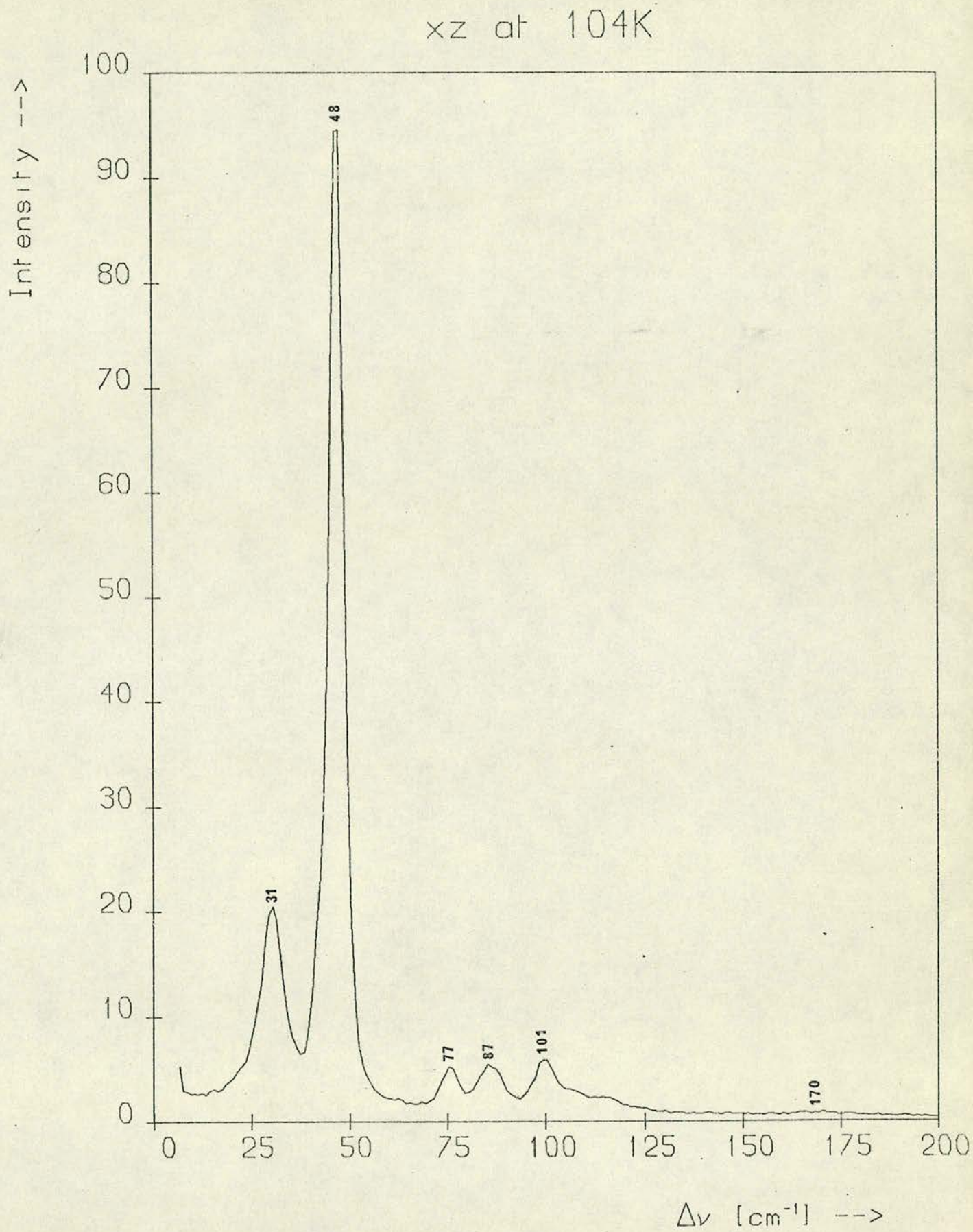
xz at 104K
Intensity -->
100
90
80
70
60
50
40
30
20
10
0
48
31
77
87
101
170
0
25
50
75
100
125
150
175
200
Δν [cm⁻¹] -->

FIGURES 6.22 TO 6.25

The yz spectrum of RHS

6.22	7 - 1025 cm^{-1} at 303K
6.23	7 - 1100 cm^{-1} at 104K
6.24	7 - 200 cm^{-1} at 303K
6.25	7 - 200 cm^{-1} at 104K

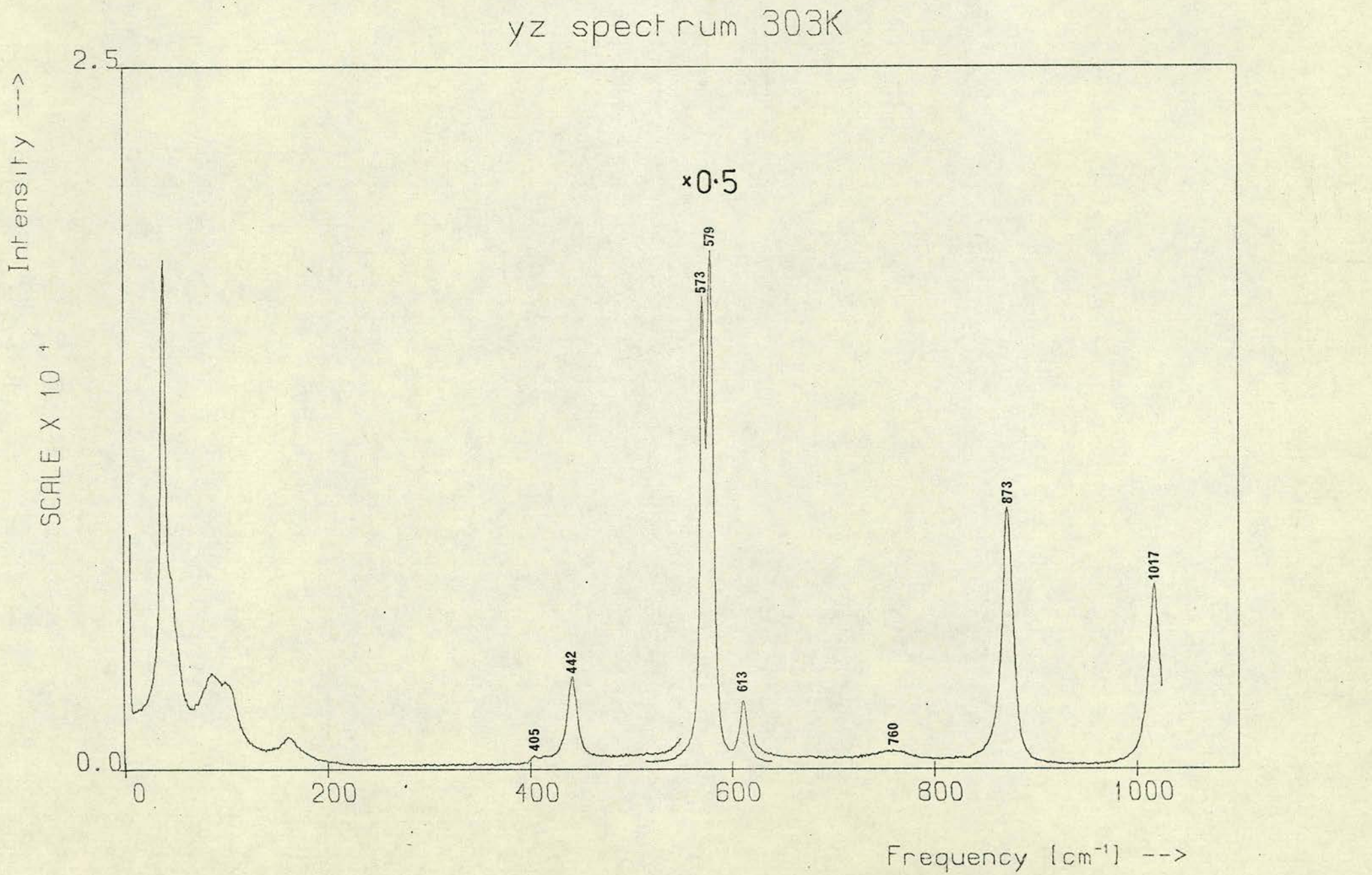
yz spectrum 303K
2.5
Intensity -->
SCALE X 10 ⁴
×0·5
579
573
442
405
613
760
873
1017
0.0
0
200
400
600
800
1000
Frequency [cm⁻¹] -->

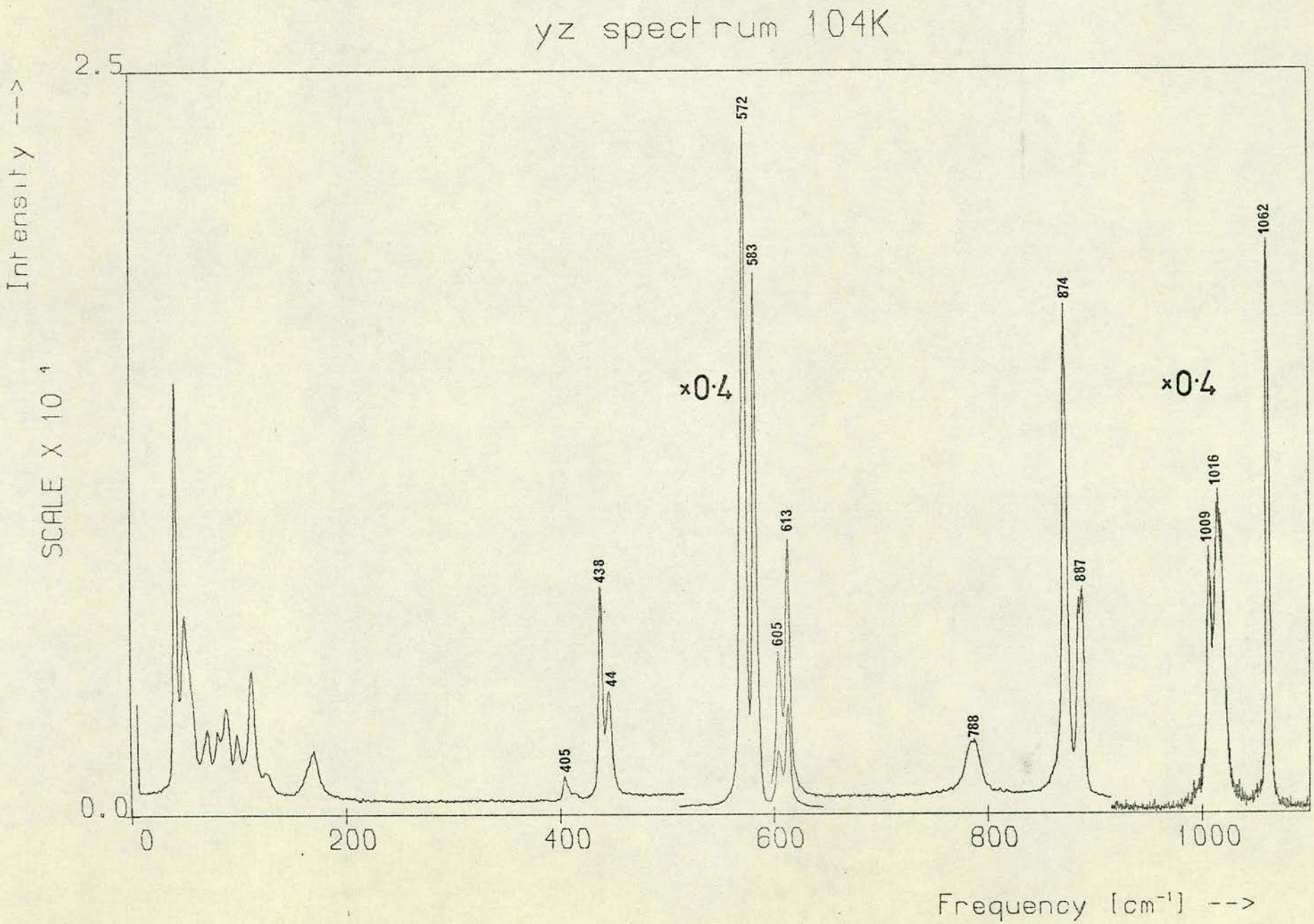
yz spectrum 104K
Intensity -->
SCALE X 10 ⁴
2.5
0.0
0
200
400
600
800
1000
Frequency [cm⁻¹] -->
405
438
44
572
583
605
613
788
874
887
1009
1016
1062
×0·4
×0·4

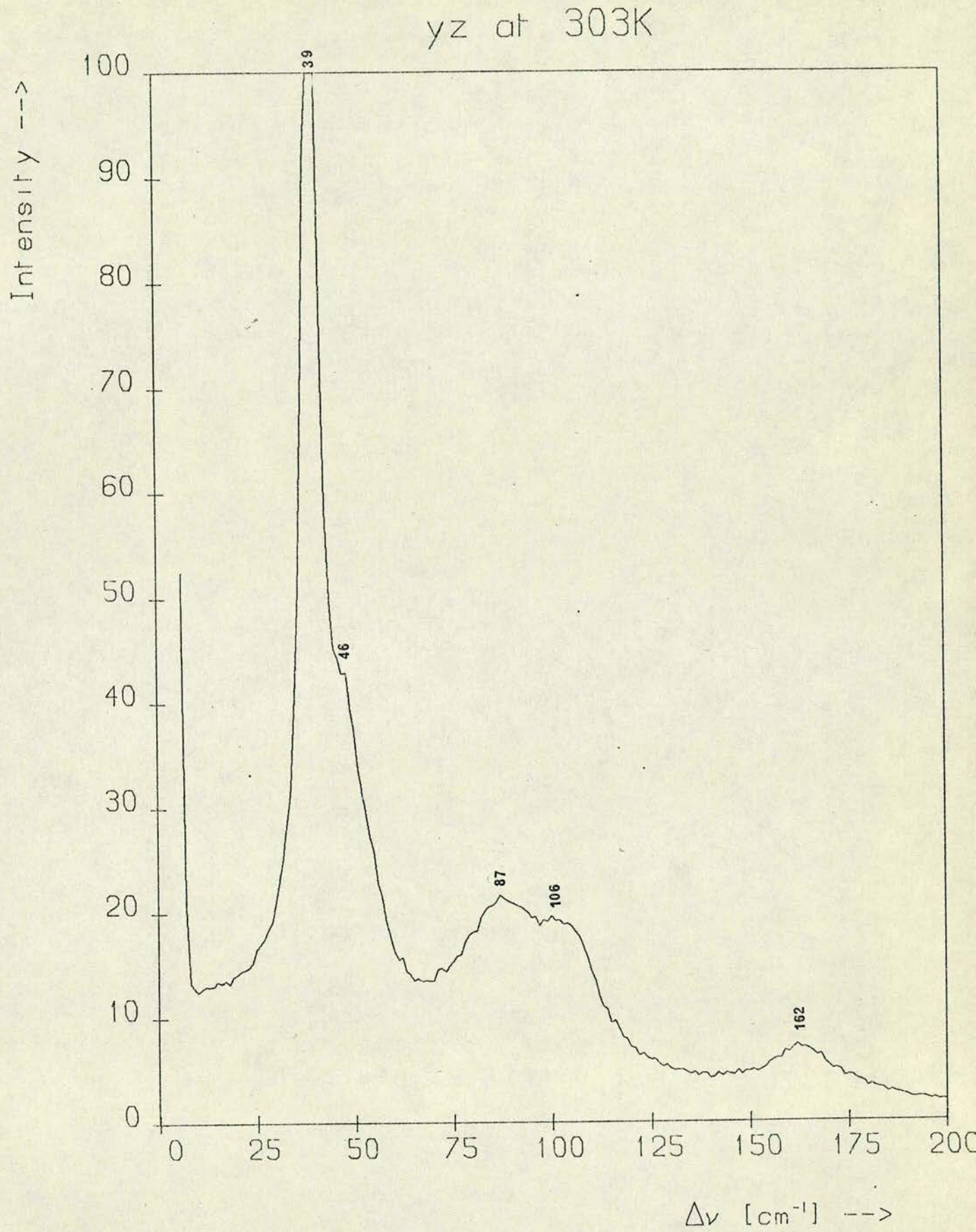
yz at 303K
Intensity -->
100
90
80
70
60
50
40
30
20
10
0
39
46
87
106
162
0
25
50
75
100
125
150
175
200
Δν [cm⁻¹] -->

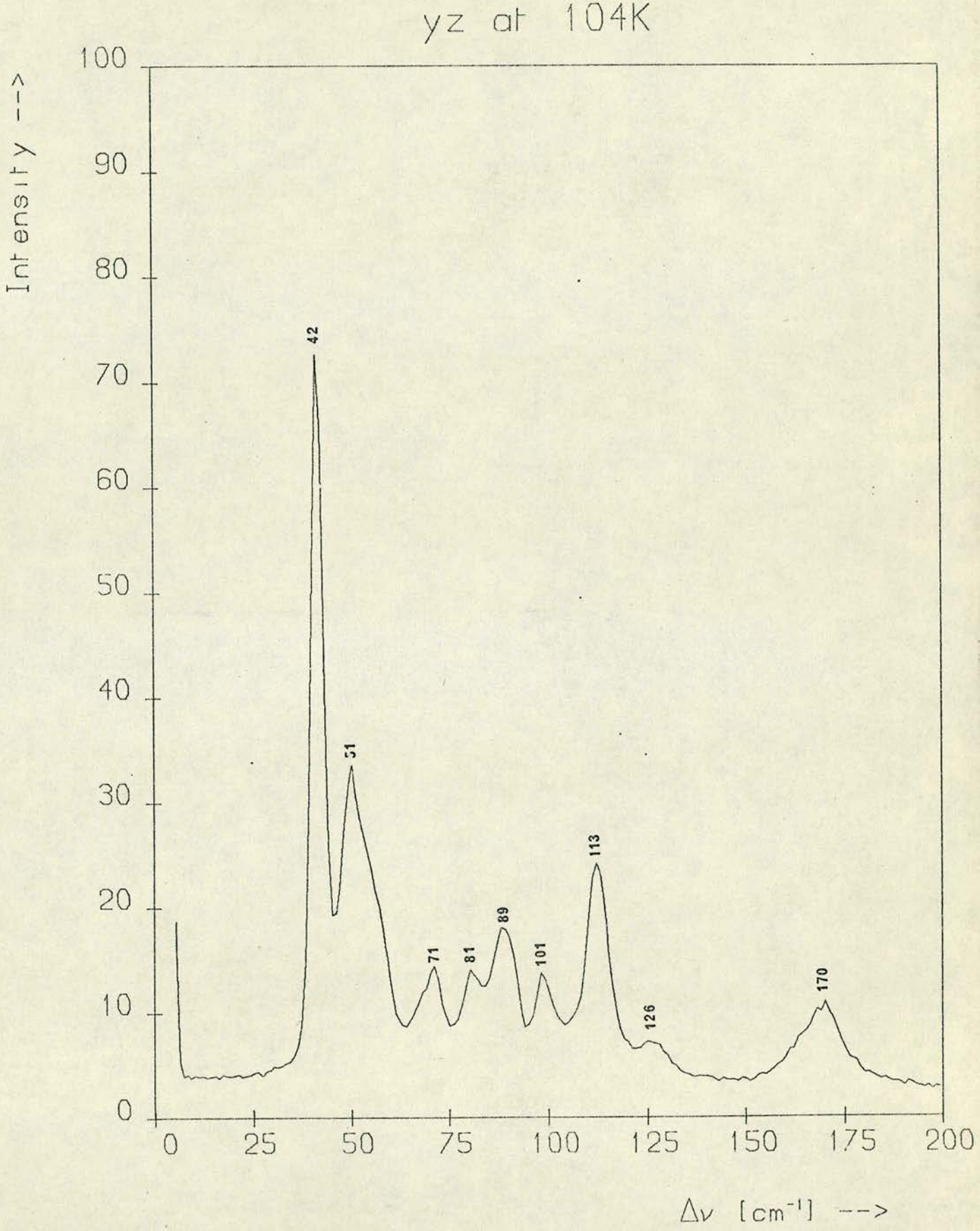
yz at 104K
Intensity -->
100
90
80
70
60
50
40
30
20
10
0
42
51
71
81
89
101
113
126
170
0
25
50
75
100
125
150
175
200
Δν [cm⁻¹] -->

6.5 The Vibration Spectra of AHS and RHS

AHS and RHS are so remarkably similar that it would be repetitious to give a full account of both materials. RHS is simpler to treat and we shall present our discussion in terms of that material. Where necessary, the differences of AHS from RHS will be pointed out, but for the moment we treat the NH_4^+ group as being equivalent to Rb. The freedom of rotational motion of the NH_4 groups found by Miller *et al.*[51] suggest that they would indeed contribute only translational degrees of freedom to the lattice vibration spectrum, the same as for a single atom.

In both substances the HSO_4 ion may be treated as a molecular group with 3 rotational, 3 translational and 12 internal degrees of freedom. The group theory for vibrations at the zone centre is particularly simple and we only state the results. The crystal point groups used to classify the modes are C_{2h} and C_s in the paraelectric and ferroelectric phases respectively. The 69 optical lattice modes transform in the paraelectric phase as:

$$36A_g + 36B_g + 35A_u + 34B_u \quad . \tag{6.1}$$

The internal modes of the HSO_4 can transform as:

$$24A_g + 24B_g + 24A_u + 24\,B_u \quad . \tag{6.2}$$

Only 'g' modes are Raman active, and only 'u' modes are infra-red active. In the ferroelectric phase these modes transform under C_s and to find the new representations we can apply the compatibility relations:

$$C_{2h}(A_g, B_u) \longrightarrow C_s\ (A')$$
$$C_{2h}(A_u, B_g) \longrightarrow C_s\ (A'') \quad . \qquad (6.3)$$

The centre of inversion is lost and all modes are simultaneously infrared and Raman active.

The Raman tensors are:

$$\begin{bmatrix} a & & d \\ & b & \\ d & & c \end{bmatrix} \qquad \begin{bmatrix} & e & \\ e & & f \\ & f & \end{bmatrix}$$

$A_g : A'$ $\qquad$ $B_g : A''$

6.6 The Internal Modes of the Bisulphate Ion

The internal modes of the HSO_4 groups may be readily distinguished. The modes of an individual HSO_4 ion may be identified according to Herzberg's notation for the SO_4 group[74], with all the degeneracies lifted, plus 3 modes attributable to the bonded proton. There are two symmetrically inequivalent sulphate groups, SO_4 (1) and SO_4 (2), in the crystal so that we have contributions from both in each representation. This picture of the HSO_4 vibrations is given in Figure 6.3. There are four major bands, $\nu_1 - \nu_4$, associated with the SO_4 vibrations, and, in addition, three associated with the hydrogen bond. A distortion of the group, elongating the S - O(H) bond, reduces the symmetry from tetragonal to trigonal, lifting some degeneracies. In reality, all degeneracies are lifted because the hydrogen lies off the S - O bond in such a

TABLE 6 (I)

Frequencies and assignments of the bisulphate ion in AHS and RHS

AHS 300K						RHS 303K				RHS 82K	RHS 104K			
XX	YY	ZZ	XY	XZ	YZ	YY	XY	XZ	YZ	YY	XY	XZ	YZ	Assignment
404		404	410			405			405	407		407	405	
			419	419	418		414	414		414	410			$\nu_2 SO_4$
	443	443				442		444	442	447		447	438	
			448	449	446		446				448		445	
								508				521		
										534				
						570				570		572	572	
578	575		576		575			573	573	576	575	576		
	582	586	583	585	583	583	583	580	579	587	582	582	583	$\nu_4 SO_4$
609	611	612	611			606		606		605			605	
				615	615		612		613	609		607		
										612	611		613	
							680				680	684		
								700						O-H torsion
						760			760	789	786	784	788	
										796	819			
881		883	880	883	882			870		810				
	887					815	874		873		874		874	$\nu_1 SO_4$
										877		875		
										890	886	882	887	

Table 6(I) (Contd.)

AHS 300K						RHS 303K				RHS 82K	RHS 104K			Assignment
XX	YY	ZZ	XY	XZ	YZ	YY	XY	XZ	YZ	YY	XY	XZ	YZ	
1014 1043	1017 1046	1014 1043	1017 1044	1017 1047	1018 1046	1019 1046	1018 1043	1018	1017	1008 1017 1064	1009 1016 1062	1009 1016 1062	1009 1016 1062	$\nu_3 SO_4$
1155 1188 1230 1275	 1188 1235 1280	1160 1220 1275	1160 1213 1230 1281	1168 1230 1280	 1235 	 1204 1249				 1177 1213 1252				$2\nu_4 SO_4$ O-H bend
    2856	 2423 2540 2870	 2860	 2420 2870	 2855	 2890	2384 2438 2547 2790sh 2850 2965				2383 2435 2550 2710 2850 3007 3007				O-H stretch

FIGURES 6.26 TO 6.30

The temperature dependence of the peak frequencies of some of the internal modes of the HSO_4 ion in the yy spectrum of RHS.

6.26 the ν_1 and ν_2 bands, with the ν_2 band of AHS plotted for comparison

| peak positions in RHS
× peak positions in AHS
□ △ ◇ frequencies from a curve resolving analysis for the ν_1 band in RHS.

6.27 The ν_4 band

6.28 The H-bond torsion band

6.29 The appearance of the ν_3 band at various temperatures.

6.30 The temperature dependence of the peaks in the ν_3 band, with an indication as to the linewidths.

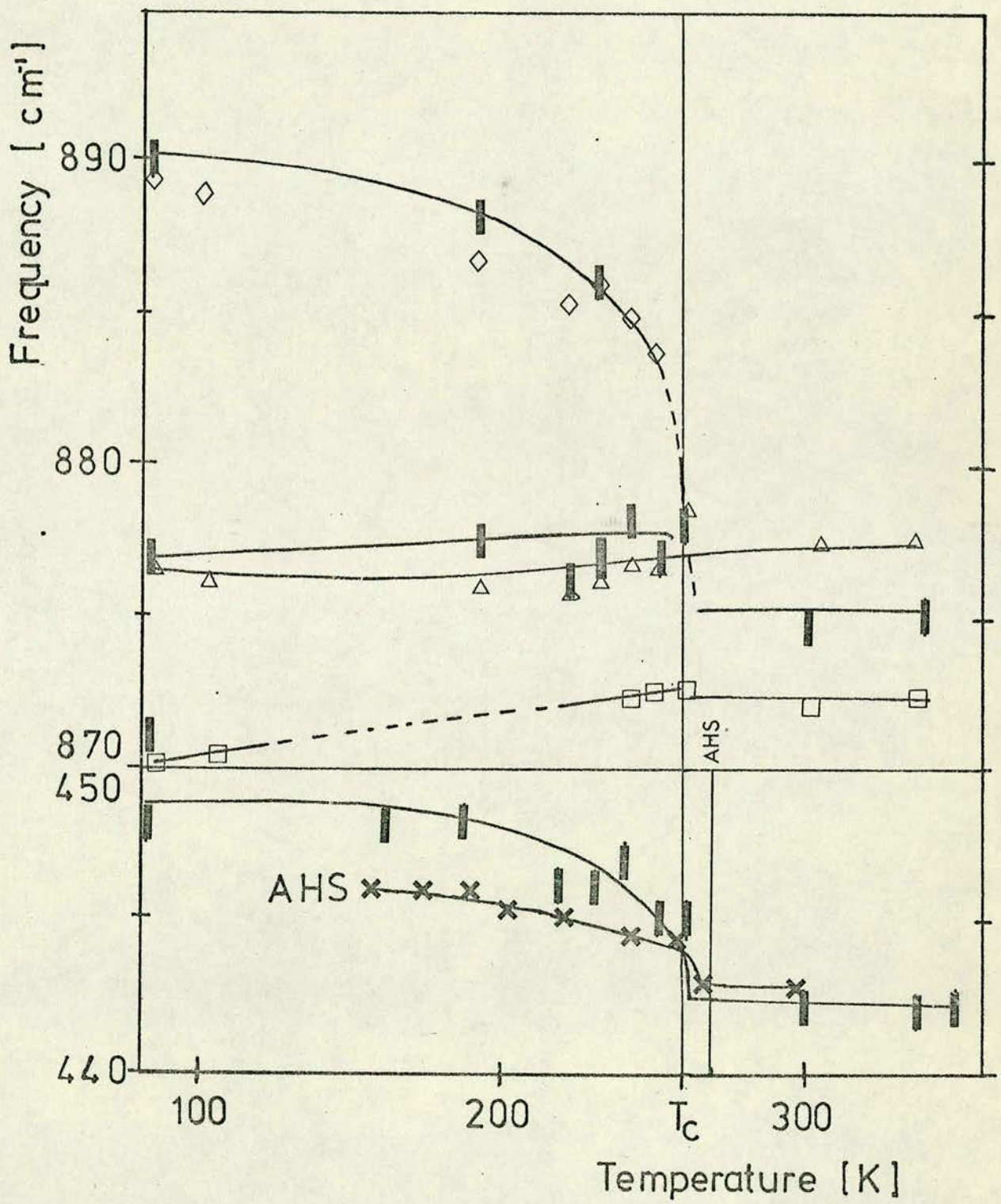
Frequency [cm⁻¹]
890
880
870
450
440
AHS
AHS
100
200
T_c
300
Temperature [K]

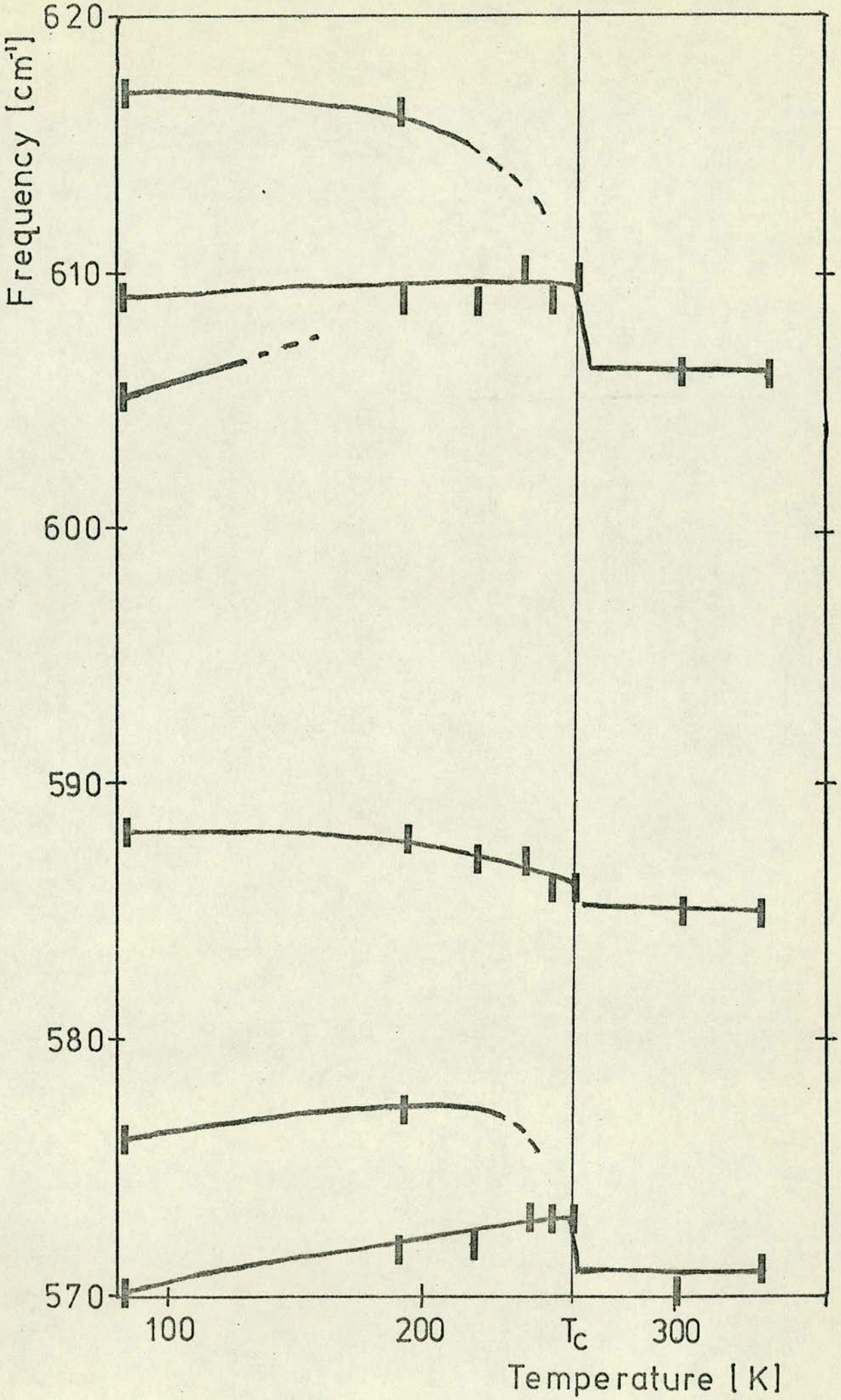
620
610
600
590
580
570
Frequency [cm⁻¹]
100
200
T_c
300
Temperature [K]

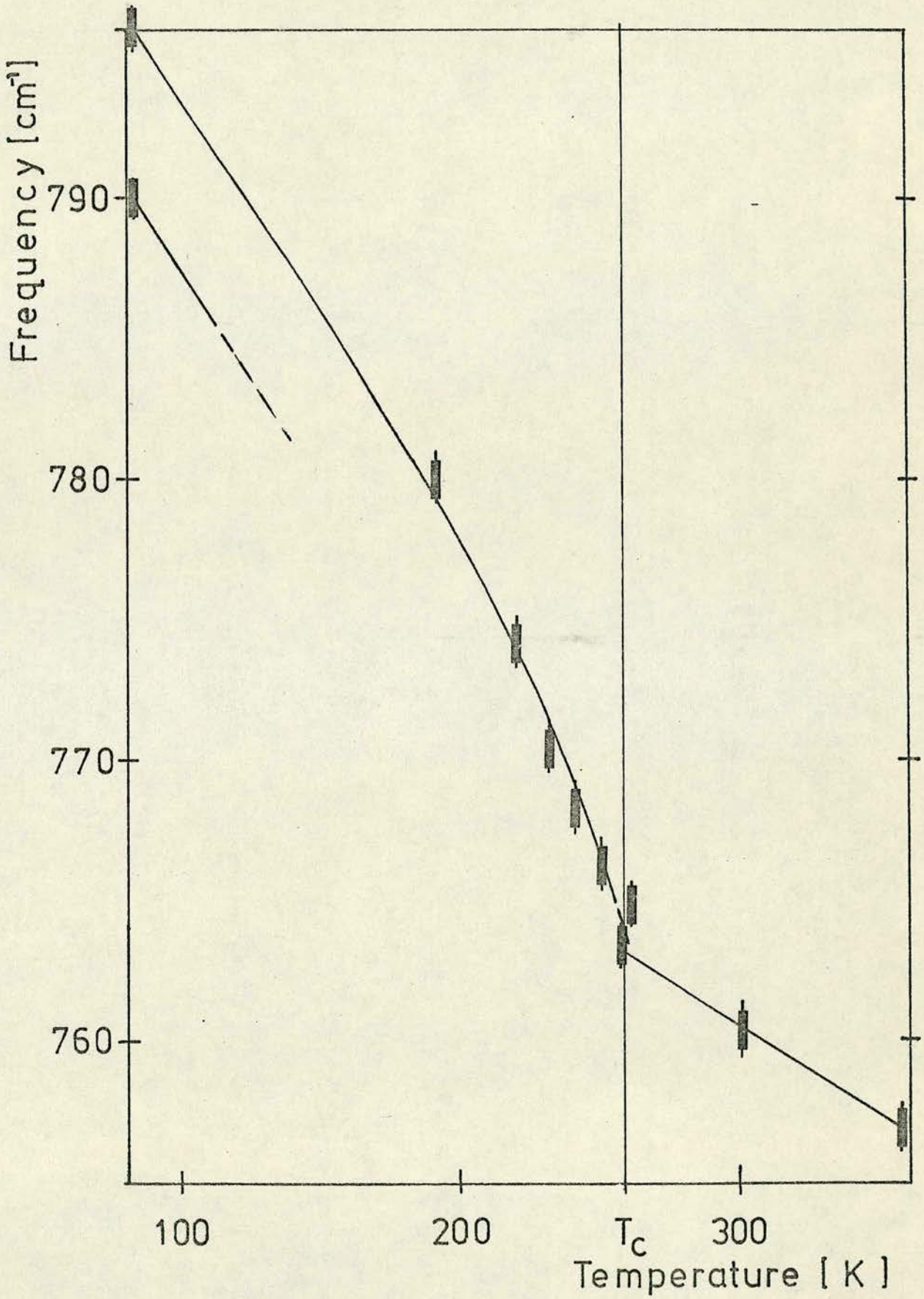
Frequency [cm⁻¹]
790
780
770
760
100
200
T_c
300
Temperature [K]

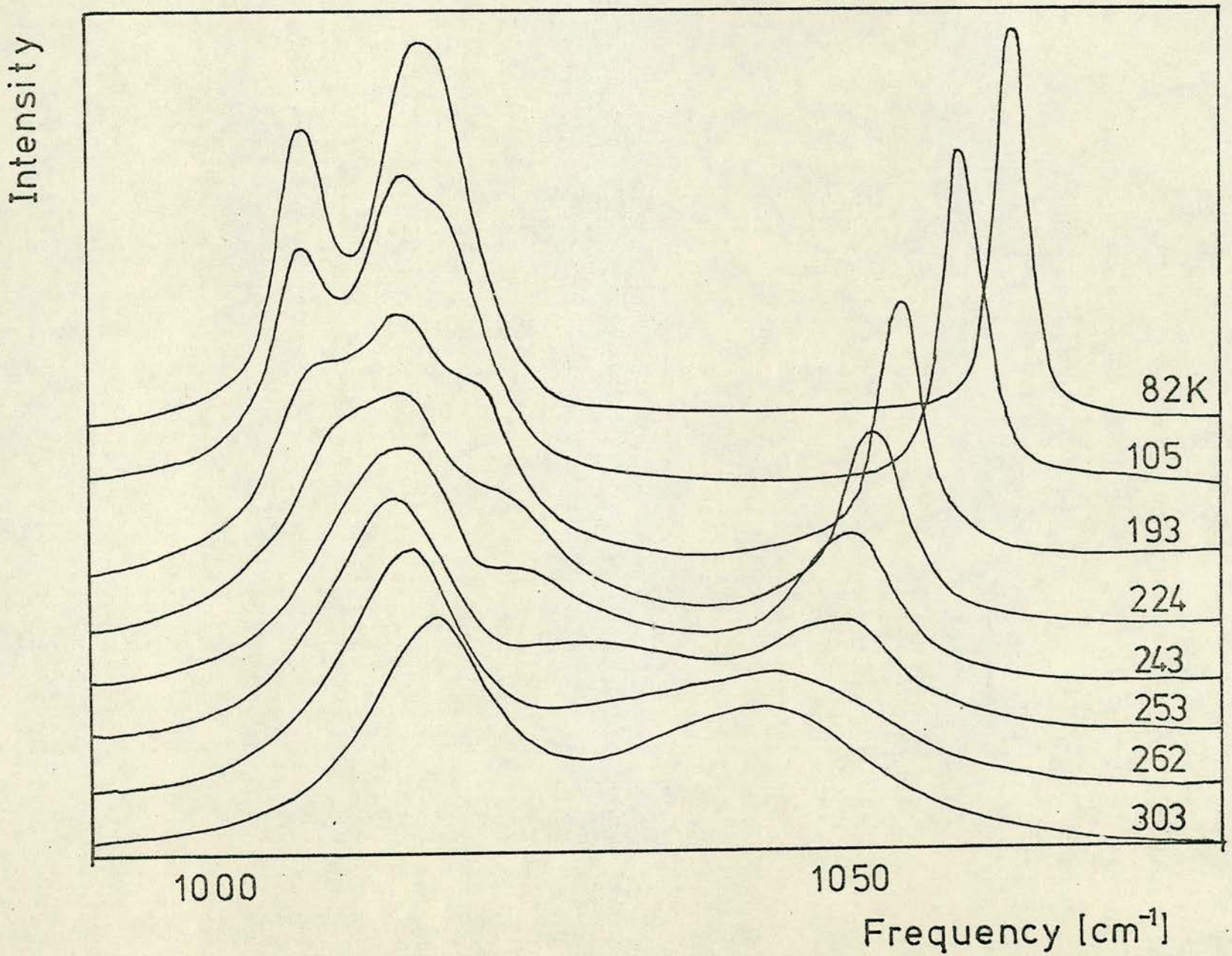
Intensity
82K
105
193
224
243
253
262
303
1000
1050
Frequency [cm^{-1}]

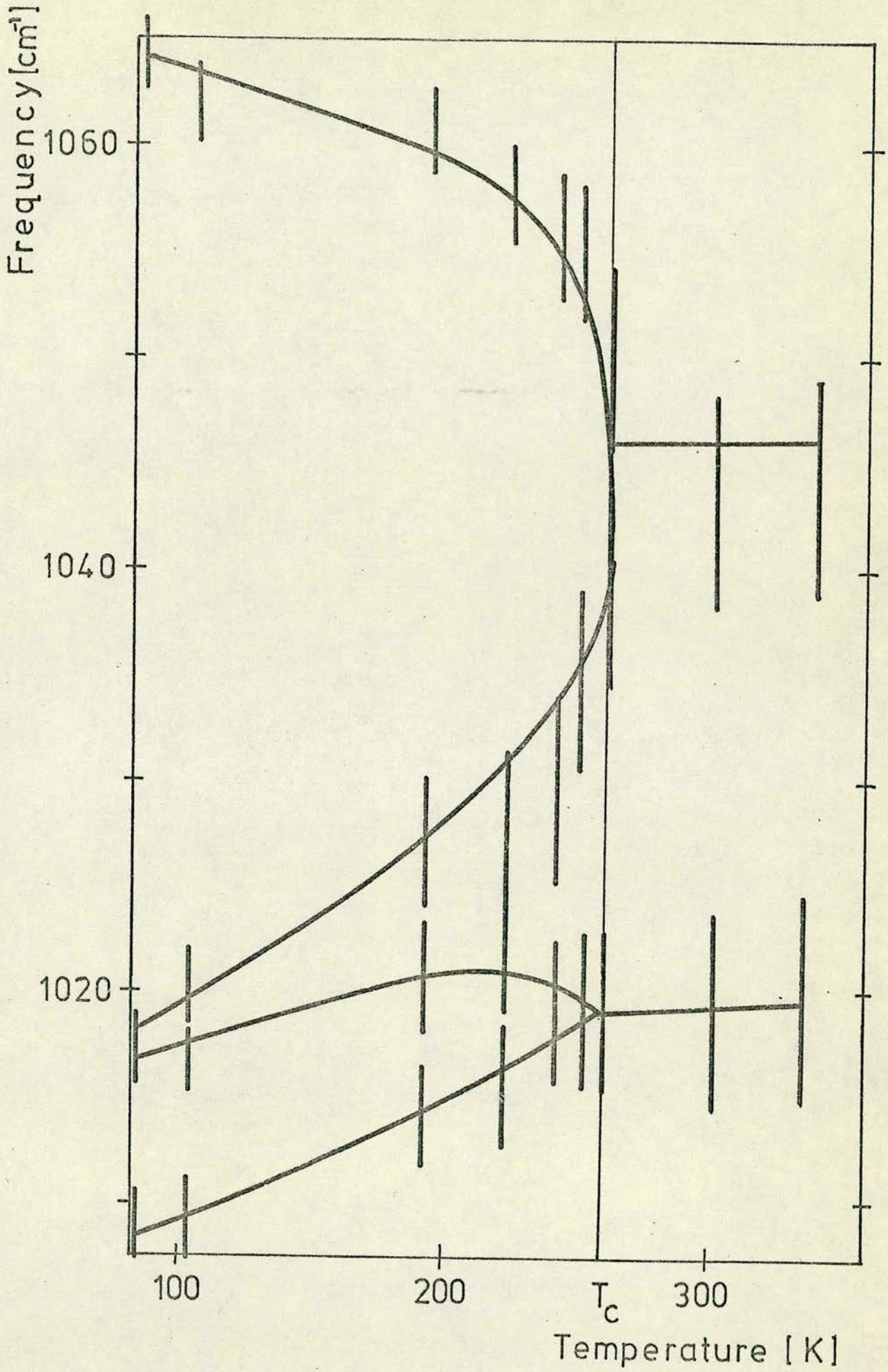
Frequency [cm⁻¹]
1060
1040
1020
100
200
T_c
300
Temperature [K]

way as to destroy all elements of symmetry, and within the crystal the vibrations of the 8 groups interact to introduce further splittings.

It is relatively easy to identify and assign these modes in RHS. In AHS more care is required because of the presence of the internal vibrations of the NH_4 group. Here RHS makes a useful comparison. The results for both AHS and RHS at room temperature are summarised in Table 6(I), and it is notable that the internal vibration frequencies of the HSO_4 ion are very similar.

6.6.1 Temperature dependence

We are interested in the temperature dependence of the HSO_4 group internal modes in as much as they may reflect the development of the ferroelectric phase within the crystal. For RHS data was taken for all the HSO_4 modes in the yy spectrum lying between 400 and 1100 cm^{-1} and over the temperature range 82K to 336K. It was found that all of these modes do reflect to some extent the onset of the ferroelectric phase, showing in some cases marked splittings and intensity changes. Some of the smaller splittings no doubt occur as a natural consequence of decreasing the temperature. The form of the more marked splittings, Figures 6.26 - 6.30, does relate to the transition and it is most probably LO-TO splitting induced as the modes become infrared active. To see this we can examine the equations of Cochran, reference (60), equations (1.12) and (1.13), for a simple dipolar mode in a simple cubic crystal. We write these in the form

$$\omega_{LO}^2 = \omega_o^2 \left(1 + 2\left(\frac{Z}{Z_o}\right)^2\right) \qquad (6.4)$$

$$\omega_{TO}^2 = \omega_o^2 \left(1 - \left(\frac{Z}{Z_o}\right)^2\right) \qquad (6.5)$$

where Z is an effective charge which reaches a constant value much smaller than Z_o far below T_c, and vanishes above T_c. We assume that Z behaves in a similar fashion to P_s, so that $Z^2 \sim T_c - T$ just below T_c. We then have for the splitting:

$$\omega_{LO} - \omega_{TO} \doteq \frac{3}{2} \omega_o \left(\frac{Z}{Z_o}\right)^2 \qquad (6.6)$$

and ω_{LO} should be twice as far from ω_o as ω_{TO}. This kind of behaviour is demonstrated, at least qualitatively, by the modes at 570, 607, 875, 1019 and 1046 cm^{-1}, Figures 6.26 - 6.30. The finite linewidth, however, makes it difficult to see what is happening until the modes have split well apart, and over a larger temperature range normal temperature effects predominate.

One feature of the spectrum which changes very little is the ν_2 line at 443 cm^{-1}. It appears to remain a single line well described by a Lorentzian lineshape at all temperatures. Neither does its linewidth show any anomalous behaviour, being quite nearly linearly temperature dependent.

Lastly, it was thought important to observe the temperature dependence of the hydrogen bond frequencies. These appear as broad, weak bands at 760, 1205 - 1255 and 2400 - 3000 cm^{-1}, Figures 6.8, 9, 12, and 13. Of these, only the one of lowest frequency shows any significant temperature dependence, Figure 6.28, increasing in frequency, eventually to about 795 cm^{-1}, and correspondingly decreasing in linewidth from 40 cm^{-1} to 12 cm^{-1} at 82K. This band is always asymmetric, but no actual structure is seen, except near 82K, at which temperature the width is small enough to show two distinct bands. None of these bands seems to show any major effect specific to the transition,

lending weight to the theory that the protons play no major role[69], [73]. The internal modes visible in the xy, xz and yz spectra have also been measured at room temperature and 104K, and they are shown along with the others in Figures 6.14 - 6.23.

6.7 The Scattering at Low Frequency

From the outset the low frequency scattering was the main point of interest. In KDP it is characterised, in the B_2 spectrum, by an overdamped wing on the Rayleigh line. As the temperature is decreased towards T_c the linewidth of this line decreases and vanishes at a temperature near T_c, consistent with an overdamped soft mode or tunnelling mode. In AHS and RHS we expect about 18 lattice vibrations in a spectrum of any given symmetry, with this number being doubled below T_c. This large number of modes gives a pessimistic outlook on the possibility of making any kind of analysis such as in KDP, unless there is some kind of dominating feature in the spectrum which shows an obvious link with the transition. Further, a ferroelectric mode is polar, and would have symmetry B_u above the transition point. This mode is not then Raman active in the high temperature phase. If the structure of the low temperature phase is still close to one having a centre of inversion, then this mode will be only a weak feature of the low temperature spectrum. And lastly, should the situation be like that of $NaNO_2$, with the ferroelectric fluctuations being very slow, Raman scattering will not resolve the ferroelectric mode.

Interestingly, however, the initial data on AHS, Figure 6.2, showed Rayleigh wing features, prominently in the yy

FIGURE 6.31

The low frequency yy spectrum of RHS in the range 7 - 200 cm^{-1} at various temperatures. Note the development of the wing feature as the temperature increases.

FIGURE 6.32

The peak positions in the yy lattice vibration spectrum of RHS plotted out as a function of temperature. The wing is indicated by a bar extending from zero frequency.

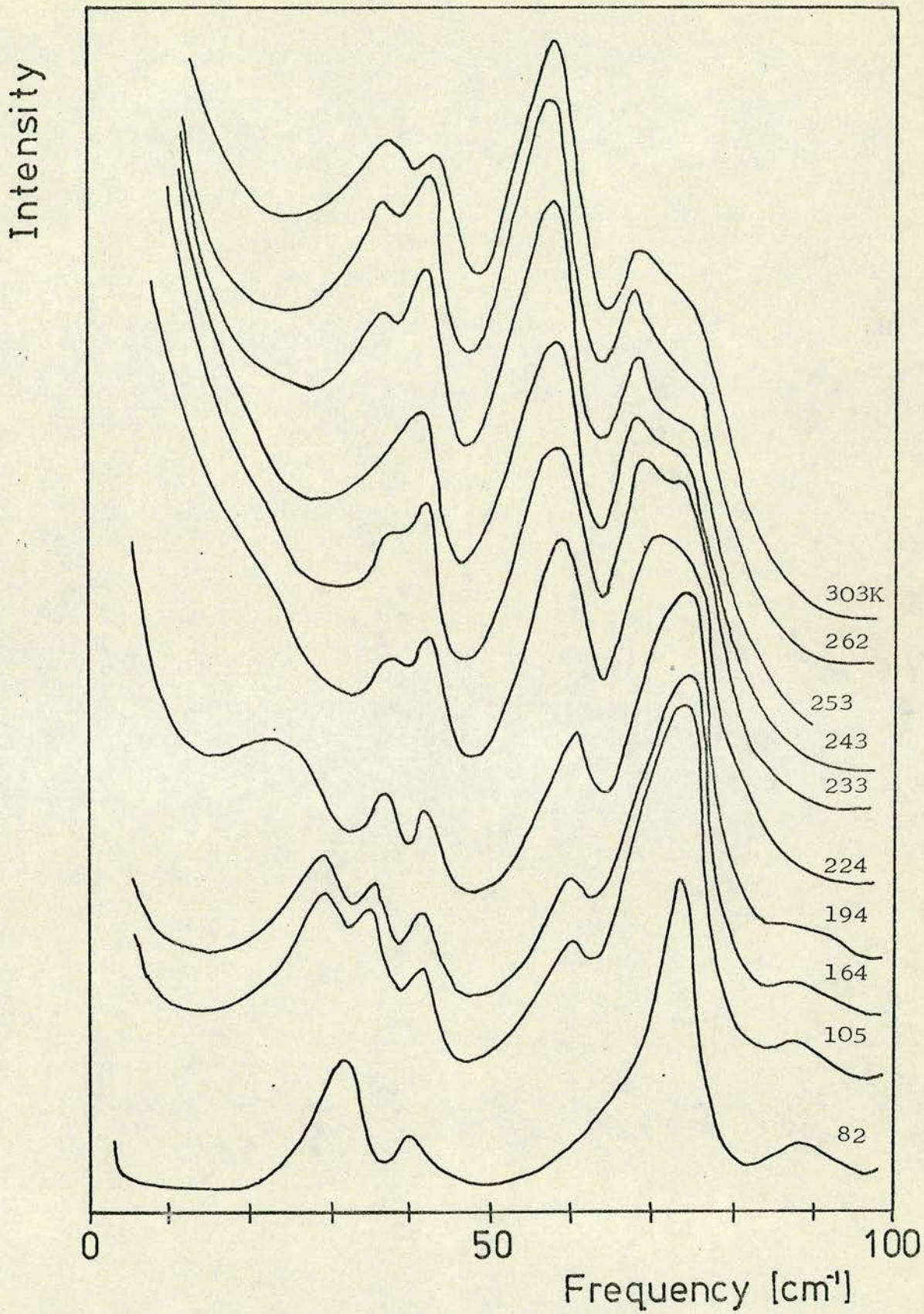
Intensity
303K
262
253
243
233
224
194
164
105
82
0
50
100
Frequency [cm⁻¹]

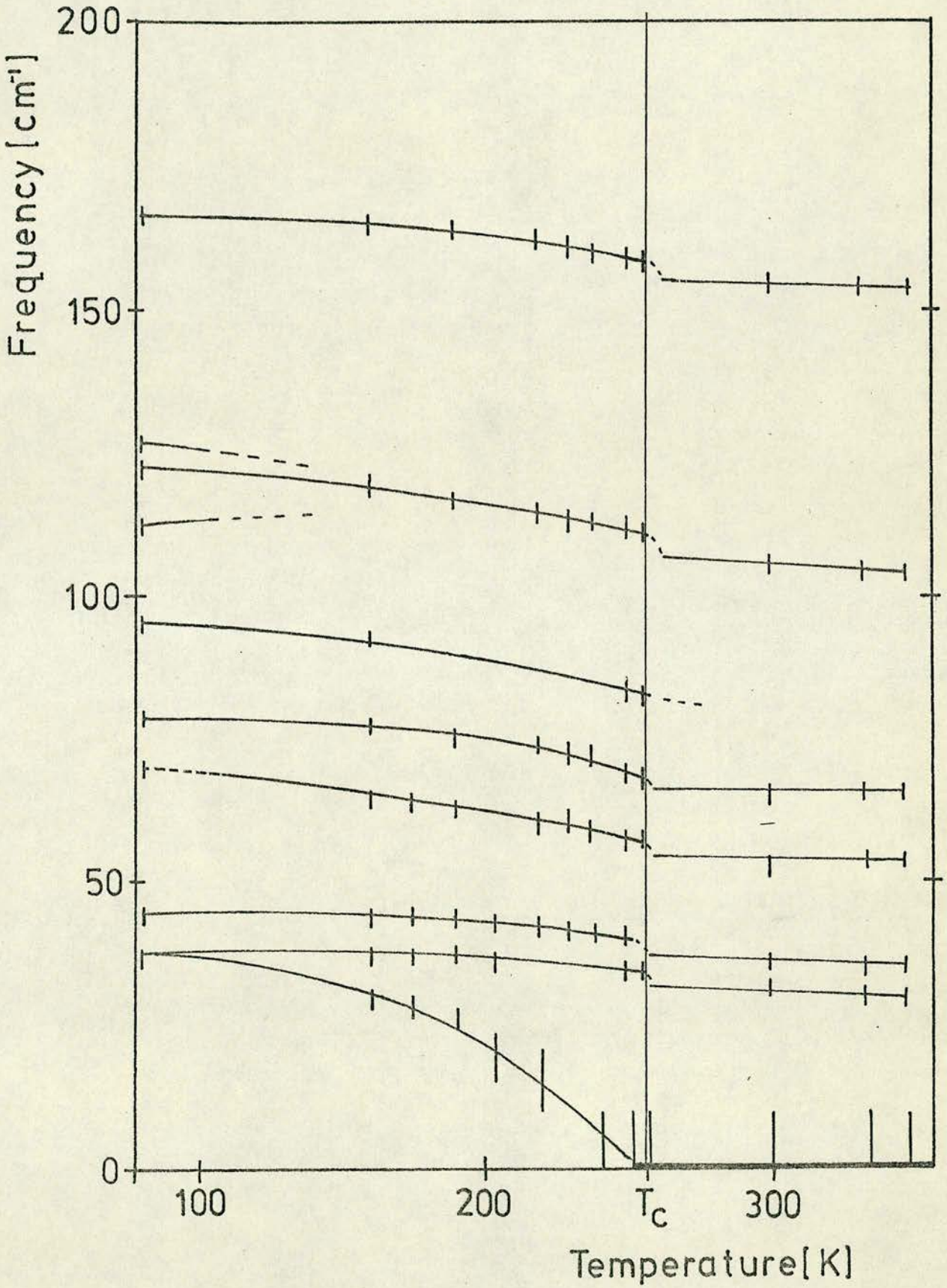
200
150
100
50
0
Frequency [cm⁻¹]
100
200
T_c
300
Temperature [K]

FIGURE 6.33

A demonstration of the temperature dependence of the wing feature in RHS.

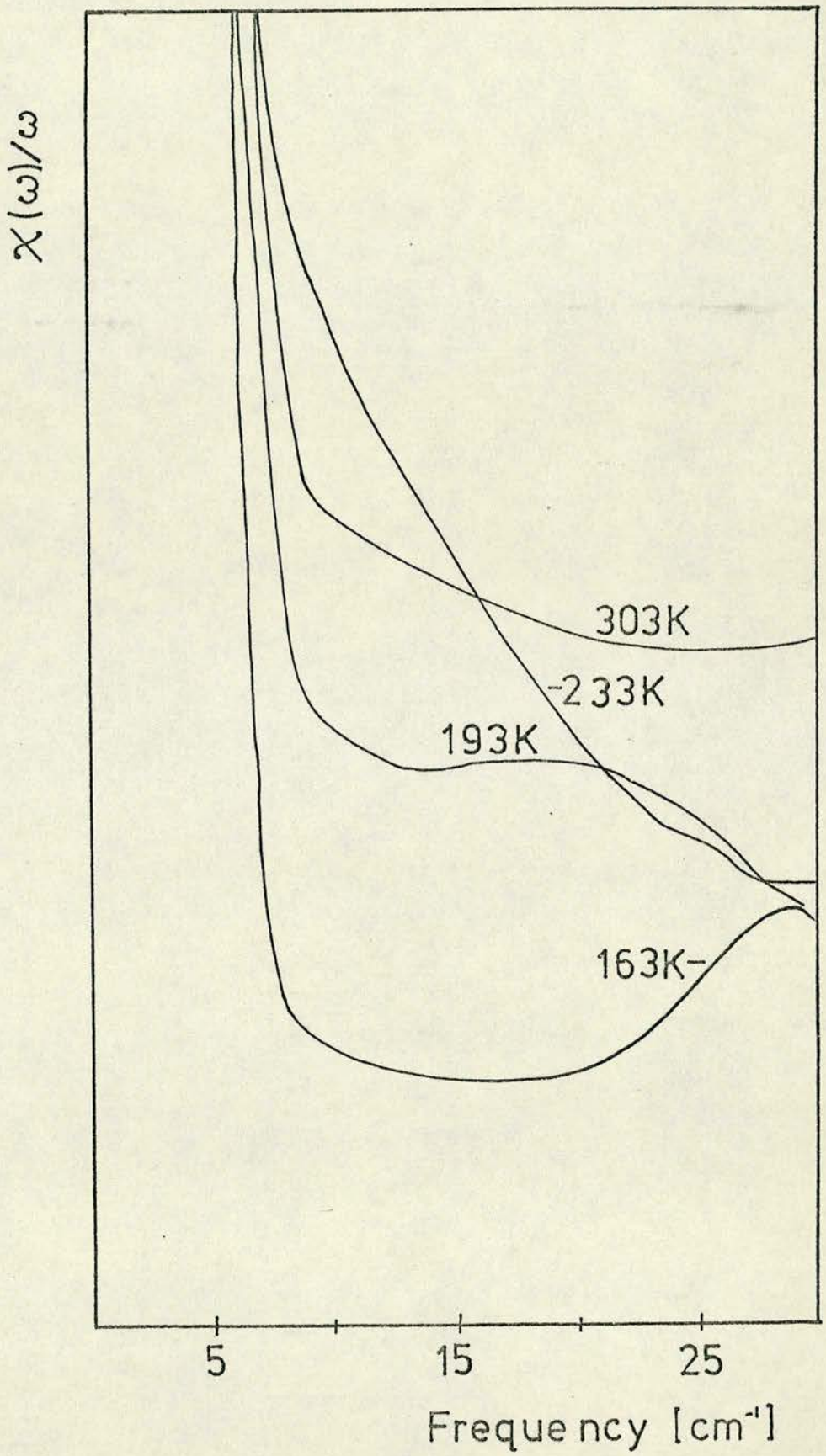
χ(ω)/ω
303K
233K
193K
163K
5
15
25
Frequency [cm⁻¹]

FIGURE 6.34

Fit to the yy spectrum in RHS at 238K over the range 7 - 25 cm^{-1} with a Debye formula.

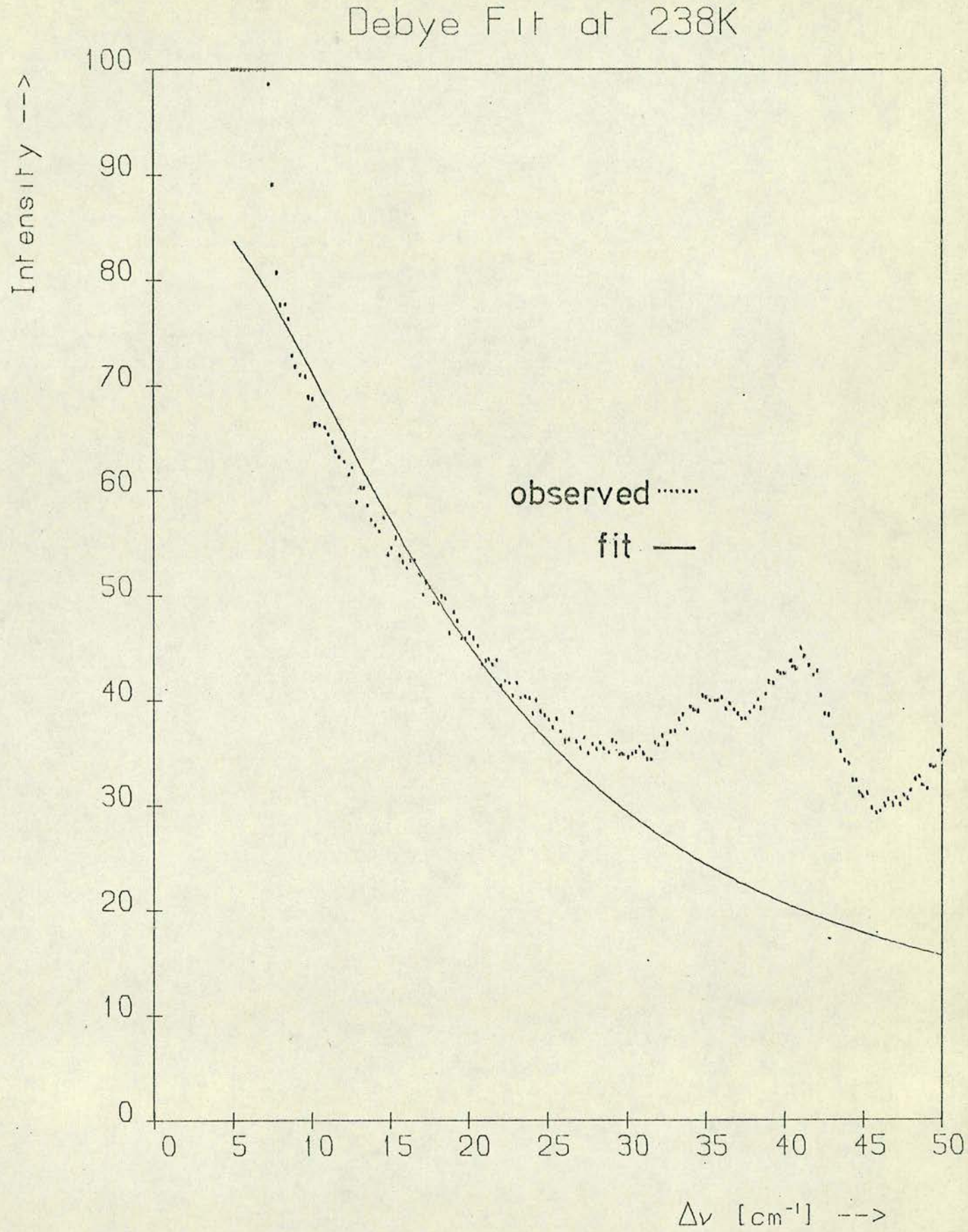
Debye Fit at 238K
Intensity -->
100
90
80
70
60
50
40
30
20
10
0
observed
fit
0
5
10
15
20
25
30
35
40
45
50
Δν [cm⁻¹] -->

spectrum. For this reason a detailed study was made of the yy spectrum in RHS, and new data was taken for AHS. We now discuss our findings in RHS.

The room temperature yy spectrum of RHS, Figure 6.10 , shows 6 distinct peaks at low frequency on broad coalescing features. In addition, there is a large amount of scattered intensity near zero frequency. As the temperature is reduced below T_c, the intensity of the low frequency scattering begins to disappear, and below 190K it appears to give way to an underdamped mode, Figures 6.31 and 6.32. As the temperature is brought down to 82K, this mode increases in frequency and finally coalesces with a mode at 36 cm^{-1}. In order to make a comparison between spectra at various temperatures, $\eta\,\chi''(\omega)/\omega$, which we define as $\mathcal{I}(\omega)/(\hbar\omega(n(\omega)+1))$, was plotted against frequency. $\mathcal{I}(\omega)$ is the experimentally measured spectrum and η is a scale factor chosen so that $\int \chi''(\omega)/\omega\, d\omega$ over the stable line at 443 cm^{-1} is constant. This effectively standardises intensities, and removes the temperature dependence due to the population factor. Comparing these plots, some of which are shown in Figure 6.33, we note a considerable temperature dependence (which is not due to the usual population factor). The intensity of this low frequency scattering is always increasing. Attempts to fit the lineshape of this scattering did not give encouraging results, but in the temperature range 220 to 250K a Debye function of the form:

$$\mathcal{I}(\omega) = \eta\,(n(\omega)+1)\,\frac{\omega}{\omega^2+\Gamma^2} \qquad (6.7)$$

gave a reasonable description over the small region 10 - 30 cm^{-1}, Figure 6.34, Γ varied weakly with temperature, having a value of about 20 cm^{-1}. No actual connexion with the phase transition

FIGURE 6.35

Contributions to the low frequency scattering intensity on RHS from the ranges 7 - 90 cm^{-1} and 90 - 250 cm^{-1}

▌ 7 - 90 cm^{-1}

● 90 - 250 cm^{-1}

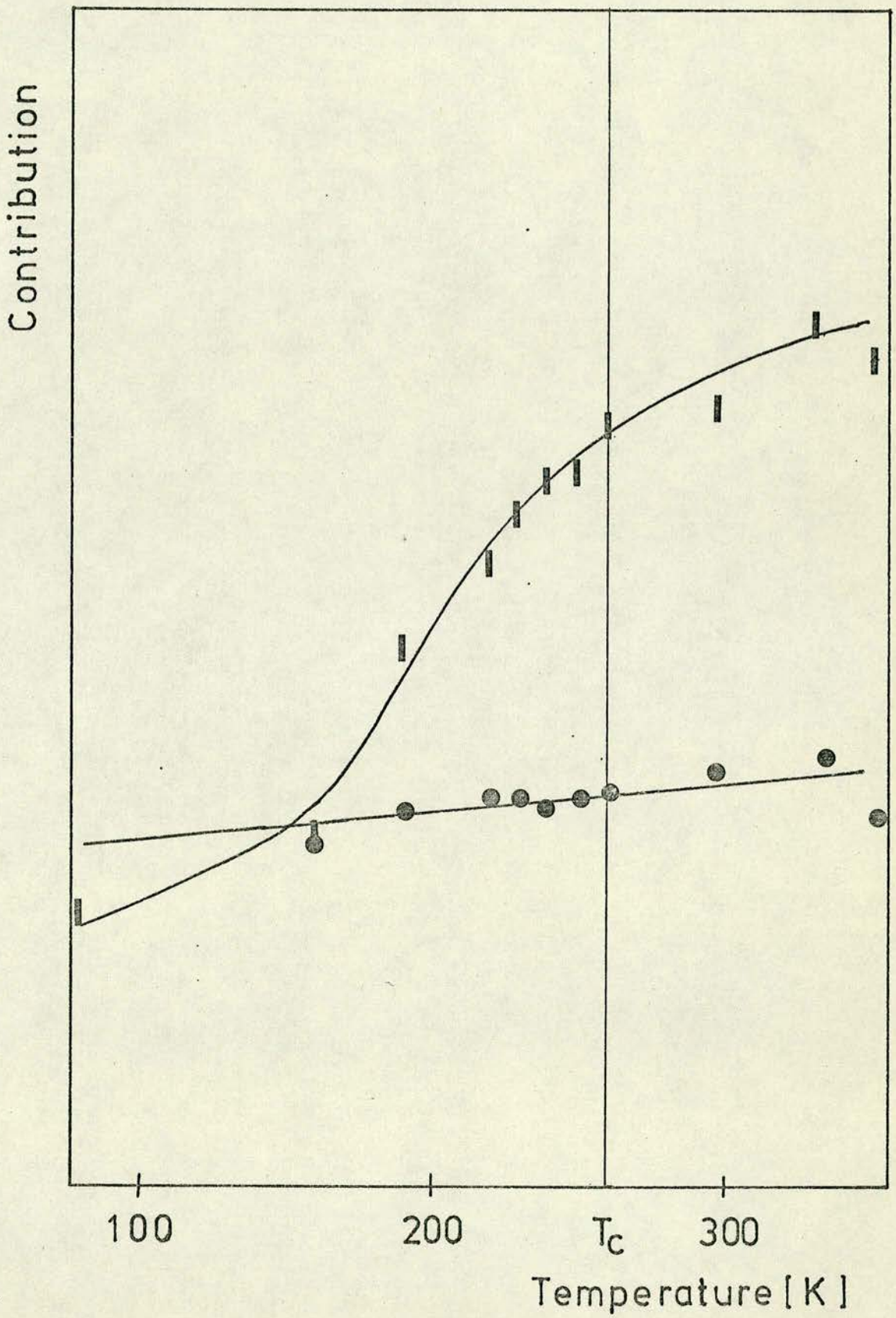
Contribution
100
200
T_c
300
Temperature [K]

could be detected. This null result is intriguing.

To further pursue the nature of this scattering the values of $\chi'(0)$, defined as $\int \frac{\chi''(\omega)}{\omega} d\omega$, integrated over the low frequency range 7 - 90 cm^{-1} were calculated. 7 cm^{-1} was the closest frequency to the exciting line attainable, and 90 cm^{-1} was reckoned to be the limit of the low frequency scattering. By comparison with the Kramers-Kronig relations[11], $\chi'(0)$ thus defined is an estimate of the response at zero frequency attributable to the observed low frequency scattering. The result is shown in Figure 6.35. For comparison, the integral over the rest of the region, 90 - 250 cm^{-1} is plotted. This once more illustrates the growing intensity of the low frequency scattering, but yet again nothing specific to the phase transition is found.

Another unusual feature is the peak at 52 cm^{-1} at room temperature. This has an anomalous temperature dependence, losing intensity as the temperature decreased. Finally at 82K it cannot be seen in the spectrum. There are too many nearby peaks in the spectrum, one with a highly asymmetric line shape, to allow this mode to be singled out for analysis. We could guess, however, that this peak originates from second order scattering, as could no doubt the scattering at low frequency. In view of the fact that the HSO_4 ions must move in a highly anharmonic potential - a double well - such an explanation is not unlikely. For second order scattering, two phonons contribute and from any point in the Brillouin zone. The conservation of wavevector (1.44) and of energy gives the conditions:

$$0 = \pm \underline{Q}_1 \pm \underline{Q}_2 \qquad (6.8)$$

$$\omega_o \pm \omega_s = \pm\omega_1 \pm\omega_2 \quad . \qquad (6.9)$$

In the limit of one mode being of very low frequency, $\omega_1 \gg \omega_2$, we have $\omega \sim \omega_1$ and the process looks like first order scattering, but with the selection rule $\underline{Q}_1 = 0$ being broken. Although large motions, as of the HSO_4 ions, cannot be considered as true phonons, equations (6.8) and (6.9) still apply in a more general treatment, for example using a spin formalism.

When the ferroelectric fluctuations are very slow the second order scattering process is equivalent to disorder induced scattering away from $\underline{Q} = 0$. This kind of process may well apply here, and of course one would expect the intensity of the scattering to increase with the amount of disorder, that is to increase as T_c is approached from below and then to level off. This seems not inconsistent with what is actually observed. In addition, there will be order-disorder modes of the HSO_4 ions which need not be ferroelectric. With four disordered SO_4 (1_D) groups in the primitive cell, only one mode, that of B_u symmetry above T_c, would be ferroelectric, but it would be the one of A_g symmetry which would be visible in our experiment. It may be that the scattering is associated with such a mode, which need not actually reflect the ferroelectric phase transition but is still characteristic of the degree of SO_4 group disorder.

AHS shows a similar low frequency spectrum with a prominent Rayleigh wing, Figure 6.6. The intensity under this wing diminishes on cooling, as in RHS. At 156K, which is close to

the lower order transition, there is still some remaining intensity, Figure 6.7. A small peak at 35 cm^{-1} is discernible, but it does not seem as though this mode actually arises out of the low frequency wing.

Because we cannot decrease the temperature further without the risk of shattering the crystal at the first order transition, it is not possible to follow this further.

6.8 Conclusion

We have found evidence of temperature dependent splittings in the internal modes on passing into the ferroelectric phase in RHS. This has also been observed for the ν_3 internal mode of the SO_4 group in AHS[47], [68], and we assume that here the other modes behave similarly. It would appear that the hydrogen-bond modes change little at the transition.

There is intense scattering at low frequency in the A_g (yy) spectrum, and a similar feature is evident in the B_g(xy) spectrum, but we can find no definite bearing on the ferroelectric phase transition; neither can we give a definite explanation of its origin. It may be feasible with additional data to perform a lineshape analysis on this feature in the domain where it is not too greatly damped, below 240K, to examine whether or not it truly has the characteristics of a soft mode.

As a trial of the automatic scanning and data collection technique the experiments carried out in this work provided a stiff test.

Data processing was found to be a major task which would have been virtually impossible without the great flexibility of the various computer processing routines.

REFERENCES

(1) Tinkham, M., 'Group Theory and Quantum Mechanics', (McGraw-Hill, New York), 1964.

(2) Nye, J.F., 'Physical Properties of Crystals', (Clarendon, Oxford) 1957.

(3) Born, M. and Huang, K., 'The Dynamical Theory of Crystal Lattices' (Clarendon, Oxford), 1957.

(4) Brillouin, L., 'Wave Propagation in Periodic Structures' (McGraw-Hill, New York) 1946.

(5) Kittel, C., 'Introduction to Solid State Physics' (Wiley, New York) 1966.

(6) Ziman, J., 'Principles of the Theory of Solids' (Cambridge, London) 1964.

(7) Cowley, R.A., in 'Phonons in Perfect Lattices and in Lattices with Point Imperfections', ed. R.W.H. Stevenson, (Oliver & Boyd, Edinburgh), 170 (1966).

(8) Raman, Sir C.V., Indian J. Phys. 2, 387 (1928).

(9) Landsberg, G. and Mandelstam, L., Naturwiss. 16, 557, 772 (1928).

(10) Placzeck, G., 'Hanbuch der Radiologie', ed. E. Marx, (Akademische Verlagsgesellschaft, Leipzig) Vol. 6, Part 2, 205 (1934) - UCRL Transl. No. 526(L), 1959.

(11) Yariv, A., 'Quantum Electronics' (Wiley, New York) 1967.

(12) Eckhardt, G., Helwarth, R.W., McClung, F.J., Schwarz, S.E., Weiner, D. and Woodbury, E.J., Phys. Rev. Letters 9, 445 (1962).

(13) Loudon, R., Proc. Roy. Soc. 275, 218 (1963).

(14) Loudon, R., Adv. Phys., 13, 423 (1964).

(15) Arthur, J.W. and Lockwood, D.J., J. Raman Spectrosc. 2, 53 (1974).

(16) Loudon, R., 'The Quantum Theory of Light' (Clarendon, Oxford) 1973.

(17) Lockwood, D.J. and Torrie, B.H,, in 'Anharmonic Lattices, Structural Transitions and Melting', ed. T. Riste (Noordhoff, Leiden), 147 (1974).

(18) Torrie, B.H., and Lockwood, D.J., Ferroelectrics 7 (1974) in press.

REFERENCES (Contd.)

(19) Lockwood, D.J. and Torrie, B.H., J. Phys. C. 7, 2729 (1974).

(20) Taylor, W., private communication.

(21) Arthur, J.W. and Mackenzie, G.A., J. Raman Spectrosc. 2 (1974) in press.

(22) Pawley, G.S., 'Thermal Scattering of X-Rays' (Ph.D. Thesis, Cambridge) 1962.

(23) Cochran, W. and Pawley, G.S., Proc. Roy. Soc. A 280, 1 (1964).

(24) Pawley, G.S., Phys. Stat. Sol. 20, 347 (1967).

(25) Reynolds, P.A., Kjems, J. and White, J.W., in 'Proc. Symposium on Inelastic Neutron Scattering' (International Atomic Energy Agency, Vienna), 1972.

(26) Powell, B.M., Dolling, G., Piseri, L. and Martel, P. in 'Proc. Symposium on Neutron Inelastic Scattering' (International Atomic Energy Agency, Vienna), 1972.

(27) Dolling, G., Pawley, G.S. and Powell, B.M., Proc. Roy. Soc. Lond. A 333, 363 (1973).

(28) Ito, M., Suzuki, M. and Yokoyama, T., in 'Excitons, Magnons and Phonons in Molecular Crystals', ed. A.B. Zahlan (Cambridge, London), 1 (1968).

(29) Cowley, R.A., Proc. Phys. Soc. 84, 281 (1964).

(30) Bruce, A.D. and Cowley, R.A., J. Phys. C., 5, 595 (1972).

(31) Pawley, G.S. and Rinaldi, R.P., Acta Cryst. B28, 3605 (1972).

(32) Rinaldi, R.P and Pawley, G.S., Nuovo Cimento, 16B, 55 (1973).

(33) Pawley, G.S., Rinaldi, R.P. and Windsor, C.G. in 'Phonons', Proceedings of the International Conference, Rennes, ed. M.A. Nusimovici (Flammarion, Paris) 223 (1971).

(34) Rinaldi, R.P., 'The Dynamics of Molecules in Crystals: Orthorhombic Sulphur', (Ph.D. Thesis, Edinburgh), 1973.

(35) Rinaldi, R.P., to be published.

(36) Montgomery, H., Proc. Roy. Soc. A309, 521 (1969).

(37) Krishnamurti, P., Ind. J. Phys. 5, 105 (1930).

(38) Ozin, G.A., J. Chem. Soc. A, 116 (1969).

(39) Scott, D.W. and McCullough, J.P., J. Mol. Spectrosc. 13, 313 (1964).

REFERENCES (Contd.)

(40) Anderson, A., and Loh, Y.T., Can. J. Chem. 47, 879 (1969).

(41) Cowley, R.A., Acta Cryst. 15, 687 (1962).

(42) Neronova, N.N., Zh. Strukt. Khim. 9(1), 147 (1968) (Translation).

(43) Almenningen, A., Hartmann, D.A. and Seip, H.M., Chemica Scandinavica 22, 1013 (1968).

(44) Steele, D., Spectrochim. Acta, 25A, 959 (1969).

(45) Steele, D., Nanney, T.R. and Lippincott, E.R., Spectrochim. Acta 22, 849 (1965).

(46) Cowley, R.A., in "The Raman Effect", Volume 1, ed. A. Anderson (Dekker, New York) 1971.

(47) Arthur, J.W., Lockwood, D.J. and Taylor W., in 'Advances in Raman Spectoscopy', Volume 1, ed. J.P. Mathieu (Heyden, London) 144 (1973).

(48) Arthur, J.W. and Taylor, W., Ferroelectrics 7, (1974), in press.

(49) Pepinsky, R., Vedam, K., Hoshino, S. and Okaya, Y., Phys. Rev. 111, 1508 (1958).

(50) Pepinsky, R. and Vedam, K., Phys. Rev. 117, 1802 (1960).

(51) Miller, S.R., Blinc. R., Brenman, M. and Waugh, J.S., Phys. Rev., 126(2), 528 (1962).

(52) Bacon, G.E. and Pease, R.S., Proc. Roy. Soc. A220, 379 (1952) and A230, 359 (1955).

(53) Slater, J.C., J. Chem. Phys. 9, 16 (1941).

(54) Blinc, R.J., J. Phys. Chem. Solids 13, 204 (1960).

(55) Tagaki, U., J. Phys. Soc. Japan, 24, 497 (1948).

(56) Tokunaga, M., Progr. Theor. Phys. 35, 581 (1966). and
Tokunga, M. and Matsubara, T., Progr. Theor. Phys. 36, 857 (1966).

(57) Cochran, W., Adv. Phys. 10, 401(1960).

(58) Kobayashi, K.K., J. Phys. Soc. Japan 24, 497 (1968).

(59) Sona, F. and Shirane, G., 'Ferroelectric Crystals', (Pergamon Press, London) 1962.

(60) Cochran, W., Adv. Phys. 9, 387 (1960).

REFERENCES (Contd.)

(61) Sawada, S, Normura, S., Fujii, S. and Yoshida, I., Phys. Rev. Letters 1, 320 (1958).

(62) Sakurai, J., Cowley, R.A. and Dolling, G., J. Phys. Soc. Japan 28(6), 1426 (1970).

(63) Fujii, Y. and Hatta, I., J. Phys. Soc. Japan 24, 1053 (1968).

(64) Kaminow, I.P. and Damen, T.C., Phys. Rev. Letters 20, 1105 (1968).

(65) Katiyar, R.S., Ryan, J.F. and Scott, J.F., Phys. Rev. B4, 2635 (1971).

(66) Di Domenico, M, Porto, S.P.S. and Wemple, S.H., Phys. Rev. Letters 19, 855 (1967).

(67) Hartwig, C.M.,Wiener-Avnear, E., and Porto, S.P.S., Phys. Rev. B5, 79 (1972).

(68) Bazhulin, P.A., Mysasnikova, T.P. and Rakov, A.V., Sov. Phys. Solid State 5(7), 1299 (1964).

(69) Nelmes, R.J., Acta Cryst. B27, 272 (1971).

(70) Nelmes, R.J., Ferroelectrics 4, 133 (1972).

(71) Ashmore, P., to be published.

(72) Nelmes, R.J., Acta Cryst. A28, 445 (1972).

(73) Kasahara, M. and Tatsuzaki, I., J. Phys. Soc. Japan, 29, 1392 (1970).

(74) Herzberg, G., 'Molecular Spectra and Molecular Structure, II. Infrared and Raman Spectra of Polyatomic Molecules' (Van Nostrand, New York) 1945.

APPENDIX I

Circuit Diagrams for the Spectrometer Control of System 1

CONTENTS

FIGURE I.1

Basic circuits appearing in the diagrams of Appendices AI to AIII. Details of the working of the integrated circuits referred to in diagrams are to be found in: 'The TTL Data Book', Texas Instruments Limited (1973).

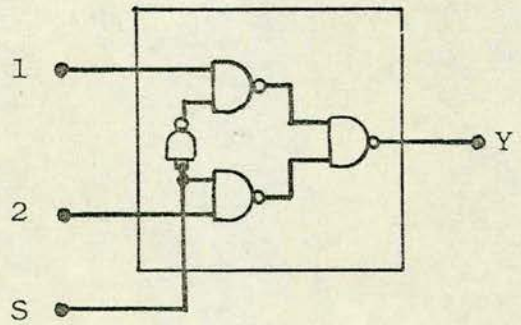

SELECTOR

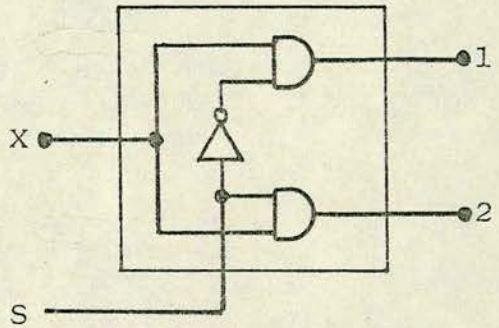

DECODER

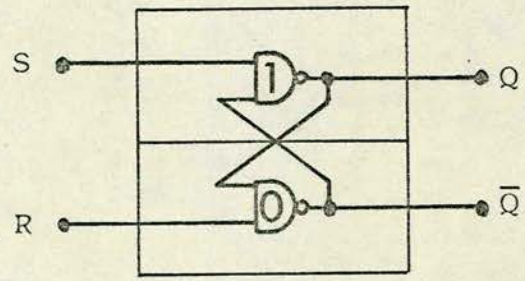

BISTABLE

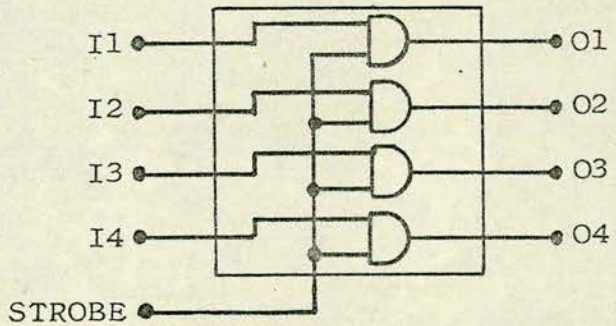

BUS GATE

FIGURE I.2

Ratemeter

LEGEND

100 Hz	-	100 Hz clock from mains
Clock 1	-	load count into storage - 50 ns pulse
Clock 2	-	reset counters - 50 ns pulse, after CLOCK 1
COUNT IN	-	photomultiplier pulses input, also to MCS
OVERLOAD	-	'1' for counts in excess of 799,999 per second
R.O.	-	output to analogue ratemeter, 0 - 100 Hz
SN7475	-	quad storage latches, both clocks connected
SN7490	-	decade counter, in divide by ten mode
SN74141	-	bcd to decimal decoder/display driver

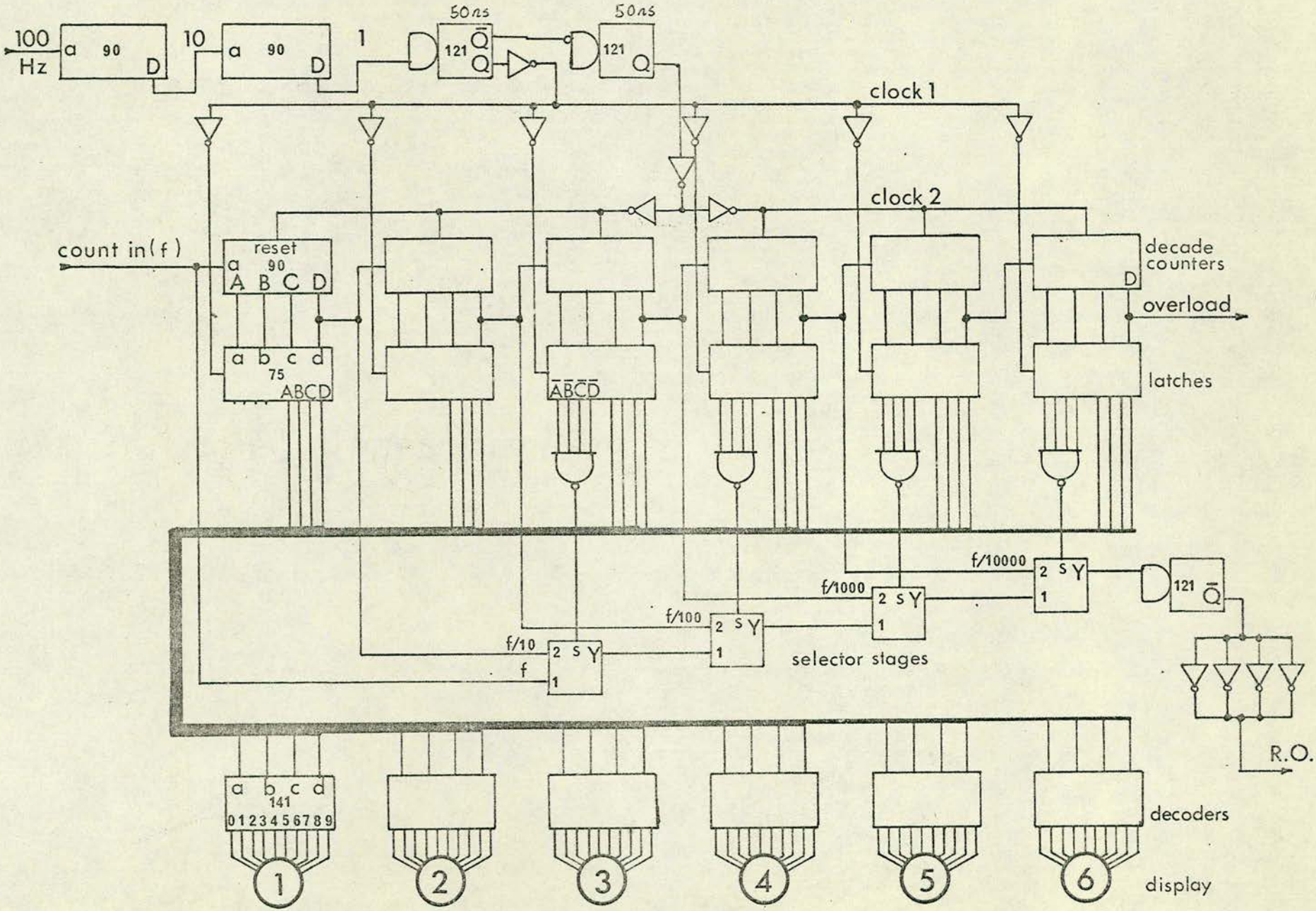
100 Hz
a 90 D
10
a 90 D
1
50ns
121 Q̄ Q
50ns
121 Q
clock 1
clock 2
count in(f)
reset
a 90
A B C D
a b c d
75
ABCD
ĀB̄C̄D
decade counters
D
overload
latches
f/10000
f/1000
f/100
f/10
f
2 S Y
1
selector stages
121 Q̄
R.O.
a b c d
141
0 1 2 3 4 5 6 7 8 9
decoders
1
2
3
4
5
6
display

FIGURES I.3.1 - I.3.3

LEGENDS

I.3.1 Scan Rate Control

COUNTER RESET LINE - '1' esets counters before scanning

FAST FORWARD - '1' prior to scanning

MOTOR CLOCK - derived from 200 Hz clock (see I.5)

MOTOR PULSES - motor stepping pulses, at .01 to .99 min/cm^{-1}

SCAN RATE - to bcd switches (1's complement)

TENS ($\overline{1},\overline{2},\overline{4},\overline{8}$) - bcd coded tens of minutes per 100 cm^{-1}

UNITS ($\overline{1},\overline{2},\overline{4},\overline{8}$) - bcd coded minutes per 100 cm^{-1}

SN74192 - decade up/down counter in count down mode

I.3.2 Channel Width Control

$\frac{1}{2}$CW - '1' selects, channel width times one half

CHANNEL CLOCK - derived from MOTOR PULSES (See I.5)

CHANNEL WIDTH ($\overline{1},\overline{2},\overline{4},\overline{8}$) - to bcd switches, (complement) for 0.1 to 1.0 cm^{-1} per channel

COUNTER RESET LINE - resets counter before scanning

STEP CHANNELS - channel stepping pulses, at selected increments

SN74192 - decade up/down counter in count down mode

I.3.3 Clock

50 Hz - 9 Vac at 50 Hz

100 Hz - 100 Hz reference for ratemeter (to I.2)

200 Hz CLOCK - System clock

SN7413 - Schmitt trigger

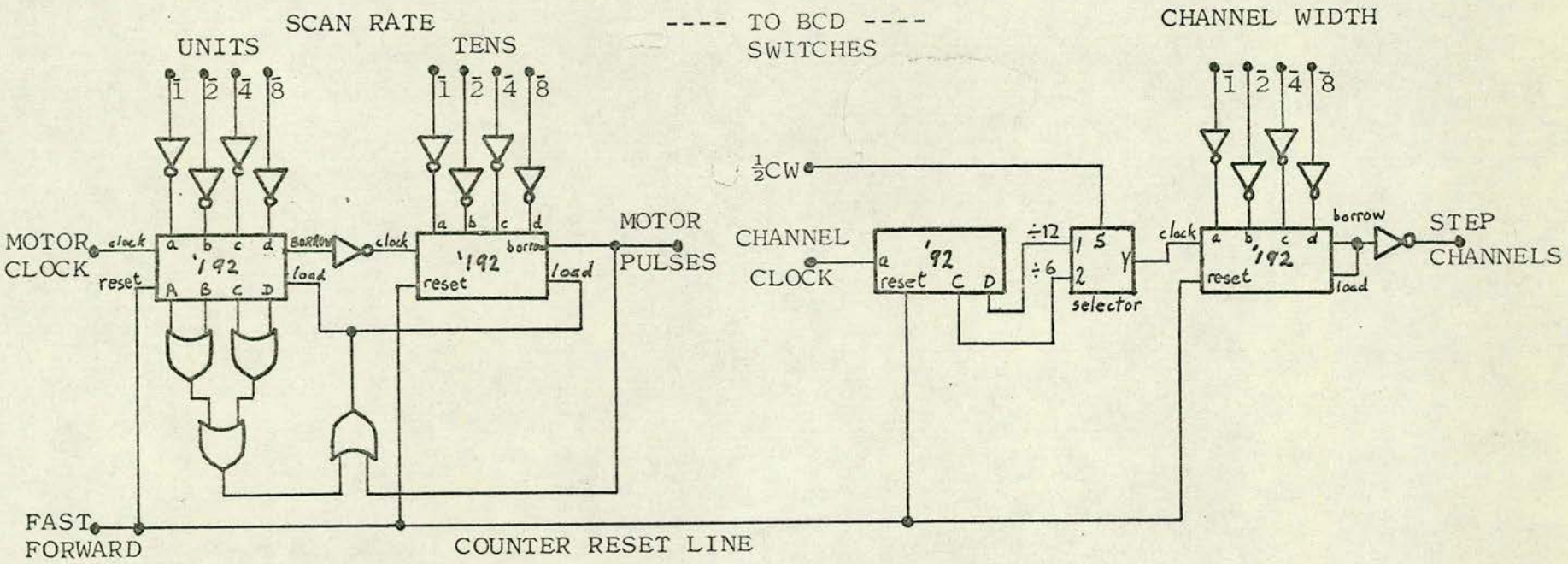
SCAN RATE
UNITS
TENS
---- TO BCD ----
SWITCHES
CHANNEL WIDTH
MOTOR CLOCK
clock
reset
'192
load
borrow
MOTOR PULSES
½CW
CHANNEL CLOCK
÷12
÷6
selector
STEP CHANNELS
FAST FORWARD
COUNTER RESET LINE

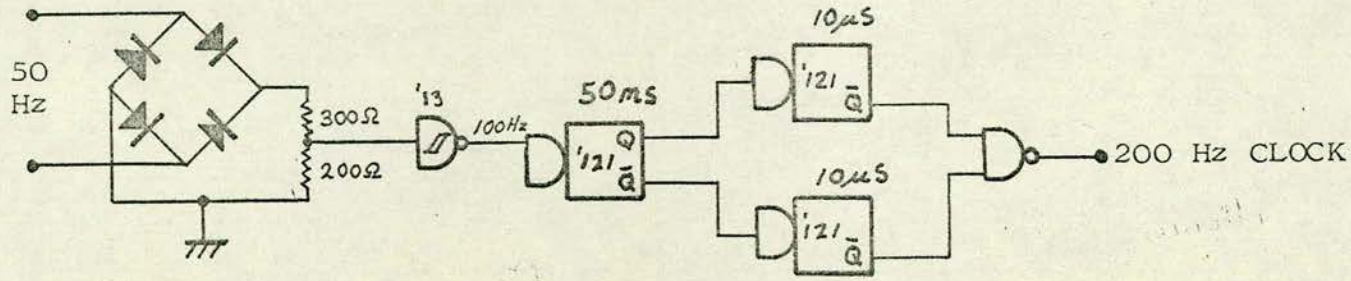
50 Hz
300Ω
200Ω
'13
100Hz
50ms
'121
10μs
200 Hz CLOCK

FIGURE I.4

Wavenumber Counter and Comparators

LEGEND

10 cm^{-1}	-	marker pulses from spectrometer
COMPARATORS	-	circuitry to compare counter with switches
FAST FORWARD	-	'1' in fast forward mode, prior to scanning
FINISH	-	output set to '1' when end of scan is
FINISH POSITION SWITCHES	-	set up finish position, 0-999 cm^{-1}
MOTOR PULSES	-	1 pulse per 1/120 cm^{-1} motor step (from I.31)
RESET $\Delta \nu$	-	from RESET WAVENUMBER COUNTER switch
REVERSE	-	'1' in reverse mode (from I.5)
REVERSE'	-	supplementary REVERSE signal to stepper motor drive
START	-	output set to '1' when start position is detected
START - 100	-	output set to '1' at 100 cm^{-1} below starting position
WAVENUMBER DISPLAY	-	to display similar to that of the ratemeter
SN7483	-	4-bit binary adder, wired to subtract 1 when FAST FORWARD is at '0'
SN7485	-	4-bit comparator
SN7490	-	decade counter in divide by ten mode
SN7492	-	duodecimal counter in divide by twelve mode
SN74190	-	up/down decade counter, controlled by REVERSE

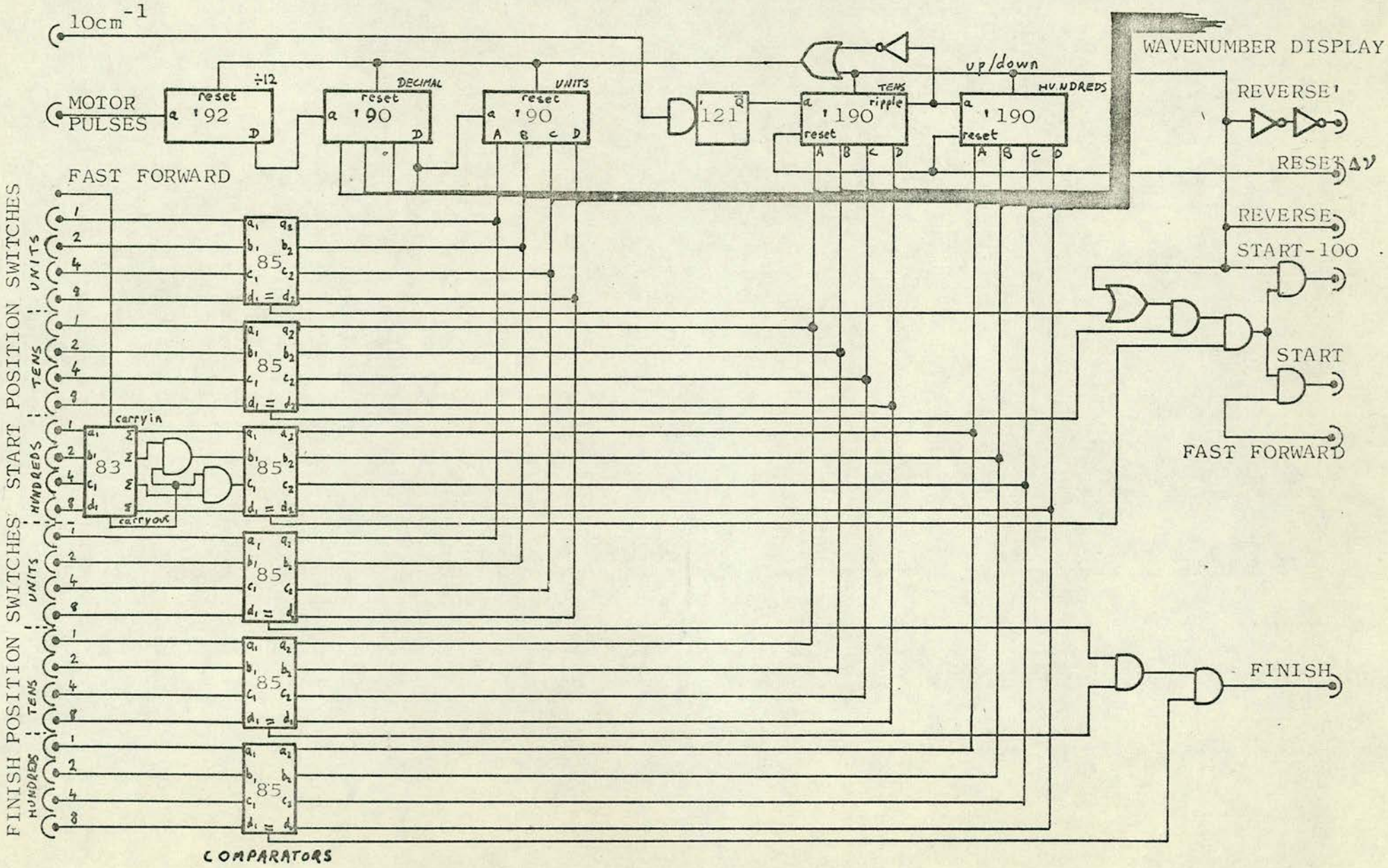
10cm-1
MOTOR PULSES
÷12
reset
'92
D
DECIMAL
'90
UNITS
A B C D
'121
up/down
TENS
ripple
HUNDREDS
'190
WAVENUMBER DISPLAY
REVERSE'
RESET Δν
REVERSE
START-100
START
FAST FORWARD
FINISH
FAST FORWARD
UNITS
TENS
HUNDREDS
carryin
carryout
'83
'85
FINISH POSITION SWITCHES
START POSITION SWITCHES
COMPARATORS

FIGURE I.5

Scan Status Memory and Control Logic

LEGEND

200 Hz CLOCK	-	System clock (from I.3.3)
$\overline{\text{CANCEL}}$	-	from OVERLOAD SWITCH, cancels overload condition
CHANNEL CLOCK	-	to channel stepping circuitry (I.3.2)
END	-	last scan signal (from I.6)
FAST FORWARD	-	output set to '1' in fast forward mode
FAST FORWARD'	-	supplementary FAST FORWARD signal
FINISH	-	end of scan signal (from I.4)
$\overline{\text{GO}}$	-	from GO switch, to start
INDICATOR DRIVERS	-	2N1711 transistor drivers for lights and relays
LOCK	-	remains at '1' until wavenumber counter has been set
MOTOR CLOCK	-	output to scan rate circuitry (I.3.1)
MOTOR DRIVE	-	output to stepper motor drive
MOTOR PULSES	-	from scan rate circuitry (I.3.1)
OVERLOAD	-	'1' when an excessive count is detected (I.2)
OVERLOAD'	-	overload signal stored in flip-flop
$\overline{\text{RESET } \Delta\nu}$	-	from RESET WAVENUMBER COUNTER switch
REVERSE	-	output set to '1' in reversing mode
SCANNING	-	output set to '1' in scanning mode
START	-	start of scan signal (from I.4)
START - 100	-	signal at 100 cm^{-1} before start of scan (I.4)
$\overline{\text{STOP}}$	-	from STOP switch, to halt
SN7476	-	dual J-K flip-flops with preset and clear to store scan status

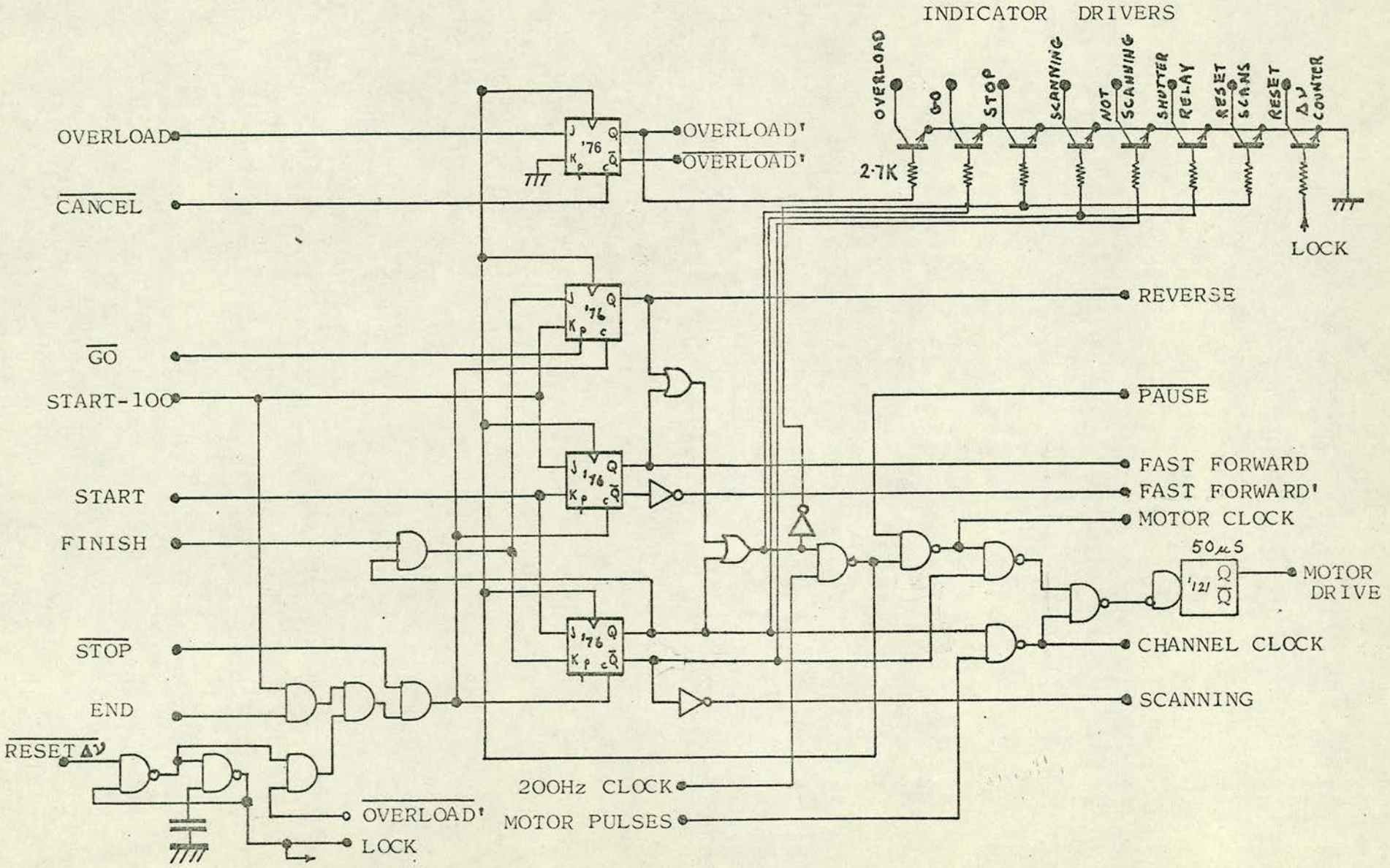
INDICATOR DRIVERS
OVERLOAD
GO
STOP
SCANNING
NOT SCANNING
SHUTTER RELAY
RESET SCANS
RESET ΔV COUNTER
2·7K
LOCK
OVERLOAD
CANCEL
'76
OVERLOAD'
OVERLOAD'
REVERSE
GO
START-100
PAUSE
START
FAST FORWARD
FAST FORWARD'
FINISH
MOTOR CLOCK
50μS
'121
MOTOR DRIVE
STOP
CHANNEL CLOCK
END
SCANNING
RESET ΔV
200Hz CLOCK
OVERLOAD'
MOTOR PULSES
LOCK

FIGURE I.6

Scan Counter

LEGEND

END	-	output set to '1' during last scan
RESET SCAN COUNTER	-	from RESET SCANS switch
SCAN NUMBER DISPLAY	-	to display, similar to that of the ratemeter
SCAN NUMBER SWITCHES	-	bcd switches setting the number of scans from 0 to 99
START	-	'1' at the start of each scan, number of 'starts' counted
SN7483	-	binary adder, used as a comparator
SN7490	-	decade counter used in the divide by ten mode

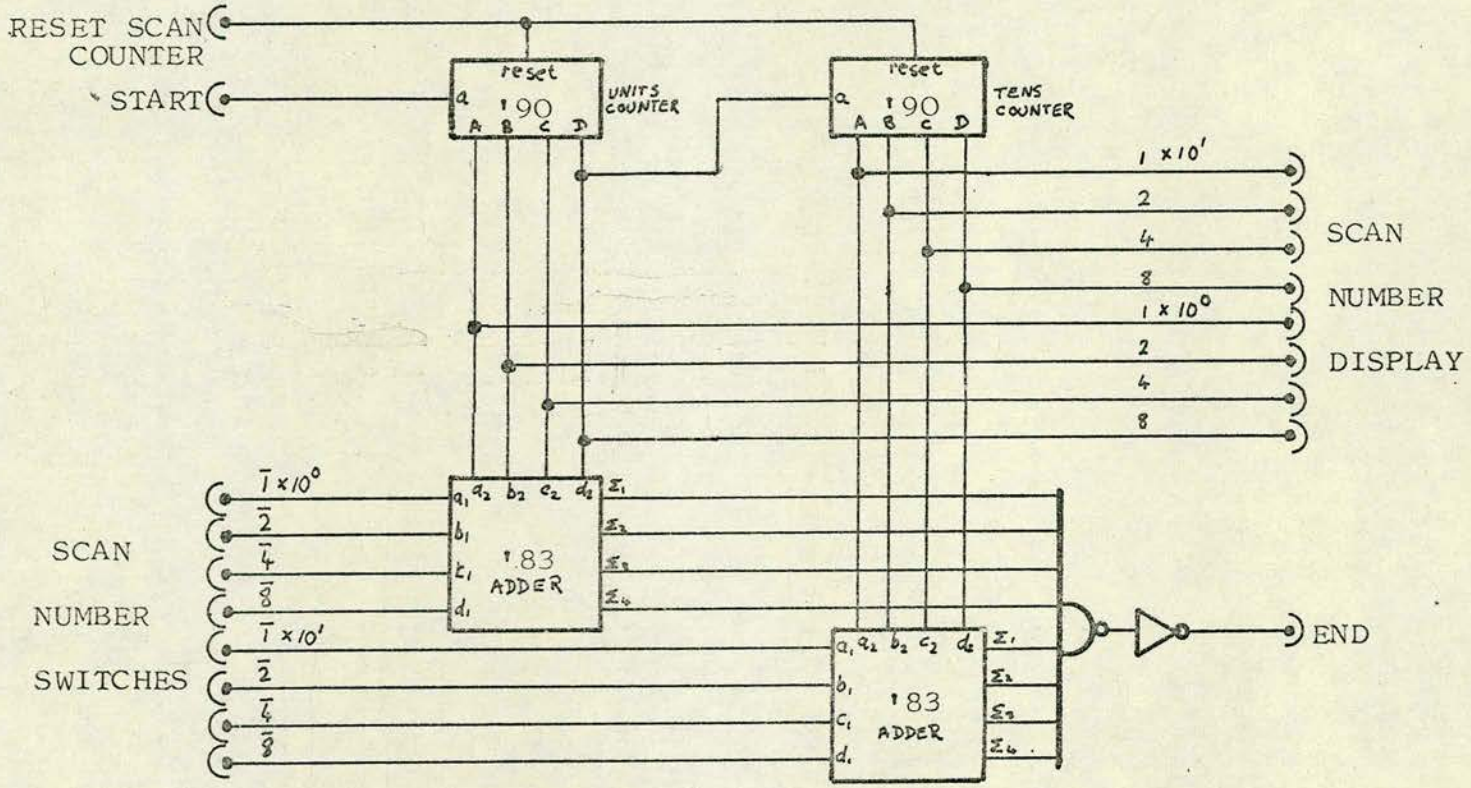
RESET SCAN COUNTER
START
reset
a
'90
A B C D
UNITS COUNTER
reset
a
'90
A B C D
TENS COUNTER
1 x 10'
2
4
8
SCAN NUMBER DISPLAY
1 x 10°
2
4
8
SCAN NUMBER SWITCHES
1 x 10°
2
4
8
1 x 10'
2
4
8
a1 a2 b2 c2 d2
b1
c1
d1
'83 ADDER
Σ1
Σ2
Σ3
Σ4
a1 a2 b2 c2 d2
b1
c1
d1
'83 ADDER
Σ1
Σ2
Σ3
Σ4
END

APPENDIX II

Circuit diagrams for the spectrometer control of System 2

Contents

FIGURE II.1

Control Circuit

LEGEND

100 Hz	-	100 Hz clock reference
COUNT	-	'1' during count cycle
COUNT DOWN	-	count down input of SN74190
$\overline{\text{DONE}}$	-	'0' when total number of steps has been completed (from II.3)
$\overline{\text{ENDTIME}}$	-	'0' pulse on completion of count cycle
$\overline{\text{GO}}$	-	input from GO switch, '0' to activate
INT	-	'1' during an interrupt condition
$\overline{\text{INTERRUPT}}$	-	from INTERRUPT switch, '0' to activate
L.E.D. DISPLAY	-	light emitting diode display of control status
LOAD	-	SN74190 load input
MOTOR ENABLE	-	'1' during step cycle
OSC	-	80 Hz oscillator for motor pulses
$\overline{\text{RELEASE}}$	-	to RELEASE switch, cancels interrupt condition
RESET	-	resets timing counters prior to count cycle
RESET STEP COUNTER	-	initialises step counter (to II.3)
RIPPLE	-	ripple output of SN74190
$\overline{\text{SLEW}}$	-	to SLEW switch, '0' to slew, during stop only
$\overline{\text{STEP}}$	-	motor steps, to stepsize control
$\overline{\text{STEP DONE}}$	-	'0' signifies end of step of selected size (to II.3)
STEP N	-	bcd switch selecting stepsize of N steps
$\overline{\text{STOP}}$	-	to STOP switch, '0' to halt
TIME T	-	bcd switch selecting count time T seconds
T × 10	-	'0' selects count time times ten
$\overline{\text{ZERO}}$	-	to RESET switch, for manually resetting step counter.

SN7413	-	Schmitt trigger, used to make an oscillator
SN7490	-	decade counter in divide by ten mode
SN74190	-	decade up/down counter, in count down mode.

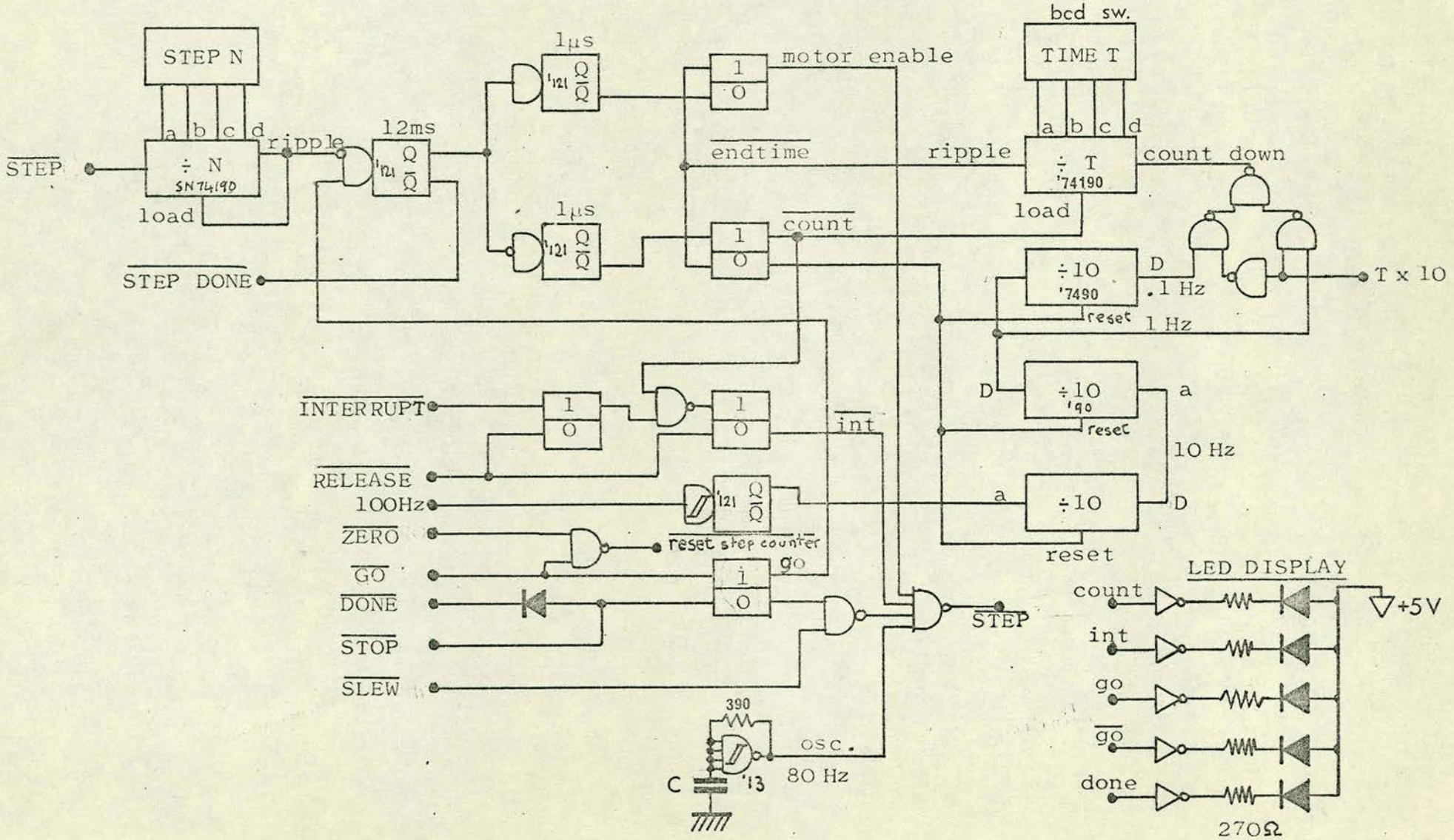
STEP N
a b c d
÷ N
SN74190
load
ripple
STEP
STEP DONE
12ms
'121
1µs
1µs
motor enable
endtime
count
bcd sw.
TIME T
a b c d
÷ T
'74190
load
ripple
count down
÷10
'7490
reset
D
.1 Hz
1 Hz
T x 10
÷10
'190
reset
D
a
10 Hz
÷10
a
D
reset
INTERRUPT
RELEASE
100Hz
ZERO
GO
DONE
STOP
SLEW
int
reset step counter
go
STEP
390
osc.
C
'13
80 Hz
LED DISPLAY
+5V
count
int
go
go
done
270Ω

FIGURE II.2

Stepper motor control circuit

LEGEND

1,2,3,4	-	outputs to motor winding drive transistors - 4 phases
DIRECTION	-	'1' or '0' from switch for forward or reverse
STEP	-	pulse producing one motor step in selected direction
SN7476	-	dual J-K flip-flop used as a left/right shift register

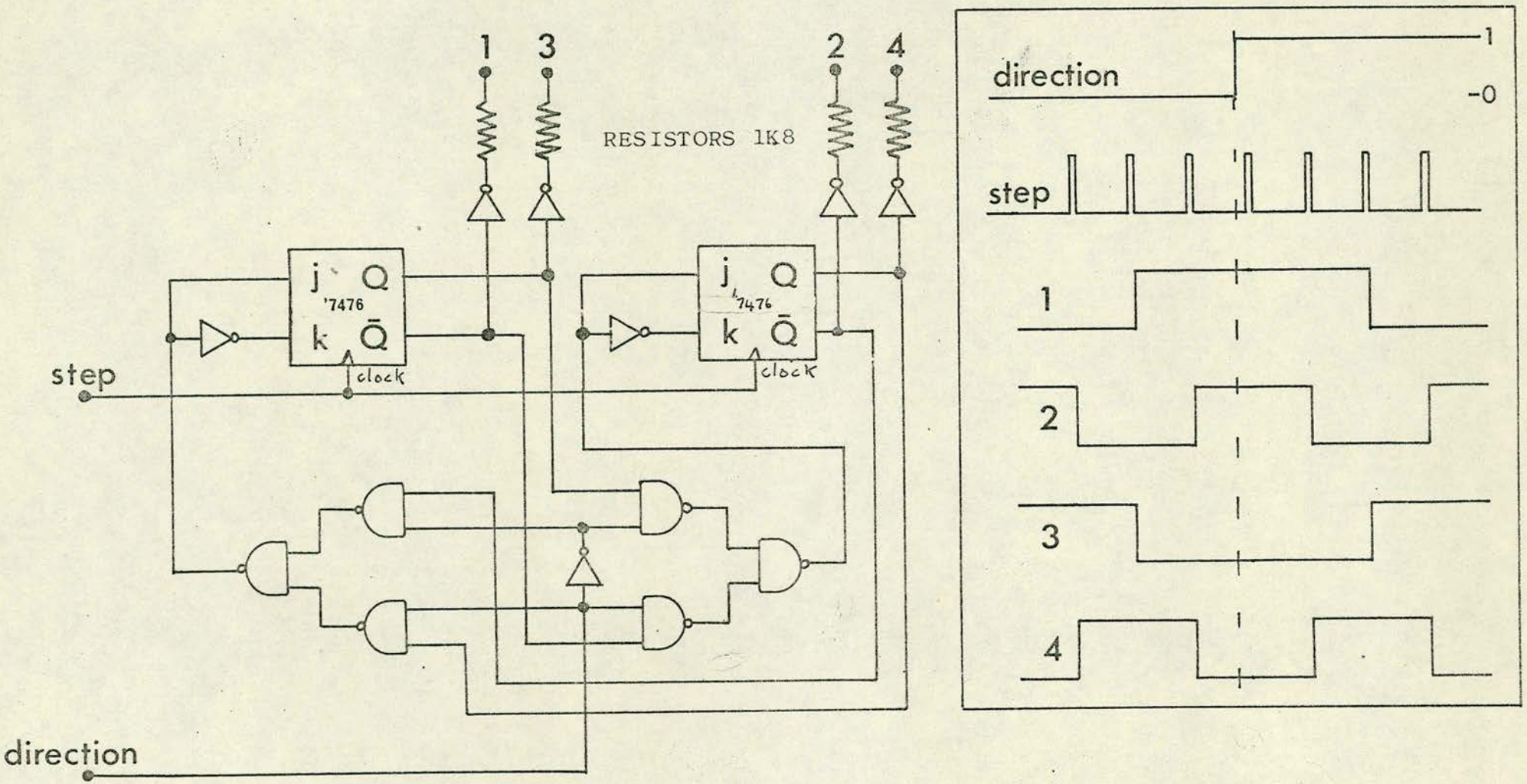
1
3
2
4
RESISTORS 1K8
j Q
'7476
k Q̄
clock
step
direction
1
-0
step
1
2
3
4

FIGURE II.3

Step counter

LEGEND

bcd SWITCHES	-	provide setting of between 0 and 9999 steps
$\overline{\text{DONE}}$	-	'0' when total number of steps completed.
RESET	-	reset for counters, from RESET STEP COUNTER of II.1
$\overline{\text{STEP DONE}}$	-	'0' pulses for each step completed
SN7483	-	adder used as a comparator
SN7490	-	decade counter in divide by ten mode

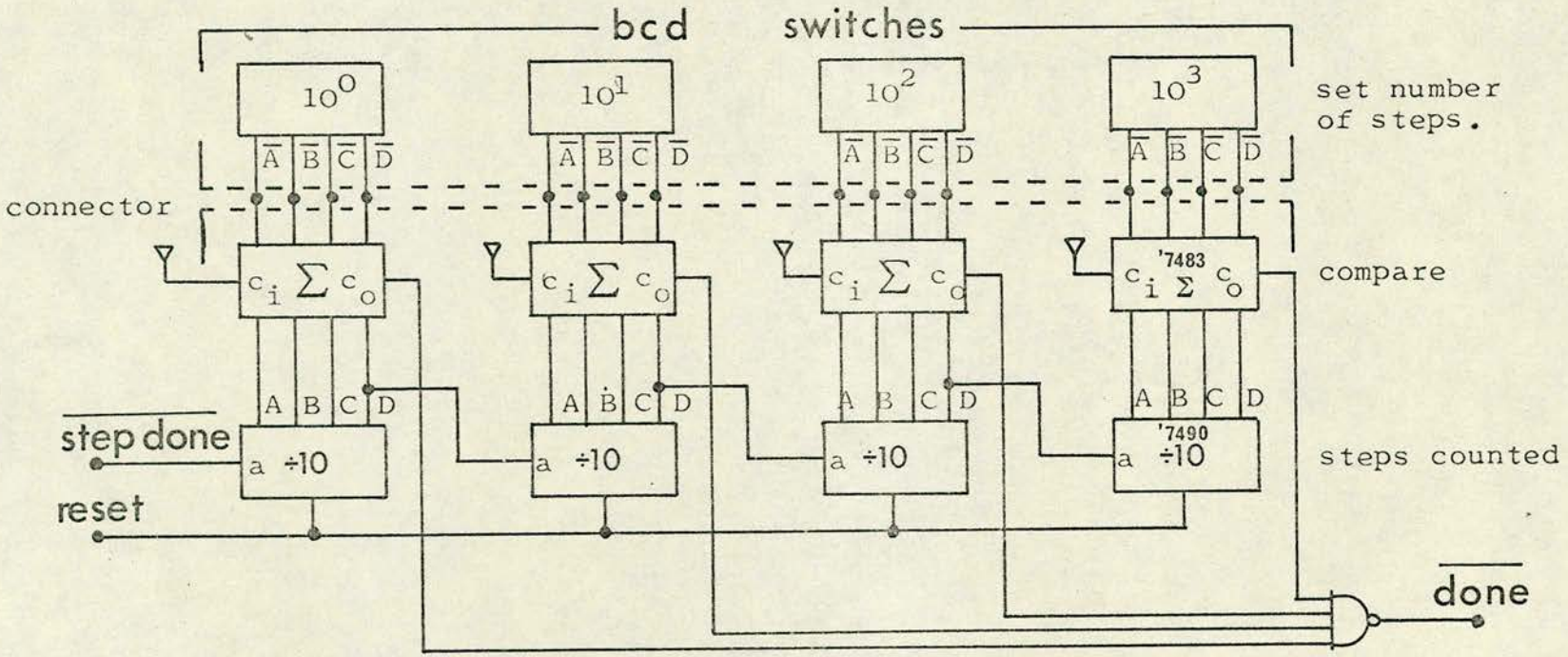
bcd switches
10^0
10^1
10^2
10^3
set number of steps.
connector
A B C D
$c_i \Sigma c_o$
'7483
compare
step done
reset
a ÷10
'7490
steps counted
done

APPENDIX III

Circuit Diagrams for the Computer Operated Spectrometer System

CONTENTS

FIGURE III.1

Computer Output and Input Data Bus Structure

LEGEND

$\overline{B0}$ - $\overline{B15}$	-	complement of command word from computer output
B0 - B2	-	used to select output subchannel
B4 - B6	-	used to select input subchannel
B15	-	flag for 'select channels'/'command word'
BUS	-	output and input buses, carrying B0-B14 and D0-D15 respectively
$\overline{D0}$ - $\overline{D15}$	-	complement of data word sent to computer input
DEMULTIPLEXER	-	see III.2, selects device on computer output bus
DEVICE	-	either an input or output device, connected to one of the buses via a subchannel
DONE	-	transfer of data complete, signal to computer
FLAG-Q	-	signal initiating transfer of data to or from a subchannel
FLAG-R	-	response from device, transfer complete
$\overline{LOAD}$	-	signal causing the loading of new subchannel addresses
MULTIPLEXER	-	see III.3, selects device for computer input bus
Q	-	see FLAG-Q
R	-	see FLAG-R
READY	-	signal from computer indicating that data may be transferred

Note: There are separate DONE and READY signals for input and output.

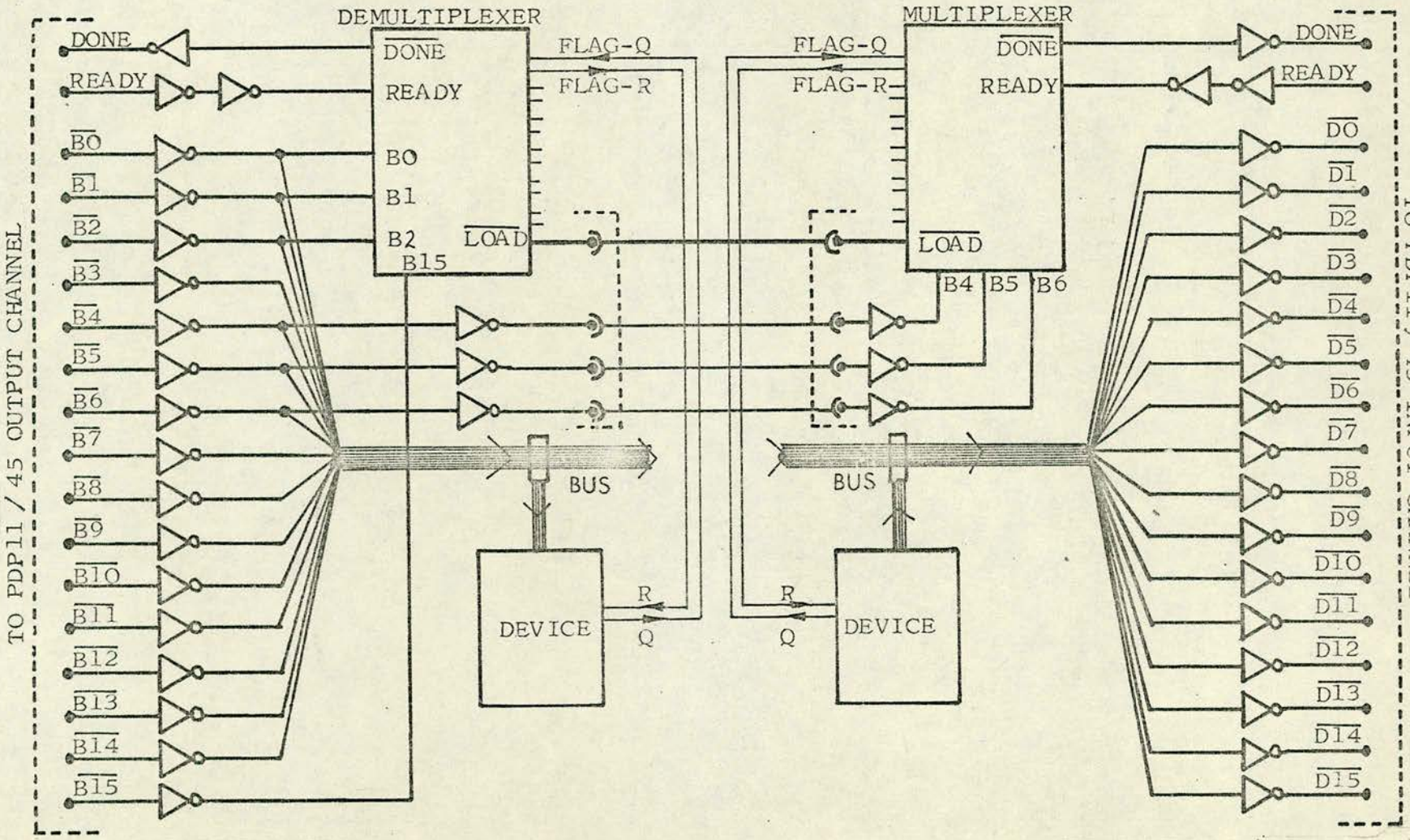
TO PDP11/45 OUTPUT CHANNEL
DEMULTIPLEXER
DONE
READY
B0
B1
B2
B3
B4
B5
B6
B7
B8
B9
B10
B11
B12
B13
B14
B15
LOAD
FLAG-Q
FLAG-R
BUS
DEVICE
R
Q
MULTIPLEXER
TO PDP11/45 INPUT CHANNEL
D0
D1
D2
D3
D4
D5
D6
D7
D8
D9
D10
D11
D12
D13
D14
D15

FIGURE III.2

Computer Output Demultiplexer

LEGEND

B0-B3	-	subchannel address inputs from data bus
B15	-	'command word'/'select channels' flag
$\overline{\text{DONE}}$	-	'transfer complete' pulse for computer
FLAG 'Q'	-	'0' when a subchannel requests data
FLAG 'R'	-	'0' when a subchannel is given valid data
$\overline{\text{LOAD}}$	-	'load subchannel address' signal to the multiplexer
L/M FLAG	-	least/most significant word flag (alternately 1 then 0)
NEGATIVE EDGE TRIGGER	-	produces $\overline{\text{LOAD}}$ pulse
READY	-	'command word available' flag from computer
SN74155	-	3 line to 8 line decoder - selects subchannel
SN74197	-	presettable binary counter, used as latch, divide by two function produces L/M FLAG

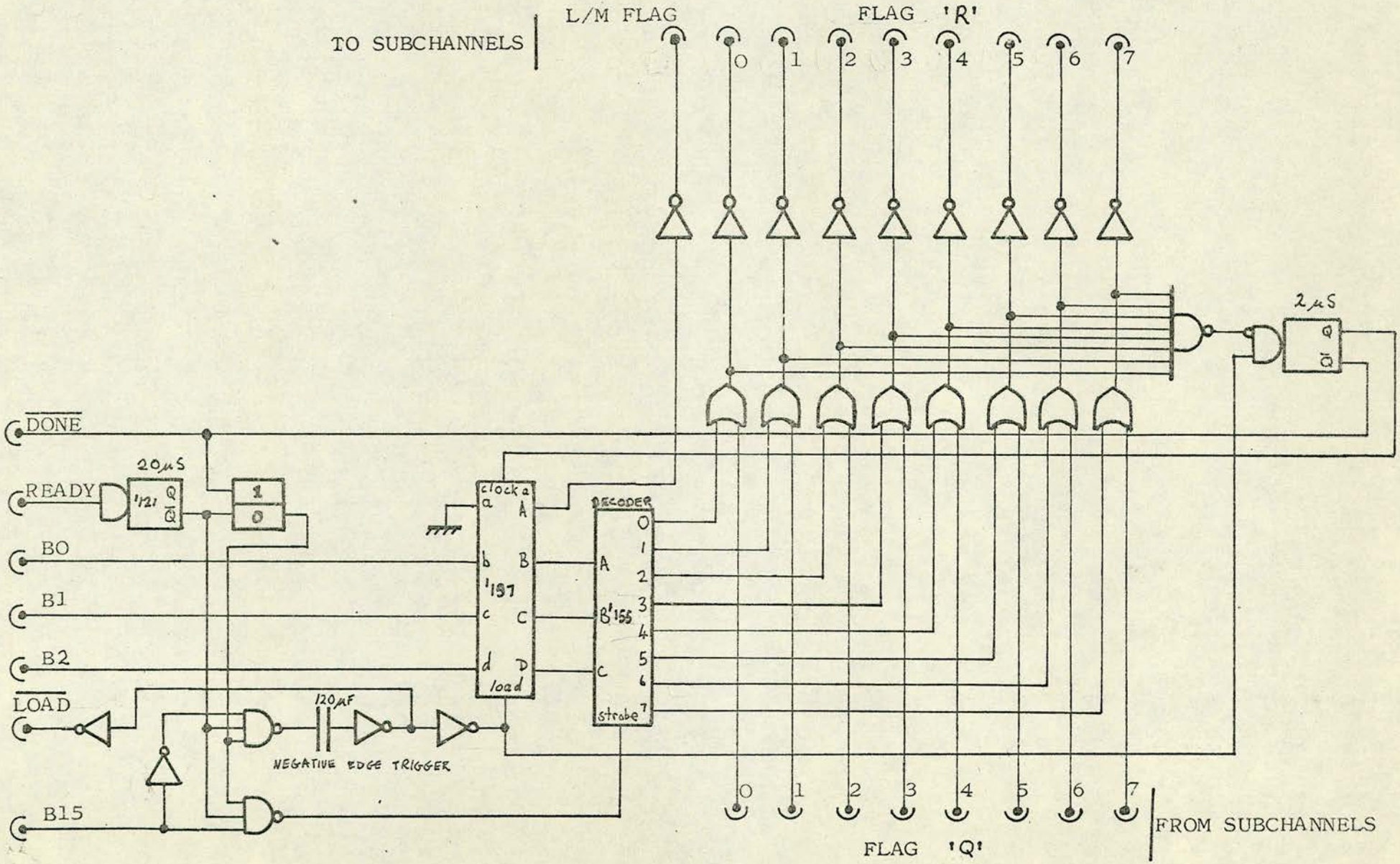
TO SUBCHANNELS
L/M FLAG
FLAG 'R'
0 1 2 3 4 5 6 7
2μS
Q
Q̄
DONE
20μS
READY
'121
Q
Q̄
1
0
BO
B1
B2
LOAD
B15
clock a
a A
b B
'197
c C
d D
load
DECODER
A
B'155
C
strobe
0
1
2
3
4
5
6
7
120μF
NEGATIVE EDGE TRIGGER
0 1 2 3 4 5 6 7
FLAG 'Q'
FROM SUBCHANNELS

FIGURE III.3

Computer input multiplexer

LEGEND

B4-B6	-	subchannel address from demultiplexer data bus
DATA READY LINES	-	see FLAG 'Q'
$\overline{\text{DONE}}$	-	return signal to computer, transfer acknowledged
FLAG 'Q'	-	from subchannel, data ready
FLAG 'R'	-	response, hold data until transfer complete
HOLD DATA LINES	-	see FLAG 'R'
$\overline{\text{LOAD}}$	-	load subchannel address signal from demultiplexer
L/M FLAG	-	least/most significant word flag
POSITIVE EDGE TRIGGER	-	detects change in READY
READY	-	'ready to accept data' signal from computer
SN74155	-	3 line to 8 line decoder, selects subchannels
SN74197	-	presettable binary counter used as a storage latch, divide by two function provides L/M FLAG

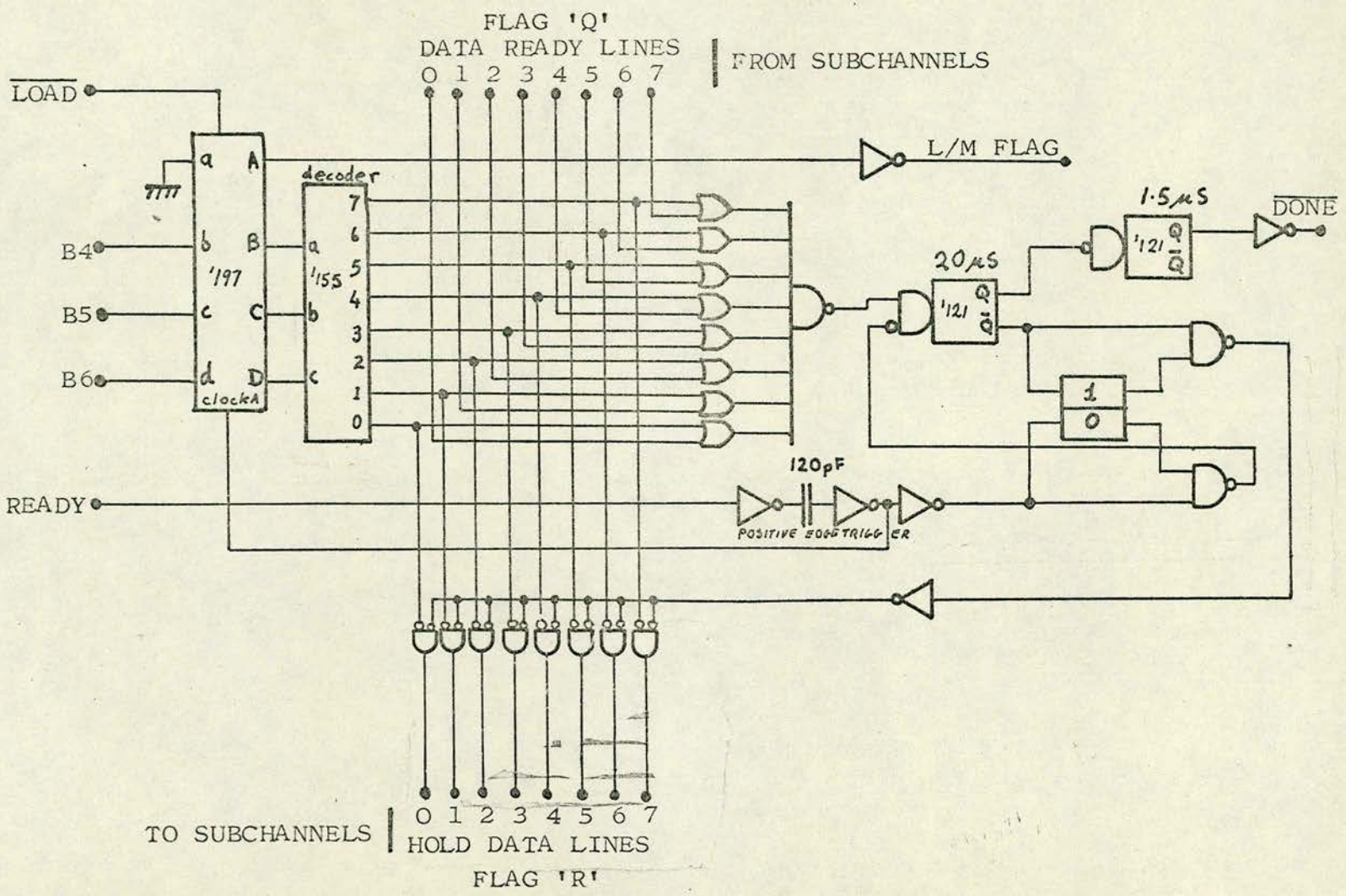
FLAG 'Q'
DATA READY LINES
0 1 2 3 4 5 6 7
FROM SUBCHANNELS
LOAD
B4
B5
B6
'197
clockA
decoder
'155
L/M FLAG
1·5μS
DONE
20μS
'121
120pF
READY
POSITIVE EDGE TRIGGER
TO SUBCHANNELS
0 1 2 3 4 5 6 7
HOLD DATA LINES
FLAG 'R'

FIGURE III.4

15-bit Storage Register

LEGEND

BUS	-	demultiplexer data bus (15 bits)
DATA	-	data stored from bus (15 bits)
$\overline{\text{DONE}}$	-	Return signal from driven device, data no longer required
FLAG 'Q'	-	new data requested (see III.1 and III.2)
FLAG 'R'	-	new data ready (see III.1 and III.2)
LATCHES	-	storage buffer
START	-	signal initiating action of driven device
SN7475	-	4-bit latch, with both clocks used

Notes:

1) one storage register is required for the spectrometer control (Figures III.5.1-2)

2) two storage registers may be coupled together and used alternately under the control of the L/M flag. This is used in the X - Y plotter driver where separate registers are required for the X and Y values (Figure III.6).

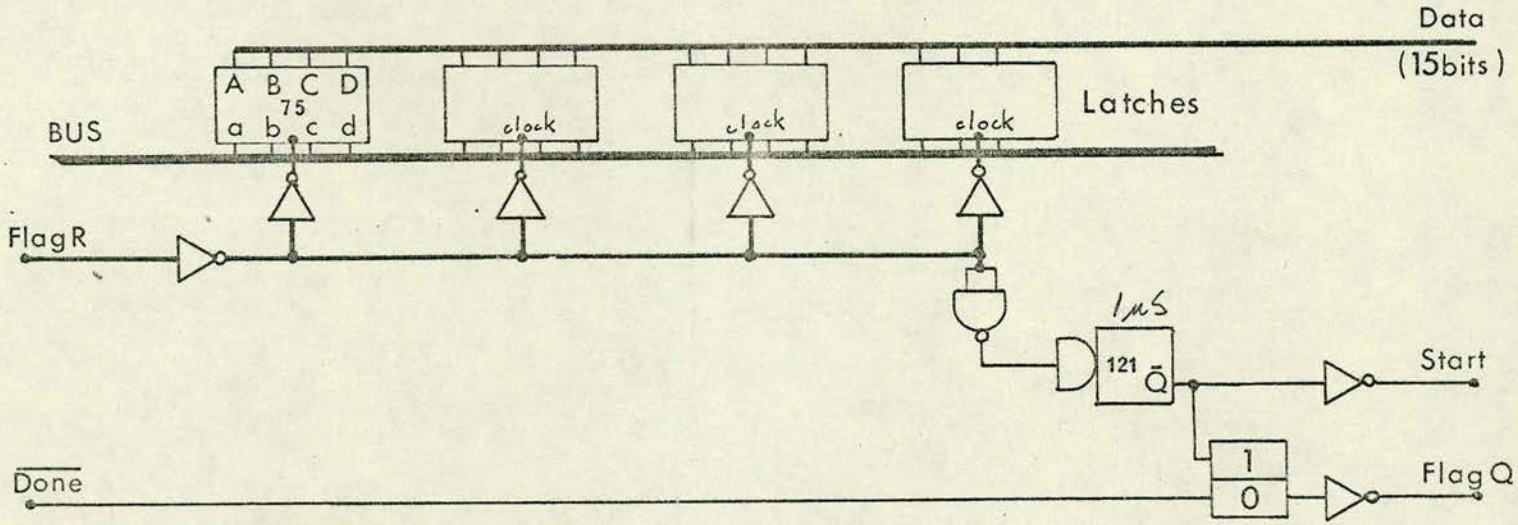
Data
(15bits)
A B C D
75
a b c d
BUS
clock
clock
clock
Latches
Flag R
1mS
121
Q̄
Start
Done
1
0
Flag Q

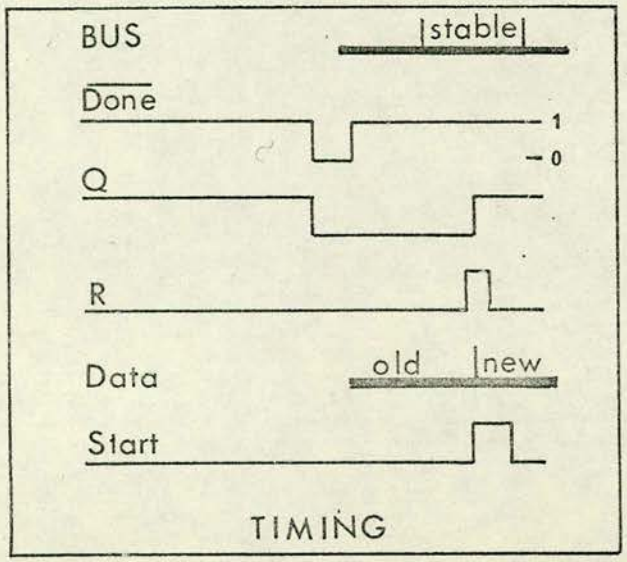
BUS
stable
Done
1
0
Q
R
Data
old
new
Start
TIMING

FIGURES III.5.1 and III.5.2

Spectrometer Control Circuit

This circuit is provided with two sets of controlling inputs, one designated COMPUTER and the other MANUAL. The inputs designated for computer use are connected to the computer output demultiplexer data bus, via a storage register, Figure III.4. The inputs used in manual operation are connected to front panel bcd and pushbutton switches. Circuitry is provided to allow the choice of manual or computer operation through the SELECT switch. This is described in Chapter Two, pp. 37-38, and is also illustrated in Figure 2.8.

LEGEND

100 Hz	-	Mains clock reference
COMPUTER	-	signal routed to computer
$\overline{\text{COUNT}}$	-	'0' when counting in progress
$\overline{\text{COUNT}}$'	-	duplicate for scaler
$\overline{\text{CYCLE}}$	-	normally '1', '0' initiates step-count cycle
$\overline{\text{DONE}}$	-	return signal to subchannel DONE input
$\overline{\text{GO}}$	-	to GO switch, '0' to activate
$\overline{\text{GO}}$'	-	for computer
$\overline{\text{INT}}$	-	to INTERRUPT switch, '0' to activate
INT ON	-	'1' during INTERRUPT condition
MANUAL	-	signal routed to manual control
MOTOR	-	step pulses to stepper motor driver
OSC	-	oscillator for motor step pulses
$\overline{\text{REL}}$	-	to RELEASE switch, '0' cancels INTERRUPT condition

$\overline{\text{REL}}$' - for computer

SELECT - to SELECT switch, '1' manual, '0' computer

SET TIME - count time setting circuitry, 0 through 15 secs

SINGLE STEP - momentary '1' for single step, during STOP only

$\overline{\text{SLEW}}$ - to SLEW switch, '0' to slew, during STOP only

START - start pulse from subchannel START output

STEP - '1' indicates stepping in progress

STEP 0 - normally '0')
) to SINGLE STEP switch (SPC0)
STEP 1 - normally '1')

$\overline{\text{STEP ENDED}}$ - '0' pulse on completion of STEP condition

$\overline{\text{STEP PULSES}}$ - '0' pulses for each motor step, derived from OSC

STEP SIZE - step size control circuitry, 0 through 15 steps

$\overline{\text{STOP}}$ - to STOP switch, '0' to activate

STOPPED - '1' when STOPPED, allows SLEW or SINGLE STEP

TIME RESET LINE held to '1' when not counting

T × 10 - to T × 10 switch, '0' for count time times ten

T × 10' - for computer

SN7490 - decade counter in divide by ten mode

SN74157 - quad 2 to 1 selector

SN74191 - up/down binary counter in count down mode

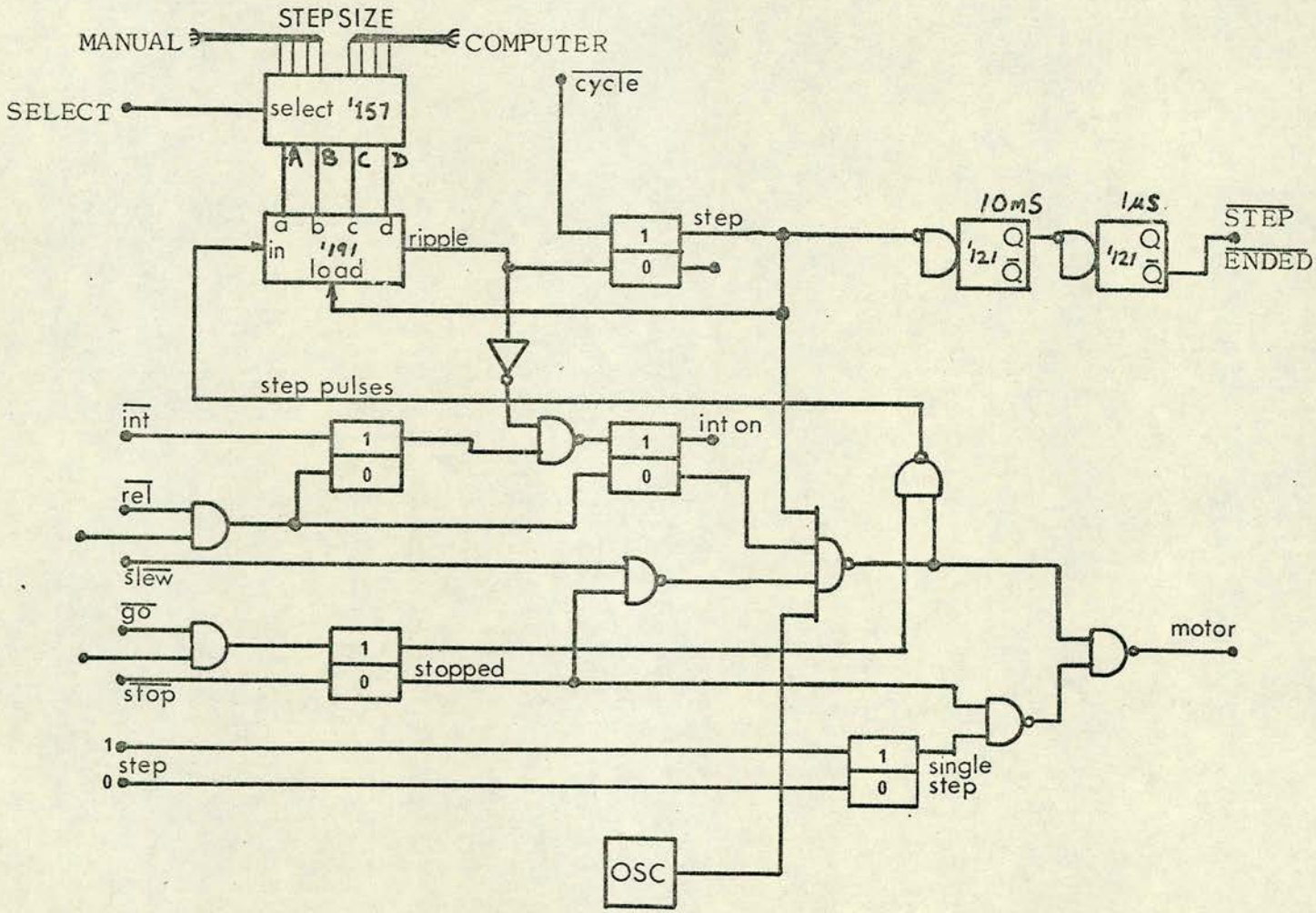
STEP SIZE
MANUAL
COMPUTER
SELECT
select '157
A B C D
cycle
a b c d
in '191 load
ripple
step
10mS
1μS
'121
Q
Q̄
STEP
ENDED
step pulses
int
int on
rel
slew
go
stop
stopped
motor
1
step
0
single step
OSC

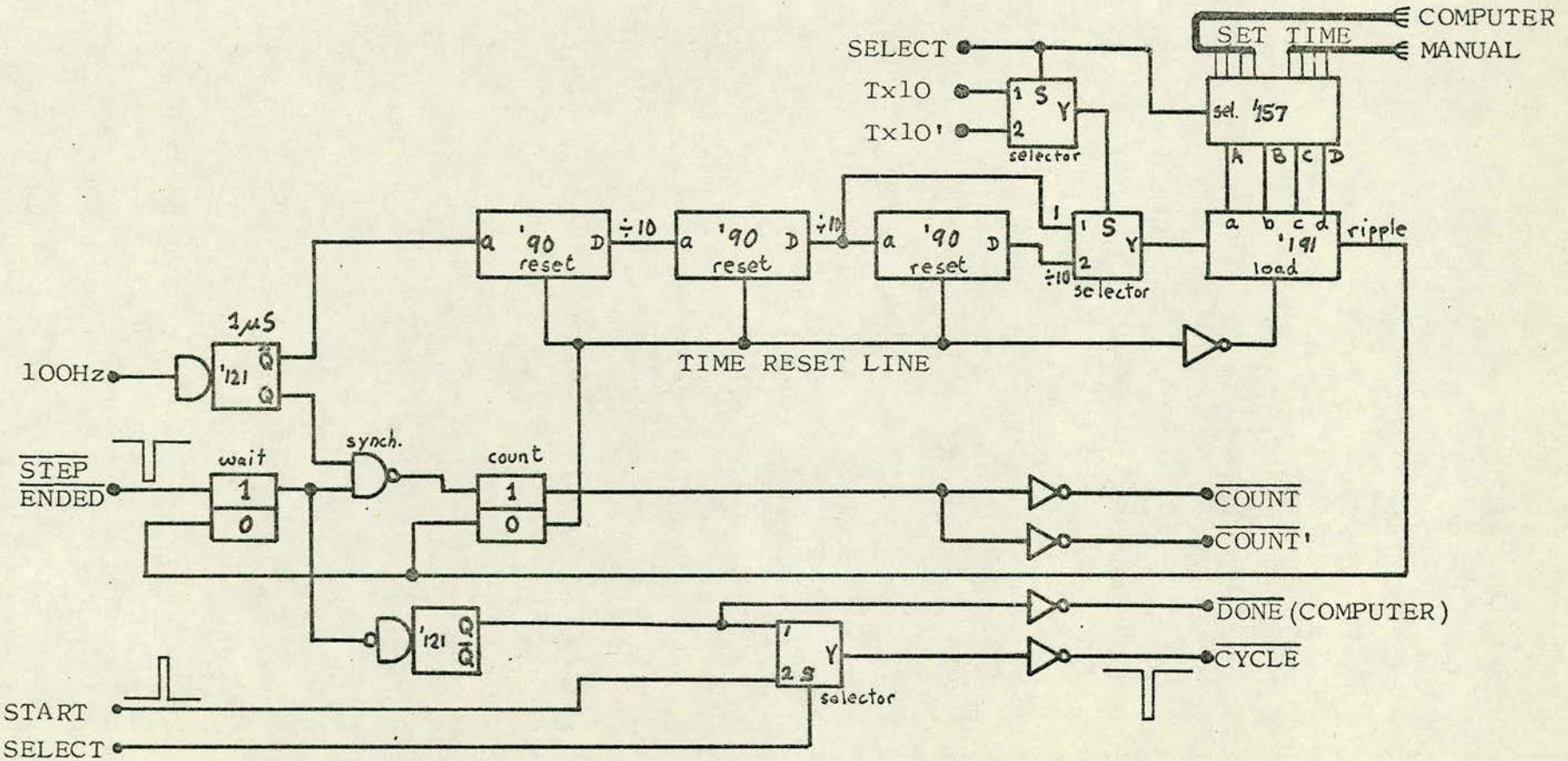
COMPUTER
SET TIME
MANUAL
SELECT
Tx10
Tx10'
selector
sel. '157
A B C D
'90 reset
÷10
'191 load
ripple
selector
1μS
100Hz
'121
TIME RESET LINE
STEP
ENDED
wait
synch.
count
COUNT
COUNT'
DONE (COMPUTER)
CYCLE
START
SELECT

FIGURE III.6

X-Y Plotter Driver

LEGEND

B0 - B14	-	data bits from demultiplexer data bus
DATA BUS	-	demultiplexer data bus
$\overline{\text{DONE-X}}$	-	(individual storage register DONE inputs (III.4)
$\overline{\text{DONE-Y}}$		(
FLAG 'Q'	-	request new data - to demultiplexer
FLAG 'R'	-	new dataready - from demultiplexer
L/M FLAG	-	indicates X or Y value
PLOT COMMAND	-	signal to X-Y plotter to plot data point
PLOT DONE	-	return from null detector on X-Y plotter
Q-X	-	(
		(individual storage register FLAG-Q outputs
Q-Y		(
R-X		(
		(individual storage register FLAG-R inputs
R-Y		(
START-X	-	unused
START-Y	-	Y is transferred last, new X and new Y ready
X AXIS	-	X axis analogue signal
X DAC	-	X axis digital to analogue converter
Y AXIS	-	Y axis analogue output
Y DAC	-	Y axis digital to analogue converter

Note: two individual storage registers (Figure III.4) are coupled together using the L/M flag to select either X or Y.

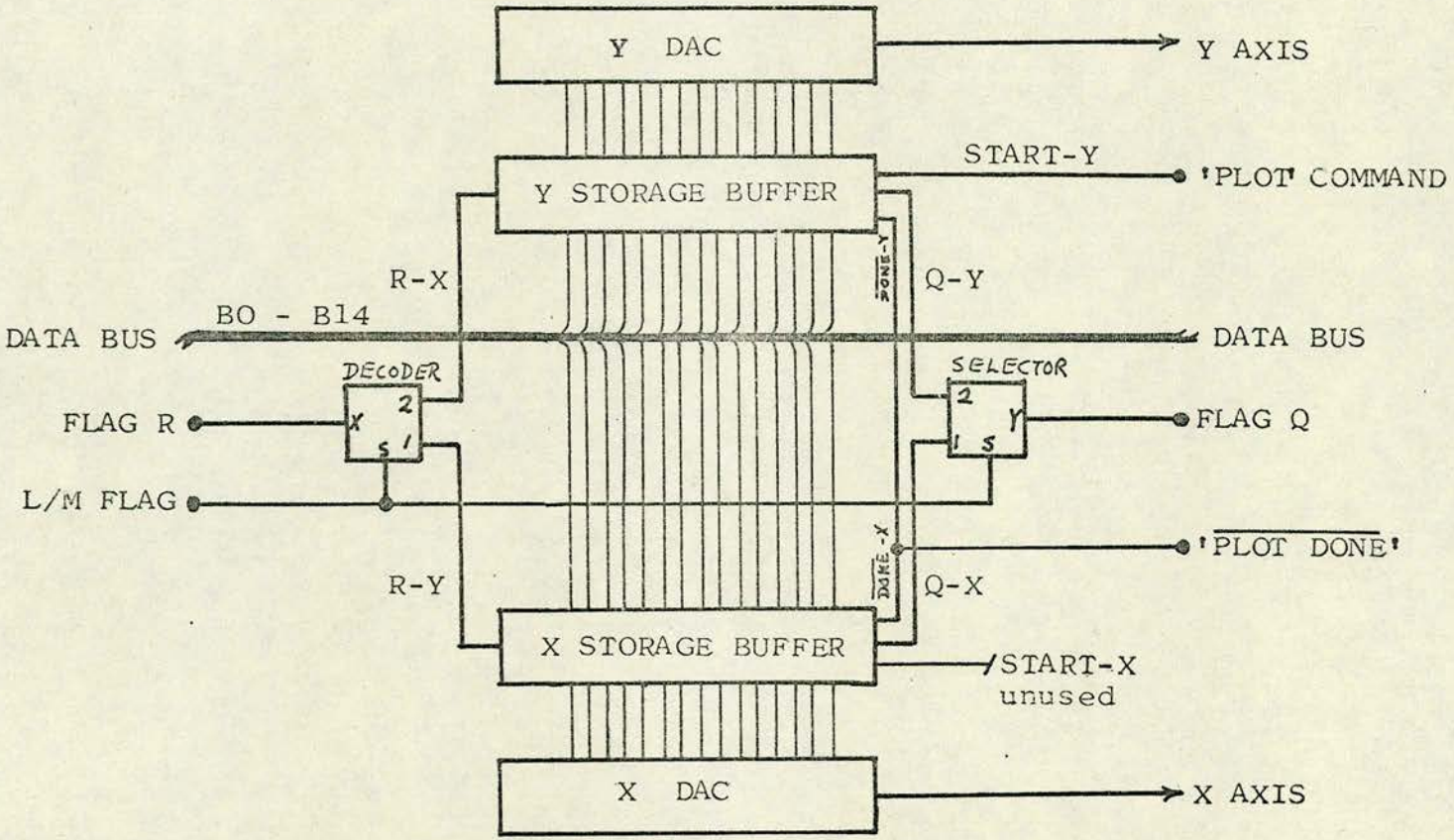
Y DAC
Y AXIS
START-Y
'PLOT' COMMAND
Y STORAGE BUFFER
R-X
DONE-Y
Q-Y
BO - B14
DATA BUS
DATA BUS
DECODER
SELECTOR
FLAG R
FLAG Q
L/M FLAG
'PLOT DONE'
DONE-X
R-Y
Q-X
X STORAGE BUFFER
START-X
unused
X DAC
X AXIS

FIGURE III.7

Photon Counter

LEGEND

BUS GATES	-	allow access to multiplexer data bus
COUNT	-	count signal from spectrometer control (III.5.2)
COUNTERS	-	16-bit photon count scaler
COUNTS IN	-	photomultiplier pulses from preamp.
D0-D15	-	data bits on data bus
DATA READY	-	FLAG 'Q' to multiplexer
HOLD DATA	-	FLAG 'R' from multiplexer
STROBE	-	bus gate control signal
SN7493	-	binary counter

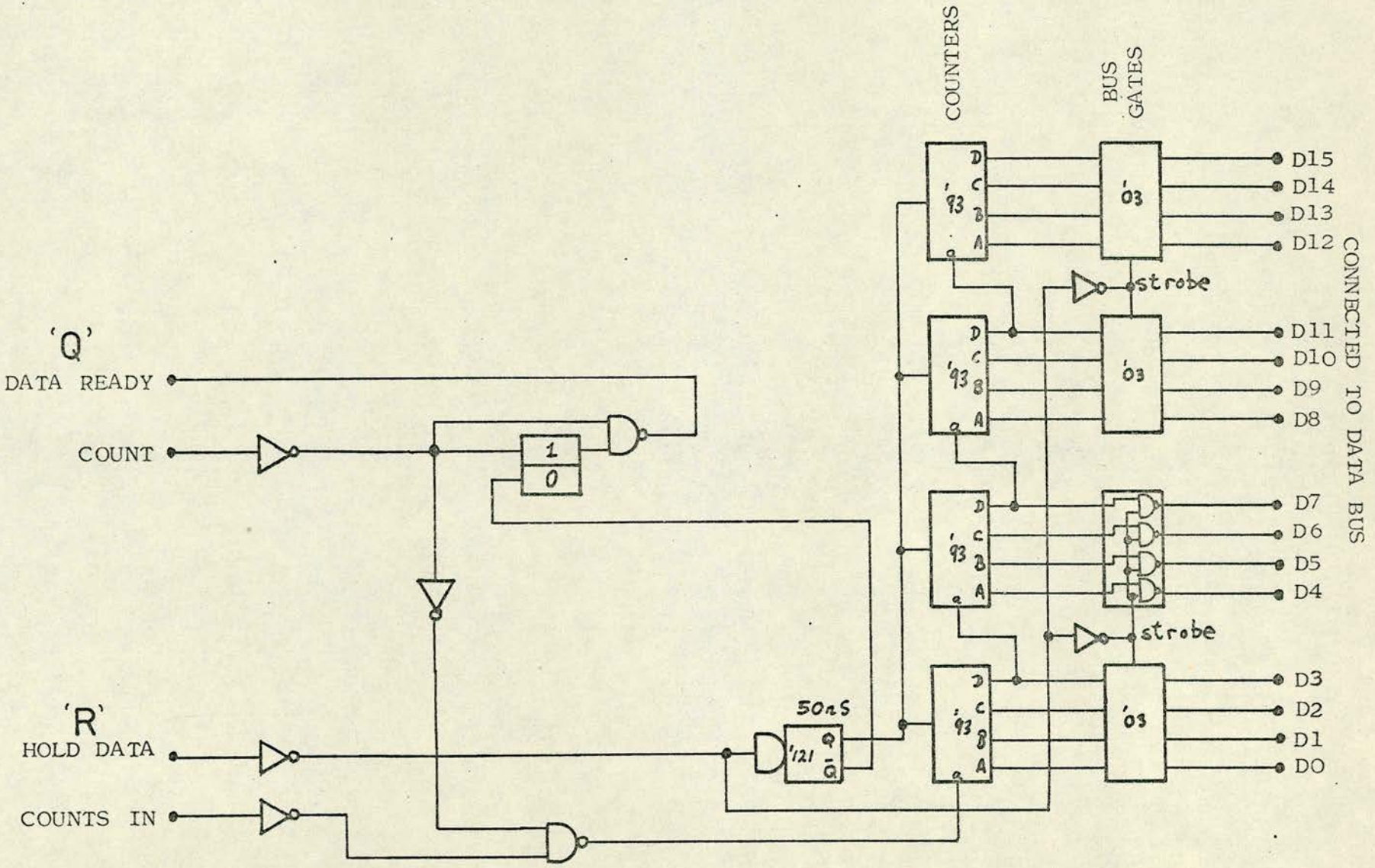
COUNTERS
BUS GATES
CONNECTED TO DATA BUS
'Q'
DATA READY
COUNT
'R'
HOLD DATA
COUNTS IN
1
0
50nS
'121
Q
$\bar{Q}$
'93
D
C
B
A
'03
strobe
strobe
D15
D14
D13
D12
D11
D10
D9
D8
D7
D6
D5
D4
D3
D2
D1
D0

PDP11/45 IMP INTERFACE INPUT/OUTPUT ROUTINES

```
%BEGIN
%INTEGER IN,OUT
IN=15
OUT=15

%ROUTINE PUT(%INTEGER C,CH)
! C IS COMMAND WORD  CH IS OUTPUT SUBCHANNEL
%IF CH#OUT %THENSTART
      OUT=CH
      LACC(OUT*16+IN)
      *EMT…361
            %FINISH
LACC(C+X'8000')
!C IS MASKED WITH '1' IN BIT 15
*EMT…361
%END

%ROUTINE GET(%INTEGERNAME D,%INTEGER CH)
! D IS DATA WORD  CH IS INPUT SUBCHANNEL
%IF CH#IN %THENSTART
      IN=CH
      LACC(OUT*16+IN)
      *EMT…361
            %FINISH
*EMT…362
D=ACC
%END

! 'IN' AND 'OUT' ARE THE CURRENT INPUT AND OUTPUT SUBCHANNELS
! LACC LOADS R0,THE ACCUMULATOR
! ACC IS EQUAL TO THE CONTENTS OF R0
! *EMT…361 ..SUPERVISOR CALL FOR OUTPUT INTERFACE
! ..LOADS OUTPUT BUFFER WITH CONTENTS OF R0
! *EMT…362 ..SUPERVISOR CALL FOR INPUT INTERFACR
! ..LOADS INPUT BUFFER INTO R0

%ENDOFPROGRAM
```

APPENDIX IV

DATA PROCESSING

An important aspect in the analysis of the Raman scattering data collected by the systems described in Chapter Two is that some sort of graphic presentation is required to convey the information in the data to the experimenter. Another is that the data must be easy to access, particularly where large amounts are involved. Finally, some standard means of performing routine analyses - such as peak finding, intensity measuring, or curve fitting - are necessary if full advantage is to be made of a digital data processing system.

While it is barely conceivable that a single computer program could perform all of the above tasks efficiently, and in a coordinated manner, many individual programs, each doing a particular job, can be made to run together, under the direct supervision of the experimenter, on a real-time computer system.

The facilities of EMAS[1], a time-sharing multi-access system supported by the Edinburgh Regional Computing Centre, have been exploited to the full in the development of a library of such programs. The experimenter can, through this system, 'interact' with his data and perform such analyses as he pleases, step by step. The results are produced almost instantly, allowing each step to proceed in a timely fashion.

The routines in the library fall into three main classes:

1) File handling - to read in data tapes and convert them into working data, to detect tape errors, and to repair such faults; to do 'housekeeping' chores on the sets of data files.

2) Information - to provide graphic or numeric information about the data: produce illustrations from the data.

3) Manipulation - to perform computations on data; least squares fitting, peak finding, integration, smoothing.

These individual routines are called upon by giving a 'command' as shown in the descriptions below. Each data tape, having been converted to a working file on disk, may be accessed by its chosen name. The result of using a command may produce a new data file, the name of which is appointed by the user. The remaining details of individual commands and their usage should be clear from the appended explanatory notes and examples. The programs were written in the IMP language[2], which is the primary programming language of the EMAS system, and they are now available for general use.

The peak finding routine

We single this program out for discussion because the algorithm is original. Special attention was paid to the problem of discriminating against peaks which occur just as a statistical fluctuation in the level of noise. The algorithm has three steps. The data is first of all numerically differentiated using a cubic fit over a specified range of data points. Secondly, the differentiated data is marked as belonging to regions of three types, +1, 0, or -1. +1 signifies a region of statistically certain positive slope, 0 a region of uncertain slope, and -1 a region of certain negative slope. The data is then scanned for changes in the regions:

0	⟶ +1	-	peak begins
+1	⟶ 0	-	peak region begins
+1	⟶ -1	-	sharp peak
0	⟶ -1	-	end of peak region
-1	⟶ 0	-	peak ends
-1	⟶ +1	-	new peak follows.

Over the peak region, any point at which the slope goes from a positive to a negative value is taken as a peak feature. Any accidental feature occurring in a region of uncertainty is then justifiably ignored. With a proper choice of the resolution parameter this routine proves highly effective.

References

(1) Edinburgh Multi Access System User Manual, Edinburgh Regional Computing Centre, ed. J.G. Burns (1972).

(2) IMP Language Manual, J.G. Burns, A. McKendrick and P.D. Stephens, Edinburgh Regional Computing Centre (1970).

JWALIB - ROUTINES FOR PROCESSING SPECTRAL DATA

ANGSTROM (DATAFILE, WORKFILE)

DATAFILE is a file created from paper tape output of SPEX 1400, containing spectral data.

The data is a string of numbers preceded by a line with the following information:

STEPSIZE, NUMBER OF STEPS, EXCITING LINE WAVELENGTH, START POSITION WAVELENGTH, TEMPERATURE (IN °K) AND ANY COMMENTS.

The data is terminated by the symbol : (colon), and a number giving the wavelength at the stopping position.

WORKFILE is a user selected file name. This file holds the data in a form readily usable in processing routines. The data is always referred to by this name in these routines, and is converted to wavenumber steps.

Example:

```
COMMAND:ANGSTROM(S8RAMAN2,S8ZX300)

 621 DATA POINTS READ,  620 EXPECTED
CW= 0.11548 A,= 0.28552 CM-1
STEPSIZE=  4
START= -10.0 CM-1 APPROX
```

The first and last lines of S8RAMAN2 look like:

```
4    620    6328.0    6324.0    300    ZZ POLARISATION
[                        ↑                              ]
                         DATA
                         ↓
:    6395.6
```

(CW = AVERAGE SPACING BETWEEN DATA POINTS)

CM (DATAFILE, WORKFILE)

This command is similar to ANGSTROM, but it is intended for data in wavenumber steps, such as produced by the Spex Ramalab or Coderg T-800 systems. DATAFILE and WORKFILE have the same significance as before, but the parameters inserted at the head and foot of the file are slightly different. At the head of the file they are:

NUMBER OF DATA POINTS, START (in cm^{-1}), CW, TEMPERATURE, and on the rest of the line, COMMENTS

These parameters must be delimited by spaces or newlines, not commas. At the foot of the file, after the last data point, the terminator 'END', or simply 'E' should be typed - on a separate line, preferably.

Example:

```
COMMAND:CM(BIPLIQ,C12F10LI)
 LIQUID,NO POLARISATION,T=4SEC
  400 DATA POINTS READ
STARTING AT -10.0 CM-1
ENDING AT  110.0 CM-1
AT  345.0K
```

The first and last lines of the data file BIPLIQ, which hold the data in parenthesis, would look like:

```
400    -10.0    0.3    345 LIQUID, NO POLARISATION, T=4SEC
 [                ↑                                    ]
                  |
                DATA
                  |
                  ↓
END
```

When data from the Ramalab system is to be processed, the channel address numbers produced by the MCS must have been previously edited out.

JOIN (F1 + F2 + ... + Fn , ALLF)

This command is a housekeeping routine used to make a single package out of several workfiles, specified in the parameter list by stringing the names together with '+' symbols. The implication is that the files will be joined, or concatenated, into a single file, ALLF in the example. The last file parameter is separated from the rest by a comma. Any number of files may be 'JOINED' provided that the whole command may be typed in a single line, and the original files are left unaltered.

Example:

```
COMMAND:JOIN(PIP2XY+PIP2X7+PIP2Y7+PIP3XY+PIP37X+PIP37Y,ALLPIP)
MONITOR ENTERED FROM IMPS
INPUT ENDED
```

COPY (ALLF #n, Gn)

A file which has been created by JOIN is different from the usual workfile. An attempt to use such a file in the normal manner would result in data from only the first file being accessed. This command however, allows any constituent of a 'JOINED' file to be copied into a normal workfile. In the parameter list, the name of the JOINED file is followed by #n where it is desired to make a copy of the nth entry. This copy is then filed under the name given by the second parameter, Gn above. The JOINED file is left unaltered.

Example:

```
COMMAND:COPY(ALLBIP≠3,BIP2XY)
BIP2XY=ALLBIP≠3
```

FIND SUB (DATAFILE)

This routine is used to locate faulty characters in data read from papertape, which is often likely to have mispunchings. If a faulty character is detected in a line, the whole line is printed with the SUB symbol ␣ indicating where the error is. From this information the faulty characters may be edited out of the file using the normal EMAS editor.

Example:

```
COMMAND:FINDSUB(DATA1)

SUB IN LINE 41
000000 000012 000038 000036 000009 000040 0000␣8

SUB IN LINE 107
001279 001193 001268 001211 001294 00␣179 001300

STOPPED AT LINE 18
```

CONTENTS (JFILE)

This is a command which allows the contents of a JOINED file to be investigated by returning a list of the original names of the files constituting the joined file. This is an aid to the use of the COPY routine.

Example:

```
COMMAND:CONTENTS(ALLBIP)
ALLBIP:
BIP2XY+BIP2XZ+BIP2YZ+BIP3XY+BIP3ZX+BIP3ZY
```

LISTSQ (FILE, START, END, STEP, XXXX.YYY)

This routine lists the contents and information contained in the workfile FILE from START (cm^{-1}) to END in steps of STEP. XXXX.YYY specifies the format of the output numbers, which in this case would have four digits before the point and three after.

More space is automatically used for numbers larger than this format but the tabular appearance of the listing will be upset.

Examples:

a) illustrates faulty parameter checking.

```
COMMAND:LISTSQ(S8ZZ300,12≠,13,5)
LIST FOR SQFILE S8ZZ300   START=12≠ !!
*PARAMETER ERROR!
```

b) with valid parameters.

```
COMMAND:LISTSQ(S8ZZ300,21,36,.5,XXX.)
LIST FOR SQFILE S8ZZ300   START=21 END=36 STEP=.5
FILE STARTS AT  -10 ENDS AT  167 CW= 0.29
TEMPERATURE=  300.0
 609  617  640  676  745  759  882  1118  1286  1524  1944  2455
 3437  4045  5635  6907  6457  5653  4363  3219  2188  1868  1362
 994  896  851  840  764  731  756
```

GRAPH (FILE, .TT, XMIN, XMAX, YMIN, YMAX, LINES)

This routine draws FILE as a graph on the teletype (.TT) or line printer (.TT parameter omitted) between the X limits XMIN and XMAX and the Y limits YMIN and YMAX. The Y axis is the full width of the page but the X axis, along the page, takes up LINES number of lines. Thus the LINES parameter controls the X-resolution of the plot.

Example:

```
COMMAND:GRAPH(DERIV,.TT,21,36,-500,+500,16)
GRAPH FOR FILE DERIV

PARAMETERS ARE:
START=21 END=36 YMIN=-500 YMAX=+500 LINES=16

-5.000@  2                                                    5.000@  2
 +------+------+------+------+------+------+------+------+------+------+
-+                                  *
 +                                   *
 +                                     *
 +                                       *
 +                                            *
 +                                                  *
 +                                                    *
 +                                            *
 +                        *
 +           *
-+        *
 +                 *
 +                    *
 +                        *
 +                          *
 +                           *

END OF GRAPH FOR FILE DERIV
```

POLYGRAPH (.TT, XMIN, XMAX, LINES, NUMBER)

does the same as graph but a total of NUMBER graphs are drawn superimposed.

The routine prompts for each graph the file name FILE and YMAX. YMIN is taken as zero.

Example:

GRAPH. 1 = S8 ZZ300, 10000

GRAPH. 2 = S8 ZZ100, 9000

This produces two graphs with plotting symbols 1 and 2 denoting S8 ZZ300 and S8 ZZ100 respectively.

Up to six graphs, occasionally more, can be drawn together in this way for comparison.

```
COMMAND:POLYGRAPH(.TT,15,40,26,2)

POLYGRAPH: START=15 END=40 LINES=26
GRAPHS=2
GRAPH.1=S8ZZ300,10000
GRAPH.2=FIT,10000
SOFILE75    S8ZZ300+FIT REPLACES S8ZZ300
-0-----+-----+-----+-----+-----+-----+-----+-----+-----+-----+
 [  21
 [  21
 [  21
 [  *
 [   *
 [   *
 [   *
 [    *
 [    *
 [     12
-[        *
 [            21
 [                  *
 [                                21
 [                                    *
 [                          21
 [                *
 [         12
 [       *
 [      *
-[     *
 [    21
 [    21
 [    2 1
 [  2   1
 [  2    1

END OF GRAPH
```

INTEGRATE (FILE, X, Y)

gives the integrated count of FILE over the range [X, Y].

The integrated count is a product of counts by bandwidth.

It is independent of the number of channels.

Example:

```
COMMAND:INTEGRATE(S8ZZ300,21,36)

S8ZZ300 INTEGRATED OVER [ 21 , 36 ]
INTEGRATED COUNT= 3.239544@  4 COUNTS.CM-1
```

SMOOTHE (FILE, X, Y, RESOLUTION, SMOOTHED)

The contents of FILE are smoothed on the range [X, Y] with a polynomial least squares fit and placed in the smoothed data file SMOOTHED (which is created or overwritten by this procedure). Thus each point in the smoothed spectrum is a convolution of neighbouring data points out to a distance of $\pm\frac{1}{2}$ RESOLUTION on either side.

Example:

```
COMMAND:SMOOTHE(IXY,10,90,4,SMIXY)
SMOOTHE: DATA=IXY START=10 END=90 WIDTH=4
```

DIFFERENTIATE (FILE, X, Y, RESOLUTION, DERIVATIVE)

Identical to SMOOTHE but instead a different convolution procedure is used to give the derivative spectrum.

Example:

```
COMMAND:DIFFERENTIATE(S8ZZ300,15,45,5,DERIV)
DIFFERENTIATE: DATA=S8ZZ300 START=15 END=45 WIDTH=5
```

PEAKS (FILE, X, Y, RESOLUTION, DERIVATIVE)

Identical to DIFFERENTIATE but the derivative is also used to give a printout of the peaks in the spectrum.

The file parameter DERIVATIVE may be omitted if not required.

The peak finding programme discriminates against noise.

Example:

```
COMMAND:PEAKS(S8ZZ300,-7,150,5)

PEAKS :DATA=S8ZZ300 START=-7 END=150 WIDTH=5
**** PEAK FROM    0 TO    1
PEAK ENDS AT    3= 1.500@   1

NEW PEAK STARTS AT    4= 7.000@   0
**** PEAK FROM   29 TO   29, 28.7= 6.772@   3
PEAK ENDS AT   36= 7.560@   2

NEW PEAK STARTS AT   36= 7.110@   2
**** PEAK FROM   49 TO   49, 48.9= 1.620@   4
PEAK ENDS AT   55= 2.012@   3

NEW PEAK STARTS AT   55= 2.095@   3
**** PEAK FROM   61 TO   61, 60.9= 8.401@   3
PEAK ENDS AT   67= 2.668@   3

NEW PEAK STARTS AT   67= 2.639@   3
**** PEAK FROM   73 TO   74, 73.4= 5.854@   3
PEAK ENDS AT  120= 1.540@   2

NEW PEAK STARTS AT  128= 1.590@   2
```

MAXIMUM (FILE, START, END)

Prints the maximum count and wavenumber at this point for the spectrum stored in FILE on the interval [START, END]. Useful for determining scales for graphing.

Example:

```
COMMAND:MAXIMUM(DERIV,15,44)

MAXIMUM COUNT FOR DERIV ON [ 15 , 44 ]

=       373 AT    26.6 CM-1
```

ALTER (FILE)

This routine allows data in FILE to be modified.

The data for a spectrum is stored as an array of points, or channels, each of which contains a count. Two parameters START and CW are also stored so that the wavenumber at any channel may be readily computed thus:

$$\nu = \text{START} + K * \text{CW}$$

START is the wavenumber at channel 0, the start of the file
K is the channel number and CW is the interval between channels.
The number of channels and run temperature we also stored.

For most purposes the user need not be concerned with channels, the conversion from wavenumber being done automatically. To access a particular data point, however, the channel number must be specified, as in this routine.

The parameter ADDR is the address of the channel in question. Altering ADDR by the use of certain commands allows access to any channel from 0 to the end of the file. This is an 'interactive routine' in which there is a dialogue between routine and user. The routine keeps the user informed about its action with messages such as:

T

0: 1093 8654 7201 5711 4986

Here *T* denotes the start or 'TOP' of the file:
B would appear at the end or 'BOTTOM'
The number to the left of the colon is the present value of ADDR which is 0, of course, at the TOP of the file. The numbers to the left are the contents of channels ADDR, ADDR + 1, up to ADDR + 4 respectively. The typed message is given

before each new set of commands issued by the user so that he sees at once where in the file he is at and what the data looks like in that neighbourhood.

To change ADDR several commands are available. They are shown here in the form in which they are actually typed but with the numerical parameters denoted by words in the angled brackets

ADDR = ⟨channel number⟩

MOVE = ⟨number of channels back or forward⟩

CM - 1 = ⟨wavenumber position⟩ and ADDR is set to nearest channel

$\left\{ \begin{matrix} > \\ < \end{matrix} \right\}$ = ⟨count⟩ . and ADDR is set to next channel $\left\{ \begin{matrix} \text{greater} \\ \text{less} \end{matrix} \right\}$ than or equal to this count.

To change the data in the channels starting at the present ADDR the command:

DATA = ⟨new count⟩at ADDR , ⟨new count⟩at ADDR + 1 ....

as many new data as required can be entered successively in this way. ADDR is incremented at each step so that at the end it is the channel number of the last data point altered.

The parameters START, CW, TEMP, may be reset by the commands:

START = ⟨new value of start position⟩

CW = ⟨new value of CW⟩

TEMP = ⟨new value of temperature⟩

In addition, these parameters and CM - 1, the wavenumber position, may be queried by typing:

? instead of a parameter. For example,

START = ?

may be responded to with a reply such as

START = - 10

where - 10 would be the wavenumber at channel 0.

It is not possible, however, to increase or decrease the number of data points, and it should be noted, with this in mind, that the only effect of changing the parameters START and CW is to translate and dilate the spectrum. There will be only one value of START and one of CW corresponding to the experimental conditions, so that the provision for altering them is only for error correction, as indeed is the primary intention of the DATA = command. To use the routine, commands are typed after the prompt '=' and may be strung together on a single line, separated by commas, if desired. Invalid commands or parameters are faulted. A line of commands is stopped at an error should any be found, so that subsequent commands in the same line are ignored. This prevents catastrophic results occurring by accident, but the user should be aware that he must retype the remaining commands as well as the corrected one. The command STOP terminates the routine and replaces the old data with the new version. QUIT aborts all action and leaves the data unchanged from at the start of the routine. Thus this command is a last ditch measure which can be taken in moments of crisis to cancel the possible ruination of the data.

Further details are best found out by exploring the routine on test data, and by studying the example.

```
COMMAND:ALTER(FIT)
*T*
    0:    407     409     411     413     415
=CM-1=?
CM-1=     12.0
*T*
    0:    407     409     411     413     415
=CM-1=28.7
CM-1=28.7

   58:   6804    6876    6500    5812    5009
=PRINT=12

   58:   6804    6876    6500    5812    5009    4237    3566    3012
   66:   2565    2208    1923    1693    1508

   58:   6804    6876    6500    5812    5009
=MOVE=-3

   55:   4763    5568    6311    6804    6876
=TEMP=?
TEMP=    300.000

   55:   4763    5568    6311    6804    6876
=TEMP=297
TEMP=297

   55:   4763    5568    6311    6804    6876
=DATA=4764,4"5569,6312,6805,6877

   59:   6877    6500    5812    5009    4237
=MØVE=-3,ADDR=55
MØVE?

   59:   6877    6500    5812    5009    4237
=MOVE=-3,ADDR=55

   55:   4764    5569    6312    6805    6877
=START
START?

   55:   4764    5569    6312    6805    6877
=ADDR=1000

   98:    469
*B*
=DATA=99,100

   95:    489     482     475      99
*B*
TOO MUCH DATA!

   98:     99
*B*
=ADDR=0
*T*
    0:    407     409     411     413     415
=ADDR=?
PARAMETER?
*T*
    0:    407     409     411     413     415
=CW=?
CW=      0.286
*T*
    0:    407     409     411     413     415
=STOP
```

FIT (DATA, FIT, START, END, MODEL, LIMIT, PRINT)

Users of this routine should be familiar with the pitfalls of parameter fitting. Handled with due appreciation and interpretation of the results, it is very useful. Handled with gay abandon the results may be meaningless.

The routine FIT fits the spectrum in the file DATA on the interval [START, END] with a specified MODEL, which at present may be one of UNCLO, UNSHO, DEBYE, TEST described below. The number of iterations taken is bounded by LIMIT, and a device or file e.g..TT, or .LP may be nominated for listing of messages produced at each iteration. These may be lengthy and time consuming to print "on-line". Experience will show the best use of this parameter.

The resulting function should be a fit to the spectrum in the least-squares sense for Poisson data (weighting factor $\frac{1}{\sqrt{N}}$). Thus a good fit is obtained when the error is dominated by noise. Whether or not the fit has any significance is another matter, to be answered on a more philosophical basis. This 'fit' function can be filed in the same manner as any other by nominating a file FIT for its storage. If FIT is set to NULL no 'fit' is filed.

UNCLO

This model uses a number of uncoupled (independent) Lorentzian functions of the form

$$\frac{\text{STRENGTH} * \text{GAMMASQ}}{(\omega - \text{WMAX})^{**2} + \text{GAMMASQ}}$$

plus a background.

The parameters are typed as in the example below.

V prefixes a variable parameter, F a fixed parameter.

END signifies no more oscillators to be used.

If an error is found the line may be retyped.

UNSHO

This model uses a number of uncoupled simple harmonic oscillator functions of the form

$$\frac{\text{STRENGTH} * \text{WMAX}^2 * \text{GAMMASQ} * \omega * (n(\omega) + 1)}{(\omega^2 - \text{WMAX}^2)^{**2} + \text{GAMMASQ} * \omega^2}$$

plus a background.

Note: WMAX^2 is now the squared frequency. $\sqrt{\text{GAMMASQ}}$ corresponds to the full width at half maximum in the underdamped limit. The bose factor $(n(\omega) + 1)$ is included. There are subtle differences from the Lorentzian model.

DEBYE

This is the same as UNSHO for all but the first oscillator which has the form

$$\frac{\text{STRENGTH} * \text{GAMMASQ} * \omega * (n(\omega) + 1)}{\omega^2 + \text{GAMMASQ}}$$

i.e. an overdamped wing. The WMAX parameter is not used for this but nonetheless should not be prefixed by V.

TEST

This allows general fitting to a user supplied function of the form

% Externalrealfnspec TESTFIT (% Realarrayname P, % Real ω)

which returns as a result of the value of a function f(P(1),..., P(N), ω) at the point ω.

```
COMMAND:FIT(S8ZZ300,FIT,21,36,UNCLD,10,.1)

IFILE=S8ZZ300
START=21 END=36
MODEL=UNCLD MAXIT=10
STRENGTH  WMAX GAMMASQ
1=V6000,V28.7,V5
2=END
BACKGROUND:
=V100


LEAST SQUARES ROUTINE LSQFIT 21.10.28  15/01/74
  4 VARIABLE PARAMETERS   50 DEGREES OF FREEDOM

ITERATION   1 PHISUM= 9.7885@  0
OLD CHISQR= 4.7907@  3 NEW CHISQR= 6.4028@  3
OLD CHISQR= 4.7907@  3 NEW CHISQR= 3.1815@  3
FLAMDA= 1.0000@ -2 DELTA= 1.0000@ -3

PARAMETERS,UNCERTAINTIES :
PARAM(  1) =  6.14591@  3( 2.83@  1)
PARAM(  2) =  2.87397@  1( 7.75@ -3)
PARAM(  3) =  1.45154@  0( 7.70@ -2)
PARAM(  4) =  4.39424@  2( 1.22@  1)
ITERATION   2 PHISUM= 7.9768@  0
OLD CHISQR= 3.1815@  3 NEW CHISQR= 2.1827@  2
FLAMDA= 1.0000@ -3 DELTA= 6.6667@ -4

PARAMETERS,UNCERTAINTIES :
PARAM(  1) =  6.41754@  3( 4.22@  1)
PARAM(  2) =  2.87345@  1( 7.21@ -3)
PARAM(  3) =  2.20768@  0( 2.78@ -2)
PARAM(  4) =  3.73292@  2( 7.75@  0)
ITERATION   3 PHISUM= 2.0894@  0
OLD CHISQR= 2.1827@  2 NEW CHISQR= 1.8870@  2
FLAMDA= 1.0000@ -4 DELTA= 4.4444@ -4

PARAMETERS,UNCERTAINTIES :
PARAM(  1) =  6.54859@  3( 3.74@  1)
PARAM(  2) =  2.87361@  1( 7.12@ -3)
PARAM(  3) =  2.24279@  0( 3.72@ -2)
PARAM(  4) =  3.54804@  2( 8.93@  0)
ITERATION   4 PHISUM= 1.9427@  0
OLD CHISQR= 1.8870@  2 NEW CHISQR= 1.8870@  2
FLAMDA= 1.0000@ -5 DELTA= 2.9630@ -4

PARAMETERS,UNCERTAINTIES :
PARAM(  1) =  6.54934@  3( 3.72@  1)
PARAM(  2) =  2.87361@  1( 6.99@ -3)
PARAM(  3) =  2.24069@  0( 3.70@ -2)
PARAM(  4) =  3.55105@  2( 9.00@  0)
ITERATION   5 PHISUM= 1.9427@  0
CONVERGENCE

CORRELATION COEFFICIENTS IN DECREASING ORDER:
  4-  3=-0.73     3-  1=-0.60     4-  1= 0.09     4-  2= 0.01     3-  2=
-0.01
  2-  1= 0.00

PARAMETERS AFTER FITTING ARE:
BAND    STRENGTH      WMAX       DAMPING
  1   6.5493@  3   2.8736@  1   2.2407@  0

BACKGROUND= 3.5510@  2
FILE FROM ..TO :
=12,40
OUTPUTFILE FIT CREATED
```

```
COMMAND:FIT(S8YY300,FIT2,40,60,UNSHO,10,HASH)

IFILE=S8YY300
START=40 END=60
MODEL=UNSHO MAXIT=10        SQFILE75   S8YY300 REPLACES S8YY300+FIT
     SQFILE76   FIT2 REPLACES FIT

STRENGTH  WMAX GAMMASQ
1=V200,V2500,456
!!PARAMETER ERROR-REPEAT
1=V200,V2500,V56
2=END
BACKGROUND:
=V292

PARAMETERS AFTER FITTING ARE:
BAND     STRENGTH      WMAX        DAMPING
  1    3.7787@  2   2.5450@  3   1.5128@  1

BACKGROUND= 1.3104@  2
FILE FROM ..TO :
=30,70
OUTPUTFILE FIT2 CREATED
```

Note that in this example the print-out is stored in a

in a file, HASH.

Faults will occur in this routine if the user tries to give more or less parameters than required by his version of TESTFIT.

Symbols used in the print-out from the fitting process are listed here:

$$\text{CHISQR} = \sum_i \frac{(Y_i - f(\omega_i))^2}{\sqrt{Y_i}}$$

$$\text{PHISUM} = \sqrt{\text{CHISQR}/(n_{obs} - 1)} \doteq 1 \text{ for 'good' fit to 'noisy' data.}$$

FLAMDA, DELTA .... ignore

PARAM(i) = value of i_{th} variable parameter

Quantity in parentheses = $\pm$ estimated error

CORRELATION COEFFICIENTS

C_{ij} indicates to what extent variable parameters i and j have the same effect on the goodness of fit

C_{ij} = 1 complete positive correlation

C_{ij} = 0 no correlation

C_{ij} = -1 complete negative correlation.

After the fitting has been done, and assuming a request to file the fitted data was made by specifying `FIT' to be something other than NULL, a prompt:
FILE FROM..TO:
is given. Here the user specifies the limits in the form
START, END
and an output-file FIT is created containing data points for the fitted function on this range. The earlier example of POLYGRAPH shows how, for example, the data file and fitted spectrum file can be plotted together.
The two examples of the use of FIT are for UNCLO and UNSHO models respectively. Note that the fitting parameters have different meanings for the different models. In one example, the output generated by the fitting procedure is listed on the teletype, .TT, whereas in the other it is filed in a text file HASH which could later be listed or edited by EMAS routines to find its contents.

GRAPH PLOTTER (FILE 1, FILE 2, ..., FILE N)

This is a routine for graphing spectral data in a form suitable for publication. Graph plotting is done on the CALCOMP attached to EMAS. This is a fairly expensive and time consuming business, not recommended for actual data analysis. Here again the program is highly interactive with reasonable flexibility - but to avoid complication the graphs take a fixed format and data is always in the form of a standard workfile containing up to 1024 data points.

The parameters FILE 1 to FILE N are the names of files from which graphs will be drawn. Below is an example of the use of this routine showing prompts - typed before the colon - and responses typed after - faults are queried when trapped.

```
COMMAND:GRAPH PLOTTER(S8XX300,S8YY300,S8ZZ300,S8XY300X,XY150B)
GRAPH NUMBER 1
X,Y,PRINT (CM):15,20,.22
TITLE:B_1@G@^ S@PECTRUM - XY
XMIN,XMAX,DX:20,60,10
X-CAPTION:W@AVENUMBER@ [@CM^-1_@] -->
YMIN,YMAX,DY:0,5000,1@3
Y-CAPTION:I@NTENSITY@ -->

PLOT 1 :S8XY300X,20,60,1.017,CURVE,_

PLOT 2 :XY150B,20,60,1.017,DASH,_

PLOT 3 :CLOSEPLOTTER
```

Points to note in the above example are;

character set translation.

interpretation of DX and DY parameters with respect to format for numbers printed along axes.

plotter data files refer back to the initial parameter list given at command time.

CLOSEPLOTTER terminates all drawing and routine returns to command level.

Example of graph plotter output corresponding to command example on previous page.

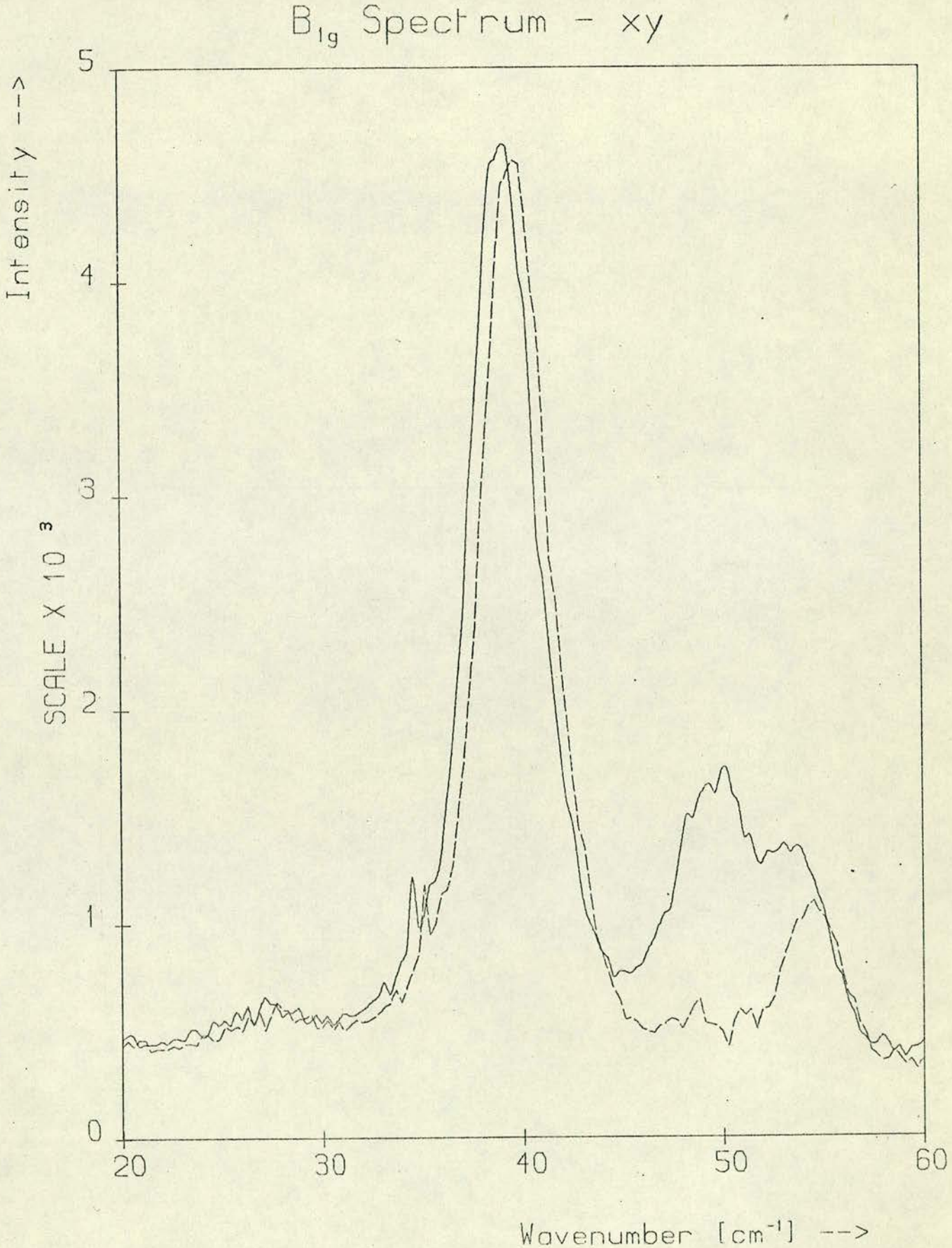

X, Y, PRINT:

Size in cms of X and Y axes on the paper and width of printed characters.

The example is suitable for A4 format.

TITLE:

The string of characters following the : on the rest of the line is reconstructed to an extended symbol set by the following rules:

@ shift to lower case from upper case (or vice versa)

? shift to Greek characters from English (or vice versa) (@ still applies to give Greek upper and lower case, for which see the table 1 below).

␣ shift to subscript mode

↑ shift to superscript.

Note $@^{-1} = @$

$?^{-1} = ?$

$\uparrow^{-1} = ␣$

$␣^{-1} = \uparrow$

The symbol ! erases all previously typed characters back to the start of the line. Numerics and other special symbols are unaffected by @ and ?

Normal mode, assumed at the start, is upper case english text.

Thus AS! ? @ A @ ? S␣8 ↑ ?C?↑1+␣M@ODES@

Is reconstructed to:

$$\propto S_8 \quad \Gamma^{1+} \text{ Modes}$$

The title appears at the top of the graph, centred and 1.5 times normal print size.

XMIN, XMAX, DX:

X axis starts at XMIN and ends at XMAX. Marks are drawn at DX with corresponding values of X printed below - in the same format as DX appears on the typed line. Where the @ (exponent) form is used the axis is labelled:

SCALE X 10^{n} (where n is the appropriate exponent.)

XCAPTION:

As for title, but here the print size is normal and the text right justified under the X axis.

YMIN, YMAX, DY: as per X axis

YCAPTION : as per X axis

Having completed the drawing of the frame for the graphs, plotting may begin. Any part of the files given in the initial parameter list may be drawn, and in several ways. Following the prompt PLOT n: ,the rest of the parameters to be typed are FILENAME, START, END, SCALEFACTOR, TYPE, SYMBOL.

The portion from START to END of FILENAME will be drawn scaled up by SCALEFACTOR. Any part lying outside the declared area of the graph will be truncated. TYPE is one of four possibilities:

POINT: data points not joined

LINE : data points joined by straight lines

CURVE: data points joined by smoothe curve

DASH : data points joined by dashed line

In each case data points are marked by SYMBOL, drawn to an appropriate size and corresponding to the table (2) below. SYMBOL is an optional parameter and is assumed to be blank if omitted.

After the desired number of plots have been completed the response: END completes the plot and starts a new graph, whereas CLOSEPLOTTER ends the routine completely.

After the first graph, the parameters for setting up the axes, etc. may be retained by typing * instead of new information. This simplifies plotting many graphs with the same format.

The completed graphing information is filed in a utility file called GRAPHILE which must be sent to the plotter via the command SENDGP (GRAPHILE).

Another utility file is used, named HASH. This contains a record of the parameters used in making a graph and of the files used. It is plotted out beside each graph as identification.

Example:

```
COMMAND:SENDGP(GRAPHILE)
JOB EGNP3131 WILL BE SENT TO THE 370
```

Update: SENDGP is no longer valid. Use SEND or LIST with device parameter '.GP'

Example:

TABLE 1

A	a	A	α
B	b	B	β
C	c	Γ	γ
D	d	Δ	δ
E	e	E	ε
F	f	Z	ζ
G	g	H	η
H	h	Θ	θ
I	i	I	ι
J	j	K	κ
K	k	Λ	λ
L	l	M	μ
M	m	N	ν
N	n	Ξ	ξ
O	o	O	ο
P	p	Π	π
Q	q	P	ρ
R	r	Σ	σ
S	s	T	τ
T	t	Υ	υ
U	u	Φ	φ
V	v	X	χ
W	w	Ψ	ψ
X	x	Ω	ω
Y	y		
Z	z		
[	{		
]	}		

Character translation from Teletype to extended symbol set using ⓐ and ?

TABLE 2

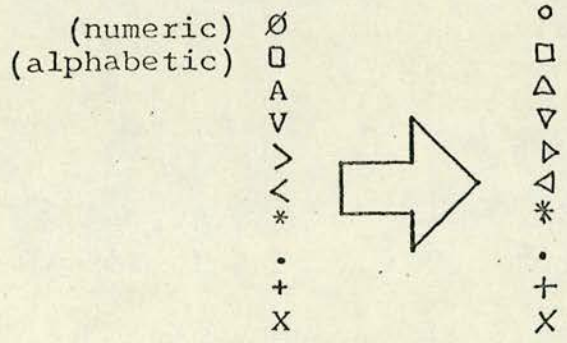

Point symbol translation from Teletype to plotting symbols.

APPENDIX V

PUBLISHED PAPERS

'The Raman Spectrum of Ammonium Bisulphate'
J.W. Arthur, D.J. Lockwood and W. Taylor, in
'Advances in Raman Spectroscopy, Volume 1',
ed. J.P. Mathieu (Heyden, London) 1973.

'Raman Study of Rubidium Bisulphate'
J.W. Arthur and W. Taylor,
Ferroelectrics 7 (1974), in press.

'Automation Techniques for Raman Spectroscopy'
J.W. Arthur and D.J. Lockwood,
J. Raman Spectrosc. 2, No. 1, 53 (1974).

'The External Lattice Vibrations of Orthorhombic Sulphur'
J.W. Arthur and G.A. Mackenzie,
J. Raman Spectrosc. 2, (1974), in press.

Ferroelectrics
1974, Vol. 7,

RAMAN STUDY OF RUBIDIUM BISULPHATE

J. W. ARTHUR and W. TAYLOR

University of Edinburgh, Scotland

(Received September 10, 1973)

Rubidium bisulphate ($RbHSO_4$) is ferroelectric below −15°C. The *yy* spectrum has been studied over the range 80 K–350 K, and the off-diagonal spectra have been recorded at room temperature and 100 K. The external vibration spectrum of the HSO_4 ion is affected by the onset of spontaneous polarization. The external vibration spectrum is complicated by the large number of modes in a small frequency range 0–80 cm^{-1}. An evident feature, however, is strong "Rayleigh-Wing" scattering. This is present in both high and low temperature phases, but at 55 K below the transition it appears to give way to an underdamped mode.

INTRODUCTION

Neither of the ferroelectrics Rubidium Bisulphate ($RbHSO_4$, here called RHS) and its isomorph Ammonium Bisulphate (NH_4HSO_4 or AHS) has received a great deal of attention of late, not least of all becuase of their complicated structure.[1,2]

Pepinsky and Vedam[3] reported that RHS undergoes a ferroelectric phase transition at 258 K (cf. 270°K in AHS[4]) and Nelmes[5] has used x-ray diffraction thermal parameter measurements to show that the transition in AHS is of the order-disorder type. The results of Ashmore[6] on RHS are consistent with this picture in which one of the two inequivalent sets of SO_4^{2-} ions of the paraelectric phase is disordered above T_c; below T_c they become ordered into one of two possible orientations giving rise to a reversible polarization. The role played by the protons is not clear but Kasahara and Tatsuzaki[7] have shown the corresponding transition point in AHS, at 270 K, to be reduced by 8 K on deuteration. It is suggested from this that the protons do not play a major role as they do in KDP type crystals.

The purpose of the present work was to extend the earlier work on AHS[8] not only to draw a comparison but also to see if in this case it would be possible to identify low frequency scattering with the transition. In AHS there is also a lower, first-order, transition at 155 K to a new paraelectric phase in which the NH_4 groups are thought to be involved. The presence of NH_4 librations also adds to the low frequency scattering, and therefore RHS is much more suitable for studying the ferroelectric transition by light scattering.

The paraelectric phase of RHS has space group $P2_1/c$ with 8 formula units per primitive cell with all atoms at general positions. The HSO_4^- ion may be treated as a molecular group with 3 translational, 3 rotational and 12 internal degrees of freedom. The results concerning the internal modes, however, will appear elsewhere.

In the ferroelectric phase the space group becomes Pc, which has no centre of inversion. As in AHS, a ferroelectric mode giving a polarization along the *c*-axis would have symmetry B_u in the high temperature phase and A' in the temperature phase. Such a mode would be expected to be Raman active only below T_c. Above T_c, however, it would be possible to see other modes associated with the SO_4 order-disorder mechanism which do have the correct symmetry but are not ferroelectric. It is also possible that a ferroelectric mode would be observed at $q \neq 0$ above T_c since disorder destroys translational invariance.

RESULTS AND DISCUSSION

With the chosen orientation of the crystal in the cryostat it was possible to measure the *xy*, *xz*, *yz* and *yy* spectra, the latter showing the most pronounced low frequency scattering.

From the outset the low frequency region was the main region of interest. As in AHS, the *yy* spectrum (Figure 1) shows pronounced scattering near zero frequency. At higher temperatures this appears as a wing rising onto the exciting line, but below 190 K this wing appears to give way to an underdamped mode which increases in frequency and finally coalesces with a mode at 34 cm^{-1} at 80 K. In order to make a comparison between spectra at various temperatures, $\chi''(\omega)/\omega = PI(\omega)/\hbar\omega\,(n(\omega)+1)$ was plotted against frequency where $I(\omega)$ is the experimentally measured spectrum and P is a scale factor chosen so that $\int \chi''(\omega)/\omega\, d\omega$ over a line at 443 cm^{-1},

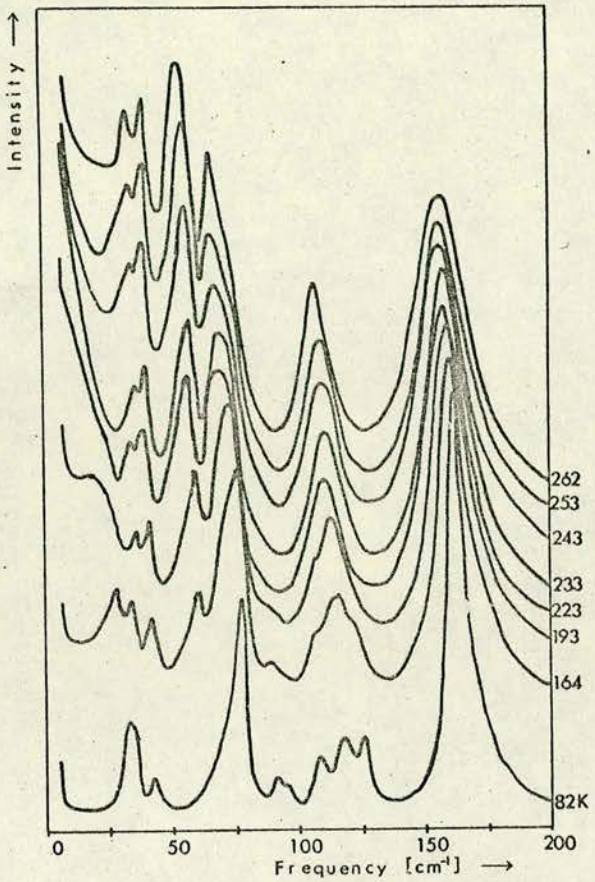

FIGURE 1 Low frequency scattering of *yy* polarization.

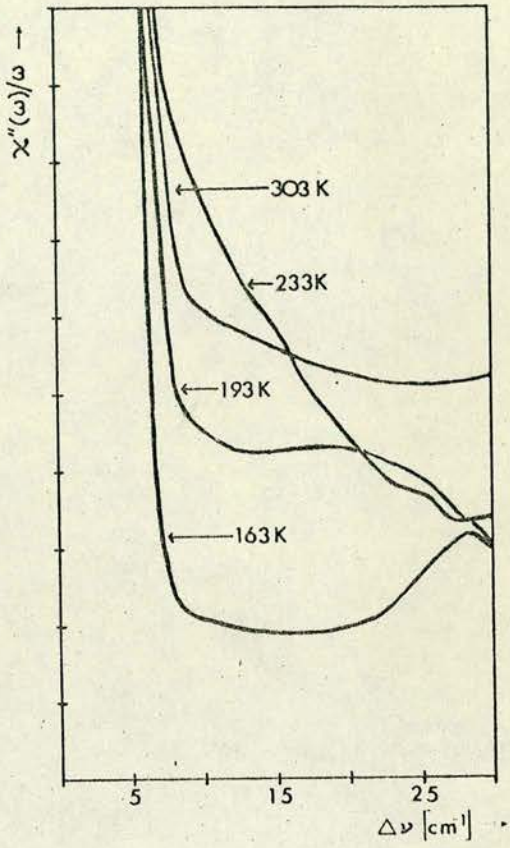

FIGURE 2 Comparison of low frequency scattering showing development of wing feature.

which is assumed to have fixed intensity, is constant. This effectively standardized the intensities and takes out the term $k_B T$ in the lowest frequency scattering. Comparing these plots it is seen that a considerable temperature dependence does exist and that a definite wing takes form near 230 K. Furthermore, the intensity of the low frequency scattering is always increasing (Figure 1).

To characterize the low frequency wing an attempt was made to fit a Debye oscillator of the form

$$I(\omega) = (n(\omega) + 1)\frac{S\omega}{\omega^2 + \Gamma^2}$$

varying S and Γ and with a fixed flat background. The parameter Γ can be interpreted as either the inverse lifetime of a relaxation process, or a quantity proportional to $\omega_0{}^2$ for a highly over-damped mode. It was found that $1/\Gamma$ had a maximum around 235 K of about 0.06 cm^{-1} and fell away to about 0.04 cm^{-1} near 220 K and 250 K, but throughout this range the integrated intensity was nearly constant. Outside this range the model does not fit the spectra.

An unusual feature of the spectra is a peak at 57 cm^{-1} with an anomalous temperature dependence. It is almost absent at 80 K but eventually dominates its neighbouring peak at 68 cm^{-1} at room temperature.

To conclude, in the low frequency region there is the possibility of a mode which goes overdamped at 190 K, but there is no divergence in lifetime or intensity at T_c and only a weak maximum in the lifetime at $T_0 \approx 235$ K (some 24 K below the transition).

In view of this and the fact that the scattering persists in the high temperature phase it may be that the scattering could be accounted for by a mode associated with the SO_4 group disorder which is symmetric in the paraelectric phase and therefore not a ferroelectric mode.

ACKNOWLEDGEMENT

The financial support of the Science Research Council is acknowledged.

REFERENCES

1. R. J. Nelmes, *Acta Cryst.* B27, 272 (1971).
2. R. J. Nelmes, *Acta Cryst.* A28, 445 (1972).
3. R. Pepinsky and K. Vedam, *Phys. Rev.* 117 1802.
4. R. Pepinsky, K. Vedam, S. Hoshino and K. Okaya, *Phys. Rev.* 111, 1508.
5. R. J. Nelmes, *Ferroelectrics* 4, 133 (1972).
6. P. Ashmore, to be published.
7. M. Kasahara and I. Tatsuzaki, *J. Phys. Soc. Japan* 29, 1392 (1970).
8. J. Arthur, D. Lockwood and W. Taylor, *Advances in Raman Spectroscopy*, 1 (Heyden and Son, London).

Reprinted from

ADVANCES IN RAMAN SPECTROSCOPY, VOLUME 1

(Proceedings of Third International Conference on Raman Spectroscopy, Reims, France, September 1972)

Heyden & Son Ltd., London

17. THE RAMAN SPECTRUM OF AMMONIUM BISULPHATE

J. W. Arthur, D. J. Lockwood and W. Taylor
Department of Physics, University of Edinburgh, Edinburgh, Scotland

INTRODUCTION

Ammonium bisulphate (NH_4HSO_4 or AHS) has three crystalline phases. At room temperature the space group is $P2_1/c$, but at 270 K there is a second-order phase transition to P_c and below this at 154 K there is a first-order transition to P_1. At the upper transition there is a sharp dielectric anomaly, below which the crystal becomes ferroelectric.[1] This anomaly, however, is much smaller than in the classic ferroelectrics KDP and $BaTiO_3$ where strong low frequency Raman scattering in the form of temperature dependent 'Rayleigh wings' has been observed[2] and interpreted variously in terms of an overdamped phonon, which in KDP is coupled with a hydrogen bond order-disorder mechanism.

The aim of the present work was to determine if scattering from a similar mechanism might be observed in AHS. It would appear that the NH_4^+ ions are not involved in the upper transition, since a similar transition exists in RHS ($RbHSO_4$) at 258 K; but there is evidence that they have a high degree of rotational freedom and take part in the lower transition.[3] Recent structural work on AHS by Nelmes[4] indicates large thermal parameters for one of the symmetrically inequivalent types of sulphate ion in the room temperature structure. Nelmes has fitted this to a model in which these ions are disordered between two orientations.[5] In passing to the ferroelectric phase the centre of inversion is lost, and the disordered ions become ordered.[6] It is possible that this ordering mechanism is associated with a ferroelectric mode as postulated by Cochran in his lattice dynamical theory of ferroelectrics.[7] It is difficult, however, to regard the sulphate order-disorder motion as a phonon, and it may be more appropriate to interpret the spectra in terms of molecular dipole reorientation.

The positions of the H^+ ions with respect to the SO_4^{2-} ions have not been determined in the ferroelectric phase, but it is clear that they are already ordered at room temperature.[4,5] In addition to this, deuteration does not appreciably affect the transition temperatures.[8] Although this seems to indicate that the hydrogens play no direct part in the transition, there may be some involvement, as suggested by infrared[9] and NMR[3] via H bonding between sulphate groups along the *b* axis.

Earlier Raman work on AHS has been carried out by Bazhulin *et al.*[10] using mercury lamp excitation, but no low frequency or extensive polarization data were reported.

GROUP THEORY

AHS has eight formula units in the primitive cell giving 264 normal modes at $q = 0$. Considering the internal molecular vibrations of NH_4^+ and HSO_4^- separately, there are 93 external lattice modes, excluding acoustic modes. In the room temperature phase the modes are classified according to the irreducible representations of the point group $C_{2h}(2/m)$

$$\begin{aligned} &\text{Translatory modes:} && 12A_g + 12B_g + 11A_u + 10B_u \\ &\text{Rotatory modes:} && 12A_g + 12B_g + 12A_u + 12B_u \end{aligned}$$

The remaining internal modes transform as:

$$42A_g + 42B_g + 42A_u + 42B_u$$

The 'g' modes are Raman active, whereas the 'u' modes are infrared active. If the Y axis is oriented along the crystallographic b axis, the Raman tensor has the form:

$$\begin{pmatrix} a & & d \\ & b & \\ d & & c \end{pmatrix} \sim A_g \qquad \begin{pmatrix} & e & \\ e & & f \\ & f & \end{pmatrix} \sim B_g$$

For infrared polarizations, $P_y \sim A_u$, and $P_x, P_z \sim B_u$.

In the ferroelectric phase, the modes transform under the irreducible representations of C_s, and the compatibility relations are

$$\begin{aligned} C_{2h}(A_g, B_u) &\longrightarrow C_s(A') \\ C_{2h}(A_u, B_g) &\longrightarrow C_s(A'') \end{aligned}$$

The centre of inversion is no longer present and all modes are simultaneously Raman and infrared active.

The 9 internal modes of the NH_4^+ ion and the 12 internal modes of the HSO_4^- ion give rise to 72 and 96 modes respectively in the crystal. In the room temperature phase these modes transform as

$$\begin{aligned} NH_4^+ &: \quad 18A_g + 18B_g + 18A_u + 18B_u \\ HSO_4^- &: \quad 24A_g + 24B_g + 24A_u + 24B_g \end{aligned}$$

The compatibility relations can be applied to give the results for the ferroelectric phase.

A rotatory motion of the SO_4^{2-} ions, as associated with the upper phase transition, transforms as B_u above, and A' below the transition. It is therefore to be expected that a related soft ferroelectric mode, if it exists, would appear in the Raman spectrum only below the transition in the xx, yy, zz or xz polarizations, unless there is a relaxing of selection rules above the transition caused by the disorder situation in the lattice.

RESULTS AND DISCUSSION

The Raman spectra of AHS were recorded using conventional techniques. The

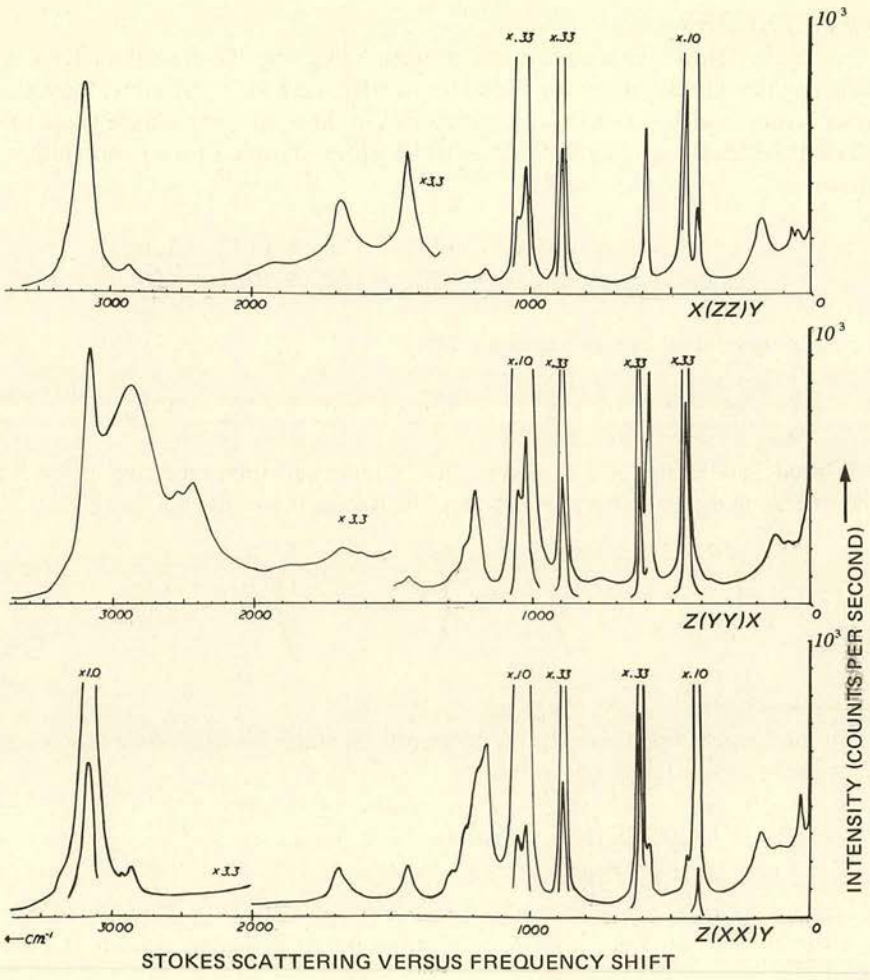

Fig. 1. Stokes scattering at room temperature.

excitation used was the 488 nm line of the argon-ion laser, and the spectrometer slit width was about 3 cm^{-1}. The sample was a single crystal of approximate dimensions 4 mm × 5 mm × 6 mm, with *X*, *Y* and *Z* directed along the *a*, *b* and *c* axes of the pseudo-orthorhombic cell. The spectra are displayed in Figs. 1–3, and the frequencies and assignments are presented in Tables 1 and 2. All the internal frequencies of the SO_4^{2-} ion reported by Bazhulin *et al.*[10] were observed, but the frequencies obtained here are higher by as much as 9 cm^{-1}. The assignments were based on free-ion frequencies and the results of other works.[9,11]

Although group theory predicts a doubling in the number of Raman active lattice modes, no significant change takes place on passing through the 270 K transition. It is possible that, as in $BaTiO_3$, the disordered nature of the lattice breaks the expected symmetry requirements.[12] On the other hand, comparison of the Raman spectra with the infrared spectra of Schutte and van Rensburg[9] shows that the frequencies of the internal vibrations are apparently exclusive, still consistent with a centre of inversion. In

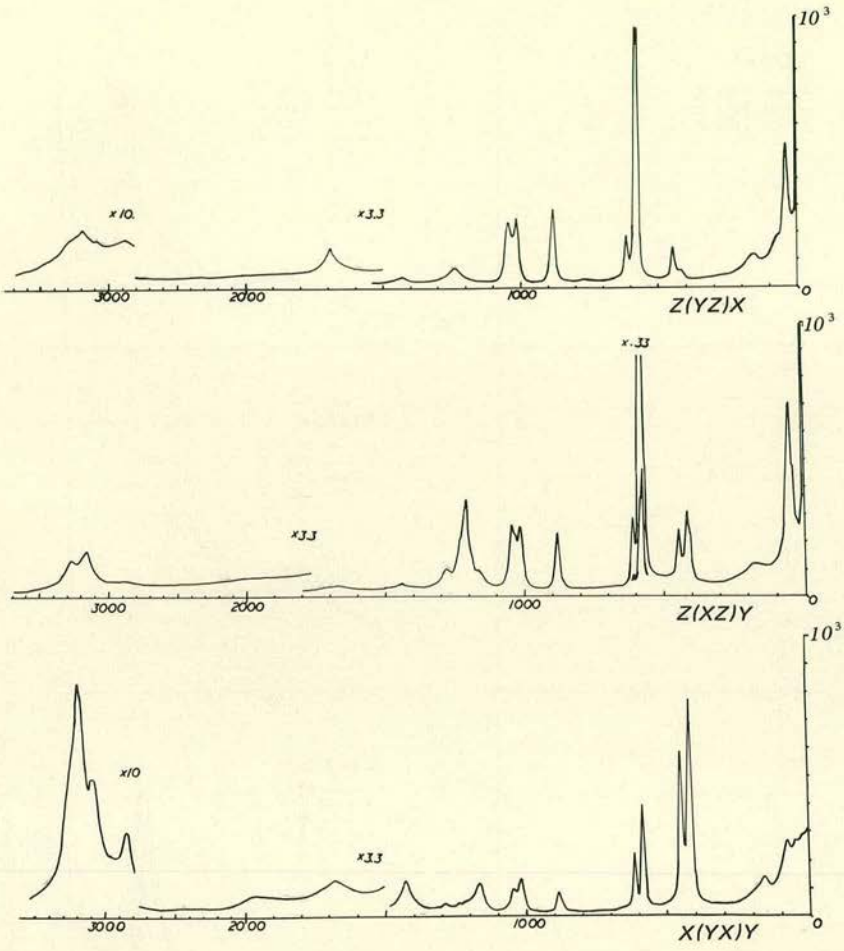

Fig. 2. Stokes scattering at room temperature.

the ferroelectric phase, the deviation of the structure from one having a centre of inversion is quite small, suggesting that most of the modes which are infrared active at room temperature become only weakly Raman active in the ferroelectric phase and are not easily seen.

In the low frequency region, principal features of interest are the prominent 'Rayleigh wings', especially obvious in the yy and xy spectra. These Rayleigh wings exhibit some temperature dependence; between 290 K and 170 K the xy wing loses intensity in an approximately linear fashion, but, perhaps more interestingly, the yy wing appears to change its profile, losing intensity and simultaneously revealing a small temperature dependent peak around 40 cm^{-1}. The yy spectrum is compatible with modes of A' symmetry, this being the expected symmetry of a ferroelectric mode involving SO_4^{2-} rotatory motions as mentioned above. It is possible, however, that the Rayleigh wings result from nearly-free NH_4^+ rotations, but some distortion of the ion from T_d symmetry would then be necessary to allow Raman activity. It is not clear that these wings can be accounted for by a soft mode at the upper transition, particularly as they change little

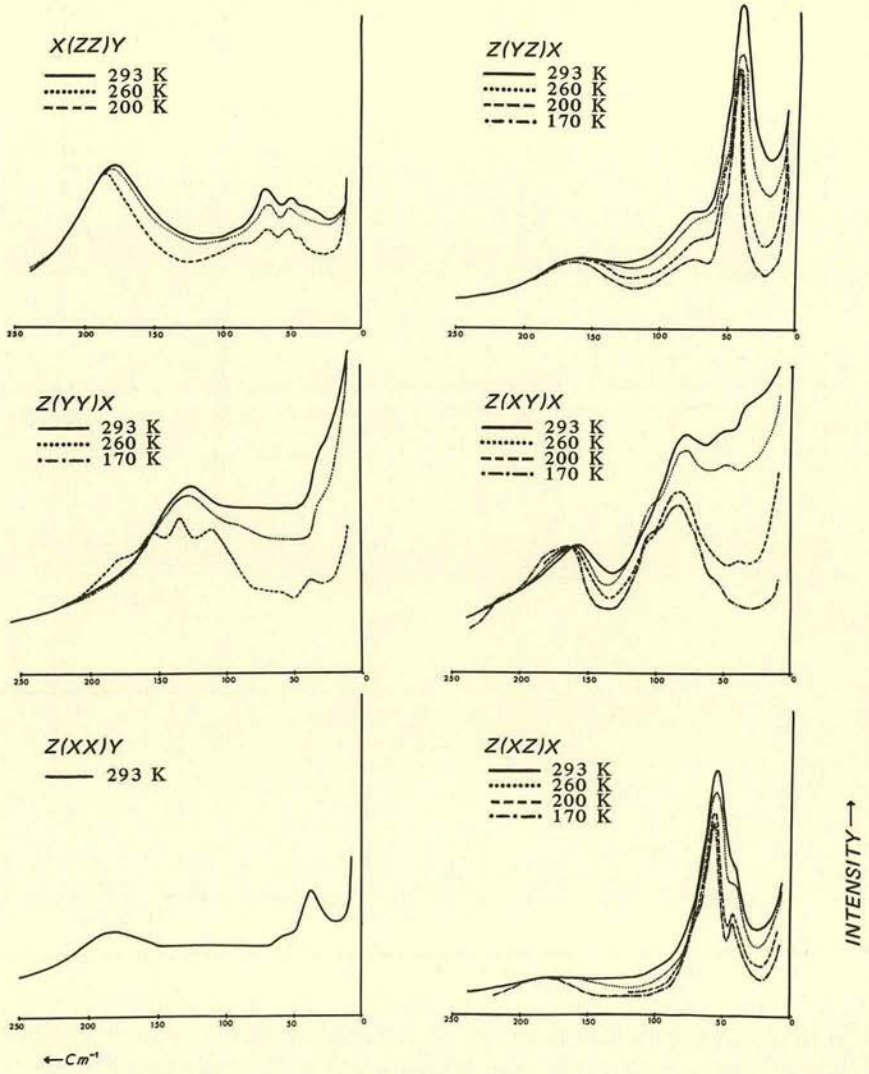

Fig. 3. Low frequency scattering.

at this point. Some additional temperature dependence is found in the frequency of some strong, low-frequency peaks. In the *yz* spectrum, for example, a peak shifts out from 40 cm^{-1} at 290 K to 45 cm^{-1} at 170 K.

In the high frequency region, a feature of interest is the very broad 2870 cm^{-1} peak in the *yy* spectrum ($\Delta\nu \approx 600$ cm^{-1}). This is presumably the O–H stretch band. Some broadening might be expected in this band because of the role played by the hydrogens in the O–H – – – O bonding which couples the SO_4^{2-} ions along the *b* axis. Unfortunately, the behaviour of this 2870 cm^{-1} peak could not be clearly observed in the ferroelectric phase because it is obscured by intensity from a strong background which appeared in the region 300–3500 cm^{-1}

Table 1. Internal molecular frequencies at room temperature, cm^{-1}.

XX		*YY*		*ZZ*		*XZ*		*XY*		*YZ*		
ν	$\Delta\nu$	ν	$\Delta\nu$	ν	$\Delta\nu$	ν	$\Delta\nu$	ν	$\Delta\nu$	ν	$\Delta\nu$	
404 s	13			404 s	16	410 sh						
						419		419	18	418		$\nu_2\ SO_4^{2-}$
445		446 s		443 vs	15	448		449	14	446	16	
578		575				576 s				575 s		
		582		586	16	583 sh		585		583 s		$\nu_4\ SO_4^{2-}$
609 s	10	611 s	11	612 wsh		611		615		615	19	
		750 vw										S-O-H torsion
881 s	18	887 s	18	883 s		880	17	883 w		882	19	$\nu_1\ SO_4^{2-}$
1014 vs		1017 vs		1014 s		1017		1017		1018		
1043 vs		1046 vs		1043 s		1044		1047		1046		$\nu_3\ SO_4^{2-}$
1155				1160 w		1160 w		1168				$\nu_4\ SO_4^{2-}$
1188 sh		1188				1213						
1230 sh		1235 sh		1220 sh		1230 sh		1230 wsh		1235 w		S-O-H bend
1275 sh		1280 sh		1275 wsh		1281 w		1280 w				
1438		1445 w		1438	95	1435 w		1435		1430 w		$\nu_4 NH_4^+$
1630 w		1630 vw		1630 vw						1635 vw		
1685		1680 w		1680		1685 w		1685 w		1680 w		$\nu_2 NH_4^+$
1900 vw,b		1860 vw,b		1900 vw,b				1900 vw,b				$\nu_1 + \nu_3 SO_4^{2-}$
		2423 w						1420 vw				
		2540 w										
2856 w		2870 ~ 600		2860 vw		1870 vw		2855 w	80	2890 vw		O-H str. and
2920 vw								3095 wsh				$2\ \nu_4 NH_4^+$
3160	~ 95	3160 ~ 100		3175	~ 140	3180 w		3210 w		3190 vw		ν_1 and $\nu_3\ NH_4^+$
						3280 w				3260 w		
				3360 wsh								$2\ \nu_2 NH_4^+$

s: strong. w: weak. vw: very weak. b: broad. sh: shoulder.

Table 2. Lattice vibrational frequencies (cm^{-1}).

XX	*YY*			*ZZ*			*XZ*				*XY*				*YZ*			
Temperature 293	293	260	170	293	260	200	293	260	200	170	293	260	200	170	293	260	200	170
		20 sh	21 sh															
	31 sh	32 sh	38 w	33 w														
37											36 w	36 w	30 w	40 w				
						42 w	40 sh	40 sh	41	42					40 ns	41 ns	44 ns	45 ns
				48 w	48 w	51 w					51 w	50 w	57 w	57 w		54 sh	54 sh	55 sh
							54 ns	55 ns	56 ns	58 ns								
59 w			63 w															
				68	68	67			70 sh	75 sh								
															75	75	75	74
						90 w					80	78	84	87				
		112	109									110 sh	110 sh	106 sh				
	130 b	130	133															
		150	155															
											158 b	163 b	163 b	163 b	163 b	163 b	165 b	166 b
182 b			180 sh	179 bs	180 bs	184 bs	175 b	175 b	*	185 b				178 sh				

w: weak. s: strong. n: narrow. b: broad. sh: shoulder.
* not measured

When the temperature is reduced from 290 K to 160 K, the profile of the ν_3 SO_4^{2-} band changes distinctly as the high frequency component shifts out in frequency and becomes clearly resolved into an unusually sharp intense peak. This feature was also reported by Bazhulin *et al.*,[10] and as they suggest, it is likely evidence of increasing distortion in the sulphate ions. No similar feature is apparent in other bands.

Although much of interest has been seen in the present work, more detailed temperature studies and work on isomorphous materials are required before a precise understanding of the relation between the ferroelectric properties of AHS and its Raman spectra can be reached.

ACKNOWLEDGEMENTS

The authors wish to acknowledge helpful discussions with Dr. Richard Nelmes. The work was supported by the Science Research Council.

REFERENCES

1 R. Pepinsky, K. Vedam, S. Hoshino and Y. Okaya, *Phys. Rev.* 111, 1508 (1958).
2 I. P. Kaminow and T. C. Damen, *Phys. Rev. Letters* 20, 1105 (1968). A. Pinczuk, W. Taylor, E. Burstein and I. Lefkowitz, *Solid State Commun.* 5, 429 (1967). M. Didomenico, S. Wemple, S. P. S. Porto and R. P. Bauman, *Phys. Rev.* 174, 522 (1968).
3 S. R. Miller, R. Blinc, M. Brenman and J. S. Waugh, *Phys. Rev.* 126, 528 (1962).
4 R. J. Nelmes, *Acta Cryst.* B27, 272 (1971).
5 R. J. Nelmes, *Acta Cryst.* (to be published).
6 R. J. Nelmes, *Ferroelectrics* (to be published).
7 W. Cochran, *Advan. Phys.* 9, 387 (1960); 10, 401 (1961).
8 M. Kasahara and I. Tatzusaki, *J. Phys. Soc. Japan* 29, 1392 (1970).
9 C. J. H. Schutte and D. J. J. Van Rensburg, *J. Mol. Structure* 9, 77 (1971).
10 P. A. Bazhulin, T. P. Myasnikova and A. V. Rakov, *Sov. Phys.–Solid State* 5, 1299 (1964).
11 B. H. Torrie, C. C. Lin, O. S. Binbrek and A. Anderson, *J. Phys. Chem. Solids* 33, 697 (1972).
12 M. P. Fontana and M. Lambert, *Solid State Commun.* 10, 1 (1972).

AUTOMATION TECHNIQUES FOR RAMAN SPECTROSCOPY

J. W. ARTHUR and D. J. LOCKWOOD
Dept. of Physics, University of Edinburgh, Edinburgh, U.K.

(Received 12 November, 1973)

Abstract. This paper is concerned with the automation and control of grating spectrometers by digital techniques. The methods outlined include: a simple manually operated digital control; a dedicated logic system with data storage; data acquisition and control systems run by a computer in real-time and time-sharing modes. The performance of these methods is evaluated. A basic spectrometer control unit is described; this unit forms a module around which more general spectrometer control systems may be constructed.

1. Introduction

Computers are increasingly being applied to problems in spectroscopy. The possibility of performing routine data reduction and calculations with spectroscopic data on a large scale poses the problem of providing data in a form readily assimilated by a computer. Chart recorder output is not a suitable medium for computers. One solution to the problem is to have a device which produces digital output from a spectrum as it is recorded and punches it on paper tape. The paper tape is read by a computer and the spectrum reconstructed from an implied relationship with the numbers on the tape. Another solution is to link the spectrometer directly to the computer through an interface. The data is actually collected in the computer so that no intermediate storage medium need exist. But having raised the question of data acquisition by computer it is as well to consider the possibility of the computer controlling the spectrometer so that a dialogue is established between the two.

This paper outlines four general methods of approaching the problem of digitisation and computerisation. Specific systems are described, the first of which uses an on-line computer for data-acquisition; different modes of operation are considered which illustrate the possibilities. The second has no direct link with a computer but instead a specially constructed control unit links the spectrometer with a multi-channel scaler which acts as an intermediate data storage device. The third method is the simplest and is a very basic circuit for collecting data on paper tape. The last shows how the basic circuit used in the previous method can be used in a full-blown computer control system suitable for time-sharing operation.

Thus it is intended to give a reasonably general survey of the possibilities as well as reporting recent developments in the problem of computer-spectrometer linkage. The descriptions apply to wavenumber scanned instruments and Raman spectroscopy in particular but there is no reason why they should not be put to use elsewhere.

2. Systems With Direct Computer Linkage

The most common digitisation requirement in spectroscopy is a simple data-logging

Journal of Raman Spectroscopy **2** (1974) 53–69.

operation, where the operator retains control of the spectrometer and ancilliary equipment, but the spectral information is obtained in a form suitable for computer analysis. The systems described in this section perform this function through the use of a small on-line computer. If such a computer is available then these systems are readily put into operation, for the computer itself provides the interface to the experiment and little additional electronic equipment is needed.

The systems are based on a DEC PDP-8 computer used as an active information processor which can operate under the control of three different programs. For each program the computer performs a function that could be carried out by an independent set of electronic equipment: the advantage is that one instrument performs the work of many, and each function can be easily modified by rewriting the control program. The modes of operation are (1) digitise, (2) photon-count, and (3) signal-average. Although the details given here relate to a particular installation the principles involved in each mode are quite general, and are separate examples of the different ways of tying an experiment into a computer. Time-shared use of the computer is possible for modes (2) and (3) but here this type of operation is inefficient, and can lead to difficulties through priority conflicts with other computer functions. The reason for this is that the sequence of operations within the computer is controlled by external devices rather than the other way round.

The three modes of operation have been in operation since 1968 [1], and examples of Raman spectra recorded with the PDP-8 operating in the photon-count mode, for example, can be found in Reference 2.

2.1. Digitise mode

In the digitise mode, the spectrometer operates in the normal manner. The computer converts an analogue signal from the photomultiplier (PM) current amplifier into digital form and punches the result on paper tape. Wavenumber information is also recorded from a marker pulse.

The experimental arrangement is outlined in the block diagram of Figure 1. Signals from the current amplifier are fed into the computer via its analogue-to-digital converter (ADC). Spectrometer wavenumber-marker pulses are processed by means of the computer skip line facility [3]. The computer recognises a marker pulse via hard-wired circuitry, and encodes the information on the output tape via the software. The connection between hardware and software is achieved by means of a device address code, which is 6412 in this case. A remote control switch is used to start or stop the program allowing the PDP-8 to be some distance away from the spectrometer. The switch also operates through the skip line. The ADC unit has provision for a multiplexer which would enable other analogue inputs to be fed to the computer. For example, the laser power can be monitored, and the Raman spectrum corrected for variations in the source intensity by performing a ratio calculation in the computer. The standard low-speed Teletype paper tape punch (10 characters/s) limits the output data rate to approximately one point every 0.2 s.

For the digitise mode the main computer program is designed to cycle in a fixed

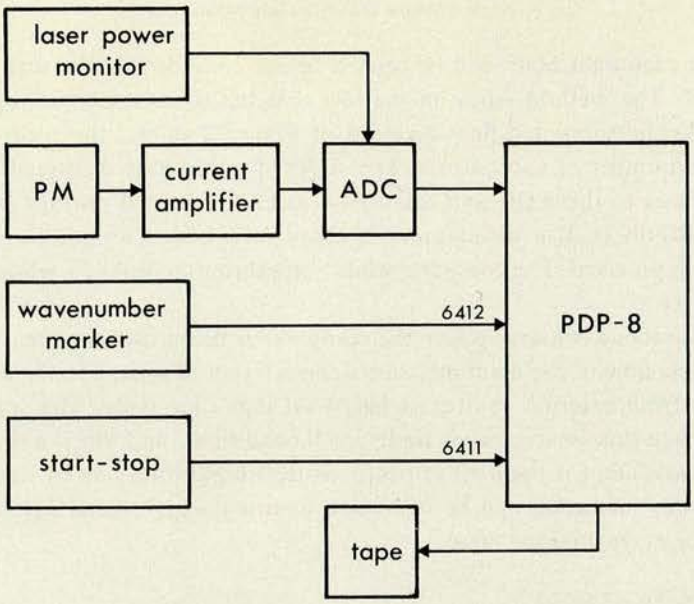

Fig. 1. Block diagram of the digitise mode of operation.

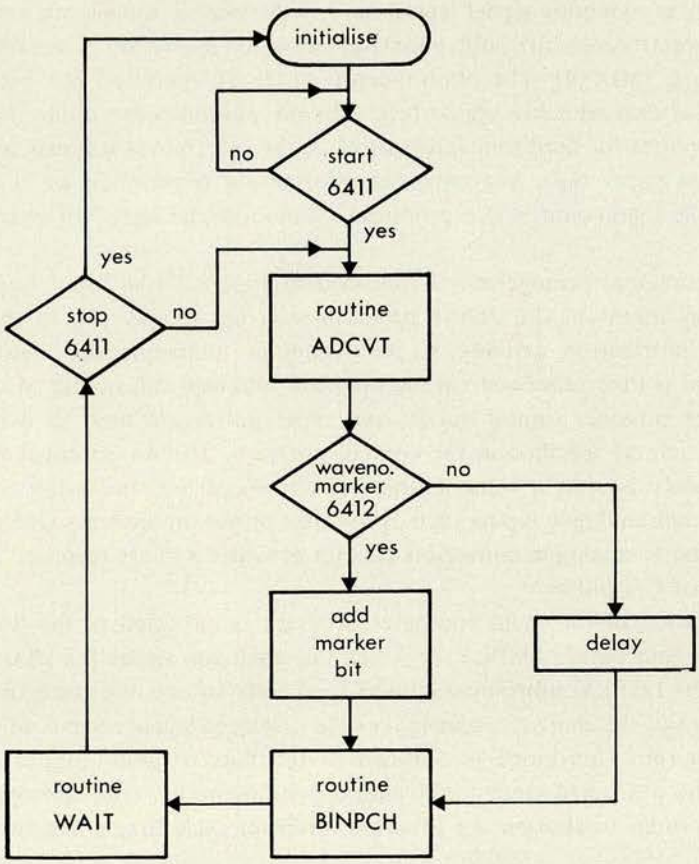

Fig. 2. Flow diagram of the digitise computer program.

time so that each data point can be related to wavenumber via the scan-rate of the spectrometer. The method relies on the fact that the spectrometer is scanning continuously. As the simplified flow diagram of Figure 2 shows, the control program consists of a number of subroutines. The ADCVT subroutine digitises the analogue signal presented to the ADC and the digital value is punched on tape by means of subroutine BINPCH. If a wavenumber marker pulse occurs an additional information bit is also punched. The computer waits – in subroutine WAIT – while the punching takes place.

The digitise mode is a case where the computer is being used as a real-time clock. The fixed cycle time of the main program defines a unit of time, and the aquisition of information from external sources is based on that time scale. The computer can not operate in a time-shared mode under such conditions, and this is a disadvantage. Another disadvantage is the limit imposed on the output data rate by the slow-speed punch, but this limitation can be overcome by using a high-speed device such as a fast punch or magnetic-tape drive.

2.2. Photon-count mode

Conventional current-amplification techniques used for recording PM signals work satisfactorily at moderate signal levels, but for the weaker signals often encountered in Raman spectroscopy the pulse-counting technique inherently possesses a superior signal-to-noise ratio [4]. The photon-count mode of operation has been designed specifically to deal with low signal levels. In the photon-count mode the computer counts PM pulses for fixed time intervals while the spectrum is scanned, and punches the totals on paper tape. Wavenumber information is recorded as in the digitise program. The total count is also produced as an analogue signal for chart recording purposes.

The experimental arrangement is outlined in Figure 3. All input information is processed by means of the PDP-8 program interrupt facility [3]. In this mode of operation, information arriving at the computer interrupts the main computer program and is then processed via the program interrupt subroutine. A crystal controlled clock provides timing pulses, and these pulses are used to determine the integration time as specified in the control program. The wavenumber marker and start-stop controls are the same as those described earlier, and again there is provision for other analogue inputs such as for laser power monitoring. One of the computer's digital-to-analogue converters (DAC) provides a chart recorder signal from the integrated PM pulses.

The operation of the main computer program is indicated in the flow diagram Figure 4(a). Subroutine DSPLY provides the analogue signal for chart recording purposes; the DSPLY subroutine is used frequently so that the comparatively long time constant of the chart recorder makes the displayed signal seem continuous. The program interupt subroutine is outlined in the flow diagram Figure 4(b). Each interrupt device is tested sequentially and, depending on its state, appropriate action is taken. In order to shorten the program interrupt cycle time some short cuts are

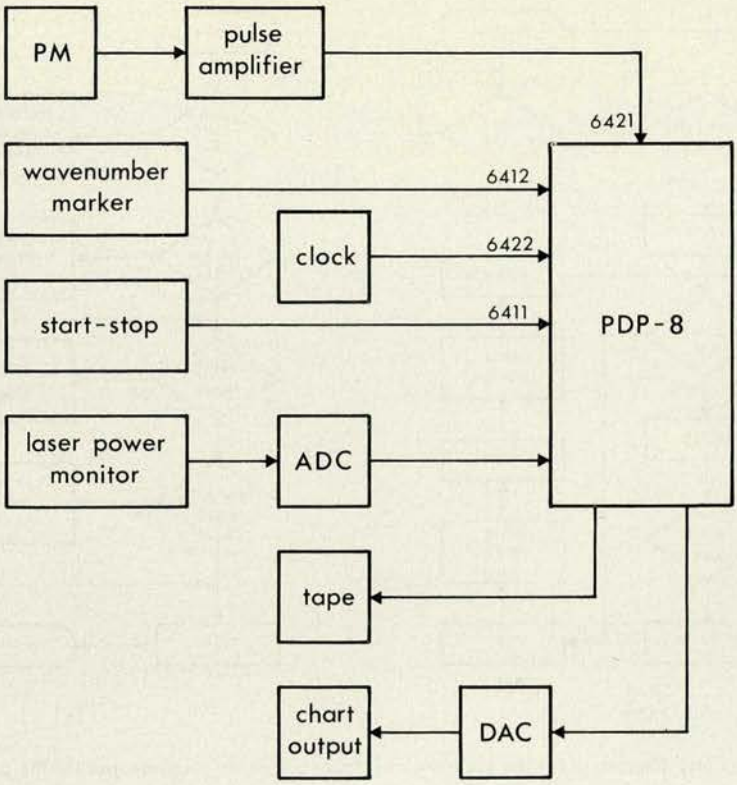

Fig. 3. Block diagram of the photon-count mode of operation.

made. PM pulses occur most frequently and these are tested first, while the low frequency clock pulses are tested last. This arrangement ensures that no clock pulses are missed and gives the lowest possible photon-count dead time. Note that an interrupt can not occur whilst the computer is running under the control of the interrupt subroutine until the 'interrupt ON' instruction is given. The photon-counting section of the program has a total computer-instruction cycle time of 15 μs, which results in a linear response for count rates $\lesssim$6 kHz.

In the photon-count mode the real-time clock is external to the computer, but, as in the digitise mode, the cycle of operations in the computer is closely controlled through the software. This leads to some disadvantages. Any change in the details of the running of the experiment, such as changing the integration time, requires an alteration in the computer program and this is not a rapid procedure; and time-shared use of the computer is only possible for the simplest of additional tasks. The use of the program interrupt line for photon counting is an inefficient method of operation: a better method would be to count pulses external to the computer for the integration period and then transfer the total count from a buffer using the data break facility [3].

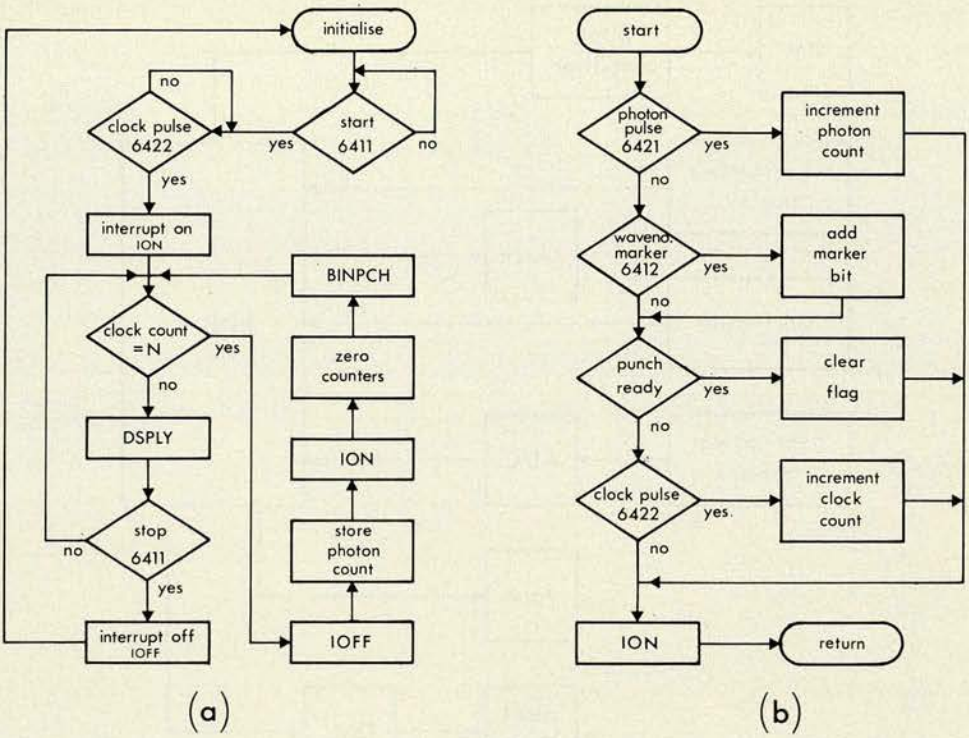

Fig. 4. Flow diagram of (a) the photon-count main computer program and (b) the program interrupt subroutine.

2.3. Signal-average mode

By repeatedly scanning a spectrum and adding the results it is possible to improve the signal-to-noise ratio (S/N). The signal increases in strength in direct proportion to the number of scans n whereas the noise increases as $\sqrt{n}$. In theory, the S/N can be improved without limit, provided the noise is completely random: non-random noise can also be reduced if it is not synchronised with the scan repetition rate.

In optical spectroscopy, the usual averaging technique is to scan through a part of the spectrum in the normal manner by rotating the grating, to repeat the process several times, and then average the spectra. It is much simpler to keep the dispersive element stationary and scan the spectrum via a rotating refractor plate. In this arrangement a parallel plate of transparent refractive material is placed behind the entrance slit of the spectrometer and the plate is rotated about an axis parallel to the length of the slit. The spectrometer experiences at the focal curve a translation of wavelength proportional to the sine of the angle of rotation.

This section describes a signal averaging technique based on the rotating refractor plate method and at the same time shows how the normal operation of a spectrometer can be extended by the use of a computer. The scanning system is built around a quartz refractor plate that is driven by a variable-speed motor. One revolution of

the refractor plate drive shaft produces two spectral scans and each scan is divided into 512 channels by a digital shaft-position encoder. Thus the refractor position – and hence wavenumber – is related to a definite channel number. Successive sweeps are synchronized by a start-scan pulse produced by another shaft-locked encoder. The repetitively scanned spectra are integrated by the PDP-8 computer operating in the signal-average mode.

A block diagram of the experimental arrangement is given in Figure 5. The PM signal and refractor plate position information is processed by the data break facility. This facility operates entirely through hardware, and so is independent of the control program. Starting at channel zero, the computer adds up the number of photomultiplier pulses received on data-break line DB1 by counting them into a switch-specified location in the computer's memory. Data-break operations occur almost instantaneously on request, but the maximum linear count rate is limited to ~ 60 kHz by the 1.5 μs data break cycle time. Higher count rates can be accommodated by using a buffered scaler between the pulse amplifier and the computer. On receipt of a channel increment pulse (DB2) the computer adds the signal pulses into the next consecutive memory location. This latter process is repeated until a start-scan pulse (DB3) is received, at which time the computer returns to the memory address corre-

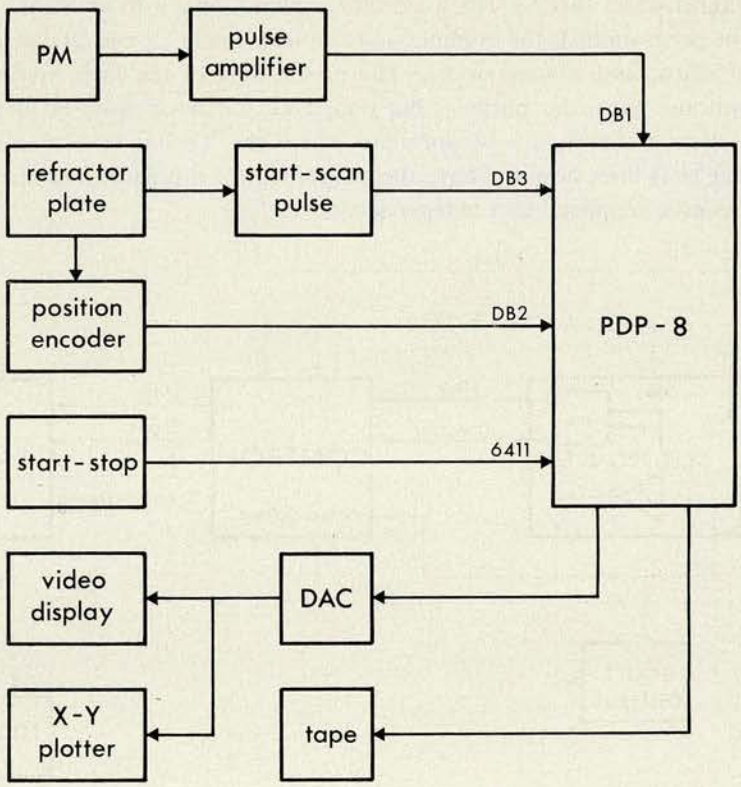

Fig. 5. Block diagram of the signal-average mode of operation.

sponding to channel zero. In this way the computer integrates the spectrum by automatically adding the signal pulses from each successive sweep. A remote stop-start switch is used to halt the computer at the end of a run. Throughout the run the computer produces an oscilloscope display of the integrated spectrum so that the improvement in the S/N can be observed. At the conclusion of the run the computer punches the spectral information on paper tape, and can also plot the data on an $X-Y$ recorder.

Time-sharing operations are possible in the signal-average mode as during a run the computer software performs the background task of providing an oscilloscope display from the data fed into the computer. The data transfer from external devices is independent of the software. However the basic operation is still real-time, since data transfers command immediate action by the computer.

The system described here has been based on the refractor plate technique for signal averaging. However, the computer linkage section is quite general and can be applied to other techniques for rapid scanning of spectra.

3. Hard-Wired System

The approach described here is to build a 'hard-wired' logic system for the specific task of controlling the spectrometer and linking it to a data storage device such as a multi-channel scaler (MCS). The logic system allows only a fixed set of scan parameters to be programmed; for example, start of scan in cm^{-1}, end of can, scan rate, number of scans, and channel width. The programme of the logic system can be made to suit any particular purpose, but once built it cannot easily be altered. This kind of system is therefore a compromise where the 'on-line' use of a computer is not possible. It does however have the advantages of a high degree of reliability, low cost, relative simplicity and independence.

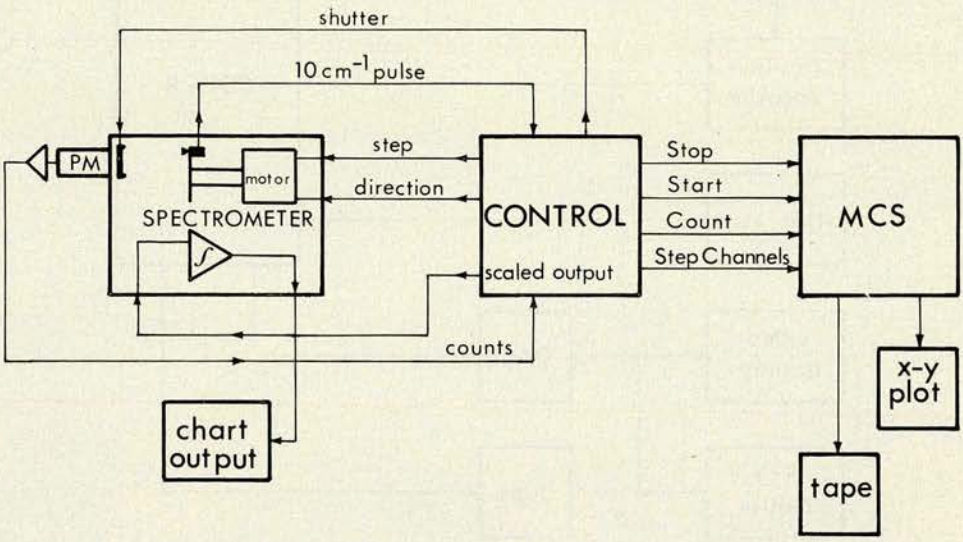

Fig. 6. Configuration of conventional spectrometer with MCS control unit.

Figure 6 shows the configuration of this type of system for a particular spectrometer and MCS. In this case as much use as possible has been made of built-in spectrometer (Spex Ramalab) equipment and functions so that the small details may vary from one instrument to another. Figure 7 shows more detail of the control system, the basic operation of which is as follows.

3.1. Motor drive

Stepping pulses for the motor are derived from the system clock. A presettable divider brings the clock frequency down to the rate required for scanning ($200/M$ Hz where M can be set from 1 to 99 on digital switches). A further divider provides a pulse for every N motor steps and N is set so that this pulse advances channels in the desired wavenumber step sizes (channel width, CW). For purposes other than actual scanning, full clock frequency is selected to drive the motor at high speed.

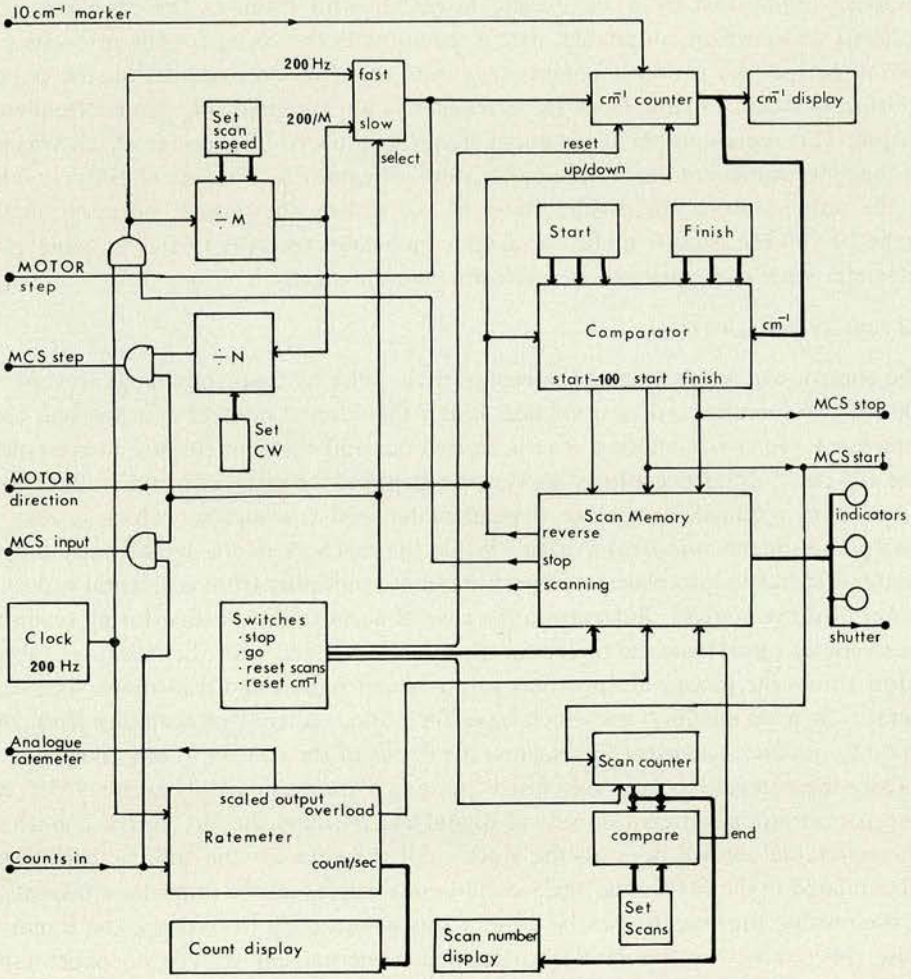

Fig. 7. Block diagram showing the operation of the hard-wired control.

3.2. Wavenumber counter

A reversible counter keeps track of motor steps and presents a readout of the wavenumber shift of the spectrometer with respect to some reference position chosen when the counter is manually reset to zero. A 10 cm^{-1} marker pulse from the spectrometer is used to synchronise the counter. The contents of this counter are compared with scan limits set on digital switches to give three possible signals: at 100 cm^{-1} below the start position, 'start − 100', at the start position, 'start', and at the finish position, 'finish'. Scanning takes place between the limits and these signals change the phases of operation of the control unit.

3.3. Count rate

The photon counts are fed to the MCS scaling input and in addition they are continuously monitored by a six decade ratemeter with display. The ratemeter is a buffered scaler which is updated once a second with the count for the previous one second period. An overflow condition is used to signal an overload on the photomultiplier. Also available from the ratemeter is an automatically scaled frequency output. This represents the input count frequency divided by a power of ten selected by the most significant digit in the buffer store. The powers of ten are readily available at the outputs along the divider chain of the scaler. The output, normally in the range 10–100 Hz, is quite useful for display on a chart recorder through an analogue ratemeter since scale changes are performed automatically.

3.4. Phases of operation

The control will scan the spectrometer over the selected frequency range, reverse to 100 cm^{-1} below the start position and stop if the selected number of scans has been completed. Otherwise another scan is carried out and the scan counter incremented. The 100 cm^{-1} difference allows backlash to be taken up after a change in direction; the amount required is machine dependent but 100 is a number which is easy to incorporate in the comparator logic! While the machine is not actually scanning a shutter is switched into place to protect the photomultiplier from accidental exposure to out-of-range sources. But even in the case of accidental exposure during scanning the overload signal from the ratemeter trips the shutter and halts the machine. Table I below shows the phases of operation with relevant signals and transitions. The scan memory is a set of flip-flops which have their states altered in changing from one phase to another. Indicator lights show the status of the control at any time.

Once the control has been initialised, running a spectrum simply requires that the scan parameters be entered on sets of digital switches and the 'go' switch is pushed. Thereafter the control does all the work until the data for the spectrum has been accumulated in the MCS. The MCS oscilloscope display allows immediate inspection of the results; more scans can be done if this is necessary to improve the signal to noise ratio, otherwise the data is committed to permanent storage on paper tape, or graphically on an $X-Y$ plotter.

TABLE I

Signals and transitions during the various phases of operation

Signal	Stop	Reverse	Fast forward	Scan
Motor step	0	Full speed	Full speed	Scan speed
MCS step	0	0	0	After N steps
Motor direction	X	0	1	1
MCS input	0	0	0	Count in
Shutter	1	1	1	0
Start-100		○⟶		
Start (MCS start)			○⟶	
Finish (MCS stop)		⟵		○
End	⟵○ (at Start-100 after last scan)			

0 = Off; 1 = On; X = Irrelevant; ○⟶ = at this transition.

This system, built basically from series 7400 TTL integrated circuits, has been in use for one year at the time of writing and has proved both useful and reliable. It has been found possible to run spectra routinely with a degree of reproducibility that would have only been painstakingly achieved in manual operation. Published results, using computer analysis of the data tapes, are found in References 5 and 6.

4. Simple Control

While the control system described in Section 3 has its merits it suffers from the disadvantage that any further expansion and sophistication would mean reconstruction. Being built for a specific task it does not lend easily to radical modification. A 'modular approach' may therefore be more appealing. The problem, therefore, is to build a basic control of little complexity which can be used both as a simple manually operated control and as a module in the more complete and automated system. Such a control has been built, Figure 8, and is described here. A different approach to the scanning problem has been adopted which has several advantages. Most spectrometers in the past have relied on high precision constant velocity motors to scan the gratings while the signal is simultaneously recorded on a chart recorder. This procedure is not necessary when a stepper motor drive is used, instead the gratings can be stepped and the function of the control is a succession of cycles of increment wavenumber, wait and count. Not only does this remove the problem of synchronising other devices such as a chart recorder or real-time computer to the scan rate, it also effectively increases the resolution because the gratings are stationary during the integration time of the counter.

The operation of the control is as follows. Individual motor steps are generated by the oscillator OSC, the frequency of which is not very important but gives a good stepping speed. The flip-flops STEP, INT and ON provide independent means of arresting the motor steps at MOTOR GATE. When steps are allowed through the gate they are counted by the stepsize counter. N individual steps make a complete

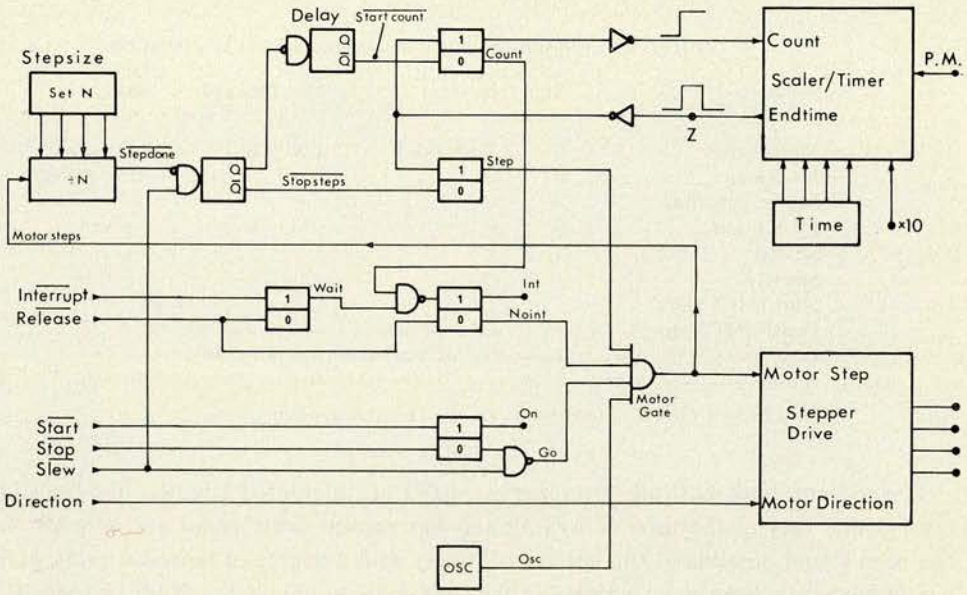

Fig. 8. Circuit of the basic step-count control.

scan step and produce a '0' level at the output, $\overline{\text{STEPDONE}}$. This signal does two things: it inhibits any more motor steps by resetting the STEP flip-flop to a '0' state, and it sets the COUNT flip-flop to a '1' state, after a short delay to allow for the lag in response of the motor. The COUNT flag initiates a scaler cycle lasting for a preset period, TIME, and terminated by a pulse ENDTIME. This pulse resets the flip flops to their former statuses allowing another cycle to proceed. Thus the operation consists of a sequence... STEP, COUNT, STEP, COUNT... which can only be terminated by the action of one of the flip-flops INT or ON.

The flip-flop ON starts or stops the operation through push-button switches. SLEW overrides the stopped condition; count cycles are inhibited so that the motor runs continuously. A separate flip-flop INT can also be used to halt operation. But here the operation is more subtle. Two flip-flops are used, the first captures the momentary signal $\overline{\text{INTERRUPT}}$ and produces a signal WAIT. When the next count cycle appears the INT condition is set preventing the control starting up at the following step cycle. RELEASE cancels this condition and the next step proceeds. This gives a means of temporarily stopping a scan without interfering with the count in progress or upsetting the calibration by stopping in the middle of a step. It is well to have these as separate means of stopping the scan, bearing in mind the uses to which they might be put in a modular system. A version of this control has been built to operate a Spex 1400 instrument adapted to take a stepper motor drive. The scan parameters stepsize and count time are programmed conveniently by digital switches with bcd outputs. In this version a step counter was included to automatically halt

the scan after a selected number of steps. The photon-count scaler outputs its data, six digits, to a Teletype, and a built-in analogue to digital converter gives graphic output on a chart recorder. It is convenient to have a chart recorder with a stepper drive operating on the same pulses that drive the spectrometer. There is no facility for repeated scans but this is not essential in the majority of experiments. Long scans however are readily done because there is no limitation of a fixed memory size.

5. A Complete System

The simple control used on its own provides a neat and effective way of programming the basic functions of the spectrometer but it has few of the luxuries of automation. Before trying to elaborate on it however, it becomes worthwhile to review the nature of the experimental problem to ascertain the general suitability of the step-count technique.

Measuring a spectrum means recording intensities $I(\nu)$ over a range of frequencies ν. I is more precisely proportional to the photon count rate than the photo-current at a given ν. Scanning at a constant rate over the required frequency range is not essential to the technique. Recording a set of intensities, or photon counts, $I(\nu_i)$ over a set of frequencies ν_i gives the information required if the steps $\delta\nu_i = \nu_{i+1} - \nu_i$ can be made reasonably small. On careful reflection it is apparent that even in the continuously scanning case there is always some window $\delta\nu$ around which the data is smeared. The magnitude of $\delta\nu$ depends on the time constant of the recording apparatus and on the scan rate. Nothing is lost, therefore, when discrete data points are taken and in fact as much information can be obtained as by any other technique.

Returning to the operation of the basic control unit, which operates in a stepping manner giving discrete points, it can be seen that the essential control parameters stepsize, count time, direction, stop and start can be collected together and represented by a logical word (string of binary bits) 12 bits long. The control unit translates this word into action by the spectrometer.

If this control word, as it may be called, is specified for each step-count cycle then any action can be accomplished. The control word can be set by some other logic system or by a computer in which case the control word is virtually an extension of the computer's commands. Figure 9 shows how this may be accomplished. The operation of the control is the same as described in Section 4 but here the step-count cycle is interrupted by the computer at point Z in Figure 8. The computer provides a control word from its output section and signals its availability to the control. The control accepts the word, translates it into action by the spectrometer and starts a scaler count cycle. When the count is complete the scaler signals the presence of data to the computer. Not until this data has been accepted and processed can a new control word be set and another cycle activated. The complete cycle time depends on the individual cycle times for control, scaler and computer but its duration is of no importance to the operation of the system. External interrupts and waits have no adverse effect because the spectrometer is forced to wait as well as the computer. This system is at once suitable for use in a time-sharing environment.

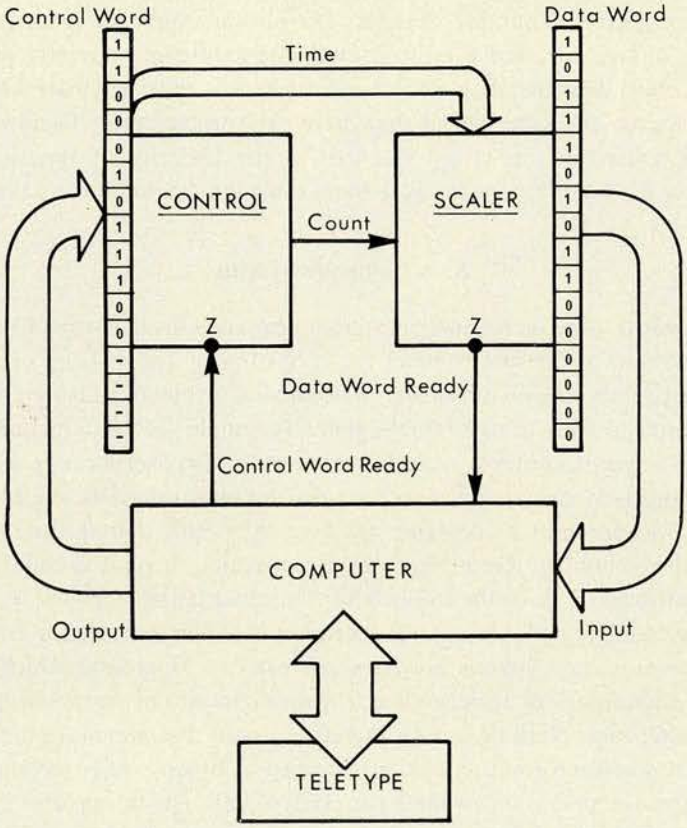

Fig. 9. Flow of data for the computer operated control.

Control of the spectrometer is by a programme initiated in the computer from the Teletype. Input of data and output of control word appear to the computer the same as input-output from normal channels (e.g. paper tape reader and punch), so that there is no reason why normal programming techniques in a high level language may not be used. The correct binary pattern for the control word can be set by an expression such as:

$$\text{CONTROL} = \text{STOP} + 2*\text{GO} + 4*\text{TX10} + 8*\text{TIME} + 128*\text{DIR} + \\ + 256*\text{STEP}.$$

At this stage the system has a great deal of flexibility and information contained in the spectrum can be recorded optimally. It is possible to multiscan, to do automatic calibration, to hunt for bands using variable stepsizes and count-times – the scope is bounded only by the limiting capabilities of spectrometer and computer. But it is a pity to have such flexibility in the spectrometer part of the experiment alone. The concept of operating through a control word and data word, however allows

immediate extensions to be made. Translator circuits may be built for other experimental equipment so that it is possible to set and record such parameters as sample temperature, light polarisation and laser power. The digital voltmeter can act directly as a translator for a thermocouple or laser power monitor. It is also possible to operate an $X-Y$ plotter and other displays all on the same basis. The control and data words for individual translators together form extended control and data words for the computer to handle. Multiplexing techniques are necessary when the sizes of these words become too large for a single input-output transfer. Such a system would be readily built along the lines of CAMAC [7].

Work on such a system is already in progress and it should be possible to report on it in the near future.

6. Conclusion

The adoption of a particular system depends on the type of computer available. There are three major categories of computer system to consider, These are: full use of a small computer ('mini-computer') to perform one task, of limited scope, at a time; time-sharing on a medium sized computer with several users running independent tasks; and computation facilities only on a large job-processing computer.

In the first category almost all of the interfacing may be provided by the computer which can be housed in the same laboratory as the spectrometer. Programming is done at a very basic level and small memory size and long instruction cycle times restrict the scope of both real-time control and off-line data reduction. No doubt most of these difficulties would be overcome by an enterprising programmer, but the experimentalist may neither have the time or desire to do so. The advantage of having the full use of even a small computer is that there are no external users or programmes to interfere with the experiment and, as a result, the user is free to use the computer as a clock to send motor pulses or set count times. Section 2 above describes examples of this type where the small computer is a PDP-8 with 4K words of store. Commercially available spectrometer-plus-small-computer systems may, however, be an attractive proposition since it falls to the manufacturer to provide a working system with software.

The category at the other extreme is the large scale computer system which is completely reserved for off-line computation. There is no reason, however, why a small computer should not be used as a control and pre-processor device. But where this is not possible the systems of Section 3 and 4 produce spectroscopic data in a form which can be processed directly on the large computer as a normal 'job'. The hard-wired logic system is intended to replicate some of the programming facilities that would otherwise be possible only under direct computer control. Multiscanning, for example, is a well proven technique for weak signals and its implementation usefully extends the capability of any system. The construction of such a control system requires a deal of constructional effort and expertise with logic systems. The operation is quite flexible but only within the bounds of the facilities provided in

the programming switches – and multichannel scalers tend to have more restricted memory capacities than computers. This type of system, however, can be justified where there is a large amount of routine work to be done, or where multiscanning is a necessity. It can be operated by personnel having no special experience with computers.

The simpler control unit of Section 4 is truly basic in its operation but its design purpose is well fulfilled. Even this simple control, without data collection on paper tape, offers an alternative mode of operating a spectrometer manually which is neat and effective. By its own nature it is suitable for use as a component in more complex circuits or in modular systems. The latter aspect is to be emphasised both as it is good constructional practice and because of compatibility with systems making use of the large range of commercially available plug-in units, e.g. NIM and CAMAC.

Many research groups have shared access for a medium sized computer such as a DEC PDP-11. A typical system would have software, an operating system for time sharing, and some mass storage devices such as disk or magnetic tape. The computer services the users tasks in a manner which preserves their independence of each other. It is not possible for a user to know that his demands for service will be met immediately on request. A special technique is required because the experiment may be forced to wait, even if only for a short while. The complete control system described in Section 5 fits the requirements of this type of computer environment. Here the situation for the experimenter is quite ideal. The computer is large enough to do both control and processing of many tasks. System programming already exists and the user can take full advantage of a powerful programming language such as FORTRAN. Expansion to a larger experimental work-load is, in principle, no problem. This type of system then, allows more possibilities than any other at a level which is easy for the experimenter to come to grips with. It should certainly find application now that the sharing of computer resources has become commonplace.

Other systems have been reported which are in some ways similar to the examples given here. Manfait *et al.* [8] describe a system using a MCS, and Schmid *et al.* [9] describe a PDP-8 system. A larger system, also controlling an infrared spectrometer, has been reported by Scherer and Kint [10]. These are specific systems and a less general approach has been taken. A novel system in which an electronic calculator is interfaced to a spectrometer is described by Warren and Ramaley [11], but this is a very specific system requiring a deal of circuitry.

Finally we wish to acknowledge the support of the New Zealand University Grants Committee for the work of Section 2 and of the Science Research Council for Sections 3–5.

References

1. Lockwood, D. J.: Ph. D. Thesis, University of Canterbury, N.Z., 1969.
2. Christie, J. H. and Lockwood, D. J.: in M. Balkanski (ed.), *Light Scattering in Solids*, Flammarion, Paris, 1971, p. 145.

3. *The PDP-8 Users Handbook*, Digital Equipment Corporation, Massachusetts, U.S.A.
4. Tull, R. G.: *Appl. Optics* **7**, 2023 (1968); Alfano, R. R. and Ockman, N.: *J. Opt. Soc. Am.* **58**, 90 (1968).
5. Arthur, J. W. and Taylor, W.: *Ferroelectrics*, to be published.
6. Lockwood, D. J. and Torrie, B. H.: in T. Riste (ed.) *Anharmonic Lattices, Structural Transitions and Melting*, Noordhoff, Leyden, 1973.
7. Barnes, R. C. M. and Hooton, I. N.: *IEEE Trans. Nucl. Sci.* NS-16, No. 5, 76 (1969).
8. Manfait, M., Beaudoin, J. L., and Bernard, L.: in J. P. Mathieu (ed.), *Advances in Raman Spectroscopy*, Heyden, London, Vol. 1, 1973, p. 76.
9. Schmid, E. D., Berthold, G., Berthold, H., and Brosa, B.: in J. P. Mathieu (ed.), *Advances in Raman Spectroscopy*, Heyden, London, Vol. 1, 1973, p. 87.
10. Scherer, J. R. and Kint, S.: *Appl. Optics* **9**, 1615 (1970).
11. Warren, L. H. and Ramaley, L.: *Appl. Optics* **12**, 1976 (1973).

THE EXTERNAL LATTICE VIBRATIONS OF ORTHORHOMBIC SULPHUR

J. W. ARTHUR and G. A. MACKENZIE
Dept. of Physics, University of Edinburgh, Edinburgh, Scotland

(Received 18 February, 1974)

Abstract. The Raman spectrum of orthorhombic sulphur has been measured in the frequency range 0–100 cm^{-1} for all polarisations. The $A_{1g}(zz)$ and $B_{1g}(xy)$ spectra have been clarified by later subtraction of unwanted scattering belonging to other polarisations. Definite assignments are made for all but one A_{1g} and one B_{2g} mode. An interpretation of the intensities observed in the A_{1g} and B_{1g} spectra is given in terms of the rotational motion of the S_8 molecules affecting their contribution to the crystal polarisability.

1. Introduction

Orthorhombic sulphur, αS_8, has been studied in many Raman experiments [1–3], and notably Ozin [4] has given results in all polarisations for the single crystal.

As an example of a molecular crystal it has also recently been the subject of structural and dynamical calculations [5–8]. The model for these calculations assumes a crystal of rigid S_8 molecules bound by a weak '6-exp' atom-atom potential. In order to compare calculations with experiment, neutron scattering measurements were made [8] giving refinements on the structure and phonon frequencies at points throughout the Brillouin zone. The purpose of this work is to make comparison between model and experiment clearer by providing, as far as is possible by Raman scattering, accurate information about frequencies and assignments of the lattice modes at the zone centre.

The technique involved automatic digital recording of the spectra on paper tape. It was later possible to improve some of the spectra, the $A_g(zz)$ and $B_{1g}(xy)$, by computer analysis, as described in Section 4.

In Section 5 we give an approximate calculation of relative intensities based on the properties of the free rigid molecule, thereby gaining some additional information on the dynamics of the molecules in orthorhombic sulphur.

2. Group Theory

Sulphur is a molecular crystal of point group D_{2h}. There are four molecules in the primitive cell. The point group of the free molecules is D_{4d} and each molecule has a C_2' axis aligned with the crystal **z** axis. Labelling the molecules as 1, 2, 3 and 4, 2 is related to 1 by C_{2x} and 3 and 4 are related to 1 and 2 by a centre of inversion.

The six degrees of freedom of the rigid molecule transform under D_{4d} as

$$B_2 + E_1 \qquad (x \text{ and } (y, z))$$
$$A_2 + E_3 \qquad (R_x \text{ and } (R_y, R_z)),$$

where, after Pawley and Rinaldi [6], we take the molecular x axis as the C_4 axis and the z axis as the C_2' axis aligned with the crystal z axis. In the crystal these give rise to 12 external lattice vibrations which are Raman active, transforming as:

$$A_{1g} + B_{1g} + 2B_{2g} + 2B_{3g}\text{: translational}$$
$$A_{1g} + B_{1g} + 2B_{2g} + 2B_{3g}\text{: rotational.}$$

The arbitrary division between rotational and translational parts has been made for later convenience.

Although group theory predicts two Raman active A_g lattice modes, Ozin [4] has reported seeing only one, a very intense peak in the *xx* and *yy* spectra at 52 cm^{-1}. In the *zz* spectrum, also A_g, the intensity is very much weaker and any peak is obscured by additional small peaks attributable to admixtures from spectra of other polarisations. This is an experimental difficulty arising from the anisotropic optical properties of the crystal and strong internal 'scattering' of the laser light within the sample. The former problem has been discussed for the uniaxial crystal calcite by Porto *et al.* [9], but his solution is technically difficult. The approach taken here was to try and remove the unwanted peaks by subtracting portions of the other spectra suspected of contributing. By finding the correct proportions to take away only the proper spectrum should remain. The assumption is that the observed spectra are simply linear combinations of the true spectra for other orientations. This kind of technique is quite suitable when it is possible to use a computer for the analysis of the data, as was the case here.

A similar problem is encountered with the $B_{1g}(xy)$ spectrum. Here the seriousness of the problem was found to be greater with some crystal orientations than with others. The same subtraction technique proved useful.

The 'leak-through' of intensity from peaks in other spectra presents difficulties in identifying peaks and making assignments, but another problem arises in sulphur because the lattice mode spectrum merges with the internal vibration spectrum in the region 70–90 cm^{-1}. There is no easy solution to this problem because in this region there is no clear division between internal and external modes. The true modes will have the character of both.

3. Experimental

The experimental configuration involved a digitally controlled Spex 1400 double monochromator with data collection on paper tape and point plotter [10]. The paper tape was processed by computer with a variety of routines for conversion to wavenumber, intensity measurement, peak finding, band fitting and graphic output. Spectra were recorded for three different orientations of the crystal, measuring one diagonal and all three off-diagonal components in each case. By correlating intensities in the off-diagonal components for different crystal orientations it was possible to correct for different scattering efficiencies in each case. Wavenumber calibration was checked against the plasma lines of the helium-neon laser and the rotational spectrum of air to be ± 0.2 cm^{-1} over the range of measurement.

4. Analysis

As a first step in the computer analysis the peak positions were determined as accurately as possible in all the spectra. The results agree well with those of Ozin, but the additional accuracy was occasionally important in identifying a peak from one spectrum to another. Secondly, treating each spectrum separately an attempt was made to identify the proper peaks in the spectra associated with each orientation.

4.1. THE A_g (xx AND yy) SPECTRA

In both these spectra very intense peaks of comparable intensity are observed at 51 cm^{-1} (Figure 1). The well separated peak at 89 cm^{-1} is undoubtedly an internal mode, and lineshape of the 51 cm^{-1} peak was found to be well represented by a single Lorentzian function. As to the question of the presence of a second A_g mode we have to conclude that it is not to be seen in either of these spectra.

4.2. THE $A_g(zz)$ SPECTRUM

The initial reason for trying to remove the unwanted peaks in this spectrum was that it was thought possible that the second A_g mode might be revealed. Peak positions at 27, 42, 49, 53, and 62 cm^{-1} correlate well with those observed in the xz and yz spectra. The spectrum, S_{zz} say, was therefore compared with a linear combination of S_{xz} and S_{yz} thus:

$$S_{zz}^{\text{experiment}} \sim S'_{zz} = \alpha S_{xz} + \beta S_{yz}$$

α and β were chosen to minimise the difference between S_{zz}^{exp} and S'_{zz}, and the 'corrected' spectrum $S_{zz} = (S_{zz}^{exp} - S'_{zz})$ was formed. Figure 2 shows this result. It is clear that the only peak remaining in the lattice mode region is a very weak contribution from the 51 cm^{-1} peak seen in xx and yy. Again we conclude that no second A_g mode is to be seen.

4.3. THE $B_{1g}(xy)$ SPECTRUM

This spectrum should also show two peaks whereas possibly six are seen in some results. Applying the same subtraction procedure proportions of the xz and xx spectra were removed leaving two peaks at 40 and 54 cm^{-1} (Figure 3). There are no peaks with matching frequencies in the other spectra. We believe that here we have been successful in isolating the proper peaks in the spectrum.

4.4. THE $B_{2g}(xz)$ SPECTRUM

Here the spectrum is fairly intense with little evidence of leakthrough (Figure 4). The only problem is that of the nature of the peak at 74 cm^{-1}. This peak would be expected to arise from the 80 cm^{-1} E_2 mode of the sulphur molecule [4]. In this particular spectrum the frequency of the mode has been considerably depressed so that it overlaps with the lattice frequencies. Here the distinction between internal and external vibrations stops, and any mode in this region may have the character of both. We can con-

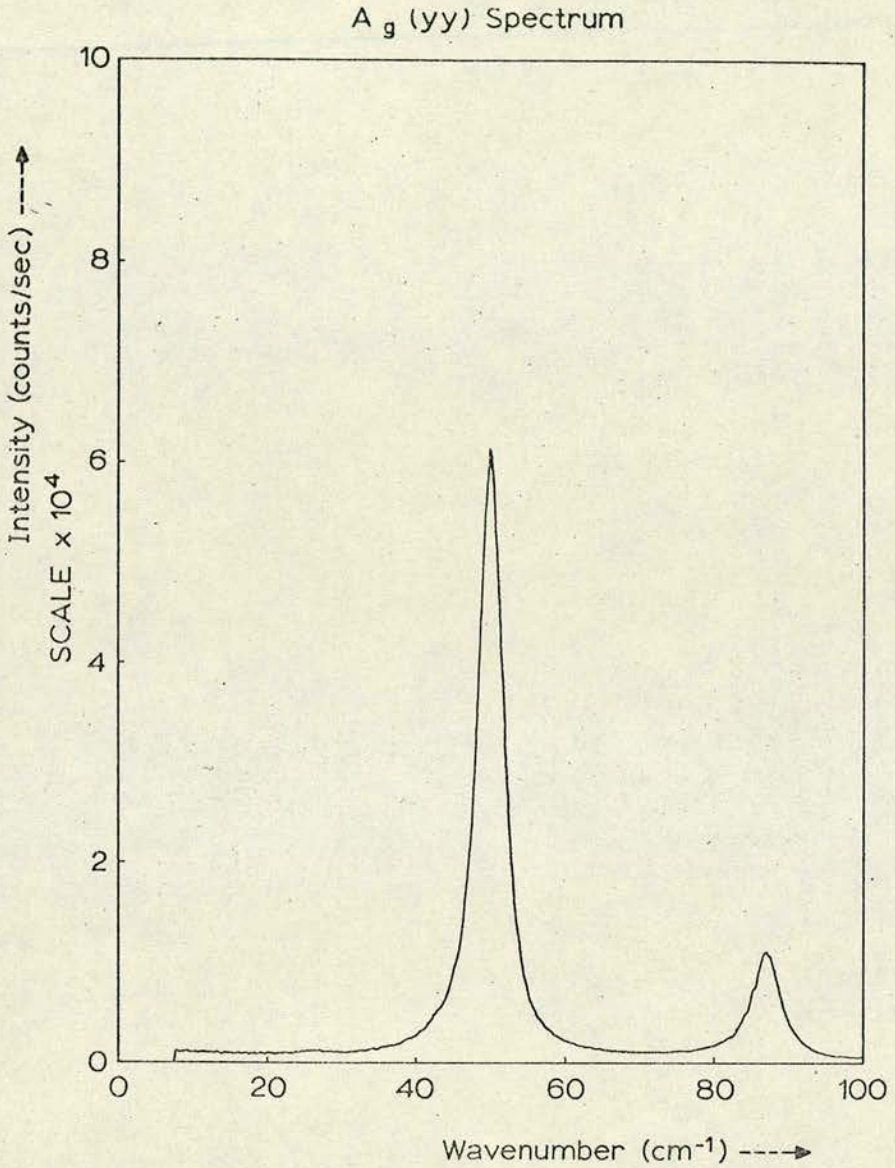

Fig. 1. A_g (yy) spectrum.

clude nothing firmer from the spectrum alone, but a calculation of the molecular frequencies in the crystal by Pawley and Kurittu [11] may resolve the problem.

4.5. The $B_{3g}(yz)$ spectrum

In this case matters are quite straightforward. A very weak peak at 65 cm^{-1} appears to complete the expected quartet of lines (Figure 5). Table I shows the measured frequencies and assignments of all the modes.

TABLE I

Frequencies and assignments of the external modes

	A_g	B_{1g}	B_{2g}	B_{3g}
1	51.1	40.0	29.0	26.5
2	not seen	54	49.0	42.3
3			60.8	53.3
4			73.8[a]	64.5

[a] See Section 4.4.

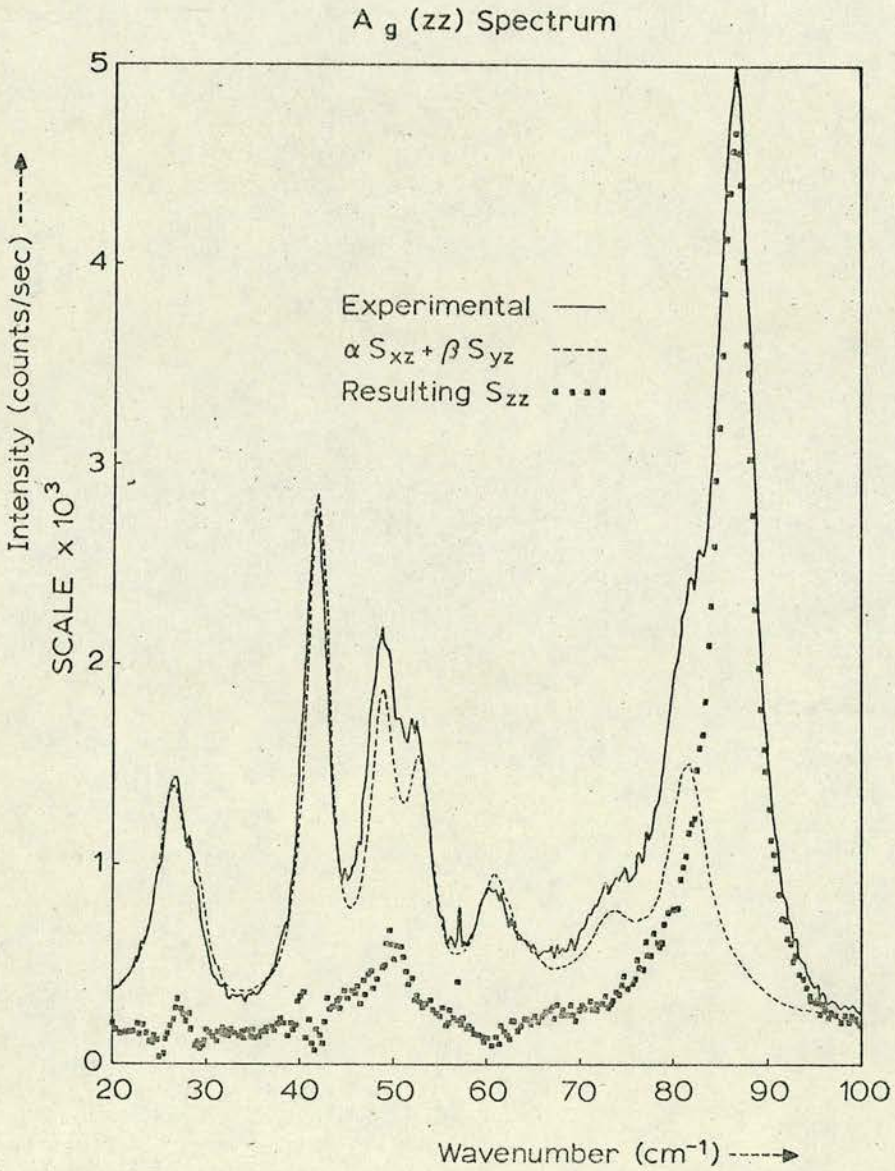

Fig. 2. $A_g(zz)$ spectrum.

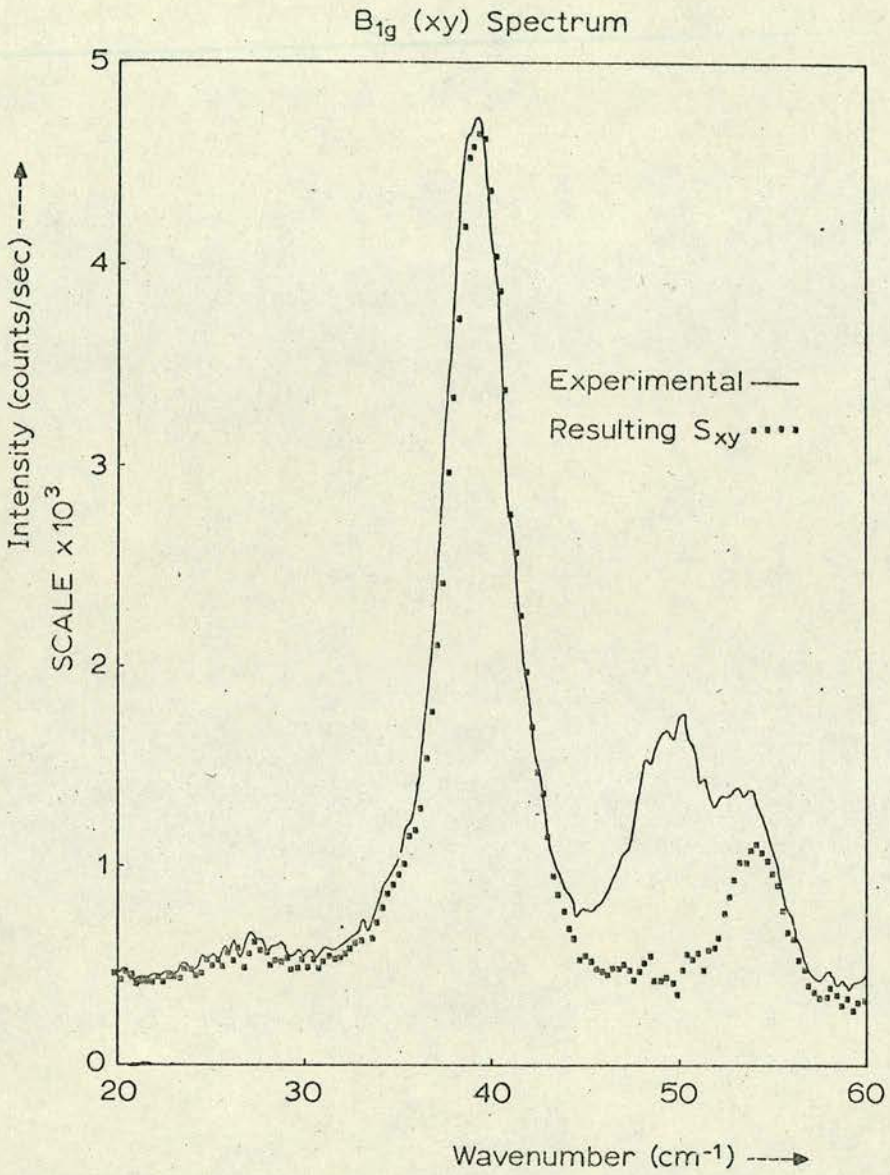

Fig. 3. $B_{1g}(xy)$ spectrum.

5. Discussion

In this section we account for the basic features of the A_{1g} and B_{1g} spectra. The discussion would also be applicable to B_{2g} and B_{3g} modes but with increased complexity since there are four modes to consider. It is assumed that the lowest order contribution to fluctuations in the crystal polarisability arises from rotatory displacement of the

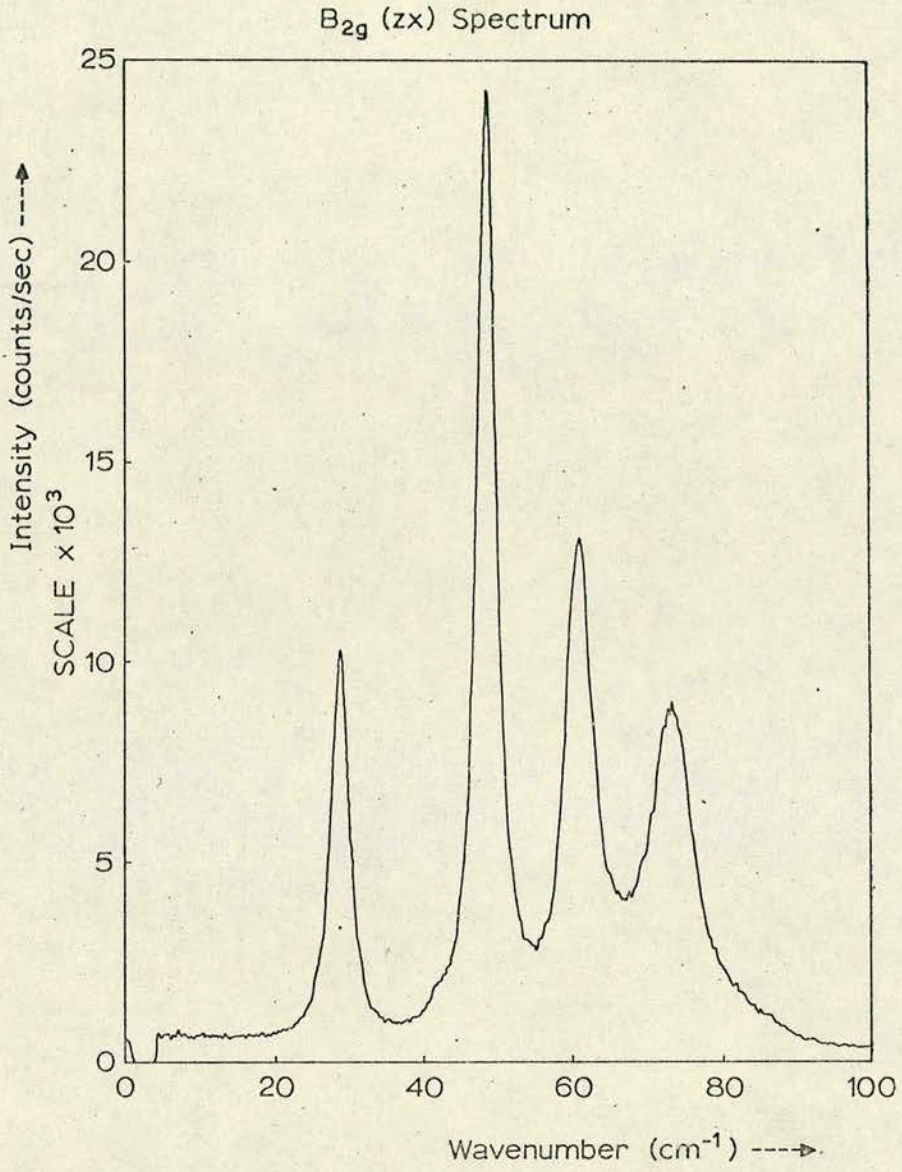

Fig. 4. $B_{2g}(zx)$ spectrum.

S_8 molecules. In this approximation translatory motion of the molecules does not modify the crystal polarisability.

Starting with a molecular polarisability of the form:

$$\alpha_m = \begin{bmatrix} a & & \\ & b & \\ & & b \end{bmatrix}$$

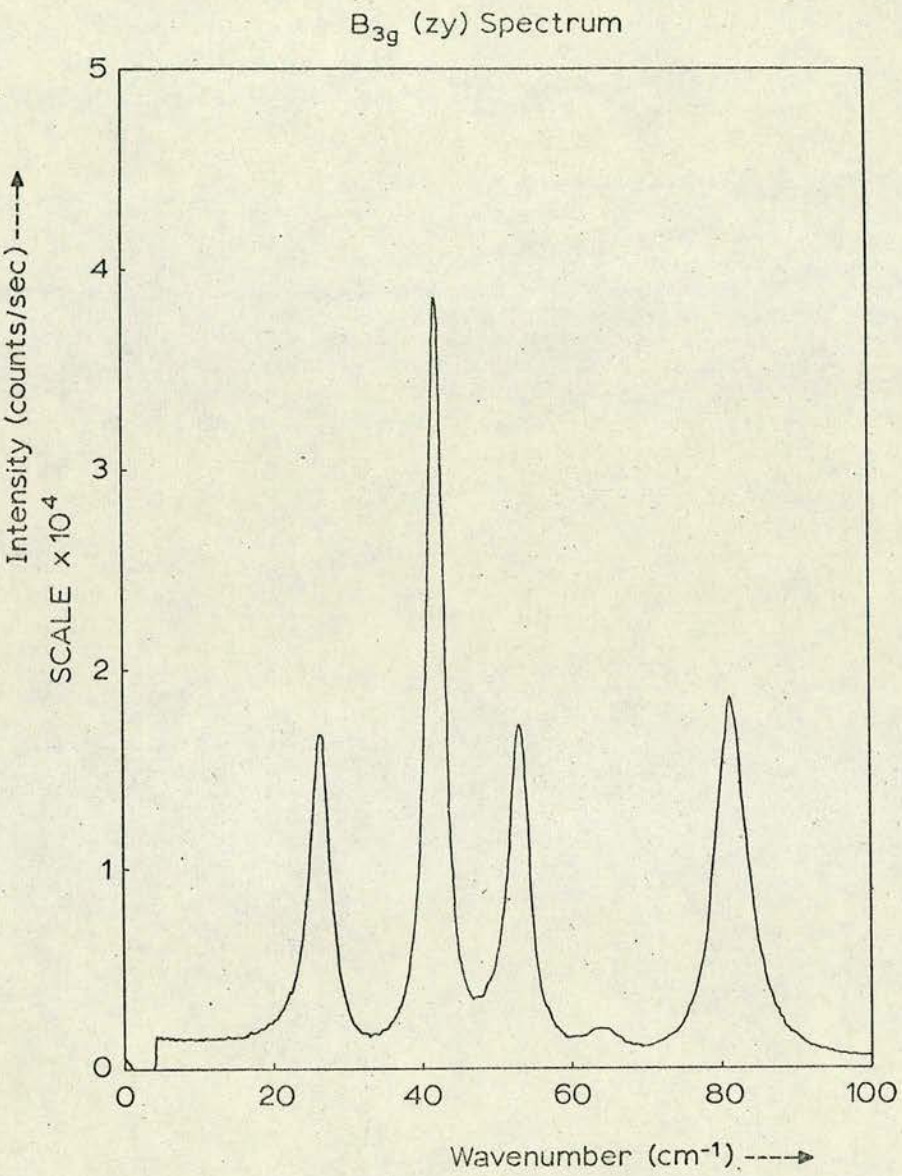

Fig. 5. $B_{3g}(zy)$ spectrum.

With the molecular x(C_4) axis rotated by ϕ off the crystal x axis, the contributions to the crystal polarisability for molecules type 1 and 2 are respectively:

$$\alpha_c^1 = \begin{bmatrix} \lambda & \nu & \\ \nu & \mu & \\ & & b \end{bmatrix} \quad \alpha_c^2 = \begin{bmatrix} \lambda & -\nu & \\ -\nu & \mu & \\ & & b \end{bmatrix};$$

where

$$\lambda = \cos^2\phi a + \sin^2\phi b$$
$$\mu = \cos^2\phi b + \sin^2\phi a$$
$$\nu = 2\sin\phi\cos\phi(a-b).$$

Symmetry coordinates for the A_g and B_{1g} modes may be introduced as follows:

	x^1	y^1	z^1	R_x^1	R_y^1	R_z^1	x^2	y^2	z^2	R_x^2	R_y^2	R_z^2
A_g	0	0	$+\delta z$	0	0	$+\delta\phi$	0	0	$-\delta z$	0	0	$-\delta\phi$
B_{1g}	0	0	$+\delta z$	0	0	$+\delta\phi$	0	0	$+\delta z$	0	0	$+\delta\phi$

Since molecules 3 and 4 are related to 1 and 2 by a centre of inversion, and only even modes are Raman active, they give an identical contribution and need not be considered further.

It can be seen that these modes correspond to in-phase and out-of-phase rotatory oscillations about the z axis, together with a displacement along the z axis which we may ignore. The oscillations, $\delta\phi$, produce a change in the polarisability as follows:

$$\delta\alpha \propto \delta\phi \sin 2\phi \begin{bmatrix} a-b & & \\ & a-b & \\ & & 0 \end{bmatrix} \quad \text{Rotations in phase}$$

$$\delta\alpha \propto \delta\phi \cos 2\phi \begin{bmatrix} 0 & a-b & \\ a-b & 0 & \\ & & 0 \end{bmatrix} \quad \text{Rotations antiphase}$$

Thus

$$\langle\delta\alpha^2\rangle \sim \langle\delta\phi^2\rangle \sin^2 2\phi \quad \ldots A_{1g}$$
$$\sim \langle\delta\phi^2\rangle \cos^2 2\phi \quad \ldots B_{1g}$$

These expressions show that no intensity is expected in the zz spectrum whereas equal intensities are expected in xx and yy. This is indeed what is observed, even if the xx and yy intensities are not quite identical. The fact that the peak at 89 cm^{-1} remains with strong intensity in zz shows that it does not have the character of an external mode for which the above analysis applies. It is therefore unambiguously identified as an internal mode.

Since the intensities of the A_g modes are both approximately proportional to $\langle\delta\phi^2\rangle$ intensity will be seen from only one mode when the eigenvectors of these modes are respectively pure translatory and pure rotatory. We interpret the observation of only one A_g mode as a demonstration of this behaviour.

A similar argument applies to the B_{1g} modes. Here the lower frequency mode should have the larger rotational component. The intensities are approximately in the ratio 5.5:1 so that the rotational components of the eigenvectors, $\delta\phi$, are in the ratio 2.3:1.

In addition we can compare the intensities for the A_g and B_{1g} modes by the ratio

$\sin^2 2\phi/\cos^2 2\phi$ where $\phi = 141°18'$ [6]. This gives a ratio of 20:1. The experimental results lie between 13:1 and 20:1, which is in reasonable agreement.

6. Conclusion

The assignments of the lattice frequencies have been clarified by applying simple computer aided methods to the spectra. The manipulated $A_g(zz)$ spectrum showed no peak in the lattice region of any significance. That this fact should be borne out by a theoretical analysis provides a good test of the effectiveness of the technique. We therefore have confidence in applying it to the B_{1g} spectrum. A similar subtraction technique has also proved successful in separating the A_1 and E modes in cubic crystals [12].

Both the A_g and B_{1g} spectra can be described by a simple model based on the molecule preserving its identity within the crystal. This bears out the central assumption that sulphur can be treated dynamically as a crystal of rigid molecules except where the lattice and internal vibration spectra overlap. The information gained about the rotational components of the A_g and B_{1g} mode eigenvectors should be of use in further comparison with lattice dynamical calculations.

Acknowledgements

The authors are indebted to Dr R. P. Rinaldi and Dr G. S. Pawley of this department for many helpful discussions about the dynamics of sulphur; to Dr J. Sherwood, Strathclyde University, who provided the sample; to Dr T. Luty who suggested the calculation. The work was supported by the S.R.C.

References

1. Venkateswarlu, K: *Proc. Ind. Acad. Sci.* **A12**, 453 (1940).
2. Ward, A. T: *J. Phys. Chem.* **72**, 4133 (1968).
3. Anderson, A. and Loh, Y. T.: *Can. J. Chem.* **47**, 879 (1969).
4. Ozin, G. A: *J. Chem. Soc.* (A) 116 (1969).
5. Pawley, G. S., Rinaldi, R. P., and Windsor, C. G: in M. A. Nusimovici (ed.), *Proceedings of the International Conference on Phonons*, Rennes, Flammarion, 1971, p. 223.
6. Pawley, G. S. and Rinaldi, R. P: *Acta. Cryst.* **B28**, 3605 (1972).
7. Rinaldi, R. P. and Pawley, G. S.: *Nuovo Cimento* **16B**, 55 (1973).
8. Rinaldi, R. P: Ph.D. Thesis, University of Edinburgh, 1973.
9. Porto, S. P. S., Giordimaine, J. A., and Damen, T. C: *Phys. Rev.* **147**, 608 (1966).
10. Arthur, J. W. and Lockwood, D. J.: *J. Raman Spectrosc.* 2 (1974).
11. Pawley, G. S. and Kurittu, J: to be published.
12. Lockwood, D. J: private communication.